Controlling Light-Matter Interaction between Localized Surface Plasmons and Quantum Emitters

Dissertation zur Erlangung des
naturwissenschaftlichen Doktorgrades
der Julius-Maximilians-Universität Würzburg

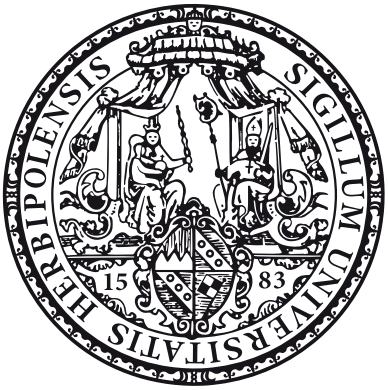

vorgelegt von

Heiko Groß

aus Schweinfurt

Würzburg 2018

Eingereicht am: 26.03.2018

bei der Fakultät für Physik und Astronomie

1. Gutachter: Prof. Dr. Bert Hecht

2. Gutachter: Prof. Dr. Matthias Bode

3. Gutachter: ...

der Dissertation

Vorsitzende(r): Prof. Dr. Stephan Reitzenstein

1. Prüfer: Prof. Dr. Bert Hecht

2. Prüfer: Prof. Dr. Matthias Bode

3. Prüfer: Prof. Dr. Björn Trauzettel

im Promotionkolloquium

Tag des Promotionskolloquiums: 17.04.2019

Doktorurkunde ausgehändigt am: ...

To my family and my fiancée Anna.

Abstract

Metal nanostructures have been known for a long time to exhibit optical resonances via localized surface plasmons. The high electric fields in close proximity to the metal surface have prospects to dramatically change the dynamics of electronic transitions, such as an enhanced spontaneous decay rate of a single emitter. However, there have been two major issues which impede advances in the experimental realization of enhanced light-matter interaction. (i) The fabrication of high-quality resonant structures requires state-of-the-art patterning techniques in combination with superior materials. (ii) The tiny extension of the optical near-field requires precise control of the single emitter with respect to the nanostructure. This work demonstrates a solution to these problems by combining scanning probe and optical confocal microscopy. Here, a novel type of scanning probe is introduced which features a tip composed of the edge of a single crystalline gold sheet. The patterning via focused ion beam milling makes it possible to introduce a plasmonic nanoresonator directly at the apex of the tip. Numerical simulations demonstrate that the optical properties of this kind of scanning probe are ideal to analyze light-matter interaction. Detailed experimental studies investigate the coupling mechanism between a localized plasmon and single colloidal quantum dots by dynamically changing coupling strength via their spatial separation. The results have shown that weak interaction affects the shape of the fluorescence spectrum as well as the polarization. For the best probes it has been found that it is possible to reach the strong coupling regime at the single emitter level at room temperature. The resulting analysis of the experimental data and the proposed theoretical models has revealed the differences between the established far-field coupling and near-field coupling. It has been found that the broad bandwidth of plasmonic resonances are able to establish coherent coupling to multiple transitions simultaneously giving rise to an enhanced effective coupling strength. It has also been found that the current model to numerically calculate the effective mode volume is inaccurate in case of mesoscopic emitters and strong coupling. Finally, light-matter interaction is investigated by the means of a quantum-dot-decorated microtubule which is traversing a localized near-field by gliding on kinesin proteins. This biological transport mechanism allows the parallel probing of a meta-surface with nm-precision. The results that have been put forward throughout this work have shed new light on the understanding of plasmonic light-matter interaction and might trigger ideas on how to more efficiently combine the power of localized electric fields and novel excitonic materials.

Zusammenfassung

Metallische Nanostrukturen sind seit langer Zeit bekannt dafür optische Resonanzen durch lokalisierte Oberflächenplasmonen zu zeigen. Hohe elektrische Felder in direkter Nähe zur Metalloberfläche versprechen dramatische Dynamikänderungen von elektrischen Übergängen wie z.B. die gesteigerte spontane Zerfallsrate eines Einzelemitters. Es gibt jedoch zwei maßgebliche Gründe warum die Fortschritte der experimentellen Realisierung von Licht-Materie Wechselwirkung ausgebremst wird. (i) Die Herstellung von qualitativ hochwertigen resonanten Strukturen benötigt modernste Strukturierungsmethoden sowie die bestmöglichen Materialeigenschaften. (ii) Die winzigen Dimensionen von optischen Nahfeldern erfordern eine präzise Kontrolle des Einzelemitters im Bezug zur Nanostruktur. Diese Arbeit löst diese Probleme durch die Kombination eines Rasterkraftmikroskops mit einem optischen Konfokalmikroskop. Dabei wird eine neuartige Rastersonde vorgestellt welche eine Spitze aufweist die aus der Ecke einer monokristallinen Goldflocke besteht. Die Strukturierung mittels eines fokussierten Ionenstrahls ermöglicht es einen plasmonischen Nanoresonator direkt an der Spitze der Sonde herzustellen. Numerische Simulationen haben gezeigt, dass die optischen Eigenschaften für diese Art von Sonde ideal sind um Licht-Materie Wechselwirkung zu untersuchen. Die hier gezeigten experimentellen Studien haben den Kopplungsmechanismus zwischen lokalisierten Plasmonen und einzelnen kolloidalen Quantenpunkten untersucht indem die Kopplungstärke dynamisch über den Abstand kontrolliert wurde. Die Ergebnisse haben gezeigt, dass schwache Wechselwirkung einen Einfluss auf die Form des Fluoreszenzspektrums als auch auf die Polarisation hat. Die besten Sonden haben gezeigt, dass es möglich ist starke Wechselwirkung mit Einzelemittern bei Raumtemperatur zu erreichen. Die resultierende Analyse der experimentellen Daten und die aufgestellten theoretischen Modelle haben die Unterschiede zwischen der etablierten Fernfeldkopplung und der Nahfeldkopplung aufgezeigt. Dabei wurde beobachtet, dass die große Bandbreite von plasmonischen Resonanzen es möglich macht kohärent mit mehreren Übergängen gleichzeitig zu koppeln und dabei die effektive Kopplungsstärke zu höhen. Es wurde auch festgestellt, dass das aktuelle Model zur numerischen Beschreibung von effektiven Modenvolumen Ungenauigkeiten bei mesoskopischen Emittern und starker Wechselwirkung aufzeigt. Zuletzt wird die Licht-Materie Wechselwirkung mittels Quantenpunkt-bestückten Mikrotubuli untersucht, die auf Kinesin Proteinen durch ein lokalisiertes Nahfeld gleiten. Dieses biologische Transportsystem erlaubt es eine Meta-Oberfläche mit nm-Präzision parallel zu untersuchen. Die Ergebnisse, die diese Arbeit hervorgebracht hat, wirft neues Licht auf das Verständnis von plasmonischer Licht-Materie Wechselwirkung und könnte als Grundlage dienen neue Ideen zu entwickeln um effizienter die Stärke von lokalisierten elektrischen Felder und neuartiger exzitonischer Materialien zu kombinieren.

Contents

1 Introduction

Light — a physical phenomenon which has already been known more than thousand years ago. Its origin and description has been boggling the minds of many prominent philosophers and scientists such as Aristotle, Plato and Sir Isaac Newton. Yet, light has already been an essential tool for many pioneers in the field of physics such as microscopy and astronomy. The accurate description of light as an electro-magnetic wave by James Clerk Maxwell about 150 years ago provides the theory which describes the majority of everyday optical phenomena.

Nowadays, light has become an indispensable asset for nearly every technological and industrial branch such as high-speed communication and semiconductor manufacturing. Advances in the fields of nanofabrication and detector sensitivity over the last decades has paved the way for the experimental field of near-field optics and the study of single quanta of light and matter.

The manifestation of these two entities are completely different: As proposed by Max Planck in 1900, the energy E of a single photon depends on its frequency ω and is quantized via the relation $E = \hbar\omega$, where $\hbar$ is Planck's constant, the quantum of action. An electric excitation is characterized via the interaction of an electron and an electron hole which are bound inside a material - an exciton.

The fundamental challenge when investigating the interaction of a single photon and a single electronic excitation is their size discrepancy. On the one hand, the size of a photon is limited due to the effect of diffraction to a dimension of about half of its corresponding wavelength. This effect also limits the minimum diameter of a perfectly focused beam which can be achieved with visible light to about 250 nm. The dimension of an exciton with the same energy, on the other hand, can be quantified by the electron-hole distance which is typically less than one nanometer. Based on this estimation, one can calculate the probability of a tightly focused stream of photons to interact with a single exciton. On average, only one of 10^5 photons is able to transfer its electro-magnetic energy to form an exciton.

In comparison to free space photons, light-matter interaction can be significantly improved by the use of an optical cavity. Reflection in between two mirrors increases the number of passes of a single photon and therefore increases the probability of absorption. Sophisticated cavity designs are capable of preserving photons

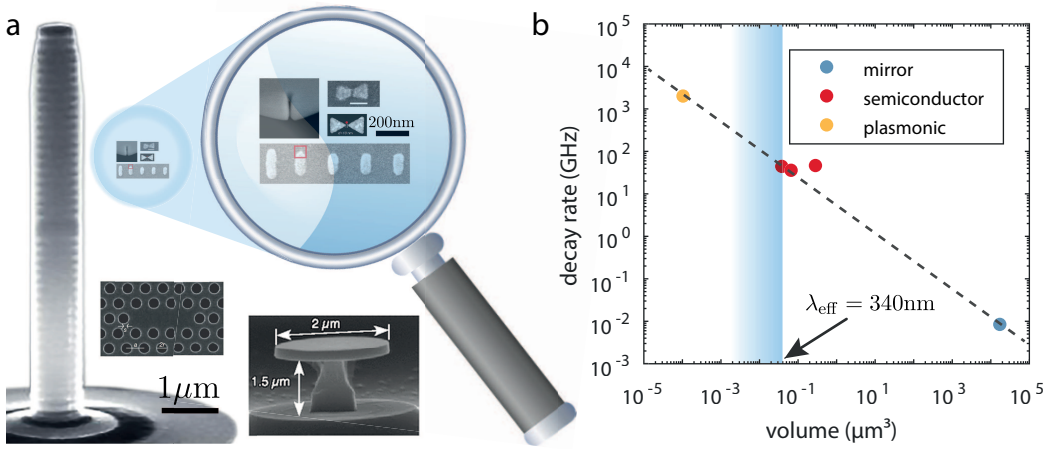

Figure 1.1 – Size and decay rate comparison between semiconductor and plasmonic resonators. a, Scanning electron microscopy image of different semiconductor cavities (bottom: micropillar, photonic crystal, microdisc) and optical nanoantennas (top: nanoslit, bowties, yagi-uda). **b,** Comparison of the of the decay rate and mode volume of different types of resonators. A volume below λ^3_{eff} (indicated by the blue shaded area) can only be achieved by plasmon resonances. Reprinted (adapted) with permission from reference [1, 2, 7]. Copyright (2018) Nature Publishing Group. From [6]. Reprinted with permission from AAAS. Reprinted figure with permission from reference [3]. Copyright (2018) by the American Physical Society. Reprinted (adapted) with permission from reference [8]. Copyright (2018) American Chemical Society.

for up to 10,000 cycles thereby mitigating the size discrepancy between the photon and exciton. The size of these semiconductor resonators fairly represent the volume of a few λ^3 which is the limit due to diffraction. Scanning electron microscopy images of different types of semiconductor resonators are shown in Fig. 1.1a [1–3].

A different approach to light confinement which has become popular in recent years is the use of plasmons, a surface wave at the interface between a metal and a dielectric. Here, significantly enhanced optical near-fields arise due to the coupling between the electric field and collective charge density oscillations. Metal nanoparticles also exhibit resonance effects due to their shape which can enhance impinging optical near-fields by a factor of 10,000. The property of amplifying electro-magnetic fields at optical frequencies has led to the name 'optical nanoantenna' [4, 5]. The law of reciprocity also ensures that emission from confined space is enhanced and efficiently connected to the far field. In addition to light confinement the shape of optical nanoantennas has also been designed to suit other purposes such as broad band or unidirectional emission. A collection of different types of optical nanoantennas and their size comparison to semiconductor cavities is shown in Fig. 1.1a [6–8].

Optical nanoantennas adopt a similar description as conventional cavities, however, with the two major differences of sub-diffractional light confinement and a broader spectral linewidth. The reduction of their 'modal volume' from the micrometer to the nanometer scale opens a new route in the field of light-matter interaction.

The broad linewidth of plasmonic modes is directly tied to a fast decay rate which is of major importance for future nano-circuit applications where the decay rate is the physical limit on how fast information can be processed. An illustration on how the decay rate scales with the size of the resonator is shown in Fig. 1.1b. A fundamental confinement limit due to diffraction is reached for semiconductor [1–3] and mirror cavities [9] when the volume becomes comparable to λ_{eff}^3, where the effective wavelength λ_{eff} within the medium is usually around 340 nm. Further reduction of the confinement by more than two orders of magnitude allows for faster decay rates in the THz-range.

Extreme light confinement, the ability to squeeze a single photon into a tiny volume, affects the fluorescence rate of single emitters such as molecules or quantum dots [7, 10]. The main contributor to this effect is the increase of the spontaneous emission rate due to an increased density of optical states. Enhanced fluorescence intensity and high quantum yields are the advantageous effects that occur in the so called 'weak coupling' regime. Further confinement eventually leads to strong coupling, the regime where the interaction between the optical near-field and the emitter is larger than the loss rates of the individual constituents. The resulting hybrid state composed of a plasmon and an exciton features novel and exciting quantum phenomena including the possible realization of a sub-diffraction single-photon non-linearity [11, 12].

An advantageous property of plasmons is the fact that coupling effects between a plasmon resonance and an emitter can be realized at ambient conditions. In case of semiconductor resonators, cryogenic temperatures are essential in order to overlap the narrow emission lines of the emitter and cavity resonance. In addition, non-radiative losses due to phonon coupling would render any coupling effects unobservable at room temperature. Plasmons and their intrinsic broad linewidth, however, make a tedious tuning of the resonance wavelength obsolete. Furthermore, the fast plasmon decay rate is capable of suppressing non-radiative processes at ambient conditions.

A major technological issue that is associated with a confined optical field is the reliable alignment of a single emitter with a plasmonic nanostructure in order to achieve sufficient interaction. While it is possible to locally functionalize the metal structure to attract a quantum emitter [6], most studies rely on arrays of structures with a layer of randomly distributed emitters [7, 13]. Eventually, one can find a structure by chance with an emitter in close proximity. This work concentrates on two different concepts on how to deliberately control the distance between a single quantum emitter and an optical near-field which allows for a much more deterministic and reliable investigation of the coupling behavior.

One approach is the use of a scanning probe in combination with a nanoantenna, a technique which has already proven to be successful [14]. The combination of scanning probe microscopy and optical microscopy represents the main experimental part of this work. The associated development of a novel type of resonant scanning probe shows unprecedented control over the interaction between a single emitter and a plasmonic mode.

Another method which is developed in this work is to make use of motor proteins, a biological transport system which naturally occurs in cells. Here, they are used to move single quantum emitters across the surface of a substrate and through the confined optical near-field of a nanostructure.

Both of the experimental approaches demonstrate a reliable and precise control over the distance between near-fields and single emitters. The conclusions that have been drawn from the experimental results have provided new insights on the coupling mechanism of quantum emitters with localized surfaces plasmons. Especially for the scanning probe concept, the broadband plasmon resonance and the corresponding plasmon decay on the fs-scale unveils coherent multi-level coupling as a novel interaction scheme.

The following chapter 2 outlines a general understanding of the coupling mechanism between light and matter. Here, established theoretical concepts are presented in a compact fashion. At first, the description of light at the interface between a metal and a dielectric material is summarized which is followed by the description of resonances in this regard. Next, the theoretical description of single emitters on a fundamental level is presented. Finally, the basic description of interaction between light and excitons is discussed in regard to plasmons and their capability to confine light.

Chapter 3 of this work presents a thorough background on the concept of colloidal semiconductor nanocrystals and the advancements of this novel type of quantum emitter. These chemically grown nanoparticles have an average diameter of 10 nm or less and are able to confine an exciton with an energy in the optical regime. The exciton energy can be tuned by adjusting the size of these quantum dot structures which makes this type of emitter a versatile tool in experiments. After the description of quantum confinement, the quantum mechanical analysis yields insights on the complex nature of this type of emitter. The current understanding of various effects which are displayed by colloidal nanocrystals is thoroughly summarized. This includes spectral diffusion, fluorescence intermittency, doping as well as the coupling properties that are displayed when metal nanostructures are brought in close proximity to the nanocrystal.

Next, chapter 4 describes the experimental techniques that are required in the field of plasmonic spectroscopy. In specific, the challenges and concept of realizing an atomic force microscope in combination with a confocal microscope are described in detail. Additionally, the fabrication process of optically resonant near-field probes as well as single-emitter decorated substrates is thoroughly described. The technique of using a scanning probe in combination with optical microscopy is an appealing but also complicated approach. Therefore, all technological aspects on how to achieve reliable and accurate results are precisely documented.

The optical properties of a resonant scanning probe is described in chapter 5. Here, the particular design and its purpose is highlighted and discussed. In particular, finite-difference time-domain simulations are employed to quantify the potential of this unique scanning probe.

Experimental realization of coupling between an optical nanoantenna and single

quantum dots is presented in chapter 6. First, measurements of the intrinsic optical characteristics of semiconductor quantum dots are presented. Next, the results of the coupling between quantum dots and an unstructured gold tip are presented. These measurements clearly demonstrate the differences to experiments with resonant scanning probes. Here, spectrally resolved measurements show how optical nanoantennas can shift the emission resonance as well as influence the emission polarization of quantum emitters.

The following chapter 7 demonstrates the results on the study with a scanning probe that enters the strong coupling regime with a single quantum dot. The flexibility of the scanning probe approach allows for various measurements such as a tunable control over the coupling strength via spatial displacement of the tip. These experimental results are verified by numerical simulations as well as full quantum mechanical models. Interestingly, a careful analysis gives a hint on the frontiers in the current description of strong coupling effects between mesoscopic emitters and a plasmonic near-field. It is found that the presence of a band-edge fine structure does impact the process of strong coupling with a quantum emitter. The broadband nature of plasmon resonances allows to collectively interact with multiple states within one quantum emitter and therefore boosting the effective coupling strength. Further studies in this chapter apply well-known methodologies of near-field coupling to highlight the promising and exciting potential of near-field strong coupling.

Finally, chapter 8 is dedicated to the experimental results of a biological transport mechanism for colloidal quantum dots. Here, quantum dots are attached to microtubules which are then being transported as their cargo. The movement is enabled via motor proteins which are distributed over a gold surface. Proof of principle measurements reveal an unprecedented precision on moving and tracking the quantum dot position relative to a plasmonic near-field.

2 Theoretical foundations

A comprehensive analysis and interpretation of experimental results requires a thorough knowledge of the theoretical modeling of the participating processes. In the field of light-matter interaction between plasmons and colloidal quantum dots several different physical phenomena come into play. This chapter provides a summary of the state-of-the-art literature of all the different topics that are covered in this work. The first section deals with the principles of charge density waves at the surface of metal nanoparticles (localized surface plasmons) and how they can be used to create subdiffractional optical resonators. In the following, the basic concept of the single emitter is introduced. Finally, the interaction between single emitters and optical resonators is discussed based on a semi-classical as well as fully quantum-mechanical framework.

2.1 Plasmons

2.1.1 Optical properties of gold

Metals are known to possess a large amount of loosely bound electrons. The delocalized charge carriers can, in first approximation, move freely through the bulk crystal. Surprisingly, many metal properties, including optical, electrical and thermal responses, can be derived solely based on the so-called free electron model. In the following this model is used to describe the optical characteristics of gold.

An external electric field $E(\omega)$ induces a force on the electrons. The dipole moment due to the microscopic displacement of single electrons adds up to a polarization inside the bulk metal. The frequency dependent polarization $P(\omega) = \varepsilon_0 \chi_e(\omega) E(\omega)$ is proportional to the external field strength and scales with the vacuum permittivity ε_0 and the material dependent electric susceptibility $\chi_e(\omega)$ [15]. The superposition of electric field and polarization is described by the displacement field which is defined as

$$D(\omega) = \varepsilon_0 \varepsilon(\omega) E(\omega) = \varepsilon_0 E(\omega) + P(\omega). \tag{2.1}$$

Here, the introduced permittivity $\varepsilon(\omega)$, also referred to as dielectric function, is a complex function defined as $\varepsilon(\omega) = \varepsilon'(\omega) + i\varepsilon''(\omega)$ which characterizes the interaction of a material with an electric field. The real part quantifies the polarizability due to an external field while the imaginary part describes the losses in the material due to electron scattering by defects, surface states or lattice vibrations.

The plasma frequency marks the characteristic photon energy where metal looses its reflectivity and becomes transparent. This frequency $\omega_p = \sqrt{ne^2/(m^*\varepsilon_0)}$ only depends on the metal specific electron density n, electron charge e, effective electron mass m^* and the permittivity of vacuum ε_0. Within the Drude-Sommerfeld free electron model one can derive an expression for the dielectric function

$$\varepsilon_{\text{Drude}}(\omega) = 1 - \frac{\omega_p^2}{\omega^2 + i\Gamma\omega} \tag{2.2}$$

where Γ is a damping term due to electron scattering [15]. A comparison of this model to experimental data at optical wavelengths is shown in Fig. 2.1. At wavelengths above 650 nm the model represents the measured data fairly well. However, below 650 nm the imaginary part is underestimated due to interband transitions which are responsible for an increased absorption. These transitions can be compared to an excitation of an oscillation of bound electrons which can be modeled in a similar fashion as the free electron model. Here, the electrons experience a restoring force described via a spring constant α. The resulting correction term has a Lorentzian form which can be expressed as

$$\varepsilon_{\text{Interband}}(\omega) = 1 + \frac{\tilde{\omega}_p^2}{(\omega_0^2 - \omega^2) - i\gamma\omega}, \tag{2.3}$$

where $\tilde{\omega}_p = \sqrt{\tilde{n}e^2/(m\varepsilon_0)}$ $\tilde{n}$ describes the oscillation frequency of the bound electrons with density $\tilde{n}$ and $\omega_0 = \sqrt{\alpha/m}$. Further higher energy transitions add up to a phenomenological constant dielectric background of $\varepsilon_\infty = 5$. The comparison of $\varepsilon(\omega) = \varepsilon_\infty + \varepsilon_{\text{Drude}}(\omega) + \varepsilon_{\text{Interband}}(\omega)$ to experimental data is displayed in Fig. 2.1 and shows excellent agreement throughout the entire visible wavelength regime.

The dielectric function of a metal provides all the necessary information about its suitability for field enhancement via surface plasmons which will be discussed in the next section. The data of Johnson and Christy and the analytic fit is used throughout this work to model the dispersion of gold in numerical simulations as well as to calculate the energy density inside the metal.

2.1.2 Plasmonic materials

An electro-magnetic mode within a dielectric medium much larger than the wavelength can undergo a self-sustaining oscillation. That means, the energy is reversibly transferred from an electric field into a magnetic field. If the mode is confined in a subwavelength volume, Maxwell's equations dictate that the magnetic energy that can be stored is smaller than the electric energy [17, 18]. This,

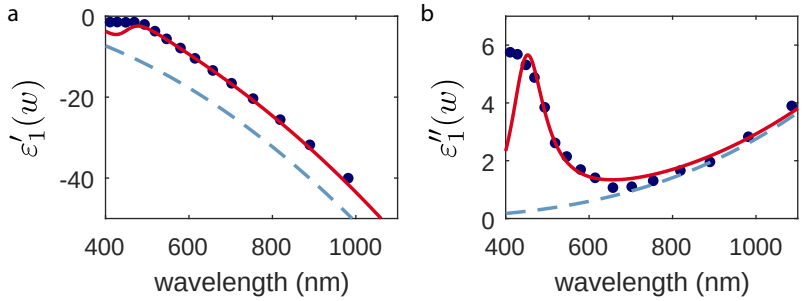

Figure 2.1 – Dielectric function of gold in the visible wavelength spectrum. Blue dots represent experimental data by Johnson and Christy [16]. The blue dashed line shows the Drude-Sommerfeld model without interband transitions. The red line represents model with interband transitions. **a,** Real part of the dielectric function. **b,** Imaginary part of the dielectric function.

however, implies that the periodic energy exchange vanishes. In order to maintain a self-sustaining oscillation, the energy has to be stored differently, e.g. as kinetic energy of free moving charge carriers. This property is predominantly provided by metals and reflected in their negative real part of the dielectric function $\varepsilon'(\omega)$ [17]. The coherent oscillation of delocalized electrons inside the metal is called a surface plasmon. Arising localized optical near-fields outside the metal are tightly confined and well below the diffraction limit.

The required negative $\varepsilon''(\omega)$, however, comes at a cost of increased losses. As the real part of the dielectric function of metals is negative, there is also a substantial imaginary part which leads to damping of the electron motion (see Fig. 2.1). This has been, and still is, regarded as the major issue with plasmons and their applicability to next-generation nanocircuitry [17, 19]. Among the variety of available metals there are substantial differences regarding ohmic damping and the suitable wavelength range. For example, silver offers significantly smaller losses in comparison to gold, especially in the wavelength regime of 500 nm. However, there are also technical aspects that can limit the practicality of certain materials for the usage in plasmonic systems. Silver, for example, is prone to exhibit oxidation of any exposed surface at ambient conditions which counteracts the superior optical performance of the bulk. The chemical stability of gold is one of the main reasons why gold is currently the primary material for plasmonic systems despite their moderate optical performance.

An active field of research is the quest to find alternative materials to silver and gold which offer superior optical properties [18, 20–23]. There have been figure of merits in order to quantify the plasmonic performance of materials solely based on their dielectric function [24]. However, it has also been shown that there are lower limits for the losses of plasmonic materials [24–26]. Further loss reduction eventually leads to a vanishing of the negative real part of the dielectric function, the fundamental ingredient for surface plasmons.

Throughout the course of this work, the plasmonic material of choice will be gold. As it will be shown in other sections, gold combines a multitude of properties

beyond the dielectric function which include crystallinity, mechanical and chemical stability as well as serving as a material being suitable for high precision nanostructuring.

2.1.3 Propagating surface plasmons

At the interface between a metal and a dielectric material Maxwell's equations allow the occurrence of surface modes. These surface modes are also called surface plasmon polaritons (SPPs) and arise via the strong interaction between the kinetic energy of the electrons inside the metal and the electric field within the dielectric material. The necessary boundary conditions for SPPs which have to be met involve the dielectric function of the metal (ε_1) and dielectric (ε_2).

A surface plasmon is bound to the interface and therefore has a real wavevector k_x along the interface and purely imaginary wavevector k_z components inside the media (Fig. 2.2a). Assuming that the metal satisfies the condition $|\varepsilon_1''| \ll |\varepsilon_1'|$ the effective surface plasmon wavelength can be calculated to [15]

$$\lambda_{\mathrm{SPP}} = \frac{2\pi}{k_x'} \approx \sqrt{\frac{\varepsilon_1' + \varepsilon_2}{\varepsilon_1' \varepsilon_2}}\lambda. \tag{2.4}$$

It can be seen that for a material combination with $\varepsilon_1'/\varepsilon_2 < 1$ the plasmon wavelength is always smaller than free space wavelength λ.

Whereas the wavelength of a surface plasmon is determined by the real parts of the dielectric function, its propagation length is also affected by the imaginary part of $\varepsilon_1(\omega)$. At a wavelength of 633 nm a plasmon at a gold/vacuum interface can propagate 10 μm before the near-field intensity strength drops to $1/e$ of the initial value.

Perpendicular to the interface plane the electric field has a purely imaginary wavevector. The evanescent field decays exponentially with a characteristic length depending on the respective dielectric function. At a gold/vacuum interface the decay length into gold is $k_{z,1} = 28\,\mathrm{nm}^{-1}$ at a wavelength of 633 nm. Towards the vacuum, on the other hand, the field decay length is much larger with a value of $k_{z,2} = 328\,\mathrm{nm}^{-1}$.

2.1.4 Metal-insulator-metal resonator

The properties of a plasmon at the interface between a dielectric and a metal, such as the effective surface plasmon wavelength, are solely described by their dielectric function. An additional interface in close proximity, however, can have a strong influence on the characteristics of the plasmon mode [27–30].

There are two possible configurations to introduce coupling between surface plasmons in order to create so called slot plasmon waveguides [31]. The configuration which consists of a metal slab surrounded by an insulating dielectric material is called an insulator-metal-insulator structure (IMI) as shown in Fig. 2.2b [32]. The

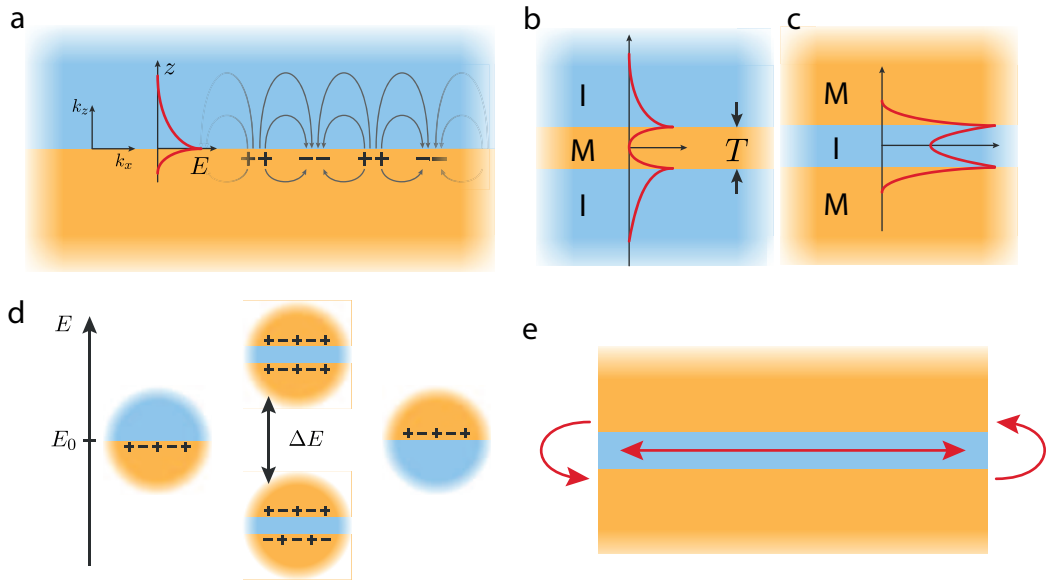

Figure 2.2 – Illustration of a surface plasmon and the corresponding configurations of slot waveguides. **a,** Planar surface plasmon. **b,** IMI configuration **c,** MIM configuration **d,** Illustration of the coupling and corresponding energy shift of two interfaces in MIM configuration and close proximity. **e,** Truncated MIM waveguide. Reflections at the ends of the waveguide lead to plasmon interference.

reverse configuration, a metal-insulator-metal structure (MIM), is sketched in Fig. 2.2c. The evanescent field of both plasmon modes extends into the slab material. As the distance T between the two interfaces reduces the two opposing plasmons experience mutual coupling which leads to a hybridization of the modes [31]. The two hybridized modes can be distinguished by their symmetries and their different dispersion relation.

The modes of the IMI and MIM configurations also have properties with respect to the ability to enhance and confine optical near-fields. For IMI modes the overlap of these fields with the dielectric medium increases as T is reduced [33]. The mode extension into the dielectric medium does not allow a tightly confined field.

The MIM configuration allows an increased confinement of optical near-fields as they get squeezed between the two metallic interfaces. It has been shown that for smaller T the mode extends less into the metal which leads to an increased confinement inside the dielectric material [34, 35]. Additionally, the overlap of the optical field with the metal is also reduced for small gaps [36]. Since this mode is mainly guided within a dielectric medium it features reduced ohmic losses and a larger decay length compared to other modes. The MIM concept is therefore an ideal configuration for the realization of highly localized optical near-fields for enhanced interaction with excitonic systems.

An additional major enhancement of optical near-fields can be achieved by creating a localized surface plasmon resonance (LSPR). Such a resonance is created by inducing a truncation to the waveguide (MIM/IMI) of a propagating plasmon mode

as shown in Fig. 2.2e [34–41]. The reflection coefficient hereby depends on the properties of the mode and increases with decreasing gap size [36]. The reflection of the propagating plasmon can lead to constructive interference and the formation of so-called localized surface plasmons (LSPs).

These LSPs are commonly localized to an isolated metallic nanostructure and characterized via a complex resonance wavelength. The ability to efficiently couple from the far field to a localized near-field has led to the novel field of research called 'optical nanoantennas' [4]. These nanoantennas consist of, in the simplest case, a metallic nanoparticle such as sphere. Here, the diameter and dielectric function of the metal determines the resonance wavelength of the LSP. More sophisticated particle geometries and multi-particle nanoantennas have been developed in order to shape the near-field and/or increase the radiation efficiency into the far field [42]. The appearance of a nanoantenna can be manifold as it is usually designed to suit a specific purpose.

Truncated MIM structures hold a variety of plasmonic properties which serves as an ideal platform for enhanced light-matter interaction. An in-depth study about the prospects of this structure are presented in chapter 5.

2.1.5 Optical resonance

An optical cavity is a well-known system which contains multiple electro-magnetic modes localized between two reflecting interfaces [43]. The resulting optical resonances in these systems can be characterized by their resonance wavelength as well as by their spectral width or lifetime. This section focuses on the origin and physical understanding of these basic properties.

The realization of a reflecting element can be vastly different depending on the size of the resonator. The oldest and most intuitive approach is an macroscopic cavity, which relies on two highly reflective mirrors separated by a few microns [9, 44]. Smaller realization of an optical cavity is achieved via highly reflective photonic crystals in one or two dimensions with an overall size of one wavelength [1,2]. Finally, the concept of surface plasmons can be regarded as photons bound to a metal surface. Their effective wavelength beyond the diffraction limit of visible light allows the realization of optical resonators on the nanoscale. A basic quantity suitable to make a comparison between different cavities is the decay rate κ of a single photon occupation which is defined as

$$\kappa = \frac{1}{\tau_{\text{cav}}}, \tag{2.5}$$

where τ_{cav} is the average lifetime of a single photon inside the cavity.

A simple yet physically accurate example of a cavity is a one dimensional Fabry-Perot interferometer with two high reflecting metalling mirrors separated by a dielectric medium with a refractive index n at a distance L [45]. Constructive interference at a wavelength λ occurs when the phase relation $\phi = \frac{4\pi nL}{\lambda}$ equals $2\pi m$, where m is an integer value and accounts for the order of the mode. This resonance

condition leads to a cavity length of $L = m\lambda/2n$, with an angular frequency of

$$\omega_{\mathrm{m}} = m\frac{\pi c}{nL}. \tag{2.6}$$

The ratio between the spectral width $\Delta\omega$ and the separation between adjacent resonances is defined as

$$\frac{\Delta\omega}{\omega_m - \omega_{m-1}} = \frac{1}{\mathscr{F}}, \tag{2.7}$$

where $\mathscr{F}$ is the finesse of the cavity which is given by $\mathscr{F} = \frac{\pi\sqrt{R}}{1-R}$ and R is the reflectivity of the mirrors [45]. It follows that the spectral width of a cavity can be written as

$$\Delta\omega = \frac{\pi c}{n\mathscr{F}L}. \tag{2.8}$$

The continuous reflection of light between the two mirrors leads to a periodic loss of photons if the reflectivity of the mirror is smaller than 1. Assuming an initial occupation of N photons inside the cavity, the amount of photons is reduced by a factor of $1-R$ for each reflection event. These loss events due to transmission through the non-perfect mirror occur at a rate of c/nL which leads to an overall photon loss rate of $dN/dt = -c(1-R)N/nL$. The solution of this differential equation $N(t) = N_0\exp(-\mathrm{t}/\tau_{\mathrm{cav}})$ yields the average photon lifetime of

$$\tau_{\mathrm{cav}} = \frac{1}{\kappa} = \frac{nL}{c\,(1-R)}. \tag{2.9}$$

In case of excellent reflectivity ($R \to 1$) it follows with equ. 2.8 that

$$\Delta\omega = \kappa. \tag{2.10}$$

A common quantity to describe the spectral width of a mode is the quality factor (Q-factor)

$$Q = \frac{\omega}{\Delta\omega}. \tag{2.11}$$

It is important to note that this formalism to calulate the decay rate assumes a 1-dimensional system with zero losses upon propagation and highly reflective mirrors. These assumptions are valid in case of cavities such as micropillars or 1-D photonic crystals where the defect mode is the fundamental guided mode [1]. However, it has been shown that 2-D photonic crystals already deviate from the previous description especially in the case of small L [46]. Further deviations are expected for plasmonic cavities due to losses upon propagation and a reflectivity which can no longer be approximated with $R \to 1$ [47].

This section has introduced the most important quantities to characterize optical resonances. The following sections will demonstrate how properties such as the Q-factor and the decay rate impact the interaction between light and matter.

2.2 Single emitter

The term 'single emitter' relates to a type of system which is able to serve as a single photon source. It can be regarded as a highly non-linear system since the occupation with a single photon completely changes the optical characteristics. These kind of systems occur at the nanometer scale where electronic bulk states are affected by quantum confinement effects. The transition between such states with an energy separation of $\hbar\omega$ can occur via interaction with a single photon with the same energy. Prominent examples of single emitters are fluorescent molecules, color centers within a crystal and quantum dots.

This section briefly revisits the most fundamental optical properties of single (quantum) emitters which will serve as a foundation for further descriptions of light-matter interaction.

2.2.1 Two-level system approximation

The experimental realization of a quantum emitter which solely consists of two states is not possible. Atoms are usually composed of many orbitals at different energies which can interact differently with a single photon depending on the quantum state of the initial and final state. Even a hydrogen atom, the most simple and thoroughly studied quantum system, consists of many different quantum states. Any optical excitation of an emitter has a finite interaction probability with every available transition. However, as it is shown in the following sections, in order to describe the most basic phenomena of the interaction between light and matter, it is not necessary to consider the entire complexity of atomic or even molecular orbitals. The required spectral overlap with the external field ($\hbar\omega$) is usually only valid for a single transition as depicted in Fig. 2.3a ($\hbar\omega_1 < \hbar\omega < \hbar\omega_2$). It is therefore possible to consider the simplest model which is a two-level system (TLS) reacting to an oscillating electric field [45, 48].

This section will be focusing on the fundamental mechanism on how light interacts with a quantum emitter and how it impacts the population of its energy levels.

The interaction between an incident photon and a TLS is described by the electric dipole operator $\hat{\mu} = e \cdot r$. The corresponding strength of a transition from the ground state $|1\rangle$ into the excited state $|2\rangle$ is given by the corresponding matrix element

$$\mu = \mu_{21} = \langle 2|\hat{\mu}|1\rangle = \int \phi_2^*(r)\hat{\mu}\phi_1(r)dV, \tag{2.12}$$

where $\phi_{1,2}$ describes the wavefunction of the ground and excited state [15].

The absorption of a plane wave can also be quantified via the absorption cross-section σ. For an isolated emitter without any dephasing the peak dipole absorption cross-section is given by $\sigma_{\text{abs}}(\omega_0) = \frac{3\lambda^2}{2\pi}$ [15]. It can be seen that $\sigma_{\text{abs}}(\omega_0)$ solely depends on the wavelength λ. This is only the case if the absorption spectrum is limited by the spontaneous decay rate of the emitter. However, at room temperature dephasing process due to phonon scattering lead to an increased spectral width and a decrease of the peak absorption cross-section.

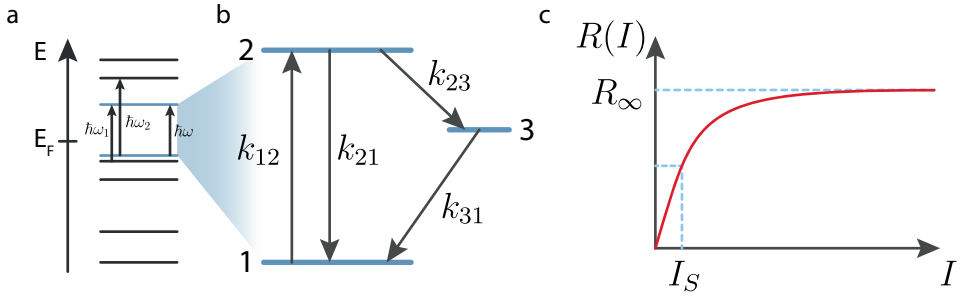

Figure 2.3 – Representation and dynamics of a quantum emitter. a, Level scheme of a quantum emitter near the Fermi energy. **b,** Close to $\hbar\omega$: Level representation of a quantum emitter with two levels with an optically active transition (1,2) and a dark state (3). **c,** Fluorescence saturation of a single quantum emitter.

The absorption cross-section can be used to determine the transition dipole moment of an emitter which has a broad emission and absorption bandwidth. Dependent on other experimentally quantifiable values the transition dipole moment can be expressed as

$$\mu = \sqrt{\frac{3}{4\pi^2}\hbar\sigma_{\text{abs}}(\omega_0)\gamma_0\varepsilon_0\lambda}, \tag{2.13}$$

where γ_0 is the FWHM of the extinction spectrum and λ the resonance wavelength [49–51]. The value of the dipole moment highly depends on the nature of the emitter. For fluorescent molecules dipole moments of about 4 D (Debye) have been reported [13] whereas other larger emitters, such as quantum dots, can reach values of up to 10 D. An overview of different emitters and their corresponding dipole moment can be found in a recent review article [52].

Another quantity which is also frequently being used is the oscillator strength f which is a dimensionless quantity. It relates to the dipole moment via

$$f = \frac{2m_0\omega_0\mu_{12}^2}{e^2\hbar}, \tag{2.14}$$

where m_0 is the electron mass and ω_0 is the transition frequency between the two states $|1\rangle$ and $|2\rangle$ [45].

2.2.2 Fluorescence intensity

Approximating the electronic structure of single emitter with discrete energy levels can be used to calculate the fluorescence intensity. As will be shown in this section, the fluorescence rate of a quantum emitter is linear to the excitation intensity in case of low field intensity. When the individual transitions within the emitter are on timescales which are much faster than the excitation rate the emitter will always be in the ground state before excitation. However, as the excitation rate increases, internal transitions have an impact on the average occupation of the ground state and therefore the fluorescence rate does not remain linear with the excitation rate. For a

quantitative investigation an emitter can be modeled as a three-level system, as depicted in Fig. 2.3b, where besides the ground $|1\rangle$ and excited state $|2\rangle$ an additional dark state $|3\rangle$ is considered. The dark state in between state $|1\rangle$ and $|2\rangle$ frequently occurs in experiments and its impact has therefore to be taken into account.

The change of occupation of all three states $\dot{p}_{1,2,3}$ for a single excitation is described by the following set of differential equations:

$$\begin{aligned} \dot{p}_1 &= -k_{12}p_1 + (k_\mathrm{r} + k_\mathrm{nr})p_2 + k_{31}p_3 \\ \dot{p}_2 &= k_{12}p_1 - (k_\mathrm{r} + k_\mathrm{nr} + k_{23})p_2 \\ \dot{p}_3 &= k_{23}p_2 - k_{31}p_3 \\ 1 &= p_1 + p_2 + p_3. \end{aligned} \tag{2.15}$$

The ground state is depopulated by an excitation rate k_{12} and gains occupations via decay from level $|2\rangle$ and $|3\rangle$. The population of the excited state can decay into the ground state via $k_{21} = k_\mathrm{r} + k_\mathrm{nr}$, where k_r and k_nr represent radiative and non-radiative transitions, respectively. Additionally, a non-radiative transition to level $|3\rangle$ is possible, which represents a dark state that takes into account a process known as intersystem crossing. The small rate k_{23} is driven by a spin-flip process which changes the spin of the excited state as the system transits from a singlet ($S = 0$) into a triplet state ($S = 1$). The resulting decay into the ground state k_{31} is dipole-forbidden and therefore associated with small decay rates. Until the event of the decay, the emitter is trapped in a dark state without the ability to interact with an external electro-magnetic field.

The amount of radiated photons R is described by the occupation of the excited state p_2 and the radiative decay rate. The excitation rate k_{12} can be described as $I\sigma/\hbar\omega$, where ω and σ are the angular frequency and absorption cross-section of the transition k_{12}, respectively. Solving equ. 2.15 for p_2 yields the expression for the fluorescence rate as a function of excitation intensity

$$R(I) = p_2 k_\mathrm{r} = R_\infty \frac{I/I_\mathrm{S}}{1 + I/I_\mathrm{S}}, \tag{2.16}$$

where the maximum fluorescence intensity R_∞ is described by

$$R_\infty = \frac{k_{31}k_r}{k_{23} + k_{31}} \tag{2.17}$$

and the saturation intensity I_S is expressed as

$$I_\mathrm{S} = \frac{k_\mathrm{r} + k_\mathrm{nr} + k_{23}}{\sigma(1 + k_{23}/k_{31})}\hbar\omega. \tag{2.18}$$

A qualitative representation of $R(I)$ is shown in Fig. 2.3c. Since theoretically, the maximum fluorescence can never be reached, the saturation intensity is described as the intensity which yields a fluorescence rate of $R_\infty/2$. Below I_S the fluorescence rate scales almost linear with the excitation intensity due to a ground state occupation p_1 close to 1. However, as I increases further, the excitation rate becomes comparable to the decay rate k_{21} and therefore p_1 decreases.

In order to get a better understanding of the emitter's dynamics, one can simplify I_S and R_∞. As discussed above, the transition k_{23} is small as it requires a spin flip which is usually caused by a finite spin-orbit coupling. In the limit of $k_{23} \rightarrow 0$ the contribution of the triplet state vanishes. It now becomes clearer that for large excitation intensities, the emission rate of the emitter is purely defined by the radiative decay rate k_r as

$$R_\infty = k_r. \tag{2.19}$$

Similarly, the saturation intensity simplifies to

$$I_S = \frac{k_r + k_{nr}}{\sigma} \hbar\omega. \tag{2.20}$$

It can also be seen that I_S recovers the same identity as the expression which was initially used for k_{12}.

With this fairly simple formalism it is possible to accurately describe the fluorescence behavior of the majority of available single emitter. The deduced parameters reveal vital information about the level structure and its dynamics. However, the validity of this model is restricted to an isolated emitter where the decay of the excited state is irreversible. As soon as this process is influenced, i.e. by an optical resonator or at high excitation rates, further details have to be added to the model. A more advanced treatment of an emitter in the environment of external optical fields is discussed in the following section.

2.2.3 Spontaneous emission

The spontaneous emission is described as the process of photon emission by an emitter which makes a transition from an energetically higher to a lower state. It is the reverse process of a photon absorption where a photon is absorbed by an emitter. The theoretical description of spontaneous emission is not possible with the framework of classical electrodynamics and requires a quantum mechanical treatment. This includes the concept of 'vacuum fluctuations' which can be thought of a perturbation to stimulate the decay process [53]. These fluctuations are a consequence of the concept of quantized electric fields which are required to derive a quantitative description for spontaneous decay rates. The lifetime of an excited state can be derived from Fermi's golden rule

$$\Gamma_r = \frac{2\pi}{\hbar^2} |\hat{W}_{if}|^2 g(\omega), \tag{2.21}$$

which describes the transition probability of a quantum system from state $|i\rangle$ to state $|f\rangle$. Here, $g(\omega)$ is the density of states and $|\hat{W}_{if}|$ the dipole matrix element of the interaction Hamiltonian. The density of states represents the number of available electromagnetic states per energy interval dw. In vacuum, the density of states is given by

$$g(\omega) = V \frac{\omega^2}{3\pi^2 c^3}, \tag{2.22}$$

where V is the volume of the mode. The electric field of such a mode has an amplitude of $\sqrt{\hbar\omega/2\varepsilon_0 V}$ (more details in section 2.3.1) which yields the following expression for the interaction Hamiltonian

$$|\hat{W}_{if}|^2 = |\mu \cdot E|^2 = \frac{\mu^2 \hbar\omega}{2\varepsilon_0 V}, \tag{2.23}$$

where μ is the transition dipole moment of the single emitter. It is therefore possible to calculate the spontaneous decay rate of a two-level system in vacuum as

$$\gamma = \frac{\omega_0^3 \mu_{if}^2}{3\pi\varepsilon_0 c^3 \hbar}. \tag{2.24}$$

It has been shown by Weisskopf and Wigner, that the approximation $\gamma \ll \omega_0$ yields an amplitude of the excited state $c_2(t)$ which decays exponentially with $c_2(t) = c_2(0)e^{-\Gamma_r t/2}$ [54]. This decay describes an irreversible process where the emitter is coupled to a continuum of free space modes. The finite probability to re-excite the emitter vanishes as the sum of all modes causes a destructive interference.

2.3 Light-Matter interaction

Based on the introduction of the TLS in the previous section it is now possible to study in more detail the interaction with external optical fields. In a first step, a description of the level occupation of a TLS is derived for the case of an incident optical field without a resonator. The formalism allows to provide an intuitive understanding of the implications due to a weak or strong field strength. A similar but more detailed description is then presented for the enhanced local density of optical states due to a resonator. Finally, the proper characterization of a resonator via a mode volume is provided.

2.3.1 Resonant interaction

The presence of an external field polarizes an emitter and influences the population of the electronic structure. The resulting population dynamics of the emitter can be categorized into the regime of weak and strong coupling which are fundamentally different. This section will provide the theoretical basics to deliver a criterion to differentiate between the two regimes.

First, the interaction will be discussed in terms of a propagating incident optical field on a TLS. This study yields an intuitive description for the level population of the emitter for the weak and strong coupling regime. The second part demonstrates how a vacuum field can also have a significant impact on the emitter population. By using the concept of optical cavities it is possible to enhance the vacuum field giving the possibility to tailor the degree of light-matter interaction.

Atom-light coupling A TLS contains the two energy levels $|1\rangle$ (ground state) and $|2\rangle$ (excited state) separated by an energy $\hbar\omega_0$. The dynamics of these pure states $|\psi_{1,2}\rangle$ that occur during interaction with light can be determined by solving the time-dependent Schrödinger equation [55]

$$\hat{H}|\psi\rangle = i\hbar\frac{\partial|\psi\rangle}{\partial t}. \tag{2.25}$$

The Hamiltonian $\hat{H} = \hat{H}_0(\mathbf{r}) + \hat{V}(t)$ contains a time-independent part in absence of any optical field and a time dependent perturbation potential $\hat{V}(t)$.

The oscillating electric field induces an energy shift of the atomic dipole which leads to an explicit semi-classical expression for the potential $\hat{V}(t) = e\mathbf{r}\cdot E_0\cos(\omega t)$, where e is the electron charge and E_0 the amplitude of the incident electric field. The unit vector $\mathbf{r}$ is aligned along the transition dipole moment of the emitter. Solving equ. 2.25 leads to a set of coupled differential equations which describe the occupation of the ground state (c_g) and excited state (c_e) as a function of time:

$$\begin{aligned}\dot{c}_\mathrm{g}(t) &= \frac{i}{2}\Omega_\mathrm{R}\left(e^{i(\omega-\omega_0)t} + e^{-i(\omega+\omega_0)t}\right)c_\mathrm{e}(t)\\ \dot{c}_\mathrm{e}(t) &= \frac{i}{2}\Omega_\mathrm{R}\left(e^{-i(\omega-\omega_0)t} + e^{i(\omega+\omega_0)t}\right)c_\mathrm{g}(t).\end{aligned} \tag{2.26}$$

Here, Ω_R is the Rabi frequency is defined as

$$\Omega_\mathrm{R} = |\mu_{12}E_0/\hbar|, \tag{2.27}$$

where μ_{12} the dipole moment of the transition between $|1\rangle$ and $|2\rangle$. The evolution of the level occupation can be addressed in the (i) weak field and (ii) strong field regime:

In case of (i), the field strength E_0 is small which ensures the condition that $c_1(t) \gg c_2(t)$. This indicates that the TLS is in the ground state most of the time and the occupation time of the excited state is negligible. Simplifying this condition to $c_1(t) = 1$ for all times yields an expression for the mean occupation of the excited state $|c_2(t)|^2 = \frac{\pi}{\varepsilon_0\hbar^2}\mu_{12}^2 g(\omega_0)t$. It follows that the transition rate from the ground state to the excited state is given by $W_{12} = B_{12}^\omega g(\omega_0)$, where $B_{12}^\omega = \pi\mu_{12}^2/3\varepsilon_0\hbar^2$ is the Einstein coefficient for absorption and $g(\omega_0)$ the density of optical states. This deviation of decay rates is an extension to the rate equations (introduced in section 2.2.2) due to the negligible driving field.

However, the decay dynamics are dramatically different in case of strong external electric fields (ii), where the occupation of $c_2(t)$ becomes comparable to $c_1(t)$. Subsequent evaluation of equ. 2.26 yields a mean occupation of the excited state described as $|c_2(t)|^2 = \sin^2(\Omega_\mathrm{R}t/2)$. It can be seen by this expression that the Rabi frequency describes how the occupation oscillates between the two levels of the transition. With increasing electric field amplitude the Rabi frequency also increases linearly.

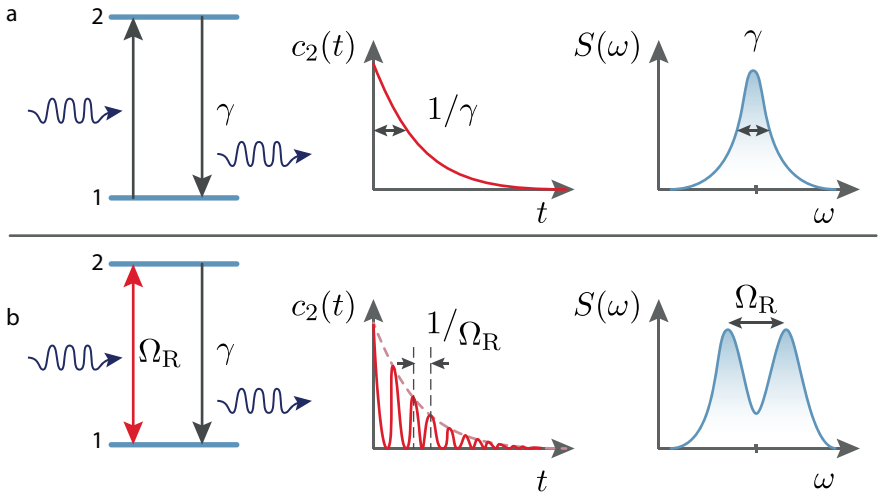

Figure 2.4 – Simplified representation of the interaction between light and a two-level system. a, The excitation of a TLS with a weak field is followed by a spontaneous decay process at rate γ. The mean occupation of the excited state $|c_2(t)|$ is reduced exponentially and the resulting spectrum shows a single Lorentzian. **b,** Strong incident fields introduce a Rabi oscillation Ω_R in the decay dynamics of $|c_2(t)|$. The resulting spectrum shows a Rabi splitting.

As shown above, the field amplitude has a major impact on the occupation dynamics of the emitter. An effect that counteracts Rabi oscillations are dephasing processes such as the spontaneous decay γ of the excited state. The process of Rabi flopping becomes prominent when the losses are small and the fields are large. The necessary requirement is therefore

$$\Omega_R > \gamma, \tag{2.28}$$

which shows that the characteristic flopping frequency has to be larger than the incoherent decay of the excited state.

The occupation of the excited state determines the spectral shape of the emitted photons. The evolution of $|c_2(t)|$ in the time domain does contain all the information about the frequency space. The spontaneous decay of a TLS shows a Lorentzian spectrum where the spectral width corresponds to the decay rate of the excited state (see Fig. 2.4a). An oscillatory behavior between the ground and excited state creates changes the occupation of $|e\rangle$ and therefore also affects the spectrum as depicted in Fig. 2.4b. When the characteristic oscillation frequency Ω_R becomes larger than the decay rate of the excited state, the spectrum broadens and eventually shows two Lorentzians which are separated by Ω_R.

It is important to note, that the description of a spectrum with two peaks simplified and does not represent the full picture. Strong external fields not only influence the transitions within the TLS, but also affects the energy of the ground and excited state. Here, each state is split into a doublet, an indication for the occurrence of a so-called 'dressed TLS' which allows for four transitions, two of which are degenerate. The corresponding emission spectrum has three peaks ('Mollow triplet')

and is the result of an electronic system coherently coupled to an external optical field [56, 57].

Atom-cavity coupling Up until now, this study on the interaction of a two-level transition and light has been restricted to an incident resonant electro-magnetic field. The resulting population dynamics of the emitter can be measured by using an isolated atom and a pulsed laser field with very high intensities. These kind of experiments show that the occupation of the excited state influence the transparency of a crystal or low density atom vapors [58–60].

The amount of photons which are involved in these measurements are huge due to the small absorption cross-section of the individual atoms. In addition, the Rabi splitting is only maintained while the atom is at constant irradiation with a strong electro-magnetic field. In order to study the same effect with a single photon it is necessary to confine its electric field by using the concept of optical cavities (see section 2.1.5 for details). Instead of passing by an atom only once, the photon is reflected (e.g. in between two mirrors) which leads to a multitude of chances for interaction between atom and photon increasing the probability of photon absorption. In terms of electric field one can also argue that the interference between two reflecting mirrors is being used to create a standing wave which exhibits enhanced field amplitudes at the anti-node positions.

The interaction $\mathscr{E}$ between a TLS and the cavity field is described in a similar manner via

$$\mathscr{E} = \hbar g = |\vec{\mu}_{12}\vec{E}_{\text{vac}}|, \tag{2.29}$$

where g describes the coupling rate between the cavity and the emitter and $\vec{E}_{\text{vac}}$ represents the electric field strength of the vacuum mode. The vacuum field of an optical mode is considered as the field strength of the mode in absence of any photon. When treating the mode as a quantized harmonic oscillator, the energy of each photon state E_n is quantized via the relation

$$E_{\text{n}} = \left(n + \frac{1}{2}\right)\hbar\omega, \tag{2.30}$$

where n is the number of photons occupying the mode. For zero photons ($n = 0$) the mode maintains a zero-point energy of $\frac{1}{2}\hbar\omega$. Random vacuum fluctuations, a consequence of the Heisenberg uncertainty principle $\Delta E \Delta t \geq \frac{\hbar}{2}$, are responsible for a non-zero field strength at any point in space.

The size of the mode defines E_{vac} as well as the field strength for additional mode excitations. Averaged over time both the electric and the magnetic field contribute equally to the energy of a mode. Therefore E_0 can be expressed solely by the electric field as

$$E_0 = 2 \times \int \frac{1}{2}\varepsilon_0 |\vec{E}_{\text{vac}}|^2 dV = \frac{1}{2}\hbar\omega. \tag{2.31}$$

Based on this relation follows the vacuum electric field strength

$$|\vec{E}_{\text{vac}}| = \sqrt{\frac{\hbar\omega}{2\varepsilon_0 V}}, \tag{2.32}$$

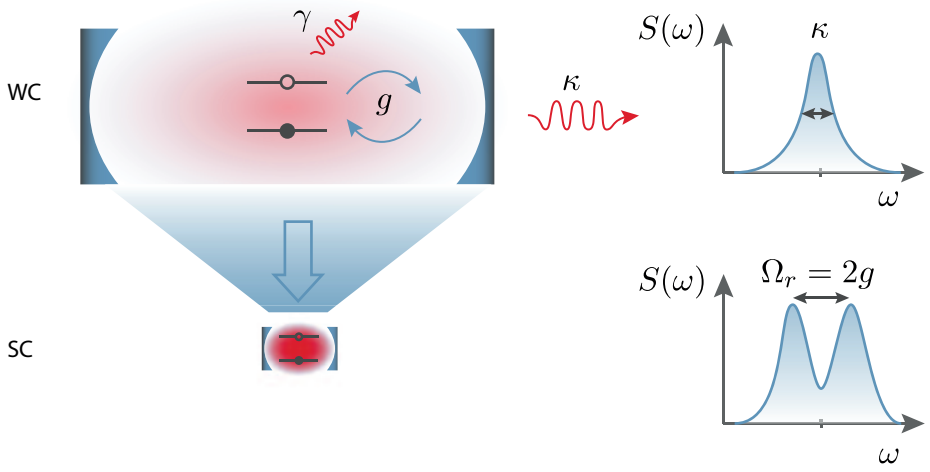

Figure 2.5 – Coupling between a single emitter and a resonant cavity. In case of a large mode volume (upper row) the interaction g is smaller than the emitter and/or the cavity decay rate (weak coupling) which displays a single Lorentzian spectrum. With reduced mode volume the regime of strong coupling becomes feasible and the corresponding spectrum exhibits a Rabi-doublet.

where V is the mode volume which represents the occupied space of a single photon. In case of macroscopic cavities [9] or micropillars [1] where the resonator length is at least one half wavelength, V is fairly represented the geometrical volume in between the reflecting elements. For plasmonic cavities, however, the determination of the mode volume is more complex. More details on how to calculate this quantity can be found in section 2.3.4.

The interaction between a cavity mode and an emitter at its field maximum can now be described via equ. 2.32 and 2.29 as

$$\mathscr{E} = \hbar g = |\vec{\mu}_{12}| \sqrt{\frac{\hbar\omega}{2\varepsilon_0 V}}, \tag{2.33}$$

where g is the corresponding coupling rate between emitter and mode. The coupling between a TLS and a resonant mode is illustrated in Fig. 2.5. Similar to the case of an emitter in a strong electric field, equ. 2.33 describes the coherent interaction between the emitter and a cavity vacuum field which is the main result of this section. The resulting Rabi splitting is then usually also called 'vacuum Rabi splitting' as it refers to the interaction between a vacuum field (no photon involved!) and an emitter. The experimental preparation of such a condition is desirable because no external driving field is necessary.

Rabi oscillations require that the interaction g between the emitter and the electric field is larger than the losses. These losses include the spontaneous decay of the emitter γ as well as the decay of the cavity photon κ which therefore leads to two different regimes that feature significantly different dynamics. For the condition

$$g \leq (\gamma, \kappa), \tag{2.34}$$

where the losses are larger than the coupling rate, the system is considered to be in the **weak-coupling** regime.

If the coupling rates dominates the losses, the condition

$$g > (\gamma, \kappa) \tag{2.35}$$

describes the **strong-coupling** regime.

More details on the coupling mechanisms of these regimes are discussed in the following sections 2.3.2 and 2.3.2.

2.3.2 Weak coupling

As described in section 2.3.1, an emitter is considered as weakly coupled to an electric field if the losses are the dominating process. These losses include the decay of the photonic mode κ as well as the spontaneous decay of the emitter into the far field. In the regime of weak coupling decay processes can be regarded as irreversible. Once an exciton decays, the photon will ultimately radiate into the far field, regardless of its decay directly into the far field or via the resonant mode.

However, the presence of an enhanced vacuum field due to a cavity can modify the decay process of an emitter via an altered density of optical states $g(\omega)$. This enhancement is described by the Purcell factor

$$F_P = \frac{\gamma_{\text{cav}}}{\gamma_0}, \tag{2.36}$$

which is defined as the ratio between the decay rate when coupled to a cavity γ_{cav} and the free space emission rate γ_0. In this context the radiative decay rate inside a cavity can be described by the local density of states (LDOS) ρ, which accounts for the number of available decay states per energy and per volume $(g(\omega)/V)$. The LDOS is of particular interests when it comes to the description of localized modes such as Fabry-Perot resonators or surfaces plasmons. Based on Fermis golden rule (and similar to equ. 2.24) one can derive the decay rate of a single emitter as function of the LDOS as [15, 61]

$$\gamma_{\text{cav}} = \frac{2\omega_0}{3\hbar\varepsilon_0}\mu^2\rho, \tag{2.37}$$

where μ is the dipole moment of the emitter. The corresponding density of states $g_{\text{cav}}(\omega)$ of a cavity resonance is described by a normalized Lorentzian $g(\omega) = \frac{1}{2\pi}\frac{\kappa}{(\omega-\omega_0)^2+\kappa^2/4}$ with a maximum of $g_{\text{cav}}(\omega_0) = 2/\pi\kappa$. Now, the Purcell factor can also be described as the ratio of the LDOS of the cavity and free space (see equ. 2.22) which leads to

$$F_P = \frac{\rho_{\text{cav}}}{\rho_0} = \frac{g_{\text{cav}}/V}{g_0/V} = \frac{2/\pi\kappa V}{\omega^2/3\pi^2c^3}. \tag{2.38}$$

Making use of equ. 2.10 and 2.11 leads to the well-known expression of the Purcell factor [10]

$$F_P = \frac{3(\lambda/n)^3}{4\pi^2}\frac{Q}{V}. \tag{2.39}$$

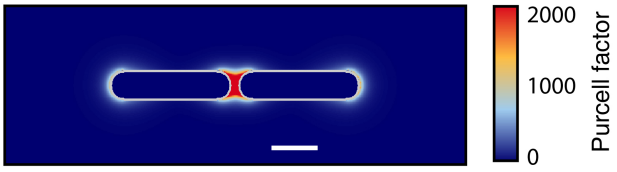

Figure 2.6 – Calculated Purcell factor map in the near field of a gold dipole antenna in vacuum. Both arms have a length of 130 nm, a diameter of 30 nm and are separated by 10 nm. Scale bar: 50 nm.

Here, n represents the refractive index inside the cavity. In case of plasmons the expression λ/n can be replaced with the effective wavelength of the plasmonic waveguide mode. It can be seen that a more confined mode increases the LDOS and therefore the enhancement factor of the radiative decay rate. The confinement can be either achieved by reducing the mode volume V or by decreasing the losses due to radiative and non-radiative processes (larger Q).

Figure 2.6 demonstrates how the LDOS is distributed in the near field of a dipole nanoantenna with a resonance wavelength of $\lambda = 812\,\text{nm}$. The corresponding calculated Purcell factor has its maximum value inside the gap which is the ideal location to enhance the emission of an electric dipole.

The enhancement of the spontaneous radiative decay rate due to the Purcell effect also affects the quantum efficiency of a single emitter $\Gamma_{\text{qe}} = \gamma_{\text{r}}/(\gamma_{\text{r}} + \gamma_{\text{nr}})$. Non-radiative processes γ_{nr}, such as resonant energy transfer to the environment or coupling with phonons, are not affected by the Purcell effect. A large Purcell factor can enhance the radiative decay dramatically which leads to an increased quantum yield. It has been reported that the enhanced radiative decay rate can increase Γ_{qe} by nine orders of magnitude [7].

The Purcell effect has been exploited in numerous studies with plasmons in order to enhance the radiative decay rate of molecules or other types of emitters [7,62–74]. The simplest method to observe the Purcell enhancement is to observe an increase of the saturation fluorescence intensity for high excitation rates. More advanced studies directly measure the reduced excited state lifetime of the fluorophore. A reduction of more than three orders of magnitude has already been reported [69, 70]. For such short excited state lifetimes the limiting factor of these experiments becomes the instrument response function. Typical response times of single photon photo diodes are on the order of 30 ps which marks the shortest detectable excited state lifetime.

In addition to the change of excited state lifetime the emitted light also changes its spectrum and polarization according to the emission properties of the localized plasmon resonance. Enhanced emission of an emitter requires a spectral overlap with the localized plasmon resonance. Each frequency component of the emitter is then increased according to the corresponding amplitude of the resonance at the specific frequency [75–80]. Consequently, the polarization of photons which are emitted via the plasmon resonance are purely polarized according to the char-

acteristics of the resonance. Experiments with a resonant antenna at the apex of a scanning probe have clearly demonstrated the change in polarization of single molecules in close proximity to the nanostructure [81, 82]. Also, the emission direction of a quantum emitter can be drastically changed via weak coupling to a Yagi-Uda nanoantenna [6].

It is important to note that the description of the enhanced radiative decay rate via the Purcell formalism is only valid in the weak coupling regime. This requires the condition that the coupling strength g between the cavity and the emitter is smaller than the decay rate of the cavity κ. The decay process therefore remains irreversible and an emitted photon cannot be re-absorbed by the emitter.

The majority of weak coupling studies are based on emitter ensembles rather than on single emitters. The fluorophores are randomly distributed throughout the highly position dependent field distribution of plasmon modes [71]. Measurements of the enhanced emission as well as the reduced excited state lifetime therefore correspond to an average value. Quantitative agreement between experiments and numerical simulations is therefore challenging and rarely observed. In contrast, single emitter experiments have been proven to show good agreement between simulated and measured values [7]. The fluorophore acts as a point probe which is able to accurately map the local electric field distribution. However, the main issue remains the determination of the exact location of the emitter [83]. In case of molecules, which are used in most studies, it is not possible to gain further information on the exact position due to their size of about 1 nm. Colloidal quantum dots are large enough to allow a localization via electron microscopy imaging [84]. However, this type of emitter is more complicated to handle and quantitative studies of the enhanced emission as a function of position have yet to be reported.

This section has demonstrated the striking impact of plasmonic near-fields on single emitters via weak coupling. The fast conversion of excitons into plasmons and the enhancement of the quantum yield holds promising applications in the field of biological and medical microscopy [85, 86].

2.3.3 Strong coupling

The regime of strong coupling can be described as a state where light, such as a localized mode, and matter, such as an atom, hybridize into a new states which have properties of both entities. Such a system emerges if the interaction rate g between light and matter is larger than any other interaction with the environment. In particular, a photon within a cavity decays into the far field at a rate κ and an atom can loose its coherence or excitation at a rate γ. Strong coupling is established when these types of losses are small and the condition

$$g > (\gamma, \kappa) \tag{2.40}$$

is satisfied.

The general theoretical description for strong light-matter interaction requires a full quantum mechanical treatment. The appropriate formalism is known as the

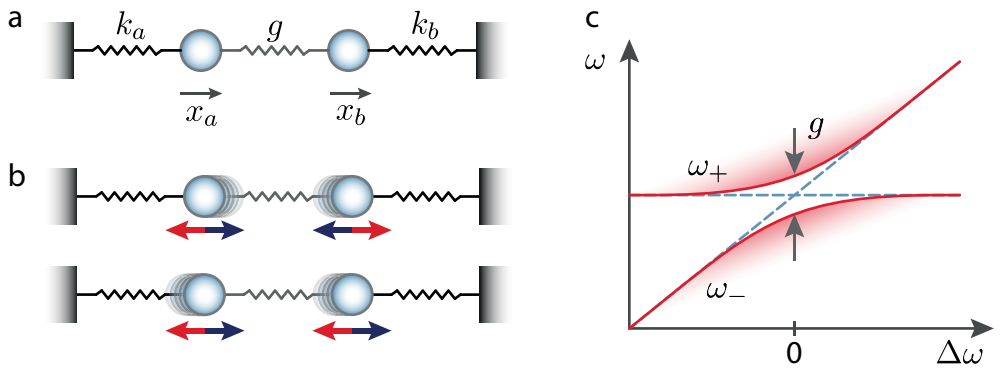

Figure 2.7 – Classical concept of strong coupling for two harmonic oscillators. a, Two masses with individual spring constants $k_{a/b}$ are coupled via a spring g. **b,** On resonance, the two masses can oscillate in two different modes. The in-phase mode ω_- (bottom) has a lower energy than the out-of-phase mode ω_+ (top). **c,** Impact of detuning between the two oscillators. For $g = 0$ the two modes do interact with each other (blue dashed lines). For $g > 0$ the hybridized modes show an anti-crossing behavior (red lines).

Jaynes-Cummings model which takes into account a single two-level system and a quantized resonant field [87–89]. Further insights on this model are discussed in the following section 2.4. In order to get a more intuitive understanding of the underlying physics it is possible to approximate the system at low field intensities by means of classical physics. The scope of this section is to provide intuitive insights and a physical understanding on the working principle of strongly coupled systems.

Coupled harmonic oscillator A basic description of strong coupling is the classical concept of two coupled mechanical harmonic oscillators which represent the emitter and the electric field for low excitation intensities [90]. These oscillators with mass m have a spring constant $k_{a/b}$ and therefore a corresponding eigenfrequency $\omega^0_{a/b} = \sqrt{k_{a/b}/m}$ as indicated in Fig. 2.7a. Both oscillators can interact via another spring with a spring constant g. The complete system is described by the following set of differential equations:

$$\begin{aligned} m\ddot{x}_a + k_a x_a + g(x_a - x_b) &= 0 \\ m\ddot{x}_b + k_b x_b - g(x_a - x_b) &= 0. \end{aligned} \tag{2.41}$$

The homogeneous solution yields a new set of eigenfrequencies

$$\omega^2_\pm = \frac{1}{2}\left[\omega_a^2 + \omega_b^2 \pm \sqrt{\left(\omega_a^2 - \omega_b^2\right)^2 + 4\Gamma^2\omega_a\omega_b}\right] \tag{2.42}$$

with $\omega_{a/b} = \sqrt{(k_{a/b} + g)/m}$ and $\Gamma = g/(m\sqrt{\omega_a\omega_b})$. It can be seen that for $g = 0$ the new eigenfrequencies $\omega_\pm$ reduce to the initial frequencies $\omega^0_{a/b}$. The two oscillators do not interact with each other regardless of their frequency. However,

a finite mutual coupling between the two oscillators ($g > 0$) gives rise to an in-phase (ω_-) and out-of-phase mode (ω_+) as illustrated in Fig. 2.7b. Introducing a detuning $\Delta\omega$ between the two oscillators via a change of one spring constant, e.g. $k_b = k_a + \Delta k$, reveals the different frequency characteristics with and without coupling. In absence of coupling (see Fig. 2.7c blue dashed lines) the frequency of oscillator a is independent of b. As the coupling increases, however, the coupling g prevents a crossing of the two resulting eigenmodes $\omega_\pm$ (red lines) which is the signature observation for strong coupling.

The observation of an anti-crossing behavior requires a resonance linewidth that is sufficiently narrow (low losses) which has not been included in the calculation. By adding damping terms to the initial differential equation one arrives at a equivalent expression of the requirements for strong coupling as equ. 2.40.

Strong light-matter interaction with plasmons The previous classical description of strong coupling between two mechanical oscillators can also be applied to an emitter (such as a quantum dot) and an optical cavity (such as a localized surface plasmon). When taking into account the damping of the plasmon and the quantum emitter the splitting of the hybridized modes is described as [91, 92]

$$\Omega_\mathrm{R} = \omega_+ - \omega_- = \frac{\delta}{2} \pm \sqrt{4g^2 + \delta^2 - (\kappa - \gamma)^2}, \tag{2.43}$$

where the plasmon decay rate and the emitter decay rate are described by κ and γ_ex, respectively, and the detuning is given by $\delta = \omega_p - \omega_\mathrm{ex}$. For zero detuning the mode splitting becomes real when the following condition is satisfied [93]:

$$g > (\kappa - \gamma)/2. \tag{2.44}$$

It is important to note that this criterion is not strict. Depending on the assumptions that are made the criterion can be set as $g > (\kappa - \gamma)/4$ [94, 95] or $g > (\kappa + \gamma)/4$ [43, 84, 96, 97].

The criteria that are described above are deduced from a theory designed for high-Q semiconductor cavities at cryogenic temperatures. The large spectral bandwidth of localized surface plasmon resonances and the associated decay rate κ, however, is much faster than the decay rate γ of the emitter and can therefore neglected in the strong coupling criterion. However, experiments with localized plasmons are commonly carried out at room temperature which can cause an increased emitter dephasing rate γ_D of up to a few tens of meV [98]. The effect of dephasing on strongly coupled system has been shown to significantly affect the resulting spectrum [99]. In order to achieve strong coupling the decay rate of the plasmon has to be faster than γ_D and therefore a more appropriate strong coupling criterion can be expressed as

$$g > (\gamma_\mathrm{D}, \kappa)\,. \tag{2.45}$$

Accomplishing strong coupling between a single emitter and a localized surface plasmons requires advanced nanotechnological capabilities. The key strategy to

reach the strong coupling regime is to increase the confinement of the plasmon and therefore reducing the mode volume. Overall, the tiny dimensions of plasmonic nanostructures are the primary experimental obstacle for the realization of strong coupling with localized plasmons. It hinders the ability to access the localized fields with quantum emitters in a fashion which is reliable and well controlled.

The most common figure of merit to quantify the performance of a localized surface plasmon is the field intensity enhancement factor M. However, this quantity M gives only little insight into the coupling performance. It has been shown that the field intensity enhancement is proportional to $Q/\sqrt{V}$ [92, 100] which is the figure of merit for strong coupling [43]. The relation demonstrates more clearly which antenna property affects the strong coupling conditions.

Losses are a predominant issue of plasmonic resonances. Typical quantum efficiencies of 0.3-0.5 indicate that the ohmic losses and the radiation losses are on the same order of magnitude [101]. The decay rate of the plasmon κ corresponds to the spectral width of the plasmon resonance (see equ. 2.10) and is proportional to $1/Q$. Designing and fabricating an optical antenna which shows reduced radiative as well as non-radiative decay is crucial to reach the strong coupling regime. It is important to note that a large Q-factor does not necessarily lead to an enhanced coupling strength [102]. Sharper resonances, however, increase the visibility of the Rabi splitting and therefore also satisfy the strong coupling condition.

Initially, propagating surface plasmons have been first used to demonstrate strong coupling with various types of excitonic materials [103–106]. With advancements in nanofabrication techniques the patterning of antenna structures covered in organic dye molecules have lead to the observation of strong coupling with localized surface plasmons [107–119]. In the work of Schlather et al. it was shown for the first time that strong coupling with a single nanoantenna and J-aggregate excitons can be realized [95]. Further studies of this type revealed more insight on the coupling mechanism between localized plasmons and many excitions [50, 91, 96, 120]. With increasing alignment precision of individual emitters with ever smaller plasmon modes it was shown that strong coupling at the single emitter level is indeed possible [13, 84, 121–123].

The coupling mechanism between quantum emitters and localized surface plasmons has also been subject to extensive theoretical studies as well [92, 94, 98, 124–152]. Here, a variety of models are employed to approach the interaction mechanism. Most of them rely partially on numerical calculations which are required to obtain the electric field amplitude if the shape of the nanostructure deviates from a trivial geometry such as a sphere or a spheroid. The interaction model based on a quantum model has been frequently used and is further outlined in section 2.4. Other popular techniques have been based on the classical Green tensor [98, 126, 130, 131]. Purely numerical calculations model the permittivity of the quantum emitter with a single Lorentzian in order to approximate the excitonic characteristic [92, 94, 124, 125]. The interaction of this material with a localized field leads to a splitting of the plasmon resonance spectrum which can be interpreted as Rabi splitting [153]. This model is also most often used in direct

comparison to experimental result of plasmons being strongly coupled to excitonic materials [84, 91, 95, 96].

2.3.4 Mode volume calculations

In the previous section the importance of the mode volume and the impact on the light-matter coupling rate g has been discussed. This section will focus on the numerical determination of mode volumes of optical nanoantennas. The concept of a mode volume has been used frequently in the past to describe the occupied space of a single photon which is bound in an optical cavity. The energy density of a photon of energy $\hbar\omega$ increases with decreasing volume which boosts the electric field amplitude. It can be seen from equ. 2.33 that the coupling strength scales with $V^{-1/2}$. In order to model the coupling strength between a plasmonic resonance and an electric dipole it is crucial to determine an exact number for the mode volume.

Electro-magnetic modes can be categorized into two types: normal modes and quasi-normal modes. A normal mode refers to the description of an oscillating system with virtually zero losses. The spontaneous decay into a far-field mode (plane wave) of an emitter embedded in a dielectric environment is a good example for an optical normal mode. The electro-magnetic mode in between two reflecting mirrors can approximated by a normal mode $\mathrm{f_c}$ with the mode volume described by [154, 155]

$$V^N = \frac{\langle \mathrm{f_c}|\mathrm{f_c}\rangle}{\varepsilon_r(r_c)|\mathrm{f_c(r_c)}|^2} = \int_V \frac{\varepsilon_r(r)|\mathrm{f_c(r)}|^2}{\varepsilon_r(r_c)|\mathrm{f_c(r_c)}|^2} dr, \tag{2.46}$$

where ε_r is the relative permittivity and r_c designates the position of an anti-node of the cavity. As it was originally used for microcavities this volume also represents fairly accurate the geometrical extend of the cavity. However, every mode with a finite Q-factor (and therefore every experimentally realized cavity) is plagued by leakage of radiation. The distribution of energy throughout the entire space leads to exponential divergence of the integral in equ. 2.46 [133,156]. Additionally, the presence of absorption of energy in metal poses another challenge to properly calculate the mode volume. In order to properly address this issue the concept of quasinormal modes (QNM) has been established [133, 150, 155–175]. These QMNs have a complex eigenfrequency $\omega = \omega^{\mathrm{R}} - i\omega^{\mathrm{I}}$ which describes the lossy nature of the mode with the corresponding Q-factor defined via $Q = \omega^{\mathrm{R}}/2\omega^{\mathrm{I}}$. Calculating the QMN analytically is only possible for a few simple geometries while for all other cases numerical simulations are required. Throughout this work, finite-difference time-domain simulations are carried out in order to determine the spatial mode distribution of plasmon resonances. The simulation volume is surrounded by perfectly matched layers (PML) which suppress any outwards propagating radiation. The resulting electric field distribution of the QNM converges for large distances and can therefore be used to calculate the mode volume.

In a study of Sauvan et al. the mode volume has been derived based on the Lorentz reciprocity theorem which yields the expression for the mode volume [133]

$$V_{\text{eff}}(r) = \frac{\int \left(\mathbf{E} \cdot \frac{\partial \omega \varepsilon(r)}{\partial \omega} \mathbf{E} - \mathbf{H} \cdot \frac{\partial \omega \mu(r)}{\partial \omega} \mathbf{H} \right) dV}{2\varepsilon_0 \varepsilon(r) |\mathbf{e}_\mu \mathbf{E}(r)|^2}. \tag{2.47}$$

Here, $\mathbf{E}$ and $\mathbf{H}$ are the fields of the resonant QNM of the cavity and $\varepsilon(r)$ and $\mu(r)$ are the relative permittivity and the relative permeability of the structure (resonator and environment), respectively. It has been shown by Kristensen et al. [170] that this approach is formally equivalent with other studies [158, 176]. However, it should be noted that there is still an currently a ongoing dispute within the community [177, 178].

It is also important to note that the described effective mode volume $V_{\text{eff}}(r)$ is a position dependent quantity. The location r relates to the position of an emitter which interacts with the localized mode and the unity vector $\mathbf{e}_\mu$ is aligned along the dipole transition moment of the emitter. Depending on the emitter location and orientation, the effective mode volume which is experienced by the emitter can be different. At the field maximum $V_{\text{eff}}(r)$ has a minimum which relates to a maximum coupling rate between the emitter and the mode. As the emitter is moved away from the field maximum the effective mode volume increases and the coupling rate consequently decreases.

The traditional mode volume V^N which strictly speaking is only valid for normal modes assumes the emitter position always at the field maximum and is therefore not a position dependent quantity.

2.4 Quantum Theory

The previous section has shown how classical theory can be used to calculate the Rabi splitting between two strongly coupled harmonic oscillators. However, besides determining the peak energies of the spectra for varying detuning, the model does not reveal further details on the spectra such as peak amplitude or width. In fact, a proper (quantum-) modeling of experimental data is a challenging task and therefore rarely carried out. The first measurements of strong coupling between a semiconductor cavity and a quantum dot, for instance, have been successfully theoretically described four years after publication of the measurements [1, 179]. The basic understanding of this quantum model is the main purpose of this section. Further on in this work, these fundamentals are used to propose a quantum optical model of a plasmonic cavity strongly coupled to the electronic states of a quantum dot.

2.4.1 Quantum Master Equation

The Schrödinger equation as stated in equ. 2.25 describes the temporal evolution of a pure state $|\psi\rangle$. However, states which interact with the environment are better described as a mixed state. This state ensemble can be represented by the density

matrix operator [180]

$$\hat{\rho} = \sum_i p_i |\psi_i\rangle\langle\psi_i|, \tag{2.48}$$

where p_i is the probability of the system to be represented by the state $|\psi_i\rangle$ and the diagonal elements $\hat{\rho}_{ii}$ describe the occupation of an explicit state i.

While each of the individual states $|\psi_i\rangle$ evolve in time according to 2.25, the temporal evolution of a mixed state is described by the Liouville-von Neumann equation

$$\dot{\hat{\rho}} = -i\left[\hat{H}, \hat{\rho}\right], \tag{2.49}$$

where the Hamiltonian $\hat{H} = \hat{H}_c + \hat{H}_e + \hat{H}_i$ accounts for the interaction in the system. The Hamiltonian $\hat{H}_c = \hbar\omega a^\dagger a$ describes the uncoupled cavity photon and $\hat{H}_e = \hbar\omega\sigma^\dagger\sigma$ represents the uncoupled exciton. Here, the bosonic creation operator $a^\dagger$ and annihilation operator a satisfy the commutation relation $\left[a, a^\dagger\right] = 1$. The anticommutator relation $\left\{\sigma, \sigma^\dagger\right\} = 1$ is satisfied by the fermionic creation and annihilation operators $\sigma^\dagger$ and σ, respectively. The interaction between the two systems is described via the interaction Hamiltonian $\hat{H}_i = \hbar g\left(a\sigma^\dagger + a^\dagger\sigma\right)$, where g is the interaction rate.

This model can be improved from a Hamiltonian to a Liouvillian description in order to account for incoherent processes such as spontaneous decay. This leads to a quantum dissipative master equation

$$\dot{\hat{\rho}} = -i\left[H_I, \hat{\rho}\right] + \frac{1}{2}\sum_k \left(2L_k\hat{\rho}L_k^\dagger - L_k^\dagger L_k\hat{\rho} - \hat{\rho}L_k^\dagger L_k\right), \tag{2.50}$$

where L_k represents the Liouville terms ('jump' operator) [180]. Each L_k accounts for a channel which delivers energy into the system as well as channels that cause dephasing and energy loss.

Theoretical investigations of the dynamics of strong-coupling interaction have revealed astonishing and quite non-intuitive results regarding shape of the emission spectrum and the occupation of the individual states of the system.

2.4.2 Calculating the emission spectrum

The use of the time-local master equation in Lindblad form (no explicit time dependence) allows the application of the well-known Wiener-Khintchine theorem to calculate the stationary emission spectrum of a coupled system [55]. In the strong-coupling regime of plasmonic systems, the dominant emission channel is assumed to be provided by far-field emission of the cavity. In other words, the electric field amplitude entering the spectrometer is proportional to the cavity annihilation operator a. This implies that, up to a normalization constant, the observed spectrum $S(\omega)$ is given by [181]

$$S(\omega) \propto 2\mathrm{Re}\left(\int_0^\infty \langle \mathrm{a}^\dagger(\tau)\mathrm{a}(0)\rangle \mathrm{e}^{-\mathrm{i}\omega\tau}\mathrm{d}\tau\right). \tag{2.51}$$

Employing the Quantum Regression Theorem [180], in the stationary regime the two-time correlation function $C(\tau) = \langle a^\dagger(\tau)a(0)\rangle$ with $C(\tau) = \mathrm{Tr}\left[\mathrm{a}^\dagger \mathrm{e}^{\mathscr{L}\tau}(\mathrm{a}\rho_\infty)\right]$ can be formally written down, where $\mathscr{L}$ is the Lindblad superoperator implicitly defined by the master equation as per $\dot{\rho} = \mathscr{L}\rho$, and ρ_∞ is the steady state density matrix that needs to fulfill the conditions $\mathscr{L}\rho_\infty = 0, \rho_\infty \geq 0, \mathrm{Tr}[\rho_\infty] = 1$. Crucially, this treatment relies on the assumption of the existence of a unique steady state. The following expression can be derived for the steady state fluorescence spectrum

$$S(\omega) = -2\mathrm{Re}\left(\mathrm{Tr}[\mathrm{a}^\dagger(\mathscr{L} - \mathrm{i}\omega\mathrm{I})^{-1}\mathrm{a}\rho_\infty)]\right), \tag{2.52}$$

where I is the identity superoperator. Note that $\mathscr{L}$ has an eigenvalue of zero, due to the trace-preserving property of the master equation. Hence, the expression $(\mathscr{L} - i\omega I)^{-1}$ should be interpreted as the pseudoinverse of the operator $\mathscr{L} - i\omega I$ to avoid a delta-like singularity at $\omega = 0$. In numerical calculations carried out in this work, the annihilation operator a is represented as a 2×2 matrix, which amounts to allowing at most a single photon in the cavity. Also, with the given parameter regime, it has been checked that numerical results are not significantly changed when more photons are allowed.

2.4.3 Further remarks

A vast amount of studies has been dedicated to strongly coupling between a cavity and a single and multiple quantum emitter [99, 102, 179, 182–192]. These results have been a crucial constituent on the further deepening of the understanding of light-matter interaction.

It has been found that the appearance of two peaks in the emission spectrum is not mandatory for strong coupling [186]. In fact, the proper description for the transition into the strong coupling regime is marked when the Rabi frequency (equ. 2.43) becomes purely real. At this point, the decay of the cavity field becomes oscillatory as opposed to being exponentially damped in the weak coupling regime. It is therefore possible to observe a single peak in the emission spectrum while the system is strongly coupled. As a result, the general association as strong coupling being the result of a periodic exchange of energy is not valid. It can be shown in the case of spontaneous emission that energy can be exchanged while the system is still in WC. In contrary, continuous pumping can lead to the case without any time dynamics of the cavity/emitter population while the system displays strong coupling [186].

Another important aspect is the pumping of the system and therefore the preparation of the initial state [102]. For example, pumping directly the cavity with an emitter in the ground state follows different dynamics compared to an empty cavity and a pumped emitter. This implies that depending on the pumping the shape of the spectrum can be vastly different. An essential step to reveal the spectral features of strong coupling has been shown to be the direct pumping of the cavity [102].

Accordance between theoretical models and measurements has been achieved in the case of semiconductor microcavities and quantum dots [179]. The matured

experimental concepts have advanced strong coupling well into the single emitter regime which provides a vast amount of data. In comparison, the field of plasmonics is currently at the verge of entering the single emitter regime. Therefore, a sufficient amount of data is not yet available in order to make a thorough comparison with the results of optical master equation. Nonetheless, plasmonic systems and the strong interaction with a single emitter have been subject to detailed theoretical studies based on this type of model [134–151].

It is important to note, that the applicability of the master equation and the implicit usage of Lorentzian decay dynamics to plasmonics systems has also recently been questioned [149]. Since plasmon resonances exhibit rather low Q-factors, the resulting photon life time of a few tens of fs leads to a non-Lorentzian resonance which is not taken into account in this model.

3

Introduction into semiconductor nanocrystals

Semiconductor materials feature a rich electronic structure and are the unique link between insulators and highly conducting metal materials. Crystal structure, shape, temperature and degree of impurities are only a few factors that are frequently used to alter the behavior of electric current as well as single excitons of various semiconductor compositions. Interaction with electro-magnetic waves at optical frequencies is one major field of research which brought up remarkable applications for photon generation such as light emitting diodes (LEDs) and solid state lasers as well as photon detectors such as charged coupled devices (CCD) cameras.

The key process of these applications is the excitation and decay of electron hole pairs (excitons) in the conduction and valence bands. The energy separations between these bands determines the most important property of the light matter interaction, namely, the photon energy that can be emitted or absorbed. It is the band structure which is the key aspect in order to understand all the optical properties of semiconductor materials. Interestingly, not only changes of the material composition and the environment can have an influence on the band structure, but simply a crystal with physically dimensions on the nm scale alters the ability to absorb or emit light. An artistic visualization is shown in Fig. 3.1 which roughly depicts the amount of atoms involved in a nanocrystal with a diameter of 8 nm. A variety of comprehensive reviews on nanocrystals can be found in the literature [193–228]. The focus of this chapter is to present a general understanding of the optical properties of semiconductor nanocrystals with emphasis on the aspect of coupling with plasmons which is important for the experimental part of this work. Despite the variety of review articles in the literature, an extensive report on the current state of the art on coupling semiconductor nanocrystals with plasmons has yet to be released.

First, the characteristics of a bulk material will be introduced which provides the basis for further restrictions and modifications towards the optical behavior of nanocrystals which includes the crystal size as well as the stoichiometric composition. Afterwards, the origin of prominent features such as fluorescence intermittency and spectral diffusion are discussed in detail. The influence of phonons on the optical characteristic via dephasing and non-radiative relaxation is described next. This chapter ends with a summary on the current progress of coupling semi-

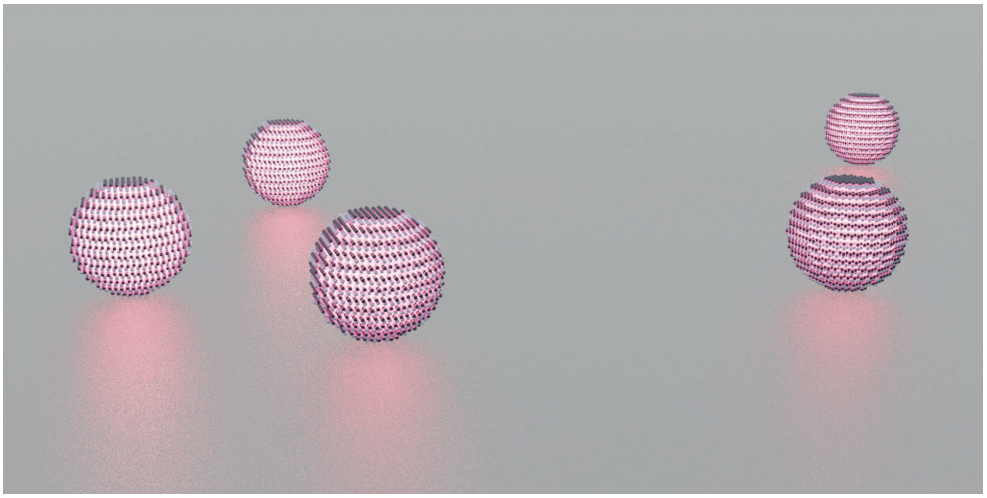

Figure 3.1 – Artistic representation of colloidal nanocrystals.

conductor nanocrystals with plasmons followed by a brief discussion on the future prospects of this kind of excitonic material due to its inherent optical properties.

3.1 Electronic structure of semiconductors

The electronic structure of a bulk semiconductor material is solely defined by its atomic composition and crystal structure. The resulting band structure features an energy gap dividing the fully occupied valence band and the empty conduction band. Optical properties of the semiconductor material, such as photon emission and the minimum absorption energy, are governed by this gap energy. Reducing the crystal size below the exciton Bohr radius a^* has a significant impact on the band gap [229, 230]. The exciton Bohr radius refers to the electron-hole distance of the ground state in a bulk material and is defined as $a^* = a\frac{\varepsilon}{m^*}$, where a is the hydrogen Bohr radius, ε is the dielectric constant and m^* is the effective electron mass. The exciton Bohr radius is the critical crystal dimension that defines the threshold into the regime of quantum extend where the spatial confinement of the electron and hole wave function contributes to the band gap. The physical restriction in all three dimensions creates a 0-D system and semiconductor crystals of these sizes are therefore usually termed quantum dots (QDs) [231].

In a very simplified model the exciton can be thought of as a particle surrounded by an infinite potential barrier. The dispersion relation of a bulk semiconductor can be simplified as a continuous parabolic function $E = \hbar^2 k^2/2m$ for small k vectors, where the particle energy is purely kinetic. Using the effective mass approximation the dispersion relation discretizes to an atomic-like distribution $E = \hbar^2 \Phi_{\mathrm{n,L}}^2/2mR$. Here $\Phi_{\mathrm{n,L}}$ is the n-th root of the spherical Bessel function of the L-th order, m is the effective mass of the electron or hole for the case of the conduction or valence band, respectively, and R is the crystal radius. The order of the quantized states follows the value of Φ which is defined by the principal quantum number and the angular

momentum. Based on this model the energy levels can be tuned with the crystal size as the band gap increases with the inverse of the square radius. The energy for the ground state ($n = 1, L = 0$) is given by $E_g = E_{g,0} + \hbar^2\pi^2/2m_{eh}R^2$, with the reduced effective electron hole mass $m_{eh} = m_e m_h/(m_e + m_h)$ and the band gap $E_{g,0}$ of the bulk semiconductor. Also, the level separation in the individual bands depends on its effective carrier mass. Many semiconductor materials exhibit large hole masses which result in a high density of states in the valence band compared to the conduction band. The Coulomb interaction, responsible for the existence of excitons in bulk, enters the energy distribution as a correction factor. The electrostatic potential scales with $1/r$ and is dominated by the confinement energy $1/r^2$ for sufficiently small QDs. Adding the Coulomb interaction form first-order perturbation theory the energy of the ground state equals $E_g = E_{g,0} + \hbar^2\pi^2/2m_{eh}R^2 - 1.8e^2/\varepsilon r$, where e is the electron charge [231].

3.2 Quantum confinement

The size of the crystal not only effects the band gap but also the valence and conduction band structure. However, as the electronic properties at this stage fairly depend on the atomic composition of the semiconductor, the material of interest from now on will be CdSe. Due to its early discovery as quantum dots it has become the most studied material for colloidal quantum dots.

As mentioned before, many semiconductor materials show effective hole masses many times larger than the electron and for CdSe the ratio is about $m_h/m_e = 6$. The resulting thin conduction band, which derived from the Cd 5s orbitals, can be approximated, even in strong confinement, as a single band with the lowest state being a 1S electron (see Fig. 3.2). On the other hand, the valence band and its high density heavy hole (hh) states displays a multi-band characteristic and various confinement effects can cause a mixing between the different bands. It is composed of the p-type wavefunctions originating from the selenite atoms. The significant spin-orbit coupling energy for CdSe (433 meV) splits the band into a doubly degenerate spin-off band (so) with an angular momentum of $J = 1/2$ and a 4-fold degenerate band with $J = 3/2$. The latter is composed of heavy and light holes (lh) with an angular momentum projection of $J_m = \pm 3/2$ and $\pm 1/2$, respectively. This degeneracy only holds for the case of a cubic lattice but gets lifted for a hexagonal close-packed wurtzite crystal lattice structure. Here, the so-called crystal-field splitting separates the heavy and light hole bands by $\Delta_{AB} = 26\,\text{meV}$.

The transition with the lowest exciton energy is composed of a 1S electron and a $1S_{3/2}$ hole. Its energy depends on the quantum dot radius and can be calculated with the formalism and its corrections as described above. In comparison with absorption spectrum, measurements of the lowest exciton energy matches very accurately the calculated value. For higher transition energies the theoretical predictions with this model deviate from the measurements. These deviations are due to mixing between the valence band states as a result of the orbital momentum of the hole envelope function. However, since the main focus in this work is on the band-edge exciton,

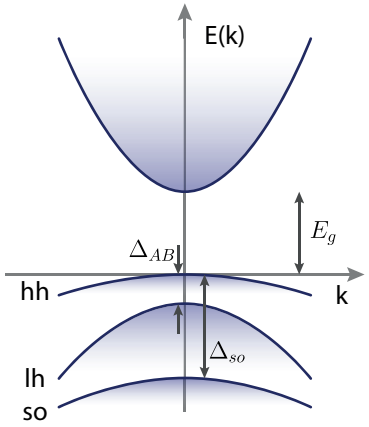

Figure 3.2 – Band structure of bulk CdSe with wurtzite lattice at the Γ point.

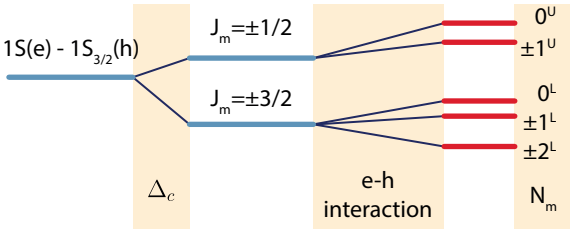

Figure 3.3 – Energy levels of the fine structure in CdSe nanocrystals

more emphasis will be put on the fine structure and further details about higher energy states are omitted. Given a cubic lattice and a symmetric nanocrystal shape, the band-edge exciton shows an 8-fold degeneracy.

In case of a wurtzite crystal structure, which is the type of structure of the QDs that are used in the experiments in this work, the degeneracy is mainly lifted by three different effects (see Fig. 3.3). Similar to the bulk state, the crystal field Δ_c splits the $J = 3/2$ state into two levels with the angular momentum projection $J_m = \pm 3/2$ and $\pm 1/2$ corresponding to heavy and light holes, respectively. The splitting energy depends on the mass ratio between the light and heavy holes $\beta = m_{lh}/m_{hh}$. In the extreme case of $\beta = 0$, the ratio can get as small as 0.2 meaning that the splitting can be as much as five times lower compared to the bulk crystal field splitting. Therefore, the transition energy of the band-edge is split into a lower energy with $J_m = \pm 3/2$ and a higher energy with $J_m = \pm 1/2$. This splitting has no influence on the size of the quantum dot as it depends solely on the effective mass ratio. However, non-spherical quantum dot shapes introduce an additional splitting factor Δ_{sh}. The total splitting adds up to $\Delta = \Delta_c + \Delta_{sh}$. Small deviations from a perfect sphere can be approximated as ellipsoid crystal with ellipticity μ that defines the ratio $c/b = 1 + \mu$ between the hexagonal axis c and the perpendicular minor axis b. The crystal shape splitting parameter $\Delta_{sh} = 2\mu u(\beta) E_{3/2}(\beta)$ can be derived by first order perturbation theory. Here, $u(\beta)$ is a dimensionless factor dependent on the mass ratio β and $E_{3/2}(\beta)$ the energy of a hole state for a QD with a radius

of $R = (b^2 c)^{1/3}$. Depending on the sign of the ellipticity the QD can be either obtain a prolate or an oblate shape for a positive or negative value of μ, respectively. Oblate QDs lead to a positive value of Δ_{sh} and therefore the splitting increases with decreasing QD size. However, prolate QD shapes contribute with a negative crystal shape splitting parameter. Decreasing the QD radius reduces the overall splitting between light and heavy holes and can eventually lead to a flipping of the band order.

Further lifting of energy degeneracy is introduced by the electron-hole exchange interaction due to the confinement of the charge carrier. This level splitting is therefore more pronounced for smaller QDs and determines the optical properties at the band-edge. In the spherical QD approximation, the interaction of the $J = 3/2$ hole state with the $S = 1/2$ electron state gives rise to a state with the total angular momentum $N = 2$ with a 5-fold degeneracy and a state $N = 1$ that shows a 3-fold degeneracy. It is noted that the splitting between the individual levels is comparatively small with regard to the overall bandgap energy. Depending on the QD radius the energy difference between the levels $N = \pm 2$ and $\pm 1^{\mathrm{L}}$ can deviate between 1 and 20 meV which is negligible compared to the bandgap energy of 2 eV or higher. This raises the question of whether it is worth looking in so much detail on the energy level distribution in the scope of coupling QDs with plasmonic resonances which generally exhibit a spectral width on the order of 50 meV and beyond. At this point, it is not the magnitude of the level splitting which is the point of interest but the transition properties when interacting with optical fields.

The band-edge fine structure has a considerable impact on the photon emission properties of the QD as not all energy levels are optically active within the electric dipole approximation. Most importantly, the lowest energy level $N = \pm 2$ is optically passive and therefore emission of a photon is not permitted as it cannot carry an angular momentum of 2. As the radiative decay is forbidden by quantum mechanics this type of exciton is called a dark exciton. Thermalization processes of higher states and subsequent relaxation to the lowest level leads to a high occupation of this particular state and therefore dominates the emission properties of the QD. This would imply that using a QD showing this band-edge structure as a fluorescence particle is not practical. However, this is only the case for low temperatures where thermal activation of the optically active $\pm 1^{\mathrm{L}}$ level is eliminated. Here, the exciton is trapped in the dark state indicated by a lifetime in the µs range and eventually decays via a phonon assisted process in order to conserve the angular momentum. Experiments from cryogenic to ambient temperatures have shown that a three-level system is sufficient to describe the exciton lifetime behavior and the energy splitting between the two lowest states [232]. This model includes a ground state and two excited states with a long lifetime (lower level, dark state) and a short lifetime (upper level, bright state) and an energy separation which is described by the Boltzmann statistic. At low temperatures the excited state lifetime is long since any excitation relaxes into the dark state. As the temperature rises, the probability for activating the bright state via phonon absorption increases which facilitates a faster decay rate of the exciton. Eventually, at room temperature both states are

equally populated and the decay time equals about two times the bright state lifetime. This simple three-level model shows good agreement with measurements with the exception of one aspect: The temperature at which the decay time drops should scale with the splitting energy. However, experiments with different QD radii which exhibit different splitting energies showed a similar trend and a drop of photoluminescence lifetime at around 2 K. The origin of this behavior has yet to be found. Many studies conclude an additional decay channel with a small activation energy which governs the emission rate in the transition temperature range. The decay rate of the bright state of colloidal quantum dots has been found to depend on the crystal size as it also scales with the resonance frequency [233].

3.3 Quantum dot classification

Quantum confinement allows to gain control over the spatial distribution of the excited charge carriers. This property, which is exclusively reserved for nanocrystals, yields a powerful method to further modify the intrinsic optical properties of the underlying bulk semiconductor. The spatial distribution of the individual charge carrier in single component QDs is mainly defined by the effective carrier mass. The radial probability distribution for a nanocrystal is shown in Fig. 3.4a [234]. The carrier distribution extends throughout the nanocrystal but also reaches into the surrounding organic matrix, a feature which is more pronounced for the electron as its effective mass is smaller compared to the hole. This distribution changes drastically in the case of heterostructured QDs where the core material is surrounded by a different semiconductor. The relative energy of the HOMO and LUMO levels in the shell material determine the attractive or repulsive influence on the charge carriers which makes it possible to actively manipulate the contribution of the charge density throughout the whole QD. Figure 3.4b shows the relative energy of HOMO and LUMO levels for a variety of semiconductor compounds which are frequently used for the synthesis of colloidal nanocrystals [235]. This technique of so called 'wave function engineering' has a vast impact on the emission properties of the QD. As can be seen in Fig. 3.4a, the coating of CdSe with a higher bandgap material (such as ZnS) shows extension of the charge carrier distribution into the shell and a significant suppression (compared to pure CdSe) in the surrounding matrix. This yields an enhanced quantum yield due to a reduced interaction of the exciton with the QD surface via non-radiative recombination or charge trapping processes. The surface passivation of QDs with an inorganic material has been proven to be very efficient to produce highly reliable single quantum emitters [236–238].

If the shell material has a similar (but still larger) bandgap compared to the core (e.g. CdS) the charge carrier distribution expands further into the shell leading to a reduced confinement therefore to a red-shifted photon emission. QDs which are coated with semiconductors that feature conduction (valence) bands which are energetically higher (lower) are termed Type I quantum dots. The resulting overall overlap of the electron and hole wavefunction is the characteristic feature of Type I QDs and therefore also tied to comparably short exciton lifetimes.

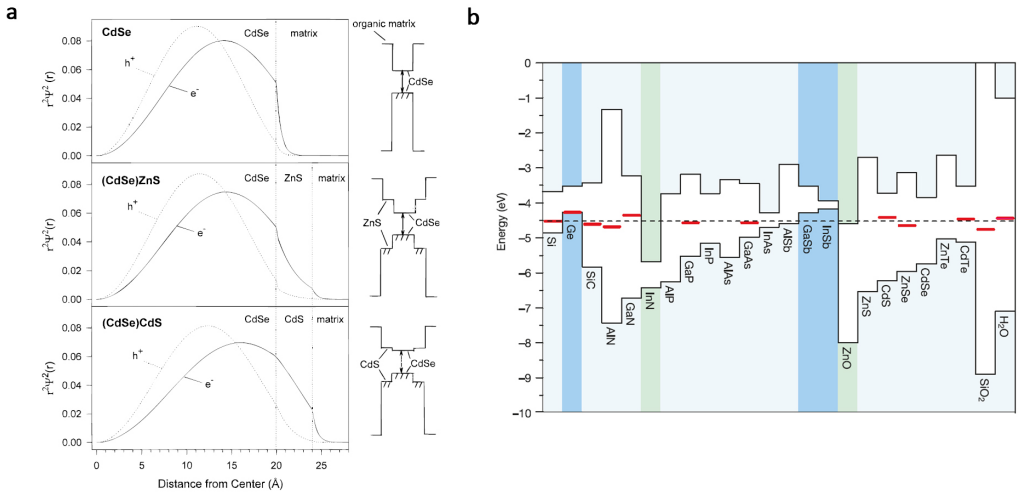

Figure 3.4 – Impact of the material composition on the carrier wavefunction. a, Radial probability distribution of a single component QD and two different core/shell combinations. Reprinted (adapted) with permission from reference [234]. Copyright (2018) American Chemical Society. **b,** HOMO and LUMO levels of various semiconductor compounds. Reprinted (adapted) with permission from reference [239]. Copyright (2018) Nature Publishing Group.

A different category of QDs (Type II) are created if the HOMO and LUMO levels of the shell material are both increased or reduced until the one of them surpasses the corresponding energy of the core material. This causes a localization of one carrier in the core and the other in the shell material which is the signature characteristic of Type II quantum dots. The emission properties of a spatially indirect transition carries inherent features which oppose those observed in Type I QDs. The most striking property is the low exciton decay rate due to the reduced overlap integral between the electron and hole wavefunction. Due to the separate confined carriers the exciton emission energy can be lower than the individual band gap energies of the core and shell material [239]. A specific composition of Type II quantum dots which are frequently studied are CdSe/CdS core shell mixtures. By using a very large shell thickness of up to 19 monolayers these QDs exhibit excellent fluorescence stability due to highly suppressed non-radiative Auger processes [236, 237]. Here, the electron wavefunction can leak into the shell material but does not reach the outer surface due to the shell thickness. The little interaction with surface states prevents charge carriers to be trapped which makes this type of QD robust against the resulting fluorescence intermittency (see section 3.5 for details). The small lattice mismatch between CdSe and CdS of less than 4% makes it possible to grow a QD shell of these dimensions [240]. Minimized strain at the interface between the core and shell material additionally decreases the probability for localized states which increases the quantum yield of the exciton decay. A schematic summary of the different QD types is shown in Fig. 3.5.

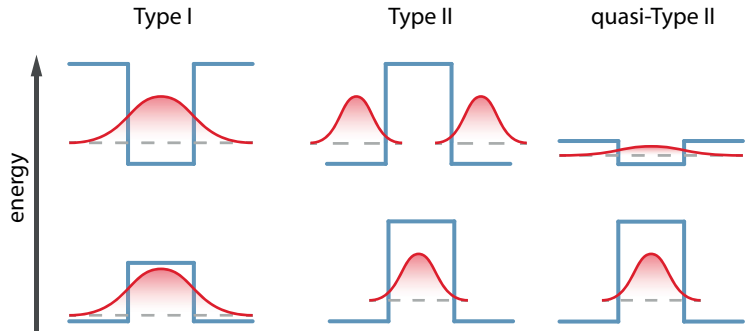

Figure 3.5 – Band gap visualization of different types of quantum dots. Type I indicates strong overlap of localized electron and hole wavefunctions. In Type II QDs the overlap is reduced due to a localized hole in the core and electron in the shell. For quasi-Type II QDs only the hole is localized and the electron is delocalized throughout the QD.

3.4 Doping

Similar to the development of bulk semiconductors the substitution of individual atoms within a nanocrystal can significantly change its electronic properties. Owing to the small crystal size, the exchange of even a single atom already represents a doping concentration on the order of one parts per thousand. Compared to a bulk semiconductor this would already be rated as heavy charge doping with a concentration of more than $10^{18}\mathrm{cm}^{-3}$ [219]. If the substituting atom has the same amount of valence electrons the nanocrystal gains no extra charge carrier and therefore remains neutral. However, the electrical and therefore also optical properties of additional impurity energy levels change the bandgap and have an impact on the emitted photon energy. This effect is commonly used to further extend the possible wavelength range of pure QDs without impurities. In particular, doping of CdSe quantum dots with tellurium makes it possible to reduce the bandgap below the intrinsic bulk value of 1.8 eV [241] and paves the way to reach the NIR regime. Tellurium substitutes selenium in the crystal lattice due to the similar electron configuration of the valence shell. Therefore, with increasing Te concentration the characteristics of pure CdSe are influenced by the ones of CdTe. The most striking property is the band gap as well as the specific energy difference between the HOMO and LUMO levels. The impact on the optical properties does not only depend on the Te concentration but also on the spatial distribution of the impurity atoms [242]. Therefore, one can differentiate between two major categories of Te doped CdSe nanocrystals: a homogeneous distribution (alloy) and a core/shell configuration (CdTe/CdSe). As the experimental part of this work deals with alloyed quantum dots more emphasis will be put on this specific nanocrystal type.

The properties of the $CdSe_{1-x}Te_x$ alloy are described by the stoichiometric ratio between selenium and tellurium [243, 244]. However, it is important to note that in case of II-VI semiconductors this is a non-linear relationship as opposed to metal alloys (e.g. $Ag_{1-x}Au_x$) where a linear behavior has been observed [245]. In fact,

a composition of CdSe and CdTe (bandgap 1.55eV) [246] can yield an effective bandgap which is smaller than the individual elements. The relationship between the composition factor x and the band gap E_{gap} can be described by a parabola via

$$E_{\text{gap}}(x) = (1-x)E_{\text{gap,CdSe}} + xE_{\text{gap,CdTe}} - bx_{1-x}, \tag{3.1}$$

hence this correlation is also termed "optical bowing" [247–249]. The optical bowing coefficient b is specific for the material composition and has been calculated to $b = 0.75\,\text{eV}$ for CdSeTe mixtures. Surprisingly, this rather simple expression can account for the increasing contribution of dopants with a different atomic size, electronegativity and anion-cation bond length. It has been shown that the band gap has a minimum of less than 1.3 eV for a tellurium ratio of $x = 0.612$. By making use of this kind of bandgap engineering photon emission wavelengths of up to 900 nm can be reached. Analogue to pure QDs, confinement for small alloyed nanocrystal already occurs for crystal diameters of 8.6 nm which can be attributed to an increased effective Bohr radius of the CdSeTe alloy [243]. With a tellurium ratio of $x = 0.6$ the emission wavelength of 800 nm has been measured for crystal diameters of about 6 nm.

3.5 Fluorescence intermittency

One of the most characteristic feature associated with colloidal QDs is the fluorescence intermittency, also known as 'blinking'. First discovered in 1996, Nirmal and coworkers [250] found that single CdSe QDs under continuous wave excitation display a fluorescence intensity which is not constant over time but describes a binary 'on'/'off' behavior. The QD shows a spontaneous switching between a radiative and a non-radiative state as indicated in Fig. 3.6a. Intensity dependent measurements indicated a mechanism that is a light-induced process as the average 'on'-time decreases while the average 'off'-time remains the same. The observation is consistent with an Auger ionization model were the QD can switch into a charged state corresponding to a delocalized charged in the core and a trapped/localized charge on the surface. Subsequent excitation of a charged QD is followed by a non-radiative Auger process rendering the QD dark ('off'). Measurements on QDs with surface passivation layers showed a reduction of charging events and therefore a more stable photoemission.

Since then, colloidal CdSe nanocrystals of different sizes and compositions have been under heavy research in order to fully characterize the processes of blinking. Even though the originally proposed mechanism of charge carrier trapping is still the basis of most of the models, none of them is capable to agree in all aspects with experimental observations which is in part due to the diversity of nanocrystal preparation and the sensitivity of the band structure to minor changes of different parameters such as size, crystallinity, composition.

Throughout many reports, the charged state is described as an ionized QD that contains an additional charge carrier which is delocalized within the QD. The additional charge carrier can be either negative or positive. Furthermore multiple charge

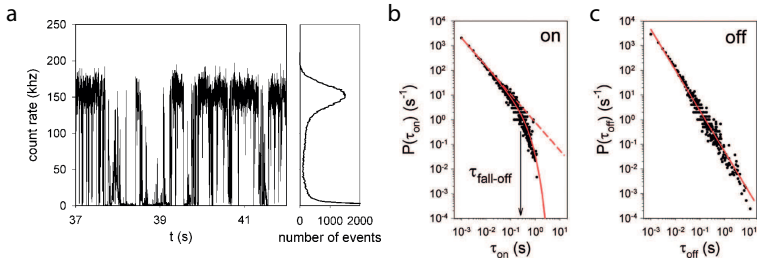

Figure 3.6 – Fluorescence intermittency of colloidal quantum dots. a, Photoluminescence trajectory of a single quantum dot. The histogram clearly indicates the difference in fluorescence between the 'on' and 'off' state. **b,** Correlation of the duration and probability of the 'on' state.**c,** Correlation of the duration and probability of the 'off' state. Reprinted (adapted) with permission from reference [251]. Copyright (2018) American Chemical Society.

carriers of the same type are possible, such as a doubly charged QD. Excitation of a charged QD does not yield a neutral exciton X but a charged exciton, called trion, which depending on its charge is called a positive (negative) trion X^+ (X^-). Higher order charged states, e.g. doubly positively charged, are consequently labeled X^{++}. Further excitation of a singly charged QD can also lead to a charged biexciton which is labeled in a similar fashion (BX^+, BX^-). The procedure to end up in a charged QD state as well as the decay characteristics of an excited charged QD state does not follow a general rule. The QD size, shape and composition as well as the intensity and energy of the excitation light do all have an influence on the dynamics of charged excitons. In the following section, an overview on the development of the description of charged QD dynamics will be presented.

Most of the studied charging events are photo-induced, that is, one or more excitons are created via photon absorption and a trapping event leads to the localized bonding of one charge carrier, i.e. an electron, leaving behind a positively charged QD. The quantum yield of charged QD states is in most cases much lower ('off' state) due to efficient non-radiative Auger processes until the trapped charge spontaneously recombines with the delocalized charge. Initial studies aimed towards assigning a characteristic lifetime to the trapped state. To this end, photoluminescence trajectories are recorded to correlate the duration $\tau(\text{on},\text{off})$ and probability $p(\text{on},\text{off})$ of the 'on' and 'off' events. It turned out that there is no exponential behavior (see Fig. 3.6b,c) that links $\tau(\text{on},\text{off})$ and $p(\text{on},\text{off})$, as early observations have suggested [250, 252, 253]. Systematic correlation studies have shown that $\tau(\text{on},\text{off})$ follows a universal power-law dependency $p(\tau) = \tau^m$, which implies that there is no characteristic timescale for the lifetime of the bright and dark state [254]. The probability of a QD to be in the neutral or charged state has been found to be almost identical [255, 256]. The corresponding exponent m has been determined in many studies and is one of the rare parameter which is virtually independent of QD properties such as size, composition, shape as well as external influences such as temperature or excitation wavelength. The value of m has been determined to be at about -1.5 over a frequency range of about 9 orders of magnitude [257]. Limiting

factor on the short time scale is the detection efficiency to determine the state of the QD. Even though single photon counting detectors are being used, integration times of at least 10 µs are necessary to collect enough photons from the QD to accurately determine its state. On the other hand, the long time scales are limited by practical reasons because of their low probability and the experimental challenge to record a PL trajectory over time periods that are longer than 10 minutes. It is important to note that the binning time of the PL trajectory can have a substantial influence on the apparent power-law exponent [258].

The power-law behavior has sparked ideas on many different models on how the 'off' state can be described. Most of these models are based on an 'off' behavior which has a low quantum yield due to non-radiative Auger recombination of the charged exciton. How to achieve a QD system that features this charge state without any characteristic lifetime is the scope of these models. Producing a large bandwidth of transition rates into a trap state can be realized by mainly two different approaches. One method has been suggested that the trap state is a combination of a larger number of states uniformly surrounding the QD core [259]. This approach, however, only leads to a power-law distribution of the 'off' state while the 'on' state remains exponentially distributed. By further adjustments regarding trapping into the outer regions of the QD a power-law behavior of the 'off' state has been established. A similar model uses multiple trap states which randomly switch 'on' and 'off' which also leads to a power-law behavior for QD states [260]. Another model uses a single trap state into which a charge carrier can tunnel [261]. The tunnel barrier width and height is time-dependent and randomly fluctuates. Even minor changes to either parameters leads to a highly multiexponential decay. Observation of correlations between the spectral diffusion of the QD resonance and the occurrence of a transition between the 'on' and 'off' state has lead to the development of a model based on resonant tunneling [262, 263]. Here, the trap state resonance energy fluctuates and goes in and out of resonance with the QD transition energy. A further advanced version of the spectral diffusion model has been proposed a few years later where also the fluctuation of the QD resonance energy had been taken into account [264]. Another approach based on spatial diffusion has been suggested where the charge carrier undergoes a random walk until it reaches a trap site [265]. This model is also able to reproduce the power-law behavior for 'off' states but also includes a non-zero probability for no return of the charge which implies that for long observation times the QD can permanently become dark.

In addition to the challenge of modeling the power-law for the two different states, early studies also observed a further unique behavior [254]. The probability distribution of 'on' and 'off' times differs only in one major aspect, which is the so called 'cut-off' time of the 'on' time probability. As can be seen in Fig. 3.6b, above a certain time τ_c, the probability deviates from the power-law dependency towards lower values which has not been observed for the 'off' times. The truncation of the 'on' time behavior can be modeled with an additional exponential parameter which leads to a distribution described as $p_{on}(\tau) = \tau^m \cdot e^{-\tau/\tau_c}$ [251]. Detailed experimental studies revealed a dependency of τ_c on various external parameters such

as excitation wavelength and pump intensity which is a significant indication for the 'on'/'off' behavior being photon induced [262]. It was shown that the cut-off time τ_c scales with the square of the pump intensity which significantly reduces the probability for a long duration of 'off' periods [251]. This has lead to the conclusion that the process of Auger ionization is responsible for the occurrence of the cut-off parameter as it relies on a non-radiative decay process of biexcitons, a state of excitation also occurring increasingly with the square of the pump intensity. During this process, one exciton can decay non-radiative as this process is much more favorable than the generation of a photon. The excess energy is transferred to the remaining charge carriers of the QD. The state density of holes is considerably larger than that of electrons which results from the sparse conduction band nature compared to the valence band. This increases the probability for the energy absorption by the hole and a subsequent injection into a trap state in the shell region. The result of this process is a QD in the 'off' state which is negatively charged. Further photo-excitation processes are rendered dark due to non-radiative Auger decay. An additional study also revealed that for high excitation intensities the 'off' times are also truncated [266].

It is the process of Auger ionization which is attributed to the majority of transitions into the dark state of the QD. However, the measurement and the confirmation of the charged state of single colloidal QDs has not been reported. So far, electrochemical cells are capable of changing the charged state by applying an electrostatic potential to the substrate [267–270]. This enables the study of QDs after injection of holes or electrons into the shell, but gives no insight on how photon absorption can lead to different charged states. Therefore, information about the QD state can only be deduced by optical measurements which includes photoluminescence intensity, exciton lifetime and state occurrence probability compared to other states. Furthermore, correlations measurements between the two states have indicated a memory effect of the QD [271–273]. This implies that even by measuring single photon events, the minimum temporal resolution in determining the QD state is in the range of 10 µs. Despite of observations such as fluorescence intermittency and non-exponential QD state characteristic, which persist in nearly every experiment, general theoretical models are rare. In specific, comparison of lifetime and quantum yield of 'on' and 'off' states with Auger recombination models have shown inconsistencies. For example, the measured lifetime of the 'off' state did not show any size dependencies [274,275]. Auger decay rates, on the other hand, have been found to be strongly QD size dependent and decrease proportional to the volume [276].

An alternative model to counteract the weaknesses of models based on a long lived trap state and the consequent quenching of excitons via non-radiative Auger processes has been proposed by Frantsuzov and Marcus [277]. In their model, every photoexcited electron hole pair quickly recombines after excitation without the need for a long-time trap state. The difference between the 'on' and 'off' state is defined by the contribution of a non-radiative decay channel. Therefore, the transition 'on'→'off' and 'off'→'on' is not accompanied by a charge which is trapped and released, respectively. In this mechanism, the reduced emission of the 'off'

state stems from a hole which is trapped in a surface state and at the same time the electron is promoted from a $1S_e$ state to the next higher $1P_e$ state in order to conserve energy. The following decay of the electron with the trapped hole is non-radiative and contributes to the 'off' state. Switching between the two optical states now depends on the energy gap ε between the two electron conduction band states. When ε is on resonance with the excess hole energy and the photon energy non-radiative exciton decay is highly probable. In comparison with the charging model, switching between 'on' and 'off' states is not related to a single charge trapping and de-trapping event but rather to an energy gap moving in and out of resonance causing slow and fast hole trapping rates. The variations of the gap energy ε can be explained by long-time light induced diffusion effects [277]. This work has shown that blinking behavior in QDs can also explained without a long-lived trap state and still reproduces the power-law behavior with the correct exponent for the 'on' and 'off' state. However, an unanswered effect remains the difference between the cut-off times which is much larger for the 'on' state compared to the 'off' state [262]. Also, measurements of the diffusion rate of the energy gap ε, which is the key mechanism of this model, have not yet been reported. Further improvements on this model introduced a variety of different trap states as the origin of the fluctuating trapping rate. Instead of having a single trap state with a varying resonance condition, up to ten trap states on the QD surface are available, each of which can toggle between an active and an inactive state. The only difference between these two states is that the active state has a much higher trapping probability than the inactive state. Switching between active and inactive can be photo-induced and is explained by jumps of single atoms on the QD surface. Similarly, the variety of different trapping rates for each active state might have its origin in the QD surface and its diversity of crystal facets. This improved model is able to cover more of the experimental observations such as correlations between subsequent 'on' and 'off' periods [273].

More systematic blinking studies depending on the charge state have been carried using a electrochemical cell [267]. Here, time-correlated measurements of QDs for different potentials in the surrounding medium were employed to observe and differentiate between two different types of blinking mechanisms. The first type of blinking (A-type) is referred to as conventional blinking and is associated with a long-time charge trapping. Further excitation of this QD state leads to a non-radiative Auger decay which renders the QD dark. Another type of blinking (B-type) occurs via an active and inactive trap state within the band gap which can be occupied by hot electrons. Similar to previous models leads the occupation of an active trap state to a subsequent non-radiative combination with the remaining charge carrier [277]. Switching to the 'off' ('on') state for B-type blinking can be achieved by activating (deactivating) the trap state via an external potential.

For QDs which exhibit A-type blinking, increasingly positive external potential significantly reduces the amount of blinking. Any Auger ionization process which caused the trapping of a hole and charging the QD negatively is neutralized by the external potential. Therefore the QD permanently remains in its neutral

state which results in a non-blinking photoluminescence trajectory and a constant average excited state lifetime. A negative applied potential, however, actively increases the probability for a negatively charged QD which results in fluctuating photoluminescence intensity and excited state lifetimes. Fluorescence-lifetime intensity distribution (FLID) maps clearly show the transition towards the X^- state which shows low photon emission due to fast and non-radiative Auger decay. The newly introduced representation of the different QD states with FLID maps represents a major improvement compared to two dimensional histogram based diagrams [251, 255, 278–286].

QDs that also show a B-type blinking behavior (called 'flickering') have an additional state (recombination center) within the band gap which also leads to a reduced fluorescence intensity. However, the process of flickering does not show any reduced excited state lifetime which is due to the fact that this recombination center is directly accessible from energetically higher states. The model reveals a mechanism where (hot-) electrons can be trapped in the recombination center via a rate much faster than the intraband relaxation rate to the band edge. The subsequent recombination with the hole occurs non-radiatively and therefore manifests the 'off' state. The intensity of the 'off' state is defined by the ratio between the direct decay rate into the recombination center and the intraband relaxation rate to the band edge. Increasingly positively external potential increases the probability for an empty recombination center and therefore decreases the likelihood for the exciton to reach the band edge. Negatively biased substrates, however, lead to a permanent occupation of the recombination center due to an increased Fermi level. Owing to the coulomb blockade hot electrons have a negligible chance to occupy the recombination center and therefor always reach the band edge followed by a radiative decay ('on' state). Increasingly negative potential eventually leads to electron injection resulting the 'off' state of a negatively charged QD.

This section has provided an overview on variety of models which have been developed to describe the effect of fluorescence intermittency in colloidal quantum dots. So far, there has not been a model which is able to account for all the different optical observations on the blinking statistic despite the large amount of further studies which have not been mentioned so far [287–307]. The mere diversity of measurements and QD configurations, however, also might impede the possibility for a universal model to describe the fluorescence intermittency.

3.6 Spectral diffusion

Quantum dot emission emanating from its neutral state does maintain a constant fluence of photons. However, a detailed spectral study of the emitted light shows deviations from a perfect two-level-system, some of them similar to observations in single molecule spectroscopy. Specifically, a non-Lorentzian lineshape as well as a spectral width in the range of tens of meV at room temperature are characteristic for nanocrystals. Initial observation of broad spectra of nanocrystal ensembles have been attributed to the inhomogeneous broadening due to variations of the QD sizes

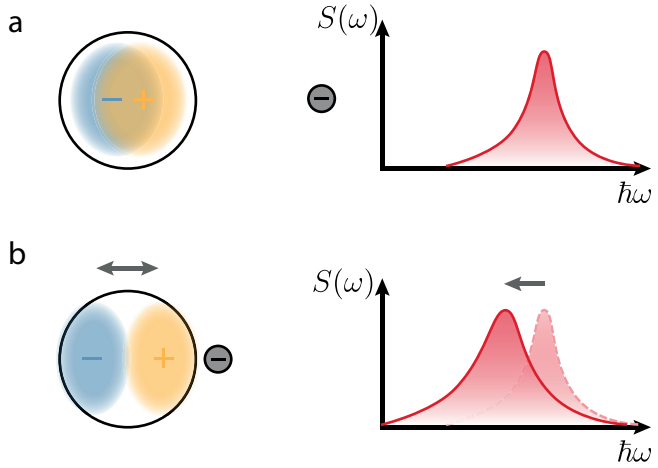

Figure 3.7 – Illustration of the quantum-confined Stark effect of a single charge close to a quantum dot. a, For large distances the charge has little impact on the exciton. **b,** Close to the surface, the static field leads to a separation between the electron and hole wavefunction. The spectrum shows a redshift and broadening.

occurring during the crystal growth. Making use of size selective techniques, however, have also been unable to yield the homogeneous linewidth [241, 308]. First cryogenic experiments on single QDs have shown a spectral width 50 times narrower compared to ensemble measurements [309]. Yet, these spectra are still broadened due to spectral diffusion, a process that shifts the emission energy randomly over time. A power broadening was also observed due to the increased spectral diffusion at higher excitation intensities. Based on the spectral changes to the initial spectrum (see Fig. 3.7a), the red-shifted emission energy (see Fig. 3.7b) indicates a similarity to the Stark effect and the origin of the spectral diffusion was therefore attributed to changes of the electric field distribution in the vicinity of the QD. Ionization processes and charge trapping directly at the QD surface were speculated to be responsible for this self-induced Stark effect. A further study confirmed a local electric field to be responsible for the emission energy fluctuation by measuring the quantum-confined Stark effect [310]. An external electric field can induce spectral diffusion which shows the same characteristics to the fluorescence spectrum. Random internal changes of the QD charge distribution changes of the exciton's energy and orientation. The width of the emission spectrum has been shown to increase with excitation intensity and energy as well as acquisition time [311]. This led to the conclusion that the absorption of photons has a direct influence on the spectral diffusion.

Observation of increasing linewidth with increasing excitation energy has suggested that the spectral diffusion is affected by phononic processes [311]. A correlation between spectral diffusion and fluorescence intermittency has been already proposed during the first observation [309]. Studies revealed that 'on'/'off' switching events are likely to follow a large spectral jump [263]. More specifically, it was shown that large spectral jumps occur more often during an 'off' period. Elongated

QD rods introduce a spatial asymmetry of the internal charge configuration enabling the possibility to gain information about the distance of the effective charge with respect to the core via the spectral position and the peak width [312–314]. With the development of fast and highly efficient spectroscopy schemes it was possible to measure spectral diffusion within 200 µs over just a few µeV [315]. A statistical analysis based on a diffusive approach shows that the spectral jumps are due to discrete hops of charges between shallow electron traps [316]. Further analysis of the temporal evolution of the spectral broadening indicated a close relation between spectral diffusion and fluorescence intermittency [317]. A sub-diffusive behavior was observed by modeling the interaction of the exciton with an ensemble of two-level-systems yielding a power law behavior with an exponent of about -1.5. The various charge configurations have also shown to exhibit a memory via measurement of anticorrelation [318]. Spectral jumps during periods without photoexcitation revealed the process to be spontaneous.

It has become clear that the resonance energy of the exciton does not depend on a single charge diffusing throughout the QD but on a complex landscape of charge density. Photo-induced manipulation of the charge configuration can create stable persisting states or meta-stable arrangements which spontaneously decay into the previous state. Theoretical approaches are used to determine that adsorbed ligands near the surface are likely to be the origin of the trap states [319]. Measurements on core/shell quantum dots also showed that the influential charges are located outside the shell in the ligand region and not within the shell material [320].

Recent studies investigated the effect on spectral diffusion due to trion transitions during 'off' periods [321, 322]. The change of polarizability and binding energy between 'on' and 'off' states as well as altered radiative and non-radiative decay rates affect the impact of spectral diffusion.

3.7 Dephasing

In general, a transition between two different electronic states in a solid always leads to a perturbation of the atomic nuclei which propagates through the lattice. The coupling between excitons and these periodic oscillations (phonons) is described as electron-phonon interaction. The occurrence of optical phonons (out-of-phase movement between adjacent nuclei) is predominant in bulk CdSe compared to acoustic phonons (coherent nuclei movement). This condition is reversed in case of small nanocrystals, where the confinement of the exciton, a reduced crystal size and additional surface modes reduces the interaction between excitons and optical phonons while promoting acoustic photons.

The width of the fluorescence spectrum of a single CdSe nanocrystal at room temperature is typically in the range of a few tens of meV due to a combination of several effects that cause a homogeneous line broadening. The lifetime-limited decay has only a minor contribution as well as non-radiative electron-hole recombination processes. The dominant contributor to the linewidth is the electron-phonon interaction, a dephasing process which broadens the transition without causing a

net loss of energy. With decreasing temperature, the linewidth reduces significantly down to values smaller than 120 µeV [309]. This observation displays the impact of electron-phonon coupling on the shape of the spectrum at ambient conditions.

The size and shape of the nanocrystal has an influence on the electron-phonon interaction coupling. Calculations have shown that with increasing QD diameter the interaction with acoustic modes slightly decreases while remaining larger than optical modes [323]. The dephasing times of about 10 fs for CdSe nanocrystals with a diameter of 1.6 nm have been calculated in *ab initio* studies.

Dephasing is often associated with a non-radiative transition between two energetically different electric states such as energy relaxation or thermalization. However, in absence of any nearby states, which is the case for quantum dots near the band edge, transitions into virtual states are also possible. The dephasing of the energy state in this case can therefore also be described as *pure dephasing* [324].

A large pure dephasing rate of quantum dots does affect the coupling behavior of a transition with a cavity mode. Theoretical investigations [325–331] as well as experiments [332–335] with microcavities have shown that at low temperature a quantum dot can transfer energy to the mode despite being off-resonant with without any spectral overlap. However, this non-resonant coupling due to phonon-assisted cavity-feeding is not yet fully understood and various exciting and surprising observations are predicted. For example, despite primarily causing loss of coherence, adding pure dephasing to a transition has been shown to induce lasing [329] or an increased Purcell factor [329, 336]. All these studies have been mainly focused on microcavity systems as well as self-assembled quantum dots with dephasing times of a few tens of ps [333, 334, 337]. Nonetheless, a similar behavior can be expected from colloidal quantum dots interacting with plasmonic resonances where the resonances are much broader and the dephasing times are in the fs range.

3.8 Hot electron relaxation

The band structure of bulk semiconductors features a dense ensemble of electric states. The charge carriers of an exciton undergo relaxation until they reach the energetically lowest state near the band gap. This non-radiative relaxation process via electron-phonon interaction converts the energy of the charge carriers into heat which is why this process is referred to as electron/hole *cooling*. A fast relaxation of the *hot* electron is ensured due to the continuous density of electronic states which provides small transition energies for efficient electron-phonon coupling.

As previously discussed in this chapter, the confinement of semiconductor nanocrystals leads to a spreading of the energy states which converts the continuum of states into a discrete atom-like distribution. This also affects the relaxation process of hot electrons due to the fact that the energy gaps are becoming larger than 30 meV, the typical energy of a longitudinal optical phonon. The necessary multi-phonon emission process has longer decay times and therefore changes the decay dynamics. Initial calculations have expected that with decreasing nanocrystal size (large confinement and therefore greater level splitting) the decay of hot electrons is even-

tually limited by the slow phonon relaxation process, a phenomenon known as the phonon 'bottleneck' [338, 339]. However, subsequent experiments have shown that the relaxation remains in the ps regime which suggested that other decay processes are involved [340–342].

Among these processes are Auger recombinations which involves the transfer of energy from the electron to the hole via coulomb interaction [343, 344]. The level splitting of the hole is three times smaller due to the larger hole mass and the degeneracy of the valence band [345]. This enables the hole to quickly relax to the band edge and diminishes the effect of the phonon bottleneck.

Another important decay channel is an observation called 'hot electron trapping'. Here, the excess energy of the electron causes a promotion into a localized trap state at the surface of the nanocrystal [267, 346]. It has been shown that a change of the excitation energy from 2.55 eV to 3.13 eV increases the photonionization rate by 2-3 orders of magnitude [347]. Measurements at different excitation rates furthermore confirmed that this effect is truly related to the exciton energy and also shows that the effect of photocharging is occurring prior to the relaxation process to the band edge [348, 349]. As a result, the delocalized hole is left behind in the core rendering the QD positively charged.

3.9 Coupling with metal nanostructures

The near-field interaction of a quantum emitter in close proximity to a metal surface is a topic which has been addressed theoretically decades ago and is nowadays a textbook standard [15, 350]. It was shown that within an emitter-metal distance h smaller than the emission wavelength the excited state lifetime changes. Depending on the transition dipole orientation those changes can be different. However, in any case the lifetime approaches zero as $h \to 0$. The energy transfer from the emitter to the metal becomes the dominant decay channel which is ultimately non-radiative for a flat metal surface. This specific distance range of below 0.6 nm is known to be the quenching regime for single molecules [351]. With the technological development of highly sensitive experimental setups detection of single emitters became eventually possible [352, 353] and theoretical models have been confirmed [354].

The initial focus on single molecules soon was extended and the investigation of single nanocrystals close to metal surfaces promised abundant insights on the inner workings of those kind of emitters [355]. The quenching of fluorescence close to the metal is observed in case of a smooth metal surface and in accordance with the behavior of single molecules. For a rough gold surface, however, the fluorescence intensity as well as the exciton dynamics undergo a significant transition. The exited state lifetime shows major decline of three orders of magnitude while the fluorescence intensity is enhanced by a factor of five. The rough surface offers many decay channels for the emitter which has also beneficial effects on its excitation rate via changes to the effective absorption cross-section. A quantum efficiency analysis has revealed that, indeed, the non-radiative decay rate can increase by a factor

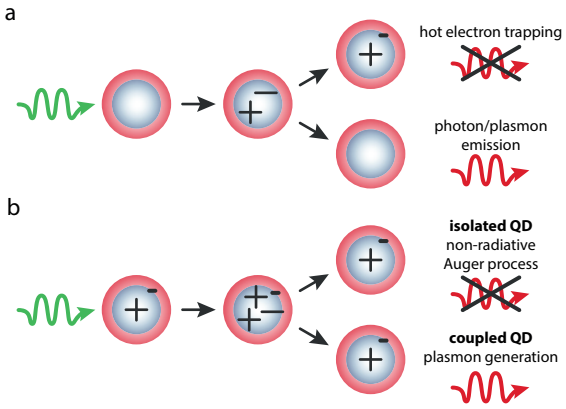

Figure 3.8 – Sketch of the charge dependent dynamics of a photo-excited quantum dot with and without coupling to a plasmon. a, Dynamics of a neutral quantum dot. **b,** Dynamics of a positively charged QD.

of 1400, but the enhanced excitation rate leads to an effective rise in fluorescence intensity [355]. A comparison to measurements on a smooth metal surface with negligible excitation enhancement has shown a vanishing fluorescence intensity. Furthermore, timetrace measurements indicate that the fluorescence intermittency on a gold surface is significantly reduced compared to a dielectric substrate which suggests radiative emission from the charged QD state. This shows that the non-radiative Auger process, responsible for the negligible photon yield of uncoupled QDs, is outperformed by the enhanced decay rate.

The mechanism on how the emission process of a CdSe/ZnS QD after non-resonant excitation is affected by plasmons is illustrated in Fig. 3.8. In case of an initially neutral QD (Fig. 3.8a), the relaxation of the hot electron can either lead to a trapping in the shell (resulting in a positively charged QD) or the exciton can decay radiatively via photon emission or plasmon generation. If the QD is already charged (Fig. 3.8b), a decay of the uncoupled QD occurs via a fast non-radiative Auger process. In proximity to a resonant plasmonic nanostructure, the enhanced spontaneous decay rate can overcome the Auger rate via the excitation of a plasmon and thus avoid the non-radiative decay.

Spectra at cryogenic temperatures have allowed to show that the fluorescence on gold comprises of two peaks, one corresponding to the neutral QD state and one to the charged state. The study of Shimzu et al. was the first to show that a metal surface can have a striking impact on the internal properties of semiconductor nanocrystals as they directly observed fluorescence of the charged QD state. This work marked the beginning of many further studies on different type of nanocrystals as well as various metal geometries [6, 14, 62, 64, 65, 69, 78, 284, 356–388].

In addition to the study of blinking suppression and fluorescence enhancement the observation of photon bunching of single QDs triggered further investigations on multiexciton decay [382]. A study on isolated quantum dots revealed a method to quantify the single-to-biexciton quantum yield ratio based on a single second-order autocorrelation measurement $g^{(2)}$ [389]. It has been shown that for CdSe/ZnS

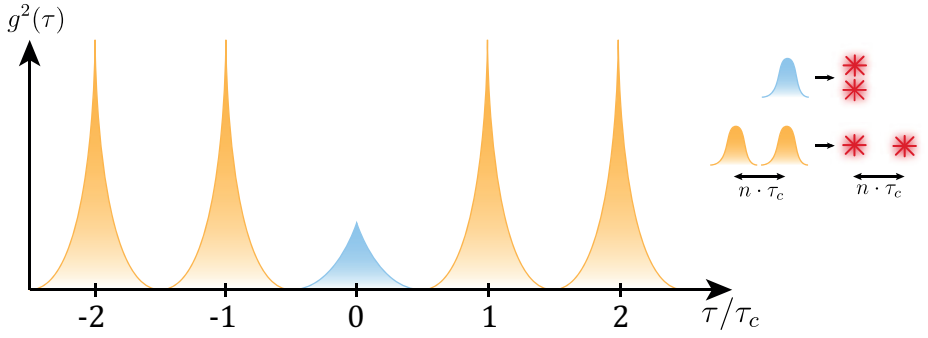

Figure 3.9 – Sketch of an autocorrelation histogram of a QD under pulsed excitation. The center peak corresponds to biexciton emission from a single excitation whereas the side peaks correspond to single photon emission from two pulses separated by $n \cdot \tau_c$.

nanocrystals the Auger process strongly affects the decay of biexcitons which leads to low BX quantum yields of 0.15. Other types of quantum dots which have been known to be less prone to non-radiative Auger recombination, such as giant CdSe/CdS QDs, exhibit a BX quantum yield close to unity. This method by Nair et al. to quantify the BX quantum yield soon became the standard technique in most of the succeeding studies on biexciton emission of quantum dots near metals [64, 375–378, 380, 381, 383–386, 390–393]. Here, pulsed excitation of a single nanocrystal creates an intensity autocorrelation distribution as depicted in Fig. 3.9, with a peak at zero delay and every integer multiple of the pulse cycle time τ_c. It was shown that for a QD which absorbs a Poissonian-distributed number of photons $\langle N \rangle$ per pulse and for $\langle N \rangle \to 0$ the value of $g^2(0)$ equals the value η_{BX}/η_X , where η_X and η_{BX} are photoluminescence quantum yield of the exciton and biexciton, respectively. The peak height a zero delay (blue) represents the probability for two photons being emitted after creation of a biexciton with a single pulse. The probability of two single exciton generations by subsequent pulses is reflected by the peak height of adjacent peaks at $\pm\tau_c$ (orange). Both of these probabilities scale with $\langle N \rangle^2$ giving rise to a finite constant value of $g^2(0)$ for $\langle N \rangle \to 0$.

Coupling experiments with CdSe/Zns QDs covered with a layer of single silver nanoparticles have shown that if the excited state decay rate is reduced below the non-radiative Auger process, multiphoton emission significantly increases. At the same time, the probability for single photon emission decreases [384]. Further detailed intensity studies of the exciton and biexciton quantum yield of giant CdSe/CdS quantum dots showed that the emission efficiency η_{BX} can actually exceed the single exciton efficiency η_X [386]. This observed super-poissonian photon statistic is only possible under two conditions. First, the non-radiative Auger rate has to be significantly reduced in order to maximize the BX decay. This has been assured by using QDs with up to 19 monolayers of CdS which has been shown to minimize the Auger decay [394, 395]. Second, the non-radiative decay into the

metal has to exceed the radiative decay [386]. This leads to a single exciton quantum yield which is smaller than unity which is necessary to reach the case of photon bunching with $\eta_{BX} > \eta_X$.

It is important to note that the amplitude of $g^2(0)$ does not yield a quantitative measure of the biexciton emission efficiency. The peak height is always measured with respect to the adjacent peaks and therefore an autocorrelation histogram can only deliver the ratio between single-to-biexciton quantum yield. An increasing $g^2(0)$ can therefore also be observed if η_{BX} is actually getting smaller when at the same time η_X drops even faster. This is mostly the case when QDs are coupled to rough metal surface where the majority of additional decay channels are non-radiative surface plasmons. The increased decay rate affects both, the single exciton as well as the biexciton decay. However, the biexciton lifetime is shorter and therefore less effected by the enhanced (non-radiative) decay. In order to achieve real enhancement of η_{BX}, the effect of the opposing Auger process has to be minimized. That means, the radiative decay rate of the biexciton has to overcome the non-radiative Auger decay rate which can be achieved by two approaches. One method is to decrease the Auger rate via specific wavefunction engineering in order to reduce the interaction of the charge carriers with the QD surface. This is the reason why giant CdSe/CdS quantum dots have been proven to exhibit significant BX emission even for low excitation rates [375–377, 383, 385, 386]. The other technique is via drastic enhancement of the radiative decay rate until the Auger process no longer efficiently suppresses the radiative BX decay. To this end, the QD needs to couple resonantly with plasmonic structure which exhibits a high radiation efficiency such as a nanorod or a bowtie antenna. While the QD properties in this case are only of minor importance, this method, however, requires a sophisticated sample preparation which includes the fabrication of a resonant plasmonic structure and the exact positioning of the QD with respect to the electric near field. There are a few recent studies of radiative enhanced QDs, however, none of them focuses on the efficiency of biexciton emission [69, 370, 387]. AFM manipulation and scanning probe techniques are also being used in order to gain control of the relative position between the QD and the metal surface [379, 396]. This enables dynamic measurements which directly show the transition of the QD from being a single photon source to a multi-photon emitter. Due to the highly enhanced radiative decay rates the use of CdSe/ZnS QDs coupled with metallic structures increases as there is no need to rely on Auger suppressing QDs such as giant CdSe/CdS nanocrystals.

A topic which has not been addressed so far in the literature is the effect of the spectral overlap between a quantum dot and an optical (plasmon) resonance. It has been pointed out in section 3.7 that dephasing can considerably influence the coupling to an external resonance. Those studies, however, have been carried out solely in microcavities at cryogenic temperatures. At room temperature and for colloidal quantum dots, the emission spectrum is much broader and represents a combination of the transform-limited emission line, spectral diffusion as well as dephasing as depicted in Fig. 3.10a. The coupling to a localized plasmon resonance can be achieved without a direct overlap with the transform-limited emission line as shown in Fig.

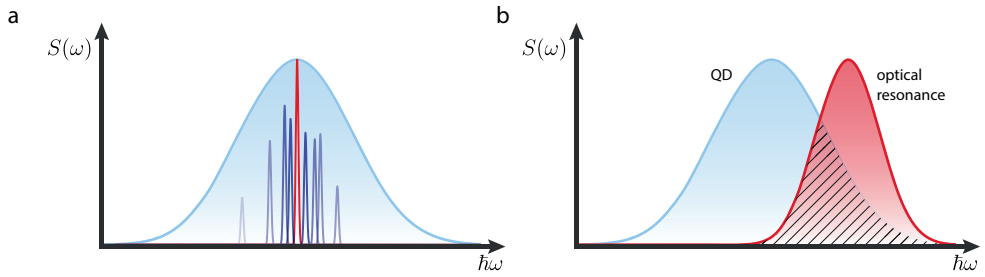

Figure 3.10 – Illustration of the spectral width of CdSe quantum dots and the coupling with an optical resonance. a, The transform-limited linewidth of the exciton (red) is shifted due to spectral diffusion (dark blue). The overall width (light blue) of the spectrum is due to dephasing via phonon interaction. **b,** A quantum dot coupling with an optical resonance. Despite the large spectral overlap (hatched area) there is negligible direct coupling with the transform-limited line.

3.10b. The energy transfer in this case would be entirely mediated by internal QD processes with different intensities across the spectrum of the plasmon resonance. Conclusive measurements on how these conditions affect the fluorescence spectrum of the coupled QD-plasmon system have yet to be reported.

The interplay between excitons and photons via additional phonon mechanisms and QD-state dependent processes pose a further complexity to understand the coupling mechanism of colloidal quantum dots and plasmons. However, the absence of any studies in this regard so far allows for unexpected discoveries which eventually further link the fields of semiconductor physics and light-matter interaction.

4 Experiment and Sample preparation

The main scope of this work is to investigate the influence of a nano-sized emitter in close proximity to resonant optical near-fields. Getting a maximum of spatial control while maintaining optical accessibility with high throughput can be realized by employing scanning probe technology. In this chapter, the implementation of a scanning probe apparatus onto an inverted confocal microscope is demonstrated. Furthermore, the preparation of single emitters protected by a thin polymer layer on a glass slide is presented. Finally, it is shown how to produce single crystalline gold probes with a optical near-field resonance which sustains direct contact with a substrate.

4.1 Scanning Probe Technology

An intuitive way to probe the interaction between two objects is by directly controlling their separation by the use of an external manipulator as it gives rise to maximum flexibility and reproducibility. This method is known as scanning probe technology which is a collection of different implementations such as atomic force microscopy (AFM), scanning tunneling microscopy (STM) or scanning near-field optical microscopy (SNOM). Serving initially as an instrument to determine the topography of a surface with atomic precision, each technique has been a technological success in nano-scale operation each featuring a different type of probe with a different implementation of approaching a flat surface or an object.

Applying scanning probe technology to the nanometer scale, however, bears great engineering challenges due to interactions which only emerge at the atomic scale. Here, gravitational and inertial forces play only a minor role compared to van der Waals interaction or surface tension which leads to unexpected behaviors when manipulating nano-objects. In the end, any nano-probe is eventually mounted on a macroscopic device which is driven via a stepper motor or a piezo-electric crystal. This makes the apparatus also sensitive to temperature changes which induce nanometer drifts within only a few degrees Celsius. The complete setup is also prone to pick up waves in the acoustic frequency range and large cable feeds are

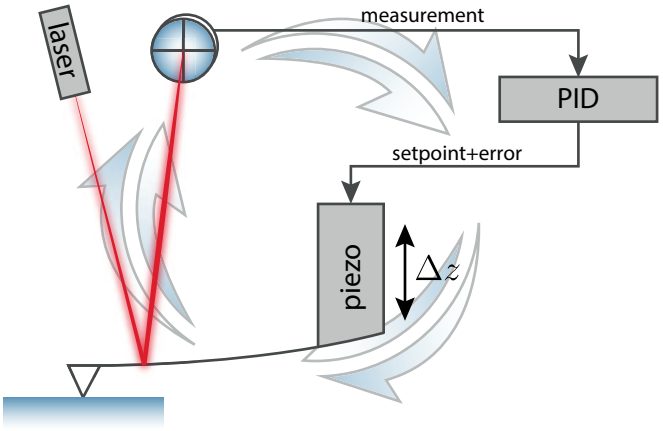

Figure 4.1 – Sketch of the working principle of an atomic force microscope. The reflected laser beam is detected by a four-section photodiode which measures the deflection of the cantilever. This quantity is used to drive the piezo which moves the tip height by Δz in order to maintain a constant probe-sample distance.

able to gather electromagnetic waves which causes additional noise in the electric circuits.

Throughout this work, all scanning probe measurements are performed with an AFM in contact-mode. In this configuration, the microscope uses a long cantilever to make direct contact with the substrate. The low spring constant of the cantilever makes it possible to press the tip onto the sample to ensure a minimum and permanent contact. An illustration of the most important working principles is shown in Fig. 4.1. The cantilever is mounted on the lower end of a piezoelectric tube. To adjust contact pressure of the tip on the surface the cantilever can be moved up and down by applying a voltage to the tube which leads to an extension or contraction. The maintenance of a constant contact pressure with the substrate is realized by closed-feedback loop. The bending of the cantilever due to contact with the sample is measured with a laser beam and its reflection from the back side of the cantilever can be accurately tracked via a four-quadrant photo diode. Any changes in deflection is processed by a PID-algorithm and which directly changes the height of the tip accordingly by either extending or contracting the piezo.

4.2 Confocal Microscopy

Measurements at the single emitter level require sophisticated photon detection schemes. Due to their sparse and sometimes limited amount of emitted photons the setup has to be capable to account for the majority of fluorescence photons while suppressing any parasitic light contributions in order to maximize the signal-to-noise ratio. In addition, high spatial resolution is another requirement for single emitter experiments in order to be able to differentiate between two adjacent fluorophores as good as possible. Therefore, all optical measurements in this work have been done in a confocal configuration. A sketch of the working principle is

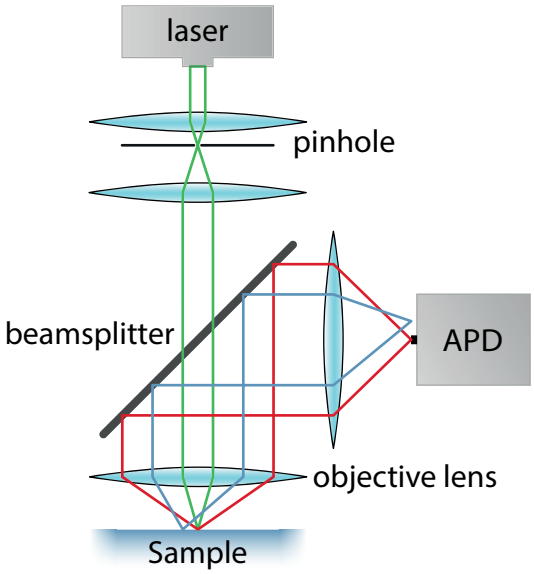

Figure 4.2 – Sketch of the confocal principle. The excitation light (green line) originates from a point-like source (pinhole) and is focused on a single spot on the sample surface. The fluorescence light is only detected from the same location (red line) due to a point-like dectector. Any out-of-focus light emission (blue line) is suppressed as it does not hit the detector.

shown in Fig. 4.2. Here, a point-like light source is created by focusing a laser beam (green line) on a pinhole. After collimation the light is focused to create a diffraction limited excitation spot. The minimum out-of-focus contribution reduces any fluorescence outside the focal point. The fluorescence light (red line) is also focused and detected with a point-like detector, i.e. an avalanche photo diode (APD), which further suppresses contributions from out-of-focus areas (blue line). To obtain a fluorescence image of the sample with maximum optical resolution it has to be raster scanned through the focus with a step size smaller than the diffraction limit.

The width of the focus area is defined by the wavelength λ and the numerical aperture NA of the microscope objective which is also a measure for the resolution of the microscope. The minimum distance d_{min} which is required to resolve two point dipoles is described by the Abbe limit as

$$d_{\text{min}} = 0.6098 \frac{\lambda}{\text{NA}}. \tag{4.1}$$

The excitation laser which is used in this work has a wavelength of 532 nm and is focused via a microscope objective with a NA of 1.45. This corresponds to a diffraction limit of 224 nm for a point-like emitter.

4.3 Experimental setup

All optical measurements are performed with a home-built inverted microscope combined with a commercial AFM (Bioscope, Bruker, Germany). The objective and the AFM head are merged by a customized stage which permits a maximum degree of freedom to manipulate the AFM tip and the sample independently with respect to the objective. The challenge of mounting an AFM lies in its susceptibility to mechanical vibrations. Especially oscillations in the acoustical frequency range can easily couple to metal framing and other parts of the mount which significantly decreases the signal-to-noise ratio during AFM measurements. A key technique to overcome this problem is to raise the mass of every mounting component which leads to a shift of the resonance to high frequencies. Therefore, common (low frequency) sources of noise that can interfere with the measurements (ventilation, traffic) are efficiently suppressed and decoupled from the AFM.

4.3.1 AFM stage

The mount of the whole AFM head has to permit a coarse translation in lateral direction in order to move the AFM tip into the focal range. Consequently, it is placed on top of two solid stainless steel frames each of which is equipped with three suspension points and stacked on a base plate (see Fig. 4.3a). The absence of any further fixation minimizes slow drifts on the nanometer scale. The suspension points are mounted on trails which enables each frame to move in a perpendicular direction. This allows to move the AFM in lateral direction with an accuracy of a few µm to the focal point via micrometer screws.

The same concept is applied to mount the sample. Therefore, two smaller metal frames are stacked on top of the base plate inside the AFM framing. Via micrometer screws they can translate in perpendicular directions in order to move a piezo stage (P-733, Physik Instrumente, not shown in Fig. 4.3a) onto which the sample mounted.

An aperture in the base plate allows the microscope objective (Plan APO TIRF 100x, NA 1.45, Nikon) to access from below. The height of the objective is changed by a micrometer stage for coarse adjustments and a linear piezo scanner (P-721 PIFOC, Physik Instrumente) for fine tuning. A sturdy pillar construction fixates the base plate on an optical table at a lowest possible height which is predetermined by the mount of the microscope objective. The complete stage with AFM head and microscope objective mount is shown in Fig.4.3b.

As described in a section 4.1, the bending of the AFM cantilever is measured via the deflection of a laser beam. The beam path at the AFM head is indicated in Fig. 4.3c. This light source poses difficulties when combining AFM with optical microscopy since the laser is pointing directly towards the microscope objective. The light intensity is partially reduced since the focus of the AFM laser is much smaller compared to the cantilever width which therefore acts as a spatial beam blocker. However, the intensity of the laser light scattering from the surface of the

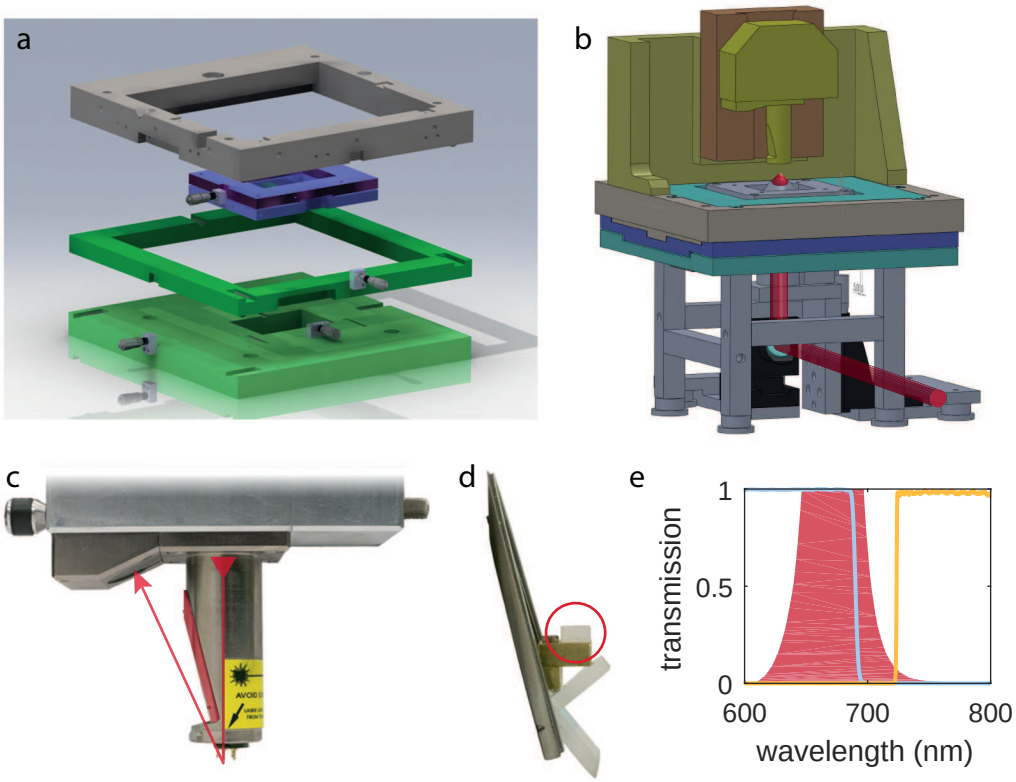

Figure 4.3 – Sketch of the stage which combines AFM and confocal microscopy. a, Base plate with inner and outer metal frames to mount the AFM and the sample piezo stage, respectively. **b,** Complete stage with AFM head on top and microscope objective from below. The optical beam path is indicated in red. **c,** Image of the AFM head with laser indicated by a red arrow. The tube can be opened from the side via a lid (red area). **d,** Customized AFM filter mounted inside the tube at the lid. **e,** AFM laser spectrum (red area) with transmission spectrum of AFM filter (blue line) and long pass filter for confocal microscope (orange line).

substrate and other parts of the AFM head still exceeds any fluorescence signals. In addition, the AFM laser (center wavelength 675 nm) has a broad spectrum in order to reduce interference fringes which can lead to erroneous deflection measurements with the four-quadrant photodiode. The use of a narrow laser-line filter is therefore not convenient as the laser light spans at least over a range from 630 to 750 nm. Since this covers a large part of the visible spectrum filtering the laser before it exits the AFM head is the most promising option. To this end, a 690 nm short pass (3RD690SP, Omega Optical) in a custom 5x5 mm shape was mounted inside the piezo tube directly in front of the laser diode aperture (see Fig. 4.3d). With this modification it is possible to perform single emitter spectroscopy in the wavelength range of 720 nm and above (see Fig. 4.3e). The decreased AFM laser intensity does reduce the overall deflection signal but it remains sufficient to provide a stable feedback. More details about the optical setup can be found in the next subsection.

4.3.2 Optical setup

The optical setup for excitation and detection is sketched in Fig. 4.4. A continuous wave (cw) laser diode (frequency-doubled Nd:YAG) with an emission wavelength of 532 nm is guided via a beamsplitter (transmission ratio 50:50) into the microscope objective and is then focused onto the sample. The excitation intensity is adjusted via an optical density (OD) filter wheel which is controlled by a stepper motor. A electro-mechanical shutter is used to turn the excitation intensity on and off. The fluorescence light is captured by the objective and passes a 720 nm LP filter (FF01-715/LP-25, Semrock) to suppress the light of the remaining AFM deflection laser. A transmission spectrum can be seen in Fig. 4.3e (orange line). An additional 540 nm LP filter is used to further reduce any residual light of the excitation laser. A flip mirror allows to image the sample onto a camera which can be used for a coarse alignment of the AFM tip. The fluorescence light passes a beamsplitter (transmission ratio 90:10) where 90 % of the transmitted light is focused via a lens ($f = 300$ mm) on the entrance slit of the spectrometer (Acton SpectraPro 2300i, 300 lines/mm) and is detected by a Peltier-cooled CCD camera (Andor DU401A BR-DD). The remaining 10 % are directed to a polarizing beamsplitter resulting into two orthogonally polarized beampaths which are detected individually by two single photon counting modules (SPCM-AQR, Perkin and Elmer). This kind of detector features an avalanche photo diode (APD) with a high quantum efficiency and a low dark count rate. Exchanging the polarizing beamsplitter with a non-polarizing beamsplitter allows to perform Hanburry-Brown & Twiss autocorrelation measurements.

Two computers are being used to control of the optical setup and to acquire the data. One computer is dedicated solely for controlling the AFM. The commercial software supplied by the AFM manufacturer is used to perform the tip approach and to control the feedback loop during optical measurements. The second computer controls all the hardware which are necessary for the various types of automated optical measurement procedures. This includes the piezo stage, shutter, spectrom-

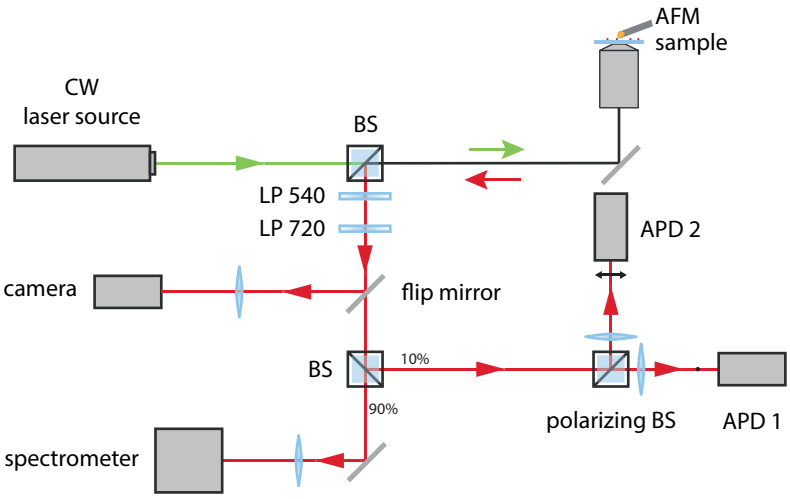

Figure 4.4 – Illustration of the optical setup for simultaneous AFM and confocal microscopy imaging.

eter, APDs, CCD camera and the OD filter stepper motor as well as the recording and storing of the data. To this end, a customized program (LabView, National Instruments) was designed to perform a variety of automated procedures within a minimum amount of time. These time-critical measurements are especially of value for single emitter experiments. Photo-induced changes to the emitter over time and its finite number of optical cycles makes it crucial to keep the amount of emitter exposure as low as possible.

4.4 Colloidal Quantum Dot samples

The preparation of single emitters for coupling experiments is shown in the following section. Colloidal quantum dots are ideal candidates due to their high photostability compared to other fluorophores such as organic molecules. Therefore, they sustain higher excitation intensities for longer periods of time which increases the number and the quality of the measurements. This is especially of importance for detailed coupling studies on isolated single emitters. Additionally, colloidal quantum dots feature a significantly larger dipole moment which makes them attractive for strong coupling experiments. Depending on there size, they also can be tuned over a large wavelength span. In this work commercially available colloidal quantum dots (QDot800 ITK Q21571MP, Thermo Fisher Scientific Inc., Waltham, USA) are used as single emitters. These nanocrystals composed of CdSe doped with tellurium have a diameter of about 10 nm and emit photons at a wavelength of 800 nm. The active QD core is encapsulated by a few layers of the large bandgap material ZnS which improves the quantum yield by decoupling the exciton from interaction with the surrounding medium. For further details on the inner workings of quantum dots are described in detail in chapter 3.

The quantum dots are prepared on a thin glass slide and covered with a polymer.

The sample preparation process begins with a thorough cleaning of the glass slides (#1, Gerhard Menzel GmbH, Saarbrücken, Germany). The cleaning procedure is divided into four steps: First, the glass slides are mounted vertically in a glass vessel filled with acetone which is placed in an ultrasonic purifier for 15 minutes. The same procedure is repeated afterwards with ethanol as a solvent. Mechanical vibrations lead to an increased temperature of the solvent which improves the effectiveness of the cleaning process. At this stage, any macroscopic dirt particles such as dust or grease are removed. To get rid of any residual solvents the glass slides are rinsed in ultra-clean water for a few seconds. In a final step, the glasses are treated with an oxygen plasma for about two minutes. This process eliminates any remaining organic molecules adsorbed by the surface leading to a decreased background fluorescence later in the experiment. In this condition the glasses have virtually zero contamination by particles which has been confirmed by AFM measurements. Furthermore, no significant photoluminescence is observed for when illuminated with a laser light source at 532 nm. These two requirements are mandatory for single emitter scanning probe experiments.

The quantum dots are dissolved in aqueous solution at different concentrations which later on defines the QD density on the substrate. The initial stock solution was diluted with purified water at a ratio of 1:1000 yielding a concentration of 8 nM. The solution was drop-casted on a clean glass slide and spincoated for 10 seconds with a rotational speed of 10.000 rpm. A thorough coverage of the glass slide with diluted QDs before starting the rotation is critical in order to get a homogeneous distribution throughout the substrate. The uniform spreading of the droplet also reduces the probability for nanocrystal clustering which greatly increases the chances to find single separated QDs. Also, keeping the time delay between the glass slide cleaning procedure and QD deposition minimal is advantageous as adsorption of moisture and other molecules at ambient conditions increases the amount of background fluorescence later on in the measurements. With the parameters as stated above, the average QD density was estimated to be less than $1\,\mu m^{-2}$. This concentration was found to be a good trade-off between having many isolated single quantum dots and a high density in order to minimize stage movement between two QDs. Figure 4.5 shows a typical photoluminescence map of quantum dots at low excitation rate (130 µW).

Finally, the QDs are embedded in a polymer layer which fixes their position and minimizes the chances of being picked up by the scanning probe. Furthermore, the polymer has also beneficial effects on the condition of the nanocrystal. The surface of the QD is preserved in a matrix without oxygen minimizing chemical reactions that can lead to photobleaching [397]. The polymer poly (methyl methacrylate) (PMMA) is dissolved in toluene and spin-coated onto the QD decorated glass slide. The concentration of the PMMA defines the final thickness of the polymer layer. First, the glass slide is covered thoroughly with the PMMA solution. Then, the rotation speed is quickly ramped up to 10.000 rpm and held at that speed for about 10 seconds until the solvent evaporates completely. The sample is now ready to be used for scanning probe experiments as baking of the PMMA film should be

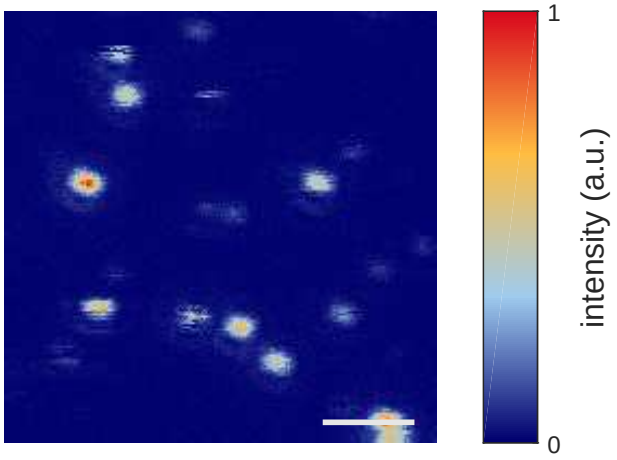

Figure 4.5 – PL image of quantum dots on a glass slide. The size of the spots limited by diffraction. Blinking is visible for a few QDs. Scale bar: 1 µm.

avoided. The high temperature during the polymerization process enhances chemical reactions on the quantum dot surface which can have a negative impact on their quantum yield. It has been found that the air-dried film is rigid enough to sustain gentle tapping by a soft metal scanning probe (such as gold) without any noticeable impact.

The thickness of the polymer layer was characterized for different PMMA concentrations while using the same rotation speed for every sample. Two independent batches of samples were prepared, each with three different concentrations. All samples are also coated beforehand with QDs in order to account for their impact on the quality of the PMMA film. The layer thickness was determined via AFM measurements. To this end, a scratch with a sharp blade at the center of the glass slide was made to create a steep trench in the PMMA layer which is ideal to measure the layer thickness. Figure 4.6a shows the rim of a trench on a sample with a PMMA concentration of 0.6 %. The straight vertical step indicates a clean scratch by the blade without any indication of fringing. A height profile in x-direction averaged over nine lines is shown in Fig. 4.6b (red line). Accurate step height determination can be made by performing a linear fit (blue lines) on both sides of the step. Erroneous contributions from typical AFM artifacts such as overshooting at a steep edge as seen in Fig. 4.6b (red line) are thereby avoided. The vertical separation between the linear fits at the position of the step yields highly accurate values of the PMMA layer thickness. The results of the measurements carried out in the same manner for both sample batches with different PMMA concentrations are shown in Fig. 4.6c. Those two batches (open circles in dark and light blue) yield almost identical results which makes this technique of spin-coating highly reliable for fabricating thin films. The indicated standard deviation originates from the evaluation of multiple height profiles on the same PMMA sample. A linear regression over all data points (red line) suggests that the layer thickness depends linearly on the PMMA concentration. The measurement also confirms that the amount of residual PMMA left after scratching the surface is small as indicated by the a minimal offset to the linear fit.

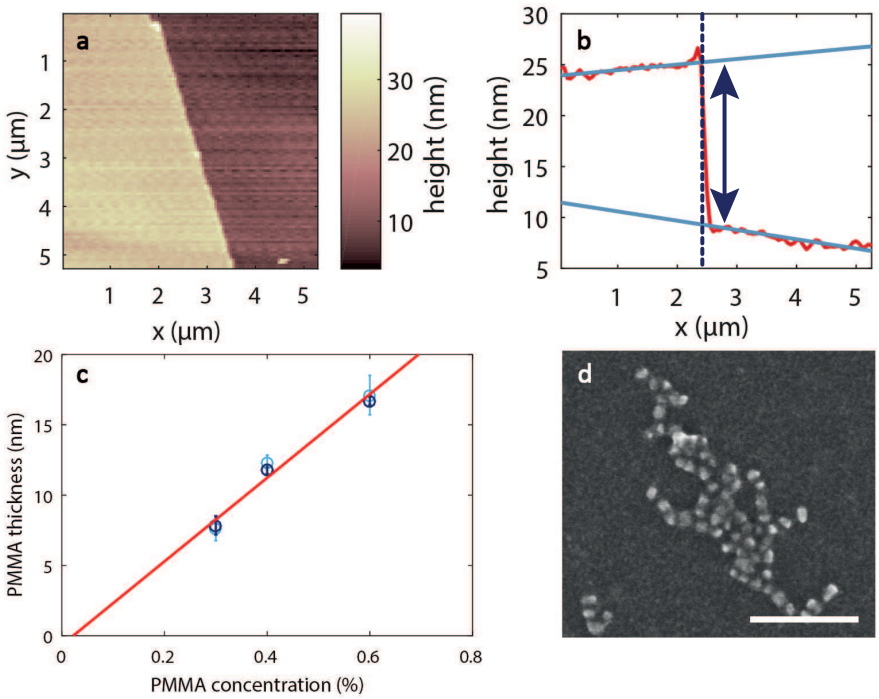

Figure 4.6 – PMMA thickness and QD size comparison. a, AFM map at the edge of a PMMA film. **b,** Height profile (red line) along x-direction at the edge of a PMMA film. Linear fits (blue line) on both sides of the step (dashed line) yield an accurate layer thickness. **c,** Measured PMMA thickness for two batches (light and dark blue circles) with different PMMA concentrations after spin-coating on a clean glass slide. The red line represents a linear fit over all data points. **d,** SEM image of quantum dots on a copper substrate. The average diameter is about 10 nm. Scale bar: 100 nm.

The ideal PMMA thickness for scanning probe measurements is determined by the size of the quantum dots. Their diameter was determined to 10 nm by scanning electron microscopy (SEM) as can be seen in Fig. 4.6d. The image shows drop-casted QDs on a conducting copper substrate. Without spin-coating clustering becomes obvious but has no influence for the purpose of QD size determination. Transmission electron microcopy images on the same type of QD can be found in the literature and shows similar results [282, 367]. Based on these investigations the PMMA concentration for all QD samples which are used in this work was chosen to be 0.4 %. The corresponding layer thickness of 12 nm guarantees complete QD embedding and a smooth PMMA surface.

The QD samples prepared as described above have been proven to show no measurable sign of degradation over time. QD samples which have been reused after more than six months of storage at a dry and dark location at ambient conditions showed similar quantum yields as fresh prepared samples.

In general, the ability to fabricate a PMMA film with a thickness precision in the nm-range is a powerful method to inherently specify the minimum distance between the probe and the fluorescent particle.

4.5 Focused ion beam milling

The ability to pattern any an arbitrarily shaped three dimensional structure is the ultimate goal of nano-fabrication as it gives rise to unprecedented possibilities. One approach is using a beam of focused ions for precise local etching of a conductive material. Due to their mass, ions can carry large momentum even at low energies which make them suitable for abrasive tasks. The transferred momentum of the ion upon impact with the target material breaks up the atomic bonds and sputters the atoms in a straight trajectory. Figure 4.7 illustrates the process of milling a gold surface with a positively charged Ga^+ beam including the most important accompanying effects which have to be taken into account when aiming high quality structures. A common ion type for FIB applications is gallium due to its technological feasibility to provide a stable and bright point-like ion source.

The incident Ga^+ beam caves into the gold surface and sputters the gold material. However, redeposition can occur in the vicinity of the etching area. Additionally, gallium ions can penetrate into the bulk gold and remain as a dopant. The typical penetration depth at 30 keV is about 5 nm. The high momentum of the ions leads to a strong interaction with the substrate which reduces the penetration depth which leads to a rather thin layer with gallium implantation. The emitted secondary electrons can be used to create an image with the ion beam which can be beneficial for monitoring the status of the etching process.

Kinetic ions have additional appealing features due to their mass and therefore outperform many other lithography techniques such as electron beam or UV lithography. The high mass of ions corresponds to a very short wavelength which significantly reduces the amount of diffraction in comparison to electrons. For a standard acceleration voltage of 30 keV an electron has a de Broglie wavelength of 7 pm. In

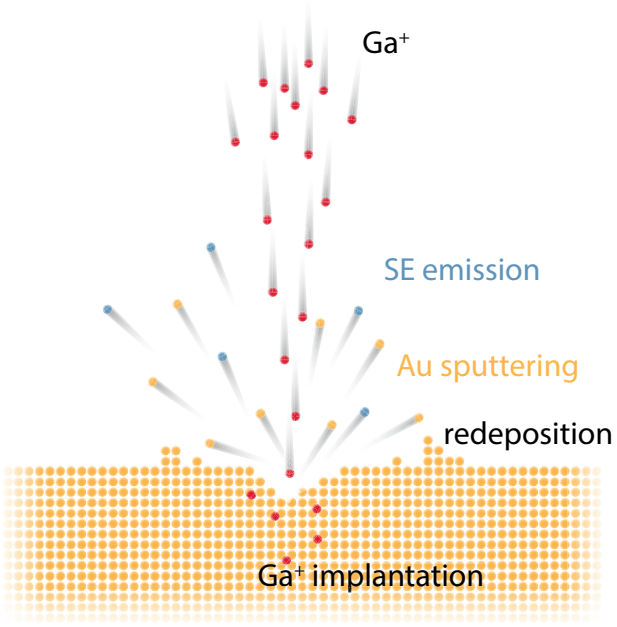

Figure 4.7 – Process of focused ion beam milling. An incident beam of high energy gallium ions impacts on a planar gold surface. The sputtered gold atoms escape into the vacuum or redeposit close to the impact location. Penetration into the bulk leads to doping of the gold material. The emission of secondary electrons can be used to create an image.

comparison, the corresponding wavelength of 20 fm for a Ga^+ ion is more than 300 times smaller which, among other effects, causes a significantly higher resolution.

In order to achieve the highest resolution the ion beam has to be perfectly focused. This includes the correct alignment of the focal plain as well as the adjustment of the astigmatism in both lateral directions. To this end, a scripted routine was employed which systematically repeats a sequence of changing the beam properties and writing a test pattern. This procedure guarantees a reliable and accurate beam alignment to ensure the highest patterning resolution can be achieved.

Another important impact has the angle of incidence of the ion beam with respect to the surface. For a non-orthogonal incidence angle the etching rate as well as redeposition effects can vary significantly. This is of major importance when structuring three-dimensional objects on the nano-scale.

4.6 Resonant Antenna Probes

Mounting a plasmonic structure at the end of a scanning probe has always been desirable to dynamically investigate the coupling between plasmons an single emitters. In the simplest case, a sharp metallic tip can be used as a scanning probe to influence the optical properties of the emitter via near-field coupling. Advancements in fabrication techniques has lead to more sophisticated structures at the apex of a scanning probe which are able to interact with an emitter [14, 81, 82, 398–405]. There are two major challenges that complicate the work with a scanning-probe based setup.

The first major difficulty it is the fabrication of the modified scanning probe itself. As mentioned before, the use of a sharp glass fiber has been proven to be a popular and reliable working base for structured metal films [81, 82, 398–400]. However, the multi-step process of pre-shaping the tip, (multi-layer) metal evaporation and final structuring via focused ion beam milling is a tedious task. The evaporated metal contains many grain boundaries which increases ohmic losses and also hinders the fabrication of smooth structures. Additionally, an adhesion layer based on a different metal, such as chromium, is required to establish a sufficiently strong bond of the structure to the glass tip. The unfavorable optical properties of chromium reduces the performance on the final antenna.

Another major issue is the reliability of the probe during the measurement. Advanced tuning fork feedback mechanisms have been proven to accurately control the tip-to-sample distance. As the glass fiber tip is completely stiff with no possibility to attenuate an impinging force the probe does not tolerate any contact with the sample. The consequence is an immediate major damage or total destruction of the antenna. Increasing the average distance between the tip and the sample increases the lifetime of the probe but also reduces the interaction between the antenna and the emitter.

The use of an AFM tip as working platform has also been demonstrated [14, 401–403] but suffers similar issues as fiber tip based approaches. A new scanning probe concept which is reliable and sustains external influences is needed in or-

der to elevate the scanning probe concept to the next level. The fabrication and characterization of a new type of scanning probe is demonstrated in the following sections.

4.6.1 Probe concept

The use of a single crystalline gold flake as a near-field probe features remarkable properties and advantages which significantly expands the opportunities of scanning probe microscopy. Single crystalline gold flakes carry a diversity of compelling properties regarding the optical performance, but even more importantly, unique mechanical characteristics, which make this material platform ideal for scanning probe operation. They have also been known to be the superior plasmonic material in comparison to evaporated gold films [406]. The lack of any grain boundary greatly improves the overall quality of the fabricated plasmonic structure. This includes the ability to pattern geometries with much greater detail and reduced surface roughness. In addition, increased ohmic losses are a well-known issue of evaporated gold films.

The mechanical properties of single crystalline gold flakes are less well studied as they are commonly only used as a substrate or as a patterning material. With the technological expertise on the concept of flake transfer which is presented in this work (see section 4.6.2) their mechanical properties such as elasticity and hardness can be revealed. It is found that the soft nature of gold, as it is known from evaporated films, also prevails in case of single crystalline flakes. It is therefore possible to crimp a flake on top of a substrate with a tungsten needle in order to create a sufficiently large adhesion in order to pick up the flake. Gold flakes are highly flexible at ambient conditions and recover their original shape after being bent by an external force. For example, the force of surface tension within a liquid a gold flake can be completely folded and unfolded without any visible signs of damage. As long as the integrity of the rim is preserved the flake can tolerate external forces to a large extend. The atomically smooth surface makes it adhesive at ambient conditions, especially in contact with other single crystalline surfaces such as semiconductor wafers or other gold flakes.

All these properties are ideal to serve as a scanning probe since it

- can be transferred and attached to other substrates,
- is not fragile due to intrinsic flexibility and has a tolerance to mechanical damage and
- has superior optical properties.

In addition, patterning a small slit at the edge of the flake creates an optically resonant structure which can be used as a scanning probe. The advantage of directly structuring the probe material is unique and avoids common issues in case of a coated glass fiber tips.

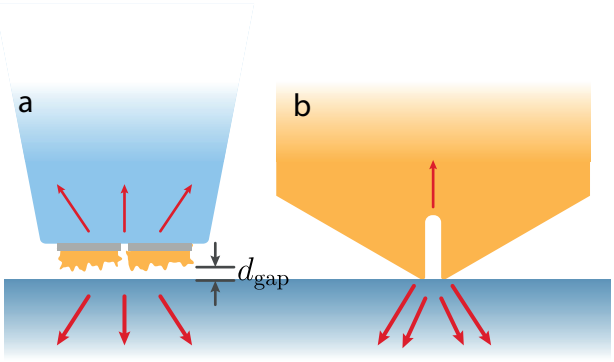

Figure 4.8 – Scheme of two opposing scanning probe concepts. a, Traditional approach based on a metal coated glass fiber tip and subsequent structuring of a dimer antenna. Gap distance d_{gap} on the order of a few nanometer. **b,** Novel concept of using a single crystalline gold flake to combine scanning probe and structuring material.

Figure 4.8 illustrates the differences between the two concepts. A grainy gold dimer structure is patterned a the apex of a glass tip on top of an adhesive chromium layer but nonetheless does not withstand tough contact with the sample (Fig. 4.8a). A tip-sample distance d_{gap} of a few nanometers has to be maintained in order to avoid damage [81]. Radiation is not only emitted in direction of the substrate but also upwards into the fiber. A gold flake, however, is composed of a single and smooth material which sustains permanent contact with the sample. As the resonant structure is part of the flake the emission towards the glass substrate is dominating.

After this brief overview about the conceptional properties of single crystalline gold flakes and their potential application to establish a new type of scanning probe the process of fabrication is discussed in more detail. The next sections feature a detailed description on how to fabricate and assemble all the necessary ingredients to produce a resonant single crystalline scanning probe.

4.6.2 Flake growth and manipulation

The chemical synthesis of single crystalline gold flakes has been shown to produce gold platelets with a lateral size of a few microns while preserving a thickness of a few tens of nm [407]. In this work, slight simplifications have been made to the recipe while still maintaining a high quality of crystalline gold flakes. In a first step 360 µL aqueous solution (0.1 M) of $HAuCl_4 \bullet 3H_2O$ (G4022, Sigma-Aldrich) is added into 40 ml ethylene glycol (324558, Sigma-Aldrich). The growth solution is prepared in a clean standard centrifuge polypropylen tube. Next, two cleaned glass slides are mounted inside the tube within the growth solution [408]. By mounting the polymer tube tilted inside the oven both of the glass slides are oriented horizontally (see Fig. 4.9a). During the growth process at 80° for 12 hours the precipitation leads to a accreditation of gold flakes on one side of the glass slides. After the growth process is completed both glass slides feature a diversity of gold flakes with a broad range of thicknesses and sizes. In order to make use of the flakes as a scan-

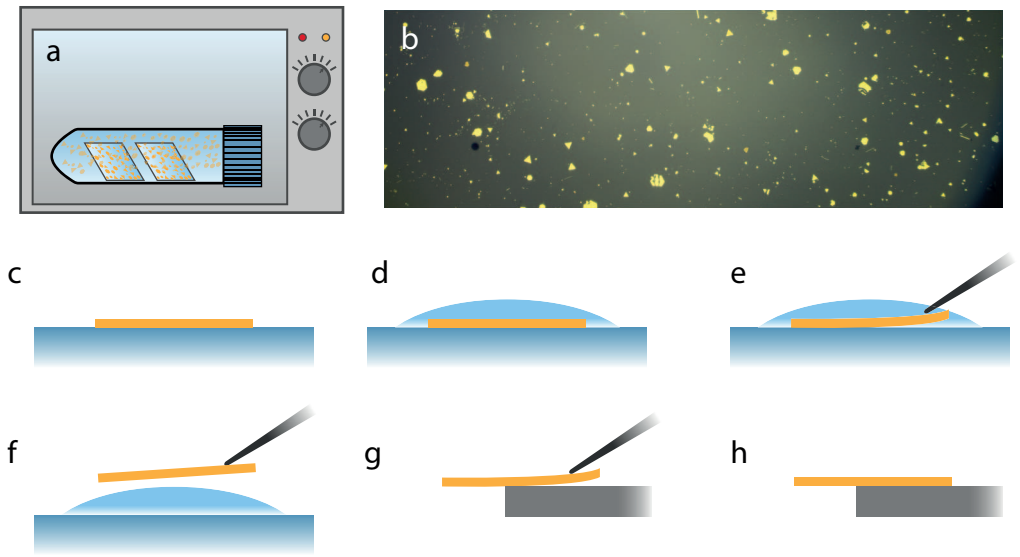

Figure 4.9 – Flake growth and transfer of a single crystalline gold flake on a distant substrate. a, Glass slide orientation during growth in oven. **b,** Optical reflection image of the glass slide after growth. **c,** Gold flake on top of a glass substrate after growth. **d,** Flake enclosed by an ethanol droplet. **e,** The flake is peeled of the glass substrate by a tungsten needle controlled by a micromanipulator. **f,** The flake is pulled carefully through the ethanol-air interface. **g,** Flake is rolled on top of a smooth substrate. **h,** Final position of the gold flake.

ning probe they have to be transferred to a suited substrate (e.g. the back side of an AFM cantilever). The complete workflow on how to transfer a gold flake onto another substrate is shown in Fig. 4.9c-h.

After visual inspection with an optical microscope (Fig. 4.9b) the selected gold flake on the glass substrate (Fig. 4.9c) is covered with ethanol (Fig. 4.9d) which serves as a lift-off agent. The liquid reduces the adhesion to the glass substrate and therefore reduces the risk of tearing or piercing the flake. A tungsten needle mounted on a micromanipulator is used to peel of the flake inside the ethanol environment (Fig. 4.9e). The adhesion of the gold flake with the tungsten needle is sufficiently strong to be pulled through the liquid-air interface due to the low surface tension of ethanol (Fig. 4.9f). Other solvents with an even smaller surface tension (e.g. pentan) are also suitable as lift-off agents but they evaporate quickly due to a low boiling point. The gold flake can be transferred to any substrate with a clean and smooth surface. To do so, the flake has to make contact with the substrate before the needle touches the surface. This way the flake can be rolled out without any wrinkles (Fig. 4.9g). If the flake is in large part in contact with the substrate the needle can be moved laterally to detach and leave the flake at the final position (Fig.

4.9h). More details on how to apply the flake transfer method to build a scanning probe will be given in the next section.

4.6.3 Fabrication procedure

Conventional AFM contact-mode cantilevers can be modified in order to serve as a resonant optical near-field probe. To this end a series of fabrication steps have to be executed which include various FIB etching steps as well as a single crystalline gold flake transfer from a glass substrate to an AFM cantilever. The next section begins with a brief overview about all the required fabrication steps followed by an in-depth study of all crucial procedures and their purposes.

Probe preparation - Overview

The complete procedure on how to use focused ion beam milling and gold flake manipulation techniques in order to create a optical near-field scanning probe is depicted in Fig. 4.10. In a first process step, the tip at the end of a contact mode cantilever (see Fig. 4.10a), doped silicon, no reflective coating, Contact-G-50, NanoAndMore GmbH, Wetzlar, Germany) is cut off via FIB milling (Fig. 4.10b). A single crystalline gold flake (typical thickness: 60 nm) is placed at the end of the tipless cantilever (as shown in Fig. 4.9) such that one corner juts out 5–10 µm beyond the cantilever (Fig. 4.10c). Next, a plasmonic cavity is fabricated at the protruding corner of the flake via FIB lithography with by performing a single line cut (Fig. 4.10d). Subsequent large-area ion irradiation of the protruding gold flake close to the cantilever induces strain and causes the gold flake to bend downwards (Fig. 4.10e,f). This ensures that the plasmonic cavity becomes the foremost part of the probe which touches the sample first (Fig. 4.10g).

More details about the individual fabrication steps are presented in the following subsections.

Flake deposition on an AFM cantilever

The process of placing a flake on an AFM cantilever an be done with a conventional inverted microscope with transmission illumination. A rough sketch of the setup (top view) is depicted in Fig. 4.11a. The tungsten needle can be freely moved and is approached to the selected flake (red arrow) inside the ethanol environment which serves as a lift-off agent. Detailed information about the process of flake transfer is given in section 4.6.2. The cantilever is mounted far away from the flake sample and its orientation can be adjusted according to the shape of the flake.

Figure 4.11b shows a close-up view of the cantilever aligned with the crystal shape. The flake is lowered until it can be rolled onto the cantilever which can be slightly bended by applying a force with the needle. When the flake is sticking to the cantilever the tip is moved backwards as indicated by the arrow while still

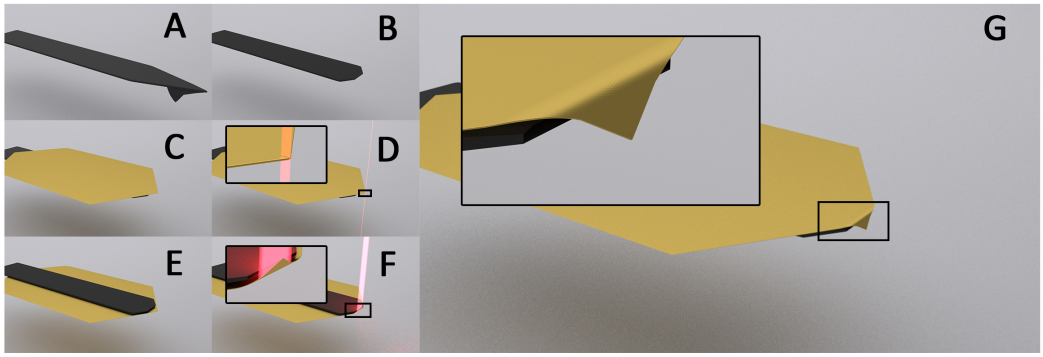

Figure 4.10 – Scanning probe fabrication. **a,** Commercial contact-mode cantilever without reflection coating. **b,** Cantilever after cutting of the tip via focused-ion beam milling. **c,** Deposition of a single-crystalline gold flake using a needle attached to a micromanipulator (not shown). **d,** Fabrication of the PNR by a single FIB cut. **e,** Back side of the probe. **f,** Large-area ion beam irradiation induces strain in the flake and causes bending. **g,** Final scanning probe with PNR as the foremost part.

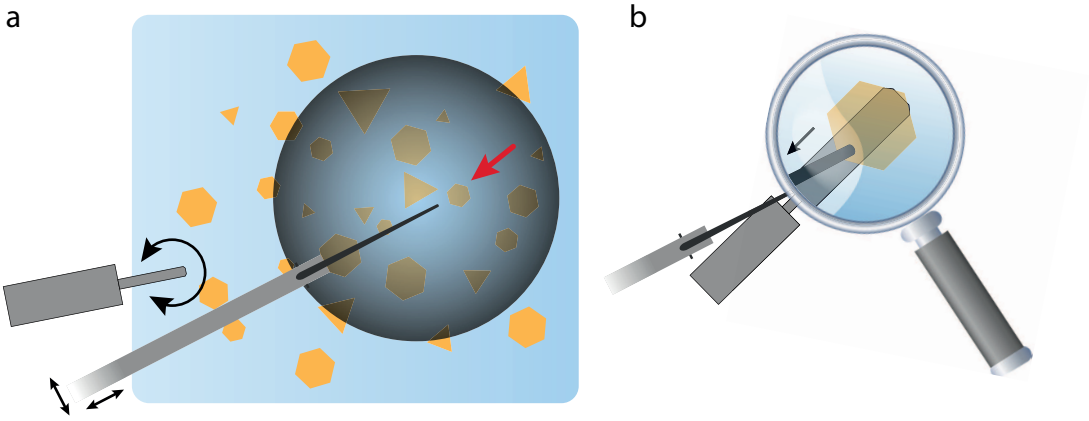

Figure 4.11 – Procedure to deposit a single crystaline gold flake on top of an AFM cantilever. **a,** Glass slide covered with gold flakes. The selected flake (red arrow) is covered with ethanol and then picked up with the needle. The AFM cantilever is mounted far away from the flakes and can be rotated according to the flake orientation. **b,** Flake deposition on the cantilever. After the flake sticks to the cantilever the needle is moved along the cantilever (as indicated by the arrow) to release the flake.

maintaining constant pressure. This way the tungsten needle looses contact with the flake and can be retracted afterwards.

After successful flake transfer the scanning probe is ready to be further processed via focused ion beam milling.

FIB etching

There are three FIB etching steps involved in order to produce a single crystalline scanning probe. Each lithography step has its own requirements in terms of ion beam dose and irradiation pattern. In a first step, the whole tip of a commercial AFM contact-mode cantilever has to be removed. As it is composed of single crystalline silicon it is very rigid and therefore requires a high ion current of 21 nA. The low resolution which is accompanied with the high beam current is tolerable as the overall final dimensions of the tipless cantilever are not critical for the following fabrication steps. The doping of the silicon is beneficial for SEM imaging and FIB patterning due to a reduced occurrence of cantilever charging and subsequent beam distortion. In order to cut of the tip it is not sufficient to make a deep cut over the full width of the cantilever. The separated tip would not simply fall off but immediately flip over and stick to the cantilever at a different location due to strong van der Waals forces which overcome gravitational forces. Therefore, the tip has to be etched entirely by starting at the apex of the pyramid and moving then up to the cantilever. In order to remove the pyramid the tip is etched from the side as indicated in Fig. 4.12a. After the complete tip is removed (see Fig. 4.12b) the edges of the tip are cut off at an angle of 30° as indicated in Fig. 4.12c in order to reduce the overall width of the cantilever at the apex from 50 µm to 15 µm. After placing a gold flake on the back side of the cantilever (see Fig. 4.12d) the scanning probe is ready for the next etching step.

The most important FIB etching process which ultimately defines the optical performance of the scanning probe is the patterning of the plasmonic cavity. The main focus of this etching step is to create a slit at the flake corner with a gap size as narrow as possible. Consequently, the lowest possible ion current of 1.9 pA is chosen for this kind of structuring as it features the highest patterning resolution. The cantilever is aligned with the upper side pointing directly towards the ion beam. This way the entire flake coincides with the focal plane and can be used to optimize the ion beam focus as described in section 4.5. Next, the correct dose for structuring the cavity has to be determined. Therefore, the stage is moved to a flake edge which is not in contact with the cantilever. The cavity pattern consists of a single line cut with the beam starting close to the rim and then moving into the flake. Depending on the flake thickness and condition the necessary ion dose to perforate the flake can be different. The smallest gap size which can be achieved is in the range of 10 nm. To reach this value, a procedure of increasing the dose and writing a test structure is repeated until the ion dose is just enough so that the groove is piercing the flake. Now that the necessary dose is determined, the actual cavity can be fabricated at the corner of the protruding flake edge. Figure 4.12e/g and f/h show SEM images of

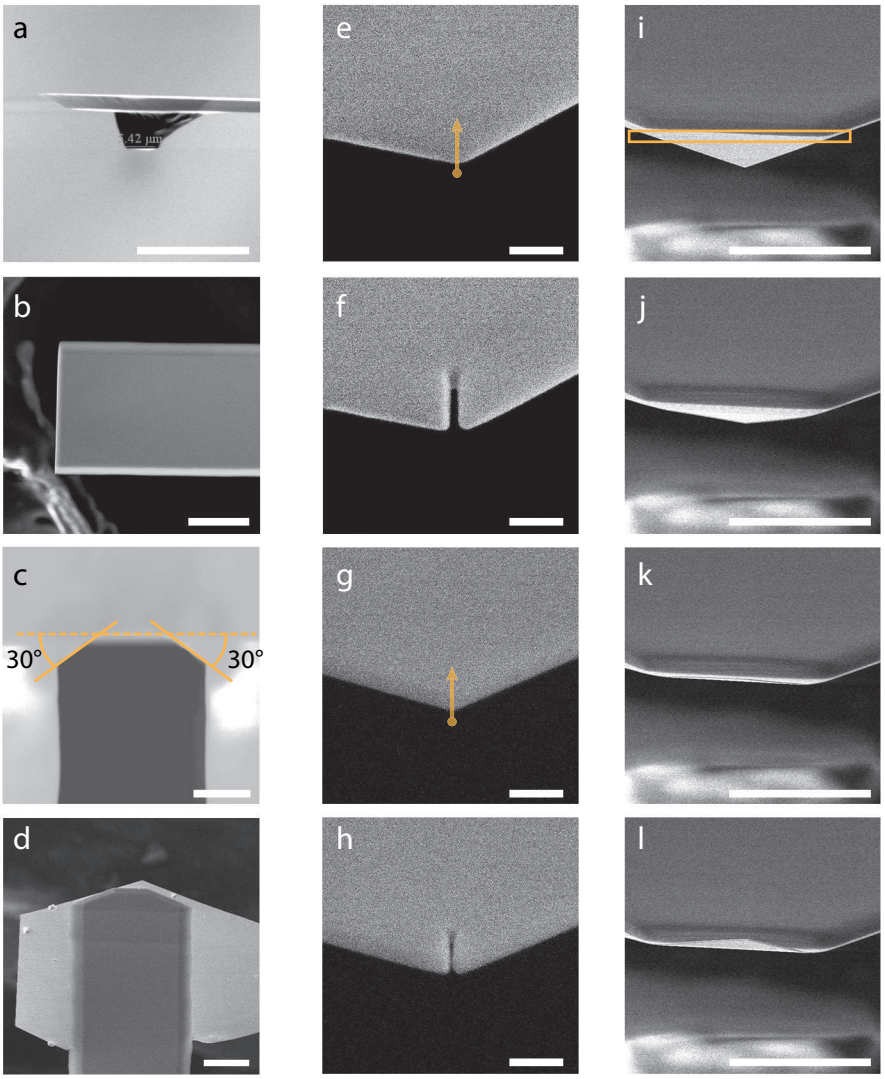

Figure 4.12 – FIB etching steps for scanning probe fabrication. a, AFM cantilever side view after etching the first part of the apex. **b,** Tipless cantilever after etching. **c,** Cantilever with removed edges. **d,** Cantilever with gold flake on the back side. **e,** Flake edge before etching the cavity via the indicated path. **f,** Flake edge after etching the cavity. **g,** Same as **e**. **h,** Same as **f**. **i-l,** Flake bending via ion beam irradiating of the marked area in **i**. Scale bar **a-d** and **i-l**: 20 µm. Scale bar **e-h**: 200 nm

two different flake edges before and after structuring, respectively. The path of the etching pattern is indicated by the orange arrows. To reach the desired resonance wavelength of 800 nm the cavity requires a length of 250 to 300 nm at a gap size of 10 to 15 nm. However, in the limit of achieving the smallest possible gap size its actual value is not known in advance of the patterning as can be seen by the different gap sizes in Fig. 4.12f/h. It is therefore not necessary to further improve the fabrication accuracy for the cavity length beyond the aforementioned range.

In the last etching step the flake is deformed in order to ensure that the final scanning probe touches the sample only with the structured flake edge. A deformation is caused by damaging the surface crystal structure via ion beam milling and consequently inducing strain on the flake. By irradiating a narrow strip across a gold flake it is bending towards the ion beam with the pivot at the predetermined fold. Therefore, the cantilever is mounted accordingly so that the lower side is facing towards the ion beam direction (see Fig. 4.12i). To control the progress of flake bending the ion beam irradiation is carried out via the live view mode of the FIB software. A narrow rectangle is selected across the flake directly at the position where it protrudes the cantilever (as indicated in Fig. 4.12i). By imaging this area with the ion beam the bending angle of the flake can be constantly monitored. Figure 4.12i-l shows consecutive SEM images of the upwards bending flake towards the ion beam (SEM view is tilted with respect to the ion beam). Depending on the flake thickness and the irradiation area the dose is adjusted accordingly. When the desired angle is reached the scanning probe is finished and ready to be mounted at the AFM.

Key parameters

The described scanning probe concept has several key steps which are critical in order to obtain a functional scanning probe. Choosing the appropriate flake is one of the most important detail which determines the quality of the probe. A lateral flake size between 30 and 100 µm is ideal for a successful transfer via a needle onto the cantilever. Larger flakes are difficult to pull through the ethanol-water interface during pick-up while smaller flakes tend to stick strongly to the needle and are reluctant to roll onto the cantilever. The ideal flake thickness is around 50 and 60 nm. While thinner flakes are prone to be damaged during the transfer, they also lack mechanical stability when the final probe is in contact with the substrate. Lateral friction with the substrate surface can easily bend the protruding gold flake (wobbling) rendering the probe unable for high-resolution scanning measurements. Gold flakes that are much thicker than 60 nm cause problems when etching the shape of the plasmonic resonator. The high irradiation dose necessary to cut through the flake also leads to a rather broad gap which has disadvantageous consequences for the optical performance of the resonator. Additionally, the shape of the flake is also critical for a high quality probe. The corner of the flake which eventually will be the apex of the probe has to have a hexagonal angle of 120°. These kinds of flake corners (as opposed to 60° corners) feature a much broader probe due to the obtuse angle and are therefore mechanically more stable and less prone to wobble during

the measurement. Another benefit of using a flake edge with a 120° angle is that the resulting plasmonic cavity is perfectly aligned with the crystal axis of the gold flake. This has another beneficial aspect on the precision of the cut and therefore on the optical quality of the structure. To further increase the stability it is crucial that the protruding part of the gold flake is not much longer than 10 µm as this unnecessarily increases the lever arm[1]. However, a short projection of the flake does decrease the chance of the plasmonic cavity being the lowest point of the probe in, especially in case of a slight tilt of the cantilever when mounted at the AFM. It is therefore also a crucial detail to reshape the end of AFM cantilever after removing the tip. The aforementioned angle of 30° matches the hexagonal shape of the protruding flake and increases the tolerance for a tilt on the AFM tip mount. Finally, the bending angle of the flake towards the substrate via large-area irradiation has also an impact on the mechanical stability of the flake tip. An angle of 90° would maximize the leverage on the flake during contact and is therefore undesirable. Smaller angles increase the mechanical stability but also lower the chance of the cavity being the lowest point of the probe due to the width and thickness of the cantilever. It is therefore best practice to estimate the angle individually for every probe depending on the length of the protruding edge of the flake.

Inherent advantages

The proposed near-field contact probe also features other inherent advantages in comparison to nanostructures fabricated on a substrate as well as other scanning probe techniques.

A potential risk of gallium ion implantation and the resulting degradation of the optical properties of plasmonic structures is a ubiquitous flaw of substrate based focused ion beam lithography [409]. However, this issue mainly (if at all) concerns the substrate below the structure as indicated by the red shaded region in Fig. 4.13a. Since the etching in case of the scanning probe takes place on a free-standing gold flake the gallium contamination is expected to be negligible.

Additionally, the structuring on a substrate always suffers an asymmetric etching as illustrated in Fig. 4.13a. The bottom edge remains broader which changes the position of maximum field confinement. In comparison, the patterning on free standing gold layers remains more symmetric as shown in Fig. 4.13b, which leads to a maximum confinement of the plasmon mode in the center of the gold layer.

Another major advantage of the proposed scanning probe involves the stability and durability of the tip compared to glass fiber probes. The contact-mode cantilever has a low spring constant and its long leverage allows to maintain a small and constant pressure of the tip onto the sample surface. This ensures that the vertical distance between the quantum dots and the tip is always specified by the PMMA layer thickness. Additionally, the single crystallinity of this unique probe is able to sustain the constant pressure and even after extensive usage the tip does show little

[1] A long protruding gold flake has the same stability issues as a short protruding but thin gold flake

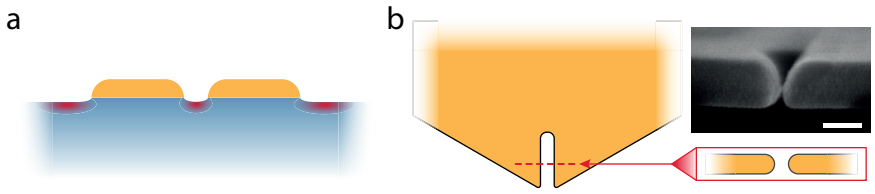

Figure 4.13 – Focused ion beam milling of free standing samples. a, Sketch of a dipole nanoantenna structured on a glass substrate. The antenna arms are asymmetric due to the round corners at the top. Red shaded areas mark potential gallium ion implantation. **b,** Structured free standing gold flake. The inner walls are more symmetric due to absence of a substrate. Inset: SEM image of structured flake. Scale bar: 50 nm.

to none signs of wear. Admittedly, the soft nature of the PMMA layer contributes to the durability of the single crystalline probes.

4.6.4 Cavity characterization

The resonance of the cavity at the tip defines the optical characteristics of the scanning probe. Coupling experiments between a tip and an emitter can differ greatly depending on whether the cavity is on- or off-resonance. Detailed knowledge about the resonance wavelength is therefore important in order to correctly interpret the measured spectra. The most common approach to determine the resonance wavelength of a plasmonic structure is to measure its scattering spectrum. To this end, the spectrally broad (white light) excitation beam interacts with the structure. The absorption cross-section of a plasmonic structure is largest on resonance which leads to a subsequent wavelength dependent emission (=scattering). A scattering spectrum can be obtained via suppression of the broad excitation spectrum (e.g. spatial filtering). The problem with this technique in case of resonant scanning probes is the contribution of additional scattering by the entire probe. The lower limit of the focus diameter of a white light beam is around 1 µm (due to the lack of coherence) which prohibits the exclusive illumination of the cavity. Therefore, the scattered light which originates from the flake edge dominates the signal and the cavity resonance can not be accurately determined.

Another approach to determine the resonance wavelength of the probe is by using the intrinsic photoluminescence of gold itself. Illuminating a gold surface leads to luminescence which shows characteristics of the band structure and also depends on the excitation wavelength. The process of this mechanism begins with the absorption of a high energy photon. The photon energy determines the position of the transition in the band structure [410]. An excitation with a wavelength of 532 nm causes an interband transition close to the L symmetry point where the density of states is highest. This photo-excitation leads to the creation of an d band hole and an sp electron above the Fermi energy E_f as indicated in Fig. 4.14a. After subsequent carrier relaxation via phonon scattering the exciton decays radiatively at a longer wavelength. This process has a quantum efficiency of 10^{-10} which is extremely

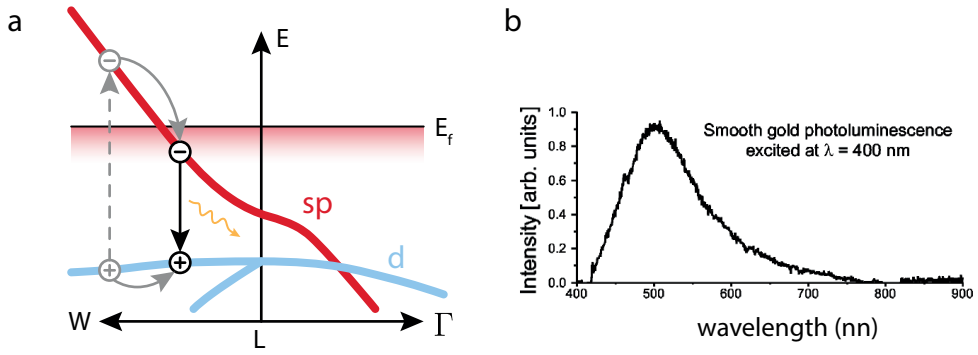

Figure 4.14 – Mechanism and spectrum of gold photoluminescence. a, Band structure with *d* and *sp* bands near the *L* point. The excitation of an electron-hole pair (gray dashed arrow) follows a subsequent relaxation (gray arrow) of each carrier along the corresponding band. Radiative emission (black arrow) occurs at lower energies. **b,** PL spectrum of gold after excitation at a wavelength of 400 nm. Radiative decay has its maximum intensity upon recombination of a hole with an electron close to the Fermi level. Reprinted figure with permission from reference [410]. Copyright (2018) by the American Physical Society.

small as the recombination as well as the scattering processes are susceptible to losses.

A PL spectrum from a smooth gold surface is shown in Fig. 4.14b for an excitation of 400 nm [410]. Due to a maximum local density of states near the Fermi energy the PL has its maximum at 2.4 eV (516 nm).

The process of gold photoluminescence can be used to locally excite plasmon resonances. Therefore, instead of radiatively decaying into the far-field as a photon, the exciton can decay into a localized plasmon. Due to the availability of additional decay channels this coupling mechanism significantly increases the quantum efficiency of the process [411]. The necessary condition is a spatial overlap of the electric field distribution of the plasmon mode and the location of the exciton decay. The resulting emission spectrum is then composed of a superposition of the intrinsic gold photoluminescence and the emission of the plasmon resonance [412–417]. In order to obtain the spectrum of the cavity the background of the gold photoluminescence can be subtracted.

Similar to the approach of measuring the scattering spectrum, the photoluminescence of the bulk material contributes and has to suppressed/filtered in order to obtain the resonance spectrum. However, the excitation source at a wavelength of 532 nm can be focused much tighter in comparison to white light. This reduces creation of excitons in the gold flake far away from the plasmonic structure and therefore improves the ratio between resonant emission and bulk photoluminescence.

This method does not rely on the absorption cross-section or the emission characteristis of the resonant structure as it is excited off-resonance and via the near-field. However, as mentioned before, it is sensitive to the spatial overlap of the mode with the gold material. This method of characterizing plasmon modes via gold photoluminescence has been popular and well suited for dipolar modes in single gold

nanorods [418] as the mode overlaps with the entire gold material which leads to a large PL quantum efficiency.

The field distribution is different in case of the plasmonic resonator at the apex of the scanning probe. This cavity mode is confined in the gap between two metals, a mode which has the attribute to have little mode with the metal itself. In fact, as shown in section 2.1.4, the mode overlap of an MIM mode with the surrounding metal decreases as the gap size decreases. Since one goal of the patterning is to achieve a gap size as small as possible this also decreases the efficiency of the resonance characterization technique. Therefore, depending on the overall quality and the gap size of cavity the PL signal can differ significantly. In fact, a weak PL emission of the scanning probe can even be a hint for a small gap size and vice versa.

It is noted that the efficiency of plasmon excitation via exciton decay also depends on the resonance wavelength. For increasing wavelength the density of states near the L point is reduced (see Fig. 4.14b) and therefore the decay of excitons in the near-infrared regime is reduced [419]. Additionally, the scattering of the hole and electron further increases their separation in k-space due to different slopes of the sp and d bands. This reduces the overall PL signal which makes it challenging to characterize plasmon modes with a resonance of 800 nm and above.

Nonetheless, the high Q-factor of the cavity plasmon resonance and therefore narrow spectral peak can easily be discriminated from the PL background even in the case of a low signal-to-noise ratio.

4.7 Scanning principle

The presence of three elements (focal point, tip and emitter) creates various possibilities on how to move one element with respect to the other two. Varying the interaction by changing the distance between the tip and emitter, however, is the main purpose of this work. Also, one experimental constrain is that the microscope objective has no lateral degrees of freedom and therefore the focal area is fixed in all measurements. Consequently, there are two possibilities to create a 2D-interaction map between emitter and tip: (i) emitter fixed at a designated location (e.g. focal point) and the tip can be raster scanned (see Fig. 4.15a) or (ii) the tip is fixed at an appropriate position (e.g. focal point) and the emitter can be moved freely as illustrated in Fig. 4.15b. In general, these two types of scanning principles are equivalent because both map the interaction between each other. However, there are a two major technological constrains which have an impact on the accuracy and reproducibility of the experiment which makes case (ii) favorable over (i).

First of all, the lateral tip movement is driven by a voltage acting on the piezoelectric ceramic tube. The electrodes are distributed into four segments which allows to apply a voltage for each opposing electrode in order to drive the tube in two perpendicular directions. However, there is no possibility for a feedback control of the lateral bending of the tube. In addition, the position as function of voltage is only linear for small amplitudes and follows an exponential behavior for large

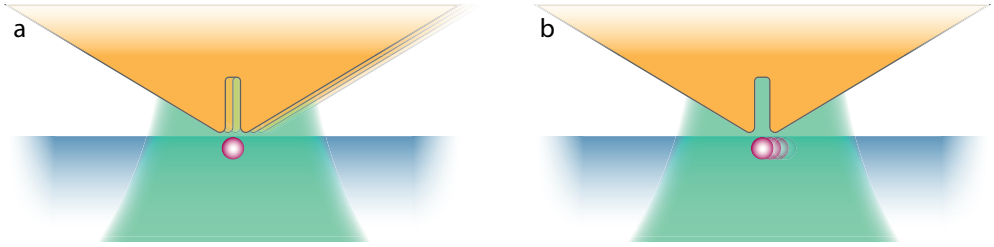

Figure 4.15 – Possible configurations for scanning probe microscopy. Due to experimental constrains the focal point does not allow lateral movement. **a,** Emitter is fixed at the focal point and the probe can be freely moved. **b,** The probe is fixed at the focal point and the emitter can be moved with respect to the tip.

amplitudes. Calibrating the movement via a gauging sample would be a possible solution, but it does not account for slow piezo creeping at low scanning speeds. Therefore, case (i) would yield an interaction map which has an uncertainty at every position and a low precision when moving back and forth between two pre-defined positions. The piezo-stage which is used to move the sample, on the other hand, has a closed feedback control loop. It allows to scan well defined motion patterns at a fast pace with a high reproducibility and without any piezo creeping.

Second, keeping the emitter at the focal point does imply a constant photo-excitation. This limits the amount of experiments which can be performed on this specific emitter as it can be subject to bleaching (dye molecules) or it can be trapped in a dark state (colloidal quantum dots). In addition, creating a single map which shows the interaction of several different emitters is, in contrast to case (ii), not possible. This decreases the throughput of QDs which can be measured in a certain amount of time.

Concluding the arguments above, case (ii) provides a more versatile and reliable approach and therefore all scanning probe measurements in the following work are performed in this configuration.

4.8 Finding the focus

As discussed in the previous section, keeping the tip at the focal point and moving the emitter via the sample stage is the most promising configuration. The necessary approach of the focal point with a scanning probe is therefore a critical procedure as it determines the quality of the following single emitter coupling measurements. In addition, keeping the tip at the focal point for a long period of time extends the time frame in which one can perform coupling experiments. A highly reliable and accurate method is to exploit the intrinsic photoluminescence of the gold probe when excited with green light. Details about the mechanism of gold photoluminescence can be found in section 4.6.4. The full procedure is discussed in the following section.

The movement of the tip into the focal point is done in four stages. At first, the

glass sample has to be moved via the piezo stage so that the focal point is in an area with a low QD density. This facilitates to isolate the gold photoluminescence from the fluorescence background of the quantum dots. In the next step the probe is approached onto the sample surface and the voltage on the piezo tubes is set to zero by moving to tip to $x = y = 0$ via the AFM control program. After retracting the tip by 5 µm, the whole AFM head is moved via adjustment of the micrometer screws of the outer stage framing (see section 4.3). The reflection of the green excitation beam at low powers is used to indicate the exact position of the focus. A typical lateral tip-focus distance that can be achieved with this coarse method is less than 5 µm. Now the tip is approached again onto the sample surface for further adjustments (see Fig. 4.16a). A minor alignment via the micrometer screws is now still possible while monitoring the tip with a camera through the objective (see Fig. 4.4). Finally, the tip is raster scanned over an area of 5×5 µm by driving the AFM piezo tube with an external voltage controlled by the LabView software (see Fig. 4.16b). A key to a artifact free mapping of the tip is a consistent line-by-line movement in one direction while measuring the photoluminescence. There is a small offset between back and forth scan due to a finite friction coefficient between the tip and the sample which can be avoided by settling for one direction. The excitation power is increased to 200 µW which is sufficient to record a gold photoluminescence map with the confocal microscope shown in Fig. 4.16c. The map clearly resolves the location of the gold probe and additionally indicates the orientation of the gold flake as can be seen from the elongated peak.

The typical acquisition time for a map with a resolution of 50×50 pixel is less than one minute. After recording the map the tip is moved to the location of maximum PL signal by applying the corresponding voltage for this position (see Fig. 4.16d). Continuously monitoring the PL intensity during the tip movement is used to confirm a successful approach of the probe into the focal area. Any additional position sensitive feedback of the tip cannot be retrieved from the AFM.

Note that the resolution of the map is not diffraction limited. As the tip only touches the glass sample at a single point the majority of the flake probe is beyond the confined laser field which reduces the resolution as well as the photoluminescence intensity.

As the tip is mechanically pre-aligned (accuracy < 5 µm) the necessary voltage on the piezo tube for the final adjustments is small (less than 20 V). This is advantageous as it reduces the amount of piezo creep and prolongs the period of the tip persisting at the focal point. Additionally, the displacement of the piezo tube is linear for small voltages which directly yields a linear map without the need for any calibration.

Scanning the tip

The photoluminescence map shown in Fig. 4.16 was measured with a single APD is an example for a high PL yield. The signal strength depends on various parameters which in some cases makes it challenging to acquire a map with a sufficient signal-

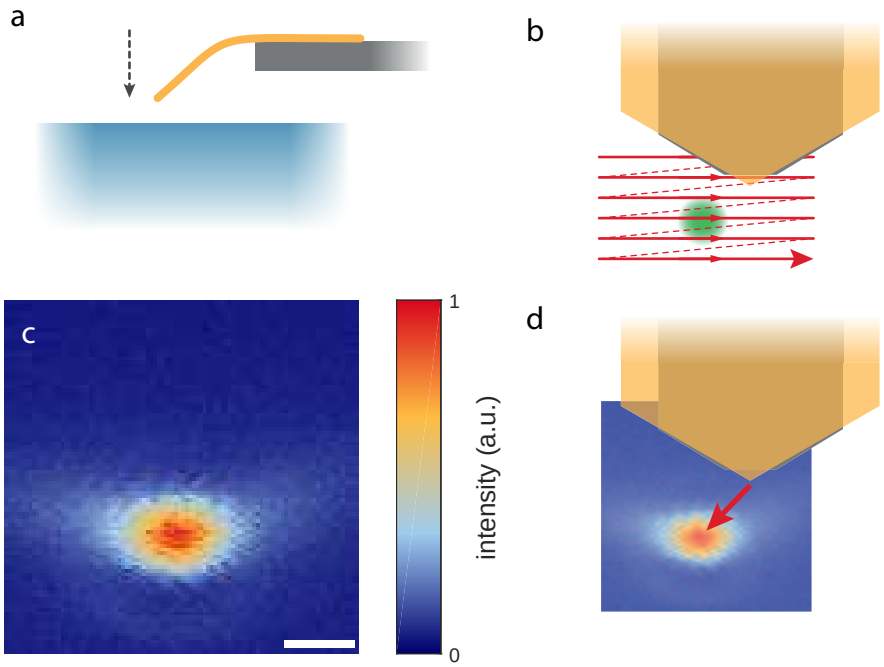

Figure 4.16 – Procedure for approaching the focal point with the probe tip. a, Approach the sample with the probe tip. **b,** Scanning the probe though the focal point. **c,** Gold photoluminescence map of a gold tip raster scanned in the vicinity of the focal point. Scale bar: 1 µm. **d,** Making the final approach by moving the tip to the position of highest gold PL.

to-noise ratio. The amount of generated photoluminescence photons depends on the absorption cross-section of the gold probe and therefore increases with the thickness of the gold flake. Therefore, a very thin gold flake probe generally leads to a weak photoluminescence signal. In case of a structured probe the presence of plasmon resonance in the visible wavelength range can enhance the photoluminescence (see section 4.6.4). This coupling mechanism, however, decreases with increasing resonance wavelength due to reduced overlap of the resonance with the intrinsic gold photoluminescence spectrum intensity. Another aspect that has a negative influence on the signal-to-noise ratio is the presence of quantum dots or other luminescent particles in the vicinity of the focus. Their fluctuating contribution to the emission signal (e.g. due to blinking) can easily dominate the measured PL map of the tip. Therefore, it can be necessary for some probes to exploit the polarization emission characteristics of the cavity resonance of the tip (see section 2.1.4). As the cavity resonance emission is polarized along one direction a polarization filter in the detection path can be used to reject unpolarized emission from the bulk gold or other sources. Even higher contrast can be achieved by using two APDs and a polarizing beamsplitter (see Fig. 4.4). Directly monitoring the degree of polarization of the emitted light can reveal the position of the tip even in case of high background fluorescence. Increasing the excitation power far beyond 200 µW to improve the signal-to-noise ratio over a long period of time can have negative impact on the integrity of the probe due to heating. Therefore, in this work the excitation power has been kept in the range of a few 100 µW during raster scans of the probe.

The absence of any lateral feedback mechanism for the position of the scanning probe makes it difficult to quantify the amount of drift that is accumulated after a certain period of time. Several effects such as piezo creep, temperature variations, mechanical drifts of the AFM framing mount as well as movement of the microscope objective leads to a continuous increase of the distance between the tip and the focal point. Depending on the conditions the alignment can last for up to 10 min before the tip has drifted on the order of 100 nm (which is half the diameter of the diffraction limited focus) and therefore needs to be centered again. A systematic study on the drift rate has not been conducted, however, as a rule of thumb one can assign a value of 10 nm/min.

Impact of drifts and friction on the measurement quality

Deviations of the tip with respect to the focus can have a more or less striking impact on coupling experiment depending on the type of measurement. For example, mapping multiple individual quantum dots to demonstrate the fluorescence-enhancing impact of the tip is only minor affected by drifts. Here, the displacement of the tip is compared with the size of the diffraction-limited laser focus which has a diameter of $d_{\mathrm{min}} = 224\,\mathrm{nm}$. Distances between focal point and tip of less than d_{min} will only result in a reduced quantum dot excitation efficiency and a non-centrosymmetric overlap between the diffraction limited and the tip-enhanced spot. As these measurements have an acquisition time of one minute or less, the resulting average

drift of 10 nm between focal point and tip is much smaller than the focus diameter. Therefore, the drift has only a minor effect on the measurement.

However, the continuous drift makes it complicated to perform time-consuming statistical measurements (auto-correlation, lifetime) with a resonant probe in close proximity to a quantum dot. In this case, the displacement is quantified by comparing the distance between the cavity near field (25 nm) and the size of the quantum dot (10 nm). Drifts of a few nanometers can already modify the coupling of the emitter with the tip and subsequently change the excited state lifetime. As measurements of photon statistics require an acquisition time of at least one minute the distance between near-field and QD changes significantly with respect to their sizes. Since there is no possibility to accurately quantify the drift over time it is difficult to draw reliable results from these kind of measurements.

The finite friction coefficient between sample and tip has to be considered when the accuracy of the positioning has to be 20 nm or less. Similar to the movement of the tip (Fig. 4.16b) any translation of the sample causes a slight bending of the tip which leads to a hysteresis behavior. This applies to PL mapping of the sample as well as to a direct movement to a specific location of the sample (e.g. a quantum dot). Each position as to be approached from the same direction in order to ensure a reliable and accurate alignment between the tip and the sample.

5 The concept of a plasmonic nanoresonator

Since the establishment of optical resonant antennas, the concept of localized surface plasmon resonances has become a well-known tool for leveraging the yield of photons interacting with matter [4]. Advances in nanofabrication has opened the path for new possibilities to realize novel types of structures in order to release the full potential of plasmon oscillations. Many observations, such as the Purcell effect, which have been studied in other optical systems (e. g. microcavities or photonic crystals) have already been demonstrated with propagating plasmons. Being able to apply those concepts to localized structures establishes a novel technological platform to study new phenomena. This vivid field of research is currently at the verge of employing the capacity of localized surface plasmon to explore the properties of other new types of 1D and 2D materials such as quantum dots, graphene and transition metal dichacogenides [96, 370, 420].

Of special interest in this regards is the prospect of strong coupling at room temperature with single emitters. The concept of a photon being re-absorbed by the same emitter before decaying into the far field bares new types of hybrid light-matter states. Despite the lossy nature of plasmons, their potential for enhanced light-matter interaction is based on their confinement beyond the diffraction limit. The key challenge to reach strong coupling is to design a plasmonic structure which meets all the necessary requirements.

The goal of this chapter is to introduce the plasmonic nanoresonator (PNR) as superior plasmonic structure for light-matter interaction. Its geometry is rather simple, as it is composed of a plain slit at the edge of a metal sheet. However, it meets all demands which are required for experimentally realize extreme light-matter interaction. These requirements can be divided into three major aspects: (i) The field confinement is the most prominent figure of merit when it comes to localized surface plasmons. In terms of light -matter interaction formalism a high field confinement translates into a small mode volume which is an equivalent description of this quantity. (ii) Besides increasing the interaction with an emitter via confined fields it is also important to keep the losses in bounds which includes radiative decay as well as ohmic dissipation. Suppressing of radiation is achieved by employing modes with a

reduced dipole character which mitigates the plasmon decay into the far field. Additionally, it is shown that by reducing the overlap between the electric field and the metal the plasmon decay rate can be decreased. (iii) The aspect which is of special interest for an experimental realization is the accessibility of the localized field for a single emitter or other types of excitonic materials. It is shown that despite the high confinement there is a substantial amount of field which is leaking out of the geometrically confined volume. The prospect of being able to use this kind of structure as a scanning probe opens new possibilities to control light-matter interaction.

After introducing the PNR concept and the analogy to other established structures numerical simulations are carried out in order to investigate the electric mode profiles for different geometries as well as the emission spectra. Furthermore, the quantum efficiency of the proposed structure as well as the Purcell factor is analyzed for various geometries.

5.1 Probe concept

Optical nanoantennas are known for their ability to significantly enhance and localize optical fields. The most prominent antenna geometry is a rod dimer due to its similarities with traditional radio-frequency antennas [101]. Figure 5.1a shows a sketch of the charge distribution, the location of maximum electric field enhancement (blue star) and the resulting dipolar radiation pattern. The field intensity in the gap increases with reduced distance between the two rods as in indicated in Fig. 5.1b. However, the increased coupling between the two rods leads to a redshift of the hybridized gap mode. By decreasing the length of the two rods (see Fig. 5.1c) the resonance can also be blueshifted in order to prevail in the optical wavelength regime.

This approach of using two linearly aligned nanorods to maximize the localized field in the visible regime is limited. The overall size of the antenna becomes very small for gap sizes below 4 nm [101]. The concomitant reduction of the scattering cross-section and increased ohmic losses reduces the quantum efficiency of the nanoantenna and therefore limits the capabilities of this kind of geometry. In addition, rod dimers with minimum gap size are also challenging from a experimental point of few. In order to benefit from the localized mode for enhanced light-matter interaction it is necessary to position the excitonic material within a volume of only a few cubic nanometers within two metal particles. This, however, requires random Brownian motion of a fluorescent particle [421, 422] or sophisticated functionalization of metal particles via DNA origami [423, 424]

In this work a slightly different geometry is used in order achieve even higher enhanced electric fields while even improving the capabilities for experimental realization of light-matter interaction. Instead of employing a insulator-metal-insulator (IMI) plasmon mode for the case of a linear dipole antenna it is also possible to exploit the beneficial properties of metal-insulator-metal (MIM) modes as they appear in between two metal surfaces indicated in Fig. 5.2a. Two side-by-side aligned nanorods can host a plasmon mode which is solely localized between the metal

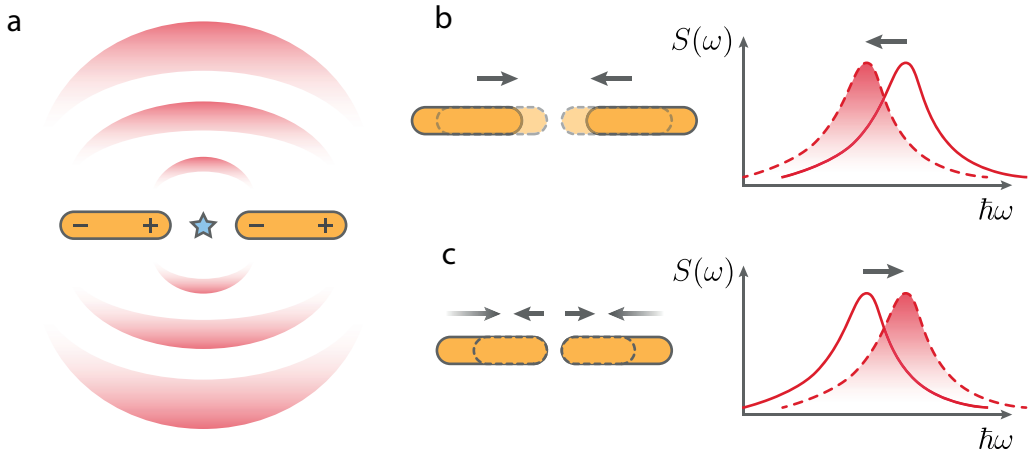

Figure 5.1 – Modifying the optical properties of a dipole nanoantenna. a, Dipolar emission of a rod dimer. The electric field is enhanced and localized in the gap (blue star). **b,** Decreasing the gap size increases the coupling between the rods and causes a redshift of the hybridized gap mode. **c,** By reducing the rod length the resonance can be shifted towards shorter wavelength.

surfaces which also redshifts with decreasing gap size (see Fig. 5.2b). However, these kind of MIM modes are capable of confinement below 1 nm [425] while the resonance can be freely adjusted via the length of the nanorods as sketched in Fig. 5.2c.

There are several advantages of nanocavities compared to standard linear dipole antennas which makes them more attractive for an experimental realization of coupling light with excitonic materials. The most important advantage is the mode localization and confinement. MIM modes have the superior property that with reduced gap size in the few-nm regime the field inside the gap increases but also the mode overlap inside the metal decreases [36]. This reduces the ohmic losses of the plasmon and increases the Q-factor. Additionally, as indicated in Fig. 5.2a, the mode has a quadrupolar character. It has been shown that the resonant excitation of such a mode is not possible without breaking the illumination symmetry [425]. The suppressed coupling to the far-field reduces the radiative decay rate of the plasmon which is again beneficial for the Q-factor. Decreasing the dipolar character of the mode therefore also implies that the radiative decay into (or excitation from) certain directions is reduced.

A major experimental obstacle in nanotechnology is the precise positioning of single emitters within the field of a plasmonic resonance. Scanning probe technology allows this kind of alignment by moving the emitter on a substrate independently as shown in Fig. 5.3a. Here, a single crystalline gold flake with a narrow gap is brought into contact with colloidal quantum dots embedded in a transparent substrate. The plasmonic structure shows the same characteristics as two side-by-side nanorods as shown in Fig. 5.3b. The shortcut at the upper end has only an effect on the reflectivity coefficient of the plasmon but does not have a major impact on the overall resonance. A field profile of the resonance is shown in Fig. 5.3c. The open

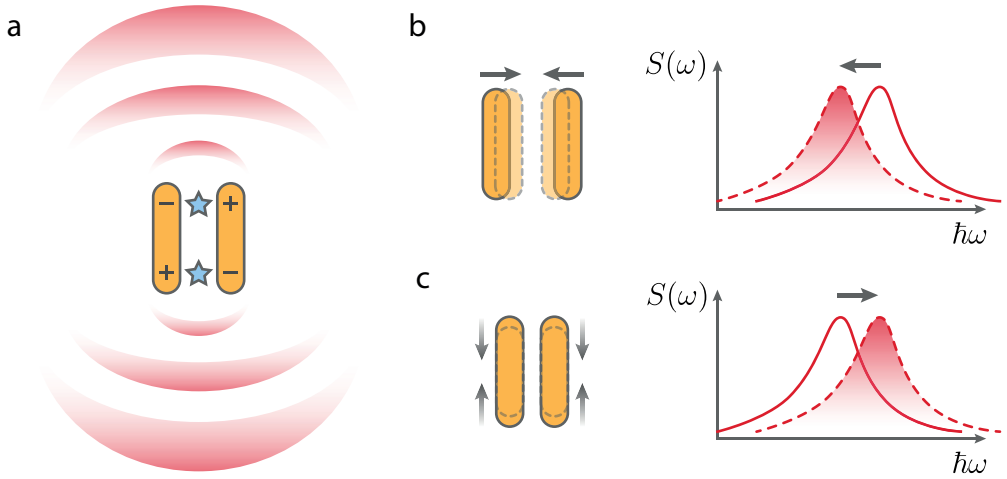

Figure 5.2 – Modifying the optical properties of a cavity plasmon. **a,** Emission characteristics of a nanocavity. Two electric field hotspots form between the rods (blue stars). **b,** Decreasing the gap size increases the coupling between the rods and causes a redshift of the hybridized gap mode. **c,** Reducing the length of the nanorods shifts the resonance towards shorter wavelength.

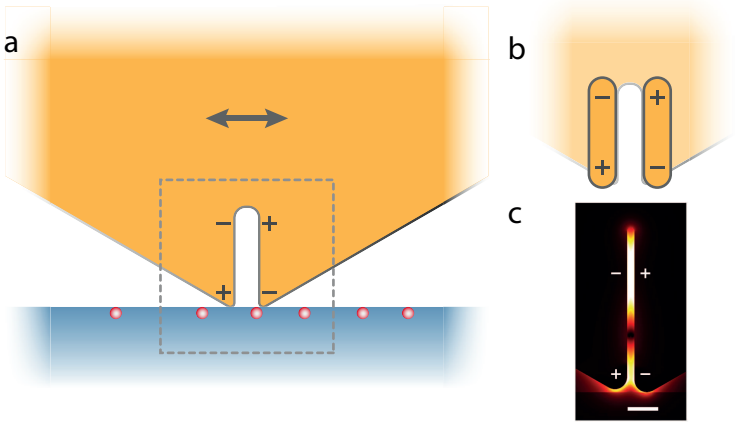

Figure 5.3 – Nanocavity as scanning probe. **a,** Sketch of the charge distribution of the PNR at the apex of a gold flake which serves as a scanning probe and can be scanned across a surface. **b,** The tip region (dashed area in **a**) has similar properties than two side-by-side nanorods. **c,** Field profile of the corresponding charge distribution. The modal field distribution leaks out of the enclosed space at the open end. Scale bar: 100 nm.

end of the slit resonator is an ideal location to position an emitter since here the modal field distribution leaks out of the enclosed space of the slit resonator similar to scanning near-field optical microscopy probes.

5.2 Finite-Difference Time-Domain Calculations

The following section discusses the numerical results of nanocavities based on finite-difference time-domain (FDTD) simulations. Comprehensive knowledge of the plasmon resonances is of great importance for several reasons. Information about the dependency of the plasmon resonance on geometrical parameters simplifies the fabrication process and increases the yield of structures which have the desired optical properties. Beyond the information about the resonance additional parameters such as Purcell factor, field enhancement or mode volume can be extracted from FDTD simulations. This extensive set of data is an important ingredient for a meaningful analysis and interpretation of optical experiments which makes FDTD (or equivalent numerical calculations) a mandatory component of any plasmonic study.

Theoretical confirmation of measurements in general is essential for all experimental studies. Optical measurements with localized surface plasmons can be completely described by Maxwell's set of equations. Solving these equations analytically is only possible for the most simplest geometries, such as a sphere. Only slightly more complex geometries do not allow a purely analytic expression for the description of the electrodynamics. It is therefore necessary to approximate the exact solution via numerical calculations. There are numerous approaches on how to solve Maxwell's equations, each designed to efficiently yield a specific result. The most prominent methods in the field of plasmonics are the boundary element method (BEM), the discrete dipole approximation (DDA) and the FDTD method.

Numerical simulations are crucial for the experimental work for two major reasons: (i) Simulations are ideal to determine distinct properties such as the resonance frequency or the field enhancement factor for a variety of structure geometries. Usually this can be done much faster than the actual fabrication and measurement. Therefore, simulations reduce the amount of samples which have to be fabricated in order to yield the structure with the desired properties. Additionally, these simulations (ii) also serve as a comparison for measured data in order to better interpret the results.

For the purpose of this work, FDTD simulations are used to calculate the electrodynamic response of plasmonic nanostructures. FDTD has an intuitive approach to solve Maxwell's equations as the simulation volume is divided into an orthogonal 3D grid which stores the local electric and magnetic field. For each time step, these values are changed according to their vicinity. According to Maxwell's equations, changes of the electric fields ($\nabla\vec{E}$) have an impact on the change across space of the magnetic fields ($\nabla \times \vec{H}$). The computational implementation of this algorithm which allows for a discrete calculation of the curl of magnetic fields is known as the Yee lattice. Details about the implementation can be found in the literature [426].

A cross-section of the complete simulation volume is demonstrated by the green rectangle in Fig. 5.4 and illustrates the boundary of the Yee lattice. Typical dimensions of these domains for the investigation of a plasmonic nanostructure is about $1.5 \times 1.5 \times 1.5\,\mu m^3$ with a mesh size dx of about $10 \times 10 \times 10\,nm^3$. The resulting distance between a structure at the center and the simulation boundary of about one wavelength ensures that the near field remains unperturbed. The simulation volume is surrounded in all direction by perfectly matched layers (PML). This kind of material absorbs all incident electromagnetic waves and therefore minimizes reflections into the volume which would otherwise cause interference effects.

The plasmonic structure itself can have arbitrary shapes and in this work is constructed by a set of overlapping geometrical primitives. Additionally, surrounding dielectric materials, such as a substrate can be realized as well. The dielectric function of all employed materials has to be available continuously throughout the optical spectrum. In case of gold, the underlying data by Johnson and Christy [16] is fitted with an analytic function which is then used by the FDTD algorithm. Figure 5.4 shows a gold flake with a slit at the edge centered within the simulation volume and touching the surface of a glass substrate. In order to resolve all fine features of the plasmon mode profile the mesh of the Yee lattice can be refined as illustrated by the fine grating in Fig. 5.4. Typical values for the volume of a single refined mesh cell is between 0.5 and $1\,nm^3$. The locally refined lattice ensures that the region of interest is reasonably resolved while keeping memory and simulation time requirements in bounds. It is noted that the memory and simulation time scales with $(1/dx)^3$ and $(1/dx)^4$, respectively.

The energy is injected into the simulation via different types of sources. There are two types of sources which are being used for the simulations in this work. One type is the dipole source which inserts the energy at a single point in space via a current loop across four mesh cells. The other type is a Gaussian source as shown in Fig. 5.4, where a superposition of plane waves are used to inject a single Gaussian pulse with a well-defined focal length, geometry (numerical aperture) and polarization towards a specified direction.

Electric and magnetic fields are recorded via monitors at predefined positions as indicated by the red lines in Fig. 5.4. These monitors are available in 0D, 1D, 2D and 3D and are capable of storing time-dependent or averaged fields as well as the transmitted power. Further details on the configuration of simulation monitors can be found in appendix A.1.

Simulations are automatically terminated when the power within the simulation volume has dropped to 10^{-5} of the initially injected power. The accuracy of the simulated field distribution and spectral responses are mainly defined by the applied mesh size as well as the configuration of the monitors. It is therefore highly recommended to make systematic adjustments in order to demonstrate the robustness of the simulation.

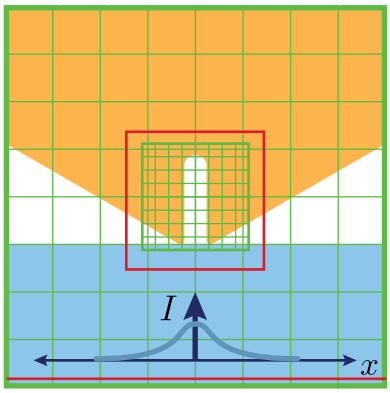

Figure 5.4 – Sketch a 2D cross-section of the basic setup of a FDTD simulation. The simulation realm (green coarse grid) contains a structured gold flake edge (orange) on top of glass substrate (blue). A Gaussian source pulse injects a focused set of plane waves upwards directed at the flake edge (blue lines). Monitors (red rectangle) store the electric field profile of the mode as well as the scattered field towards the bottom (red line). A mesh refinement (green fine grid) increases the spatial resolution of the recorded fields.

5.3 Resonant scanning probe

5.3.1 Geometry

The shape of a PNR at the edge of a flake is defined by the geometry of the flake and by the etching process of the focused ion beam which is used to pattern the slit (see section 4.5). In order perform numerical simulations of this rather complex and ambiguous shape, it is necessary to break down the geometry into a superposition of many different primitives. It is then possible to describe the shape by a minimal set of parameters. A side view of a 3D model as it is used in a simulation is depicted in Figure 5.5a.

The rough shape of the scanning probe is defined via a polygon as indicated by the gray area in Fig. 5.5b with an overall thickness t_f. However, the edge of single crystalline gold flakes is not flat and is therefore modeled by an elliptic cylinder with an effective radius r_f as indicated in Fig. 5.5b by the two red rectangles. The second radius is scaled to $t_\mathrm{f}/2$ in order to match the height of the gold flake. The shape on the inside of the slit is defined by the geometry of the gallium ion beam and secondary etching processes such as gold re-deposition. Therefore the side walls of the slit are also modeled by an elliptic cylinder with a separate effective radius r_c (see two light blue rectangles) which is generally larger than r_f. In order to ensure a smooth transition between the two radii a tri-axial ellipsoid is positioned according to the sketch. The first axis matches half the flake thickness t_f while the second axis matches the shape of the flake edge r_f. The length of the third axis defined by $\sqrt{\frac{1-r_\mathrm{f}^2\cdot\sin(\alpha)^2/\mathrm{r}_\mathrm{c}^2}{\tan(2\alpha)^2/\sin(\alpha)^2\cdot\mathrm{r}_\mathrm{c}^2}}$, where the angle $\alpha = 30°$ is defined by the flake geometry.

In order to finish the design large sets of secondary primitives are necessary to

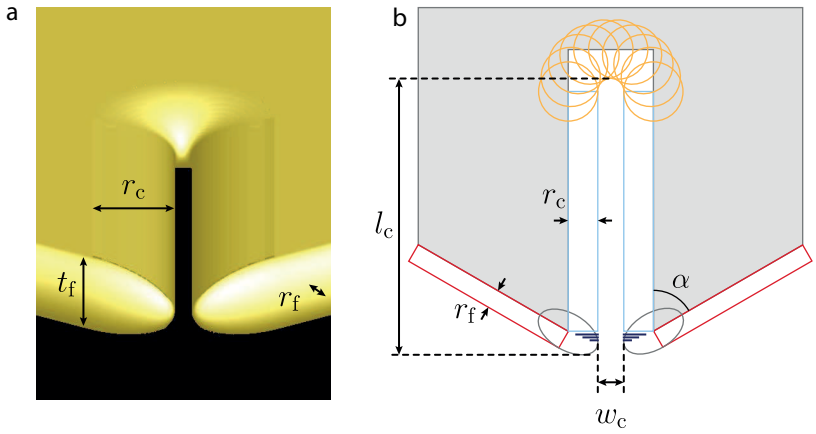

Figure 5.5 – Illustration of the geometrical description of a PNR at a flake edge. **a,** 3D sketch (side view) of the structured flake edge. **b,** Geometrical sketch (top view) with all necessary parameters to determine the shape of the structure.

achieve a seamless structure. The smoothing at the tip region is done via a set of thin slices of ellipsoids as indicated by the blue lines in Fig. 5.5b. The closed end of the slit is shaped by a set of spheroids (see orange circles in Fig. 5.5b) with one axis matching the flake thickness t_f and the other fitting to the inner nanoslit radius r_c. The number of secondary primitives and their overlap is increased in order to fall below the mesh size of the simulation.

With this scheme, the entire geometry of the flake edge is described via the parameters t_f, r_f, r_c, w_c and l_c, where w_c and l_c are the nominal length and width of the slit, respectively. Throughout this work and if not specified elsewhere, a flake thickness of $t_f = 60\,\text{nm}$, a flake rim radius of $r_f = 10\,\text{nm}$ and a inner nanoslit radius of $r_c = 55\,\text{nm}$ was used as a standard value for all simulations.

5.3.2 FDTD results

The most fundamental characterization is the determination of the resonance wavelength as a function of the nanoslit length l_c and gap width w_c. Figure 5.6a-c shows the normalized near-field spectra for a gap width of $w_c = 10, 20, 30\,\text{nm}$ and a length of $l_c = 100...10...600\,\text{nm}$.

These results clearly indicate several resonances above 600 nm depending on the length of the resonator. Examining the field distribution along the PNR at different wavelengths yields more information about the nature of these resonances. Figure 5.7 shows the electric field distribution of the 2^{nd} (3^{rd}) for a resonator with a gap size of 12 nm and a length of 250 nm at a wavelength of 800 nm (600 nm). For a longer nanoslit length the structure supports higher order resonances as can be seen by the number of anti-nodes in the electric field. A single anti-node (1^{st} order) is only supported for short cavities with a broad gap and, however, does not enter the visible wavelength regime. The main emphasis in this work is put on the second order resonance (two anti-nodes) as it can be tuned through the entire visible wavelength

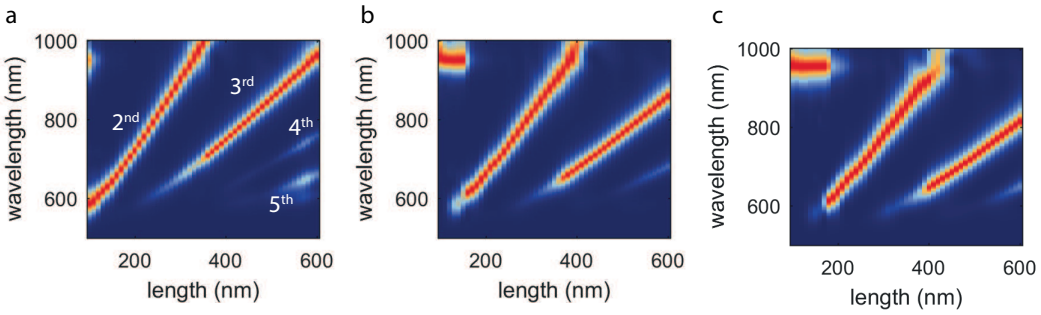

Figure 5.6 – Shifting resonances with increasing resonator length and width. a, Near-field spectra of a slit resonator with a length l_c between 100 and 600 nm and a gap width of 10 nm. **b,** Gap width 20 nm. **c,** Gap width 30 nm.

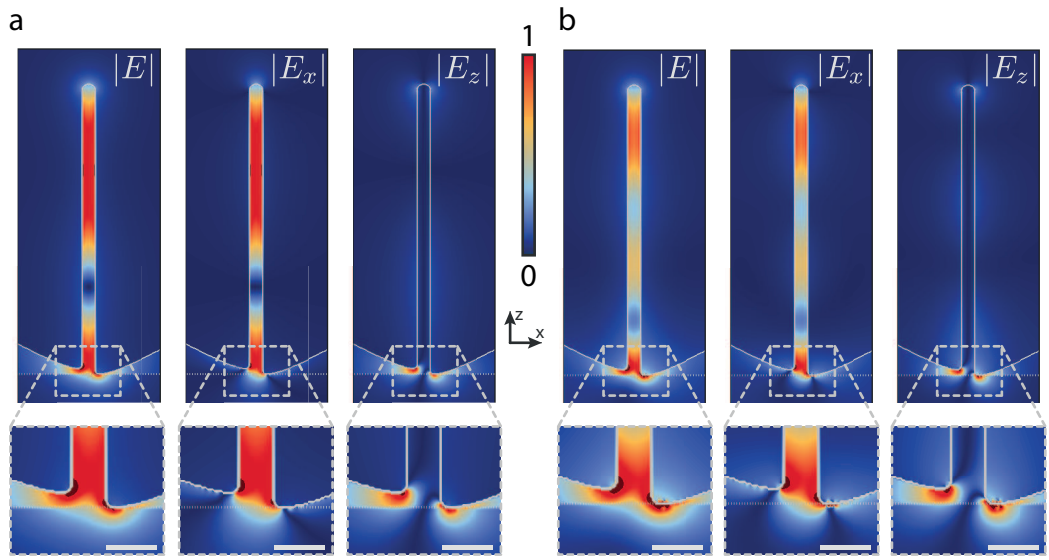

Figure 5.7 – Normalized electric field distribution of the 2nd- and 3rd-order mode of a plasmonic resonator standing on top of a glass substrate. a, Mode profile of the 2nd resonance ($w_c = 12$ nm, $l_c = 250$ nm) at $\lambda = 800$ nm. The left hand side map shows the total field strength. The map in the middle and on the right hand side show the field components in x and z direction, respectively. Scale bar: 20 nm. **b,** Mode profile of 3rd order resonance for same dimensions as **a**.

regime.

The contribution of the individual field components is also shown in Fig. 5.7 for $|E_x|$ and $|E_z|$ of the 2nd and 3rd order mode. It can be seen that the electric field inside the slit is completely polarized perpendicular to the slit due to the metallic boundary condition. At the open end, however, the x-polarized field only displays a minor extend into the glass substrate. Here, the field is mostly polarized in z-direction which reaches out further into the dielectric medium. Due to symmetry the $|E_y|$ component is zero for all positions in this plane.

The 2nd order resonance, as well as all other higher order modes, are in particular interest due to the high localized fields which are leaking out of the gap region. When used as a scanning probe, this part of the mode is able to overlap and interact with any optically active material which is embedded within the substrate. In fact, since the electric field at the apex is localized to the metal edges and is polarized in z-direction, this probe is similar to a sharp metal tip. The major difference, however, is the integrated resonator which causes the plasmon interference and significantly enhances the local density of optical states. A more detailed discussion on the differences between the 2nd and 3rd order mode and the possible applications can be found in appendix A.6.

The numerical simulations also reveal that the gap size has an impact on the Q-factor of the resonance. Fig. 5.8a shows the near-field spectrum which displays the 2nd and 3rd order resonance for three different gap sizes. The length of the nanoslit is adjusted in order to compare the 2nd order resonance at the same resonance wavelength close to 800 nm. In particular, for the gap size of 10, 20 and 30 nm the nanoslit lengths are 240, 290 and 310 nm, respectively. With decreasing gap size the Q-factor increases from 15.6 at a gap size of 30 nm to 22.6 for a gap size of 10 nm as indicated in Fig. 5.8b. This observation is attributed to an altered effective wavelength of the MIM mode and a change of the reflection coefficients of the open and closed end. The increased confinement reduces the overlap of the mode with the metal which increases the propagation length of the plasmon. The open and closed ends of the PNR act as a radiating antenna. With reduced gap size the radiation efficiency decreases which increases the reflection coefficient.

It is noted, that the determination of the spectral width of a plasmonic resonance is not trivial. The exact settings of the temporal apodization of the FDTD monitors, which is necessary in order to suppress the excitation source, have a crucial impact on the shape of the spectra. On the one hand, if the apodization begins too soon, the source modifies the shape of the spectrum. On the other hand, an apodization well after the excitation narrows the spectra and shows non-Lorentzian shapes. For Fig. 5.8 an apodization center $\tau_c = 40$ fs and width $\tau_w = 10$ fs have been chosen. More details on this topic can be found in appendix A.1.

Another important quantity which contributes to the performance of an optical nanoantenna is the radiation efficiency η [101, 427]. It specifies the ratio between radiative (R_r) and non-radiative (R_nr) decay of the plasmon mode via $\eta = R_\mathrm{r}/(R_\mathrm{r} + R_\mathrm{nr})$ in analogy to the description of quantum efficiency of single emitters. In this description, the radiation efficiency appears as a fixed and intrinsic parameter of the

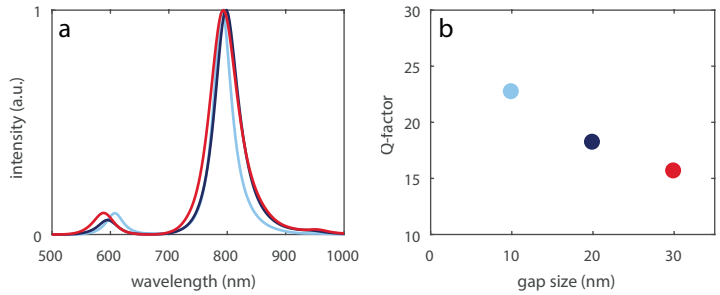

Figure 5.8 – Influence of the gap width on the Q-factor. a, Near-field spectra of three different cavities with a gap size of $w_c = 10\,\text{nm}$ (light blue), 20 nm (dark blue) and 30 nm (red). The PNR is tuned via the length to a resonance of 800 nm. **b,** Corresponding Q-factors with the same color coding as in **a**.

PNR. However, as described in the following, the position of the quantum emitter relative to the PNR is also important.

The total amount of dissipated energy always equals the injected energy which, in the experiment, originates from a quantum emitter. This energy is not constant, as the coupling of the emitter to the antenna mode changes with its location due to a position dependent local density of optical states (see section 2.3.2 for details). If the coupling to a specific antenna mode is small, the contribution of other channels such as propagating plasmon modes or the intrinsic nonradiative decay of the emitter increases.

In order to determine η via FDTD simulations it is crucial to employ the same geometrical constrains like they occur in an experiment. Therefore, the emitter is placed inside a glass substrate 5 nm below the surface with the dipole orientation parallel to the surface normal as it is sketched in Fig. 5.9a. The emitter radiates over a broad wavelength range which allows to calculate η over the whole visible spectrum. The PNR is placed on top of the substrate and one tip is aligned with the emitter. The energy decay channels that are monitored in this simulation are threefold:

- **Radiative decay:** All energy that is leaving the simulation volume is recorded and adds to the radiative emission. Contribution from propagating surface plasmons towards the simulation boundary are excluded in this channel.

- **Propagating surface plasmons:** The PNR is part of a gold sheet which supports propagating surface plasmons. They can be excited either directly by the emitter or via the decay of the plasmon mode. Since the simulation volume is finite, additional monitors collect the energy inside and up to 40 nm above the gold at the simulation boundary as indicated by the red line in Fig. 5.9.

- **Ohmic losses:** Any other loss of energy has to originate from ohmic losses in the metal itself. This channel therefore accounts for the difference of the energy injected into and leaving the simulation volume.

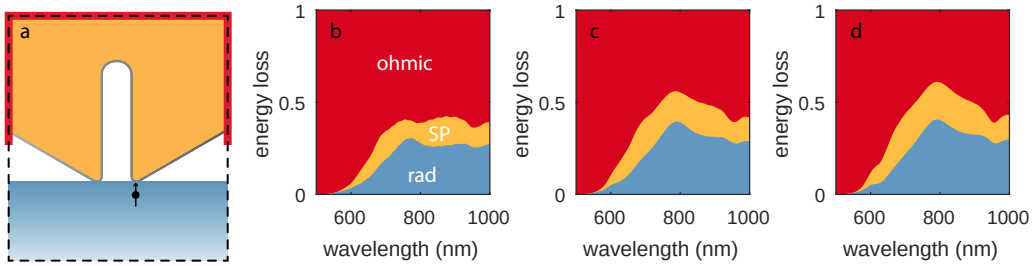

Figure 5.9 – Radiation efficiency of nanocavities. a, Geometry of the FDTD simulation (not to scale). The PNR is standing perpendicular on a glass surface. The emitter is located below the right tip 5 nm into the substrate. At the simulation boundary (dashed line) near the flake the SPP intensity is captured by additional monitors (red line). **b,** Power dissipation of individual decay channels normalized to the total amount of injected power for a PNR width of $w_c = 10$ nm and a length of $l_c = 240$ nm. **c,** Same as **b** but with PNR parameters $w_c = 20$ nm and $l_c = 290$ nm. **d,** Same as **b** but with PNR parameters $w_c = 30$ nm and $l_c = 310$ nm.

The contribution of these three channels is displayed in Fig. 5.9b-d for the three previously studied cavities with gap widths of 10, 20 and 30 nm. Here, the dissipated energy is normalized to the injected energy which is a wavelength dependent property due to resonant near-field enhancement. The simulations show that the ohmic losses are responsible for about half of the energy dissipation throughout the entire wavelength range from 500 to 1000 nm and for all gap widths. Below 600 nm the contribution even rises which can be attributed to the increase of interband transitions of the gold material [410]. Due to these inherent gold properties this observation is independent of the nanoantenna geometry [101, 428, 429]. Around 500 nm the emission of the emitter is completely quenched and all the energy is dissipated by the metal via coupling to non-radiative higher-order modes [15, 73]. The contribution of propagating plasmons remains fairly constant above 600 nm and accounts for 10-20 % of the total energy loss. As the gap size becomes smaller, the SPP contribution increases slightly. The radiative emission efficiency also rises above 600 nm and peaks at around 800 nm due to the 2$^{\text{nd}}$ order resonance which occurs at this wavelength as shown in Fig. 5.8. The maximum reached radiation efficiency of 30-40 % increases with increasing gap width w_c. This observation of decreasing η for smaller PNRs is attributed to the increase of the quadrupolar mode character. The resulting slower radiative plasmon decay times increases the coupling to non-radiative decay channels and therefore reduces the radiation efficiency.

At a wavelength of 600 nm the presence of the 3$^{\text{rd}}$ order resonance has also a slight impact on η as well. However, the radiation efficiency is much lower due to the high ohmic losses despite a confinement and mode profile similar to the 2$^{\text{nd}}$ order resonance. Nonetheless, the 3$^{\text{rd}}$ order resonance is capable of enhancing the emitter fluorescence by several orders of magnitude due to a high local density of optical states.

In this simulation, the emitter has no non-radiative decay channels and therefore a quantum efficiency of 1. This neglects the effect that single molecules with a low

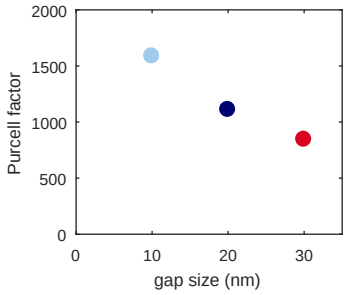

Figure 5.10 – Purcell factor of nanocavities with different gap widths. The dipole is located at a distance of 5 nm below the tip as depicted in Fig. 5.9a. The length of the nanoslit is adjusted for a resonance wavelength of 800 nm.

intrinsic quantum efficiency (2.5 % [7]) can significantly increase their efficiency when coupled with an antenna. Also, emission into the upper half sphere is also counted as radiative emission even though in conventional experiments only light which is emitted towards the glass substrate can be detected.

It is important to note that the normalization of the total energy loss notably diminishes the impact of the enhanced emission due to resonant coupling with the plasmon resonance. The enhancement of the spontaneous emission rate is quantified by the Purcell factor as described in section 2.3.2. In numerical simulations this factor is extracted by monitoring the amount of energy which is injected into the simulation environment by a dipole emitter in close proximity to a localized near-field. The ratio of this value to the radiated energy in a homogeneous dielectric environment yields the Purcell factor. The change of the Purcell factor for PNRs with different gap sizes and a resonance at 800 nm is shown in Fig. 5.10.

The dipole orientation and position is the same as depicted in Fig. 5.9. As the gap width decreases, the increased confinement of the mode leads to a higher local density of optical states and therefore a larger Purcell factor. The simulation shows that values above 1000 are readily achieved. These results are similar to other studies where a dimer antenna geometry is used to confine the mode in between two metal particles [7]. The fact that this kind of confinement is possible at the apex of a tip without the need of a dimer configuration is remarkable. Likewise, the prospect of being able to move an emitter even closer to the PNR via scanning probe techniques comprises the possibility for even higher Purcell factors.

5.4 Conclusion

This chapter has introduced the PNR geometry at the apex of a gold flake scanning probe as an highly promising configuration for a comprehensive investigation of light-matter interaction. The study of similarities to side-by-side dimer geometries has highlighted that all necessary requirements, such as high Q-factor and high field confinement, are provided. It has been shown how the shape of a realistic PNR can be described by simple geometry primitives and only five parameters. The optical

performance is characterized via FDTD simulations. The results have demonstrated that plasmon resonances in the optical regime are supported for slit sizes of 10 nm with Q-factors higher than 20. When excited with an emitter at 800 nm close to the tip a radiation efficiency of 30 % can be achieved while the emission rate is enhanced by three orders of magnitude. High intensity of localized fields at the open end of the slit makes this type of structure an ideal geometry for studying the interaction between quantum emitter and localized plasmons.

6 Weak coupling of plasmons and quantum emitters

Manipulating the radiative performance of a single emitter is of great interest, both from a technological as well as from a scientific standpoint. The development of smaller light sources with even higher performance challenges the capabilities of the active material. Highly photostable single emitters with high quantum yield and a fast decay time are becoming more and more feasible and therefore technologically attractive. Additional improvement of the emitter performance can be achieved by changing the local environment of the emitter which further enhances the properties of the emitter. The process of reducing the excited state lifetime of an emitter is known as weak coupling which is quantified by the local density of optical states and proportional to the number of available modes which radiate into free-space.

Plasmonic near-fields are able to tailor the spatial distribution of the local density of optical states. Over the past decade advances in nano-fabrication has lead to major improvements of the Purcell factor reaching emission enhancement factors of up to one million [13]. Interestingly, quantitative measurements and, in particular, comparison with numerical simulations are still rare due to a manifold of reasons.

Experimentally, it is difficult to accurately determine the decay rate as it quickly reaches values close to the instrument response function of the measurement setup. The largest measurable Purcell factor is defined by the ratio between the intrinsic excited state lifetime of the emitter and the instrument response function and therefore depends on the type of emitter and the quality of the experimental setup. Measured enhancement factors in the range of three orders of magnitude have been reported [69]. Another experimental challenge is the spatial position of the emitter or the emitter ensemble which is a key parameter and often cannot be accurately measured.

From a theoretical perspective, it is known that strongly localized optical fields often feature large gradients. The resulting implications for weak coupling, however, are still largely unexplored. Additionally, in case of single emitters which are macroscopic and of the same size as the field confinement, the dipole approximation

does not hold anymore. Colloidal quantum dots for example can have dimensions of 10 nm (see chapter 3) and are therefore much larger than individual dye molecules.

Using a scanning probe approach to modify the distance between a plasmonic near-field and a single emitter, which directly alters the coupling strength, is a sophisticated method to investigate the coupling process. It allows a pre-characterization of the near field as well as the emitter and therefore does not rely on statistical evaluation of many measurements. Nonetheless, detailed information about the optical properties of the emitter is crucial. This is especially the case for complex types of emitters (such as colloidal quantum dots) which feature, among other things, various emission states (blinking).

This chapter focuses on the study of colloidal quantum dots which are either isolated on a glass substrate or weakly coupled to a single crystalline gold scanning probe. In the first section, the optical properties of isolated quantum dots are investigated in detail. Understanding of their internal dynamics are a vital ingredient for the interpretation and understanding of the following coupling experiments. These measurements start with the most basic approach, the coupling with a pure gold tip to study the influence of the metal. Analysis of the emission characteristics show that the enhanced emission is dominated by an increased excitation rate. Further experiments demonstrate how the use of a plasmonic nanoslit (PNR) at the apex of a scanning probe can significantly alter the emission characteristic of a quantum dot due to weak coupling. Finally, the prospect of resonant high-resolution microscopy is discussed.

6.1 QD characterization

Transitions in the optical regime define the interaction between light and a quantum emitter. For an ideal two-level system the optical characteristics stem from a single transition which leads to identical absorption and emission spectra. Colloidal quantum dots comprise of a vast collection of transitions at different energies. These transitions originate from the multitude of hybridized orbitals of the specific constituents of the quantum dot. This includes dipolar as well as multipolar transitions which give rise to radiative as well as non-radiative processes, respectively. In addition, coupling with thermal phonons alters the occupation of individual energy levels and therefore the response with photons. All these processes lead to significant differences between the absorption and emission spectrum of colloidal quantum dots. In order to investigate the coupling of these kind of emitters with plasmonic near fields it is crucial to understand their internal dynamics in terms of absorption and emission.

In this section colloidal quantum dots (QDot800, see section 4.4 for sample preparation) are characterized optically to quantify various properties such as emission wavelength, excited state lifetime, saturation intensity and dipole moment. This kind of emitter has also been subject to a variety of studies in the literature [6, 266, 282, 367, 372, 430, 431] The data has been acquired either for individual emitters or ensembles which can lead to different observations depending to the

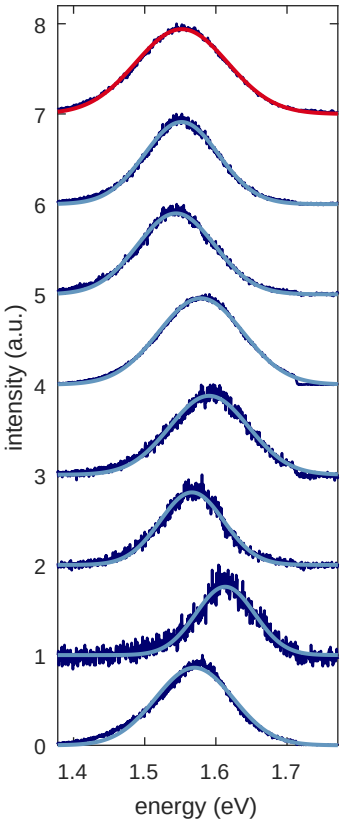

Figure 6.1 – Spectra of several individual and an ensemble of quantum dots. Spectra #0 to #6 are recorded on individual QDs, spectrum #7 corresponds to an ensemble measurement. All spectra are fitted with a Gaussian.

type of measurement.

6.1.1 Fluorescence spectra

The colloidal growth of the quantum dots in solution is a process which leads to a distribution of various nanocrystal sizes and shapes. By starting the growth process as abrupt as possible (hot injection) the variance of the distribution is small but nonetheless noticeable [432,433]. These settle variations result in different confinement energies which changes the resonance wavelength. Through most part of this section, fluorescence measurements with a confocal microscope and an excitation wavelength of 532 nm (for details see section 4.3) are used to study colloidal quantum dots. Figure 6.1 shows the spectra of different individual quantum dots (spectra #0 to #6).

All of the spectra are fitted with a Gaussian (light blue line) which shows excellent agreement with the data (dark blue). It can be seen that the peak energy (1.54 – 1.61 eV) as well as the FWHM (97 – 141 meV) fluctuates which is attributed to the structural variation of the nanocrystals. As mentioned before, the QD size most prominently impacts the resonance wavelength whereas the width can be in-

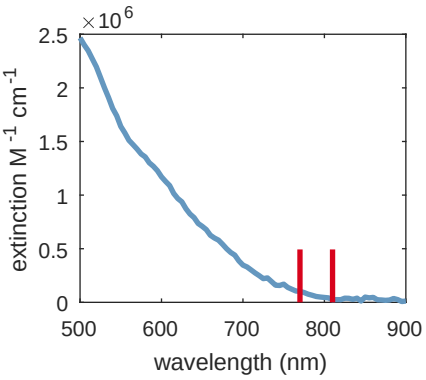

Figure 6.2 – Extinction spectrum a colloidal quantum dots QDot800. The extinction increases for higher photon energies. The emission range is indicated by the red lines.

fluenced by the shape as well as details in the atomic composition of the shell. Processes which lead to the broad spectral emission, such as spectral diffusion, originate from charge fluctuations at the core-shell interface which is therefore sensitive to the nanocrystal surface (see section 3.6 and 3.7). The spectrum #7 in Fig. 6.1 shows the emission of an ensemble of many quantum dots. It can also be fitted with a Gaussian (red line) but shows a broader spectrum compared to the individual quantum dots. Due to the averaging over many different emitters the width of the spectrum increases which is also known as inhomogeneous broadening.

6.1.2 Extinction measurements

Further information about the optical properties of quantum dots can be obtained by studying the interaction with light over a broad wavelength range. Of special interest is the wavelength dependent extinction coefficient $\varepsilon(\lambda)$ which accounts for the sum of the scattered and absorbed light. An extinction spectrum therefore yields great insights on the availability of optical (dipole-) transitions of the quantum emitter. All of those transition are able to absorb a photon which leaves a fingerprint on the extinction spectrum. Figure 6.2 shows an extinction spectrum of a thick film of colloidal QDot800 quantum dots over a large spectral range. Details on the experimental setup are described in appendix B.2.

As shown by the emission spectra, the maximum fluorescence energy of these types of quantum dots is 1.55 eV which corresponds to a wavelength of 800 nm. Photons with smaller energies are not absorbed by the quantum dot and therefore the extinction is zero. The extinction shows a finite value at 800 nm and increases significantly for higher energies due to an increased density of states. A slight modulation of the shape of the extinction spectrum yields hints on the transition energy of higher states in the conduction/valence band.

Each available transition contributes to the extinction via its oscillator strength (see section 2.2). It is therefore possible to extract quantitative information about the dipole moment for a specific wavelength range. The oscillator strength f depends

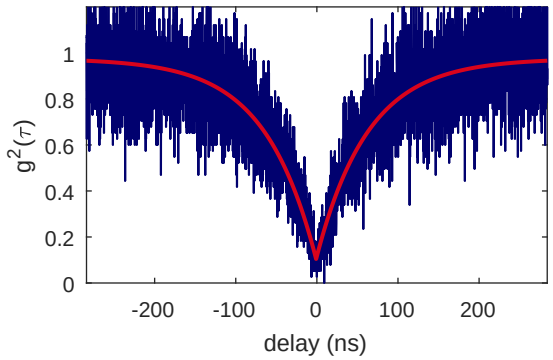

Figure 6.3 – Intensity auto-correlation measurement of a single quantum dot. The excitation power is kept low at 200 nW to avoid non-linear effects. The fit yields a number of emitters of 1.12.

on the extinction via

$$f = \frac{4m_0}{e^2} \frac{0.2303 n_a c \varepsilon_0 \langle \nu \rangle}{|f_{lf}|^2 N_A} \int \frac{\varepsilon(\nu)}{\nu} d\nu \tag{6.1}$$

where m_0 is the electron mass, f_{lf} the local field factor, ε_0 the is the permittivity of free space, e is the electron charge, n_a is the refractive index of the surrounding medium, N_A the Avogadro constant and $\langle \nu \rangle$ is the average frequency of the emitter transition [434]. The local field factor $f_{lf} = 3/(2 + n_{qd}^2/n_a^2)$ accounts for the changes of the electric field due to differences of the refractive index between the surrounding medium and the inside of the quantum dot (n_{qd}). The calculated oscillator strength over a spectral width of 40 nm yields a value of $f = 5$. Further details and discussion about the interpretation of this value can be found in chapter 7. It is noted that the extinction spectrum does not take into account the internal dynamics of the QDs as discussed in detail in section 3.5 and appendix B.2.

6.1.3 Intensity auto-correlation measurements

When preparing quantum dot samples as described in section 4.4 the quality of the sample depends in part also on the distribution of emitters throughout the glass slide. The goal here is to achieve a small clustering rate and a high amount of isolated single quantum dots. Due to the diffraction limit it is not possible to resolve two quantum dots which are separated by less than ≈ 200 nm. By evaluating the photon statistic of a fluorescent object it is possible to deduce the number of quantum emitters. Figure 6.3 shows the intensity auto-correlation function $g^2(\tau)$ of a single quantum dot recorded at an excitation power of 200 nW (see appendix B.1 for details).

For a delay of $\tau = 0$ the correlation reaches a value far below 0.5 which is a sufficient indication for a single emitter. This is also confirmed by the fitting of the $g^2(\tau)$ (red line) which yields a number of $N = 1.12$. It is important to remain in the regime of low excitation in order avoid contribution of biexcitons and other

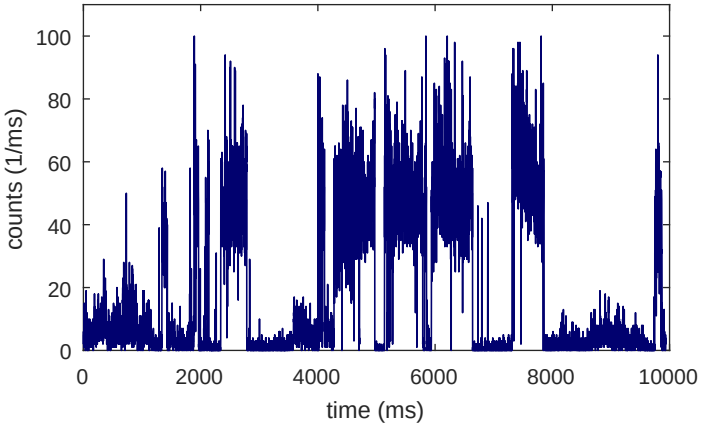

Figure 6.4 – Timetrace of an individual quantum dot. The fluorescence intensity is fluctuating between two distinct amplitudes.

non-linear effects. High excitation rates can lead to the occurrence of two photons being detected simultaneously and the corresponding auto-correlation measurement shows an increased $g^2(\tau = 0)$ [389].

Evaluation of various auto-correlation measurements confirms a high dispersion of single quantum dots on the glass sample.

6.1.4 Quantum dot blinking

Colloidal quantum dots are known to exhibit fluorescence intermittency. The time resolved fluorescence intensity over 10 seconds of a single quantum dot is shown in Fig. 6.4.

It can be seen that the emission intensity fluctuates between two distinct states ('on'/'off'): a bright state with a fluorescence intensity of about 50 counts/ms and a dark state which barely shows any emission (< 5 counts/ms). On the one hand, the bright state is attributed to the neutral QD state ('on') which is characterized by the radiative recombination of the exciton and exhibits therefore a high quantum efficiency. The dark state, on the other hand, has a low quantum efficiency due to the presence of an additional charge which is induced via photo-ionization. The decay of an exciton in this charged state ('off') is dominated by a non-radiative Auger process with a decay time faster than the radiative recombination. More details on the neutral and charged states and their decay mechanism can be found in section 3.5. The duration of 'on' and 'off' states follows a power-law distribution and is not associated with a characteristic time scale. The binning time is 1 ms which is the limit of the shortest detectable duration of a specific QD state.

6.1.5 Excited state lifetime

The lifetime of the excited QD state is of central interest when investigating the coupling mechanism with resonant near fields. Accurate determination of the radia-

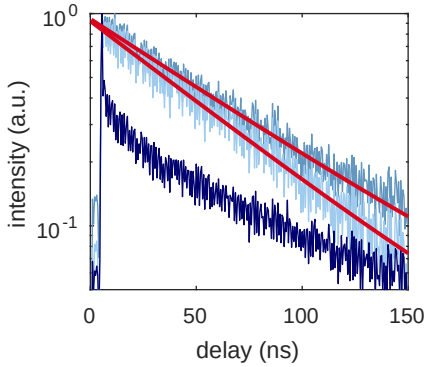

Figure 6.5 – Lifetime measurements of individual quantum dots. Combined histogram for 'on' and 'off' state is shown in dark blue. Histogram which only considers the on times is shown for two QDs (light/gray blue). An exponential fit is shown in red.

tive exciton decay, however, requires careful data analysis due to the occurrence of different excited states which have an influence on the decay time. A pulsed laser source is used in order to measure the excited state lifetime. Details about the optical setup can be found in appendix B.1. Figure 6.5 shows a histogram of the photon delay times for different QDs and with different analysis techniques.

By taking into account all delay times over a certain amount of time, the histogram shows a multi-exponential decay as shown in dark blue. Contributions of a fast decay and a slow decay are visible in this representation. The fast decay originates from the charged QD state which is dominated by the non-radiative Auger recombination with a low quantum yield. The neutral QD has a longer excited state lifetime and contributes to the slow decay of the photon delay times. Individual fitting of the two intervals is challenging because they gradually overlap which leads to an arbitrary selection of fitting ranges. A more advanced technique is to make use of the microscopic times which are acquired during a TTTR measurement. Details on this technique are described in appendix B.1. By selecting only the photons which arrive during the 'on' state of the QD and discarding all others, the histogram changes and only accounts for the neutral QD. Figure 6.5 (light blue) shows a histogram of the same data-set as the histogram in dark blue, but only accounts for intensity intervals above 60 % ($> 40\,\mathrm{counts/ms}$). Now the histogram shows a single exponential decay which can be fitted (red line) without the necessity of arbitrarily choosing a fitting interval and yields a corresponding excited state lifetime of 56.5 ns. The gray blue line shows another QD evaluated in the same manner with a resulting lifetime of 66.2 ns. Fluctuations of the excited state lifetime between different QDs is also a consequence of the size and shape variations of the chemically grown nanocrystals. The impact of these geometrical constrains on the resonance frequency and decay rate is discussed in detail in section 3.2.

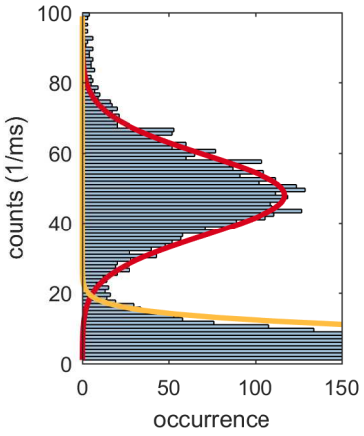

Figure 6.6 – Histogram of a fluorescence timetrace of a quantum dot. The mean emission of the 'on' state is determined via a Gaussian fit (red line). The contribution by the 'off' state is also fitted with a Gaussian (orange line).

6.1.6 Saturation

The quantum dot has a finite exciton recombination rate which sets a limit to the maximum possible cycle rate and naturally leads to a saturation of the emission rate for high excitation rates. Determining the saturation behavior is important as it reveals the excitation intensity range where a linear increase of florescence can be expected. Similar to the measurement of the excited state lifetime, the blinking behavior of quantum dots does not permit a simple extraction of fluorescence intensity. Reliable results can only be obtained by carefully differentiating between the 'on' and 'off' state during the data analysis.

In order to determine the fluorescence intensity for a specific excitation rate a complete time trace is recorded. A histogram of the time trace data is shown in Fig. 6.6. The two QD states are clearly separated and fitted independently by two Gaussians. The 'off' state (orange line) has its maximum at zero counts and cannot be differentiated from the background noise. The mean fluorescence intensity of the 'on' state (red line), however, is precisely determined by the Gaussian fit.

Measurement and subsequent analysis of time traces at various excitation rates yields a highly accurate value for the saturation intensity. Figure 6.7 shows the averaged fluorescence intensity of eight different quantum dots for different excitation intensities. Each quantum dot has a slightly different maximum fluorescence intensity which leads to a standard deviation as indicated by the error bars. These variations of maximum fluorescence can be attributed to effects such as a diversity in quantum efficiency due structural differences between the QDs[1] or heterogeneous emission characteristic based on the orientation of the bright plane [222]. The overall shape of the saturation behavior remains the same. The mean values can be perfectly fitted (red line) via equ. 2.16 and yields a saturation intensity of 647 nW.

[1] owing to the colloidal growth

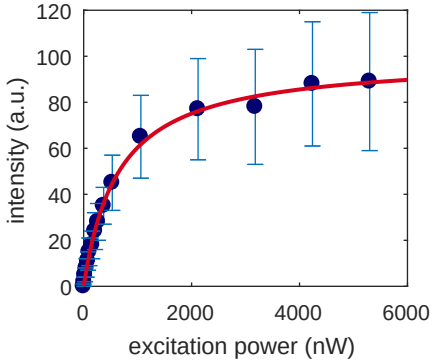

Figure 6.7 – Average saturation behavior of colloidal quantum dots.

The fact that the model agrees well with the data suggests that only single excition emission processes are involved. Upon higher excitation rates non-linear processes such as biexciton generation are expected which will also have an impact on the maximum fluorescence rate.

6.1.7 Conclusion

The careful measurement analysis of the employed quantum dots has demonstrated their most common emission properties. Profound knowledge on the excited state lifetime, dipole moment and saturation excitation rate of single quantum dots is a key requirement for further investigation on the coupling mechanism with localized plasmons.

6.2 Bare gold probe

The dynamics of a single emitter are always changed in the close proximity to a metal surface. Even without the presence of a resonance the local density of optical states and therefore the excited state lifetime is altered. Additionally, any incident light interacts with the metal which alters the intensity at the emitter position. In case of a metal tip the lightning-rod effect can significantly enhance the field intensity. This effect is especially prominent in experiments using a scanning probe to demonstrate the field confinement at the apex of a sharp metal coated tip [435–438].

Naturally, the edge of a gold flake provides a robust and well-defined tip due to the colloidal growth of the crystal. The single crystallinity of the flakes intrinsically yields a robust platform for scanning probe operation but the use of a bulk single crystalline metal tip has not yet been reported. Chemically grown gold particles have been attached to the apex of a scanning probe in order to demonstrate their field enhancing effect [72, 73, 439, 440]. However, the application of this kind of scanning probe is rare due to the high risk of loosing the particle and the elaborate fabrication process of the tip.

The interest of using an unstructured gold flake as a scanning probe to investi-

gate the coupling with a quantum dot is versatile. For one the coupling process in general between colloidal quantum dots and a metal surface in close proximity is of great interest. As already discussed in detail in section 3.9 the internal dynamics of the QD are changed. The occurrence of increased biexciton emission has been studied in various type of gold geometries but the exact mechanism, however, is still subject to debate [64, 375–378, 380, 381, 383–386, 390]. The altered photon statistics in addition to a reduced excited state lifetime are the only effects reported to this date but these experiments also lack clear statements on the metal-QD distance dependency. The use of a scanning probe is therefore well suited to further study the influential effect of metal surfaces close to the QD.

The usage of a pure flake edge as scanning probe is also of great interest as it also constitutes as a reference to compare with measurements of more sophisticated probes. All effects that occur with an unstructured tip also appear for structured tips in addition to resonant coupling processes.

Measurement

It is known that even without a resonance the presence of the gold tip in close vicinity to the QD affects its absorption and emission characteristics. In this measurement it is shown how this impacts the intensity of fluorescence, degree of polarization as well as the emission spectrum. The probe preparation is carried out in the same manner as described in section 4.6.3 except for the step of patterning a nanoslit. The quantum dot sample is prepared as described in section 4.4. Figure 6.8a shows an SEM image of the unstructured corner of the gold flake. The presence of the gold tip enhances the fluorescence as evident from the PL map in Fig. 6.8b (see section 4.7 for measurement procedure). The observed fluorescence peak from a region smaller than the area associated with the diffraction-limit corresponds to the coupling of the tip with the QD.

In order to study the origin of the enhanced emission it is necessary to investigate the polarization and the spectral characteristic of the emitted fluorescence photons. The excitation power was adjusted to 10 µW. By measuring both polarization components simultaneously via separate single photon counting modules (see section 4.3.2) one can calculate the degree of polarization (DOP) defined as $(E_{\text{trans}} - E_{\text{long}})/(E_{\text{trans}} + E_{\text{long}})$, where E_{trans} and E_{long} are the electric field components in transversal and longitudinal directions, respectively, as indicated in Fig. 6.8a. The DOP depicted in Fig. 6.8c shows no significant polarization modulation of the QD in close proximity to the gold tip.

Further insights on the coupling characteristics can be obtained by measuring individual spectra for different QD-tip separations. These spectra are are measured in discrete steps (lateral distance about 20 nm) while moving the QD through the localized field at the apex of the tip as indicated by the arrow in Fig. 6.8b. Each spectrum has an acquisition time of 1000 ms. The measured spectra shown in Fig. 6.8d are normalized and fitted with a Gaussian. As the QD approaches the tip the fluorescence is enhanced which can be seen by an increased signal-to-noise ratio

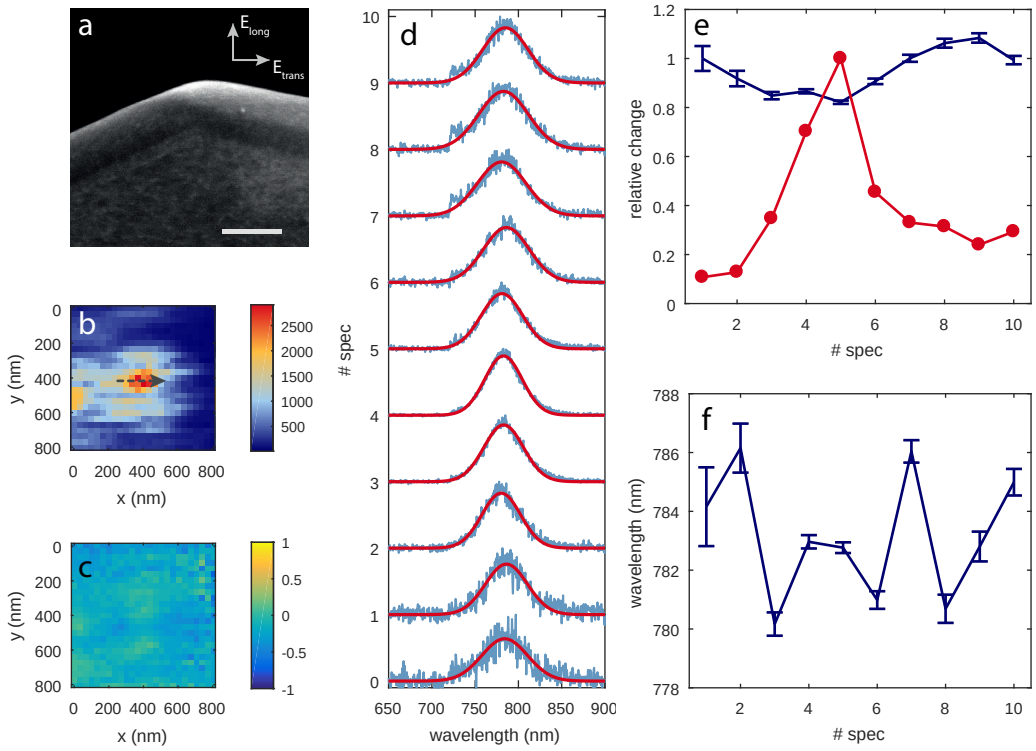

Figure 6.8 – Coupling of a QD to an unstructured gold tip. a, SEM image of an unstructured gold flake. Scale bar: 100 nm. **b**, PL map of the emission of a QD scanned beneath the tip with the probe centered in the focus. The fluorescence intensity increases in close proximity to the unstructured gold tip. **c**, Degree of polarization of the emitted light. No significant change in the DOP can be observed at the location of enhanced fluorescence. **d**, Spectra (blue line) measured while moving the QD underneath the tip. For small tip-QD distances the amplitude of the spectra increases (all spectra are normalized). All spectra are fitted with a Gaussian (red line). **e**, Width of the Gaussian fit (blue line) and amplitude of the spectra (red line). **f**, Peak position of the Gaussian fit.

(spectrum #1 to #5, bottom to top). This process is reversed as the QD increases the distance with respect to the tip (spectrum #5 to #10, bottom to top) as the spectrum gradually recovers its initial intensity. The amplitude and width of the peaks extracted from the fits are shown in Fig. 6.8e. Here, the fluorescence enhancement can be quantified to a factor of 10 between the lowest and highest amplitude between spectrum #1 and #5, respectively. At the same time, the peak width shows the opposite behavior and reduces as the fluorescence intensity increases. The width of the spectrum has a minimum at the same position where the fluorescence reaches its maximum (spectrum #5). Overall the spectral width shows a maximum reduction of a factor of 0.8. The error bars are obtained from the confidence interval of the fit and are small enough to unambiguously claim a spectral narrowing of 20 %. The spectral position of the resonance, however, remains unchanged in the presence of the tip. As depicted in Fig. 6.8f there are only minor fluctuations with a maximum span of 7 nm.

Discussion

The detailed investigation of the photon emission properties gives great insight on the coupling process. Up until now, no systematic study has been carried out on the variation of the coupling between colloidal quantum dots and a metal surface. Besides enhanced emission of the QD close to the metal tip there are only minor changes to the emission characteristics. The degree of polarization does not describe the same trend as the fluorescence intensity since it remains at values between 0.2 and 0.2. Colloidal quantum dots feature a degenerate dipole moment (bright plane) which leads for most QD orientations[2] emission contribution of both polarization directions. Therefore, the value of the DOP is mostly close to zero.

The absence of a change in emission polarization and spectral shape is an indication that the quantum dot is mostly affected by the enhanced local excitation field at the apex of the tip. Coupling to a resonant mode does effect the spectrum as each frequency is enhanced according to the spectral density of the mode. Since the measured resonance wavelength of various QDs remain unaltered in close proximity to the metal tip it can be concluded that the probe has no resonance in the considered spectral window and that the enhanced fluorescence is exclusively attributed to an increased excitation rate. In other works it has been shown how a nano-antenna has an affect on the polarization of the fluorescence of single molecules depending on the character of the plasmon mode [81, 82]. It is important to note that the QD in fact can couple to propagating surface plasmon modes which does reduce the excited state lifetime. However, these modes propagate upwards along the gold flake and either decay non-radiatively due to ohmic losses or decay into photons which do not enter the microscope objective. Emission into these states is not observed in the measurement and therefore contributes to non-radiative quenching.

[2] colloidal QDs have a fixed bright plane (two orthogonal dipole moments) with respect to the crystal axis. Except for one distinct QD alignment (bright plane perpendicular to sample plane) the emission has always contributions of both dipole moment orientations [15]

The reduced spectral width can be attributed to the interaction of the tip and the QD in close proximity. It has been shown that a metallic tip can influence the charge distribution in a PMMA matrix giving rise to reduced spectral diffusion and narrower spectra [441].

The maximum achievable fluorescence enhancement can be different for the same tip and even for the same emitter. Depending on the alignment of the tip with respect to the optical axis, the enhancement can vary significantly. A detailed study on the relative tip position and orientation can be found in appendix A.2. It is noted, that the position dependent field enhancement is sensitive to distances smaller than 100 nm which is well below the diffraction limit and a determination of the position with such an accuracy is not possible with the available experimental setup.

6.3 Resonant coupling with a QD

A metal tip in the vicinity of a single emitter strongly manipulates its optical response. As shown in the previous section, the enhanced electric field at the corner of a gold flake can be used to locally excite a single emitter. Depending on the geometrical shape of the tip, occurring localized surface plasmon resonances can also modify the emission properties of the emitter. A single cut towards the center of a gold flake serves as a PNR as demonstrated in chapter 5. Resonant coupling between an emitter and a plasmon has a significant impact on the fluorescence properties of the emitter such as the emission spectrum and the polarization.

This section shows measurements on the resonant coupling process between a PNR and colloidal quantum dots. The enhanced fluorescence is a combination of two effects and can be attributed to (i) enhanced emission due to the plasmon resonance as well as (ii) enhanced excitation as a result of the field enhancement caused by the metallic tip. The contribution of pure excitation enhancement has been measured and discussed in the previous section. Depending on the resonance wavelength of the localized plasmon the fluorescence spectrum shows changes in the emission spectrum as well as the degree of polarization.

6.3.1 Resonant emission

Increasing the contrast via resonant interaction with the tip is often one of the major goals of scanning probe microscopy. As show in the previous section, the pure presence of a sharp gold edge provides an enhanced field which locally excites a quantum dot. A different approach on how to increase the fluorescence of an emitter is by coupling with the near-field of a plasmonic resonance. Here, the fluorescence enhancement can be additionally amplified by providing additional decay channels. To this end, a resonant scanning probe is fabricated according to the description which is given in section 4.6.3. In order to facilitate the interpretation of the emission characteristics during the coupling with a quantum dot it is necessary to pre-characterize the optical properties of the PNR. Employing FDTD simulations

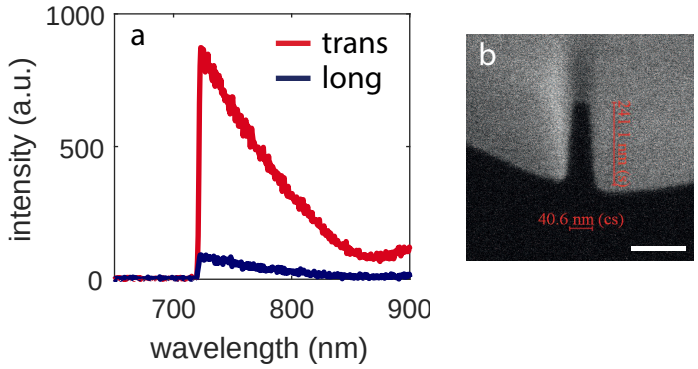

Figure 6.9 – Resonant scanning probe. a, PL spectrum of a PNR with a resonance below 700 nm. The transversal emission polarization is significantly stronger than the longitudinal polarization. **b,** SEM image of the probe tip. The width of the gap of 40 nm yields a broad resonance. Scale bar: 100 nm.

with the exact geometry based on detailed SEM analysis would be a possible approach to determine the resonance and the quality of the PNR. However, determining the exact three-dimensional shape of a structure is tedious and requires many SEM images. Additionally, exposure to high doses of electron beam irradiation is not recommended for plasmonic gold structures as accompanying carbon deposition lowers its optical performance. The most promising approach is the direct optical characterization via the intrinsic gold photoluminescence as it is described in section 4.6.4.

Polarized emission The polarization resolved PL spectrum of a PNR is shown in Fig. 6.9a. After moving the tip towards the focal point the PNR characteristic is determined via two individual measurements using a polarizing filter in two perpendicular orientations. It is clearly seen that the transversal polarization of the tip is much stronger than the longitudinal direction. This is a clear hint for the occurrence of a localized plasmon. The same polarization behavior produced by this kind of resonance has also been observed by Hancu et al. [430]. The resonance peak, however, does not fall into the observable spectral range and can only be anticipated in the range of 650 nm.

The SEM image of the tip after fabrication as shown in Fig. 6.9b reveals that the gap is rather large (about 40 nm) which is in agreement with a broad plasmon resonance. A spectral overlap and therefore a resonant enhancement of the QD emission is nonetheless possible as shown in this section.

Figure 6.10a shows a PL map of an area of $5 \times 5\,\mu$m with quantum dots. The PNR is not well aligned and therefore does not coincide with the laser focus. However, a systematic spot of enhanced emission on the left hand side of several QDs demonstrates the contribution of the tip. By moving the tip accordingly via the piezo tube leads to a perfect alignment with the focus as shown in Fig. 6.10b. All diffraction limited spots are superimposed with a small spot due to the local coupling with the tip. Therefore, the fluorescence intensity is significantly enhanced as the QD-tip

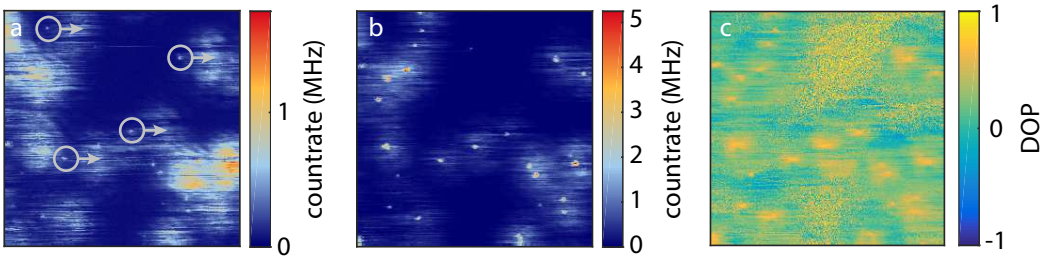

Figure 6.10 – Aligning the PNR for high resolution microscopy. **a,** PL map of an area of 5x5 µm. The probe is misaligned as can be seen by the systematic offset of the tip enhanced emission spot. **b,** Same PL map after moving the tip according to the direction indicated in **a**. The fluorescence intensity increases drastically. **c,** Corresponding DOP map of the same area as in **a**. At the location of the probe the emission is highly polarized along the transversal direction.

distance reaches a minimum in the center of the laser focus.

The resonant nature of the PNR can be demonstrated by calculating the DOP of the same area (see section 6.2 for definition) as shown in Fig. 6.10c. In order to account for different quantum efficiencies for photons with different polarizations in the individual optical paths the count rate on APD channel 2 is adjusted accordingly. The correction value is determined by comparing the PL map for both polarizations. The average intensity for several different quantum dots is expected to be equal on both APD channels. Any deviations are attributed to the detection efficiency and corrected accordingly. Large segments of the PL map have a DOP value of close to 0. However, at the position of the tip the DOP has always a value close to 1 which clearly indicates a change of emission polarization towards the transversal orientation. With this representation it is shown that the tip has a resonant character and can interact with a QD within the near field.

Further information of the coupling behavior can be extracted from spectra that are recorded at different distances between the tip and the QD. Figure 6.11a shows a map with a range of 650×650 nm with a single emitter. The corresponding DOP of this area is shown in Fig. 6.11b where the polarizing properties of the PNR is further confirmed. Individual spectra are recorded at the positions indicated by the open circles in Fig. 6.11a. Each spectrum is recorded with an acquisition time of 1 s and an excitation power of 8 µW while at the same time two single photon counting modules record a time trace for each polarization. Details on the optical setup can be found in section 4.3.2. The measured spectra and the associated time traces are shown in Fig. 6.11c-i. For the sake of clarity a histogram of both timetraces is shown in the right column. All the acquired data is normalized in order to better observe the shape of the spectra and the intensity of the timetraces. For large distances the fluorescence intensity is low as can be seen by the low signal-to-noise ratio of the spectrum. The intensity of both polarizations is similar and describes the same temporal profile which indicates the blinking characteristics of the QD. With reduced tip-QD distance the spectrum intensity increases as well as the ratio between the transverse and longitudinal emission contribution as can be seen

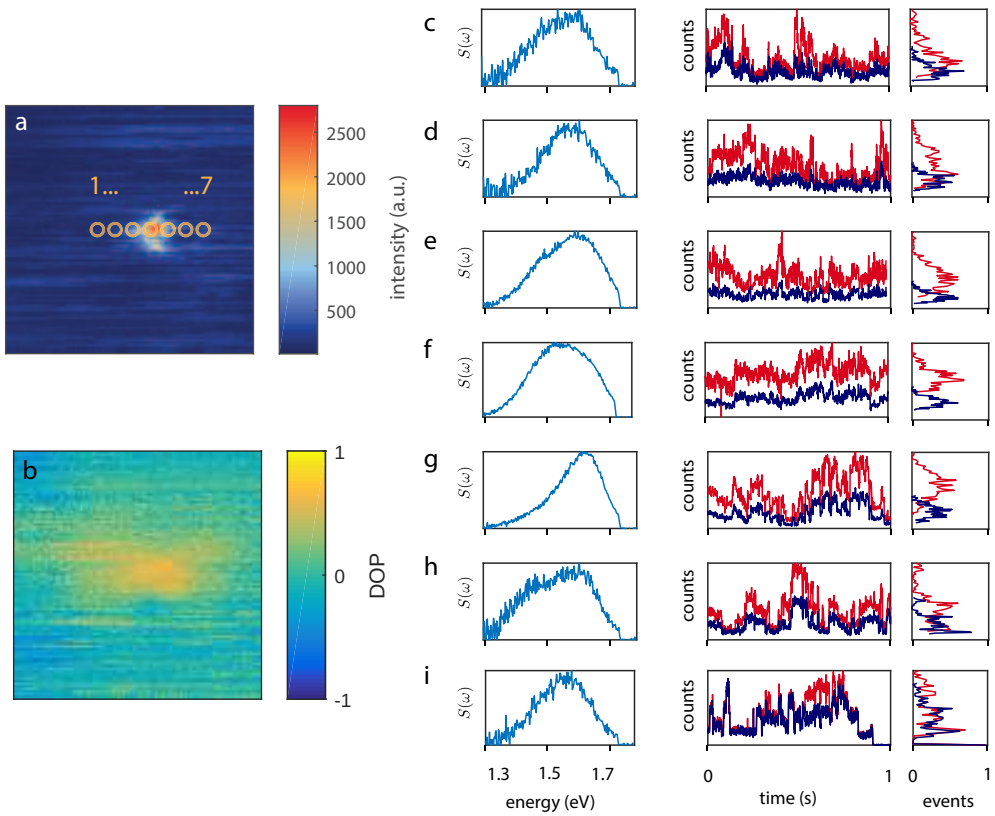

Figure 6.11 – Modified emission characteristics of a quantum dot. a, PL map of an area of 650×650 nm with a QD coupling with a resonant probe. **b,** DOP of the same area as in **a**. The emission is strongly polarized along the transversal direction for close proximity to the tip. **c-i,** Modified emission spectra for various distances of the QD with respect to the PNR. For each position the spectrum is recorded while monitoring the fluorescence dynamics for two polarizations (red line: transversal, blue line: longitudinal). Both contributions are depicted in a histogram.

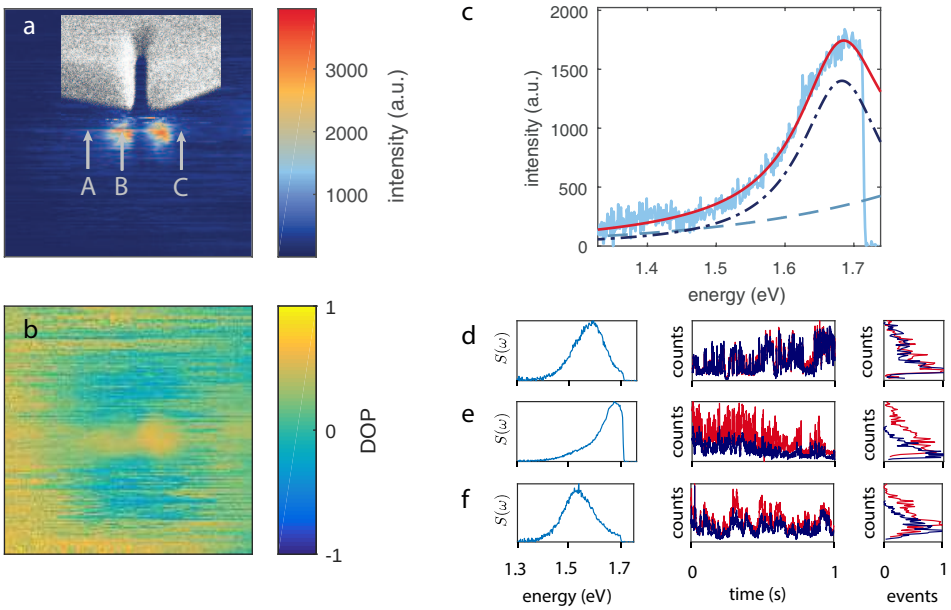

Figure 6.12 – Detuned PNR coupling with a quantum dot. a, PL map of an area of $650 \times 650\,\text{nm}$. Due to the alignment of the tip both tines are able to couple with the QD. The overlaid SEM image of the PNR is shown for a size comparison. Spectra are recorded at the indicated positions A, B and C. **b,** Degree of polarization of the same region as **a**. Both peaks show transversal polarized emission. **c,** PL spectrum of the resonant tip. **d-f,** Left column: Spectrum of the positions A, B and C in **a**. Center column: The timetrace shows the transversal (red) and longitudinal (blue) emission during the acquisition of the spectrum. Right column: The histogram of the timetrace.

from the histogram. The following increase of the tip-QD distance leads to a return of the initial emission characteristic which demonstrates a truly reversible process. The shape of the fluorescence spectrum does not significantly change between coupled and uncoupled QDs. Due to the broad tip resonance above 1.8 eV the spectral LDOS distribution has only a small variation across the emission spectrum of the quantum dot. In fact, if any, there is a small tendency of the spectrum to show a slight blueshift towards the resonance of the PNR.

Each PNR has its own characteristic due to slight geometrically differences. Figure 6.12a shows a typical example for the case where the tip lines up perfectly with the substrate. The PL map ($650 \times 650\,\text{nm}$) therefore shows two peaks in the presence of a single quantum dot. This is the result of the convolution of a point-like object (in this case the QD) with a larger object such as the apex of the resonant tip. An SEM image of the PNR with the same scale as the PL map is overlaid to demonstrate the size comparison. Both peaks are show a transversal polarization as shown in Fig. 6.12b where the DOP reaches a value close to 1 at the corresponding position of enhanced emission. The PL spectrum of the tip is shown in Fig. 6.12c. Here, the peak of the plasmon resonance is within the detectable spectral range and therefore the position and shape can be determined. The measured PL spectrum (thin red line)

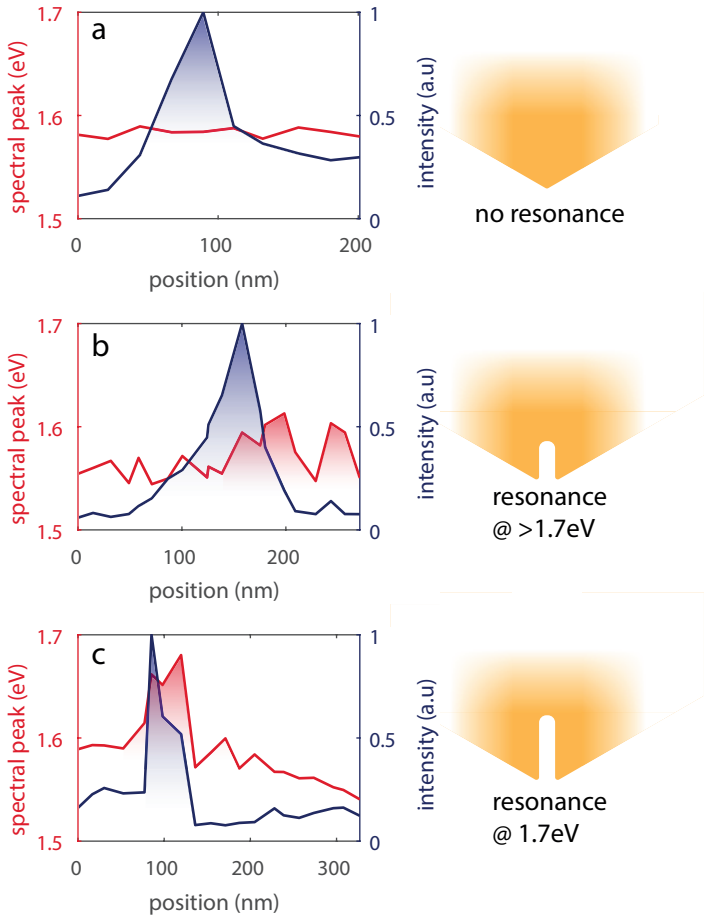

Figure 6.13 – Comparison of the fluorescence intensity and spectral peak position. **a,** Fluorescence peak width and intensity while scanning a quantum dot through the near field of a bare gold flake edge. **b,** Same as depicted in **a** but with a PNR featuring a resonance above 1.7 eV. **c,** Same as depicted in **a** but with a PNR resonant at 1.7 eV.

is fitted with an exponential background (blue dashed line) and a Lorentzian (black dashed line). Details on the characterization technique can be found in section 4.6.4. The emission characteristic of the plasmon resonance can also be seen from the QD emission while coupling with the near field. Figure 6.12d-f shows the spectra and the corresponding photon polarization for three different positions as indicated in Fig. 6.12a. After acquisition of the PL map consecutive spectra are measured while the QD is moving through the plasmonic near-field. Before the QD couples with the plasmon (A) the fluorescence spectrum is determined by its intrinsic spectrum with a resonance at 1.55 eV and the emission polarization is equal for both orientations. As the QD is at the maximum field intensity (B) the spectrum is strongly modified and assumes the shape of the plasmon resonance. In addition, it is observed that the transversal component of the emitted light increases in comparison to the longitudinal component. With decreasing coupling strength (C) the spectrum transitions back to the initial shape and emitted photons become less polarized.

Discussion The observation that the features in the DOP maps are less confined than the fluorescence peaks occurs for the majority of the measurements. The origin of this difference in contrast is attributed to the fact that the resonant emission process (which is visualized by the DOP) depends solely on the field intensity of the resonant mode. The fluorescence peaks, however, also depend on the enhanced non-resonant excitation field which contributes to the total amount of emitted light. In addition, the enhanced excitation field also has a different spatial distribution (see appendix A.3) than the resonant field. These are the two factors which cause the different contrast between the PL and the DOP maps.

The main features of the three different scanning probes is summarized in Fig. 6.13. Here, the evolution of the fluorescence peak position as well as the integrated fluorescence spectrum is demonstrated while scanning a quantum dot through the local near-field of different probe tips. In Fig. 6.13a shows the data of the bare gold tip as discussed in section 6.2. The enhanced emission does not correlate with any spectral shifts which is attributed to the nature of purely increased excitation. In case of a plasmon resonance at the apex of the tip the fluorescence spectrum changes its peak position according to the plasmon. Figure 6.13b and 6.13c demonstrate the data for a resonance above 1.7 eV and at 1.7 eV, respectively. It can be seen that the spectral shift accompanying the intensity enhancement is more pronounced for larger spectral overlap between the plasmon and the quantum dot. The position of maximum spectral shift and fluorescence intensity, however, do usually not coincide. The effects of excitation enhancement and resonant coupling act independently and have their maximum at different spatial positions (see appendix A.3 for details).

In general, the ability to introduce a spectral shift of about 150 meV is remarkable. Comparable experiments that show a similar manipulation of the fluorescence spectrum has not yet been reported.

6.3.2 High resolution imaging

Figure 6.14a demonstrates the maximum achievable confinement within an area which covers only one QD. The DOP map (see Fig. 6.14b) shows that the QD couples resonantly with the PNR as the polarization is oriented in transversal direction at the location of highest fluorescence. A line cut through the center of the QD is shown in Fig. 6.14c (open circles) is fitted with a Gaussian (red line) and yields a FWHM of less than 26 nm. It is noted that the PL map was acquired at an excitation rate of 8 µW in order to saturate the QD even during resonant coupling with the plasmon resonance. The peak width for resonant coupling depends on the excitation rate and decreases with increasing pump rate. Further details on this aspect are given in section 6.3.3. Higher excitation rates, however, increases blinking of the QD and leads to a broadened diffraction limited spot. Furthermore, even though CdSeTe/ZnS QDs are known for their photostability, heavy incoherent excitation can eventually lead to bleaching or structural damage making further experiments on a pre-characterized QD impossible.

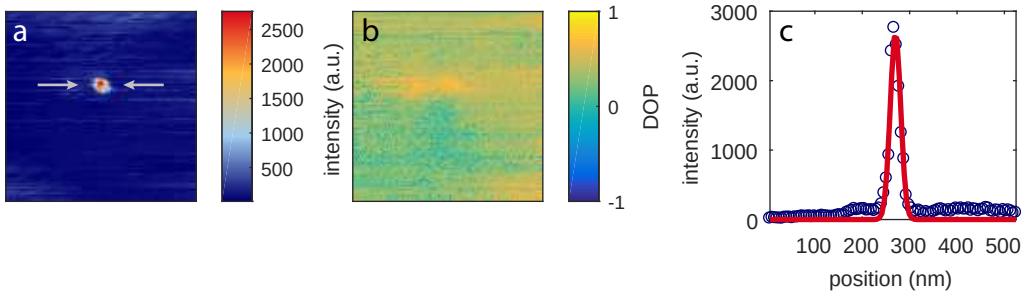

Figure 6.14 – Highly confined emission from a single quantum dot. a, PL map of an area of $520 \times 520\,\mathrm{nm}$ with a single quantum dot. **b,** Degree of polarization of the same region as **a**. The increased DOP value indicates a resonant emission process. **c,** Horizontal linecut as indicated in **a**. The measured fluorescence (open circles) is fitted with a Gaussian (red line).

Determining experimentally the local enhancement factor Λ via a PL map is challenging. A simple approach to quantify the enhancement is to calculate the ratio between the fluorescence for maximum coupling Γ_c with the tip and the fluorescence of the pure QD Γ_p. Based on the linecut in Fig. 6.14c the enhancement factor can be estimated to about $\Gamma_c/\Gamma_p = 20$.

However, this value can depend significantly on the excitation rate due to the fact that the PNR features enhanced excitation and emission. Additionally, the location of maximum excitation and emission does not necessarily coincide (see appendix A.3). For low excitation intensities (below QD saturation) the emission enhancement has only an impact on the quantum efficiency of the radiative decay. Since colloidal quantum dots have already an efficiency of about 0.5 the emission enhancement has only a minor contribution.

With increasing excitation intensity the QD becomes saturated and the additional radiative decay channels provided by the PNR does enhance the fluorescence rate Γ_c and therefore the enhancement factor Λ. For high excitation intensities, however, non-linear effects such as biexciton generation also increase the fluorescence of the uncoupled QD as well which reduces the ratio Γ_c/Γ_p. In addition, if the enhanced emission stems primarily from the process of resonant coupling the contribution of enhanced excitation vanishes due to the displaced locations of enhanced excitation and emission.

Overall, the maximum achievable value of Λ depends on a variety of properties. The exact geometry of the PNR determines the field enhancement, Purcell factor as well as the degree of confinement. Whether the increased fluorescence occurs due to excitation or emission enhancement always depends on the ratio between the excitation rate and the saturation of the emitter (see section 6.3.3). Also, the condition of the quantum dot has an influence on the enhancement factor. Depending on the quality of the core-shell interface the efficiency of Auger processes can be different which directly affects the radiative decay rate of biexcitons in uncoupled QDs.

6.3.3 Power dependent high resolution

The fluorescence rate F of an ideal two-level system can be described by $F = F_\infty \frac{I/I_S}{1+I/I_S}$, where I is the excitation rate, F_∞ is the fluorescence rate for infinitely large excitation rates and I_S is the saturation rate where the fluorescence rate equals $F_\infty/2$. More details on the derivation can be found in section 2.2.2. Since F_∞ and I_S are proportional to the radiative decay rate γ_0, both, excitation and emission enhancement causes an increased fluorescence rate. However, the enhancement ΔF can be different depending on the relative magnitude between the excitation rate I and the saturation rate I_S as discussed in the following.

Excitation enhancement solely alters the electric field at the position of the emitter and therefore increases the excitation rate. Figure 6.15a shows the fluorescence characteristic of a single emitter. Significant improvement of the fluorescence fate can be expected by enhancing the excitation below the saturation rate of the emitter which leads to a fluorescence boost ΔF_{low}. Above the saturation rate the increased fluorescence rate ΔF_{high} becomes smaller and eventually gets negligible as the limiting process is the spontaneous emission rate of the emitter.

The opposite behavior is expected for enhanced emission which leads to a reduced excited state lifetime of the emitter and therefore increases the saturation rate. Figure 6.15b shows the emission characteristic of an emitter with decay rate γ_0 and $2\gamma_0$ as indicated by the blue and red lines, respectively. Observation of a significant fluorescence rate change is only expected for excitation rates in the regime far above the saturation rate of the isolated emitter (ΔF_{high}) where the fluorescence rate is limited by the saturation rate. It is noted that excitation above the saturation rate can turn into excitation below saturation for sufficiently enhanced decay rates. The fluorescence rate below saturation is mainly limited by the excitation rate and any further reduction of the excited state lifetime has no significant influence on the fluorescence (ΔF_{low}).

In a scanning probe experiment the emitter is moved through the near field of a localized plasmonic field which causes a change of both, excitation and emission rate. However, since the emission of the emitter is on resonance with the plasmon, emission enhancement becomes the main contributor to the increased fluorescence. The assumption that the fluorescence rate is solely proportional to the LDOS of the mode (Purcell factor) is only valid for very large excitation rates. Since this is not the case in a typical experiment the fluorescence rate strongly depends on both, the excitation rate and the Purcell factor. Figure 6.15c shows the fluorescence rate as a function of position for different excitation rates. The field profile is assumed to have a Gaussian shape with a maximum Purcell factor of 1000. In case of an infinitely high excitation rate the fluorescence rate is expected to follow the field profile (blue line). It is noted that all graphs are normalized in order to demonstrate the change of fluorescence as function of position. An excitation rate of $I = \gamma_0$ for an uncoupled emitter is above the saturation rate and therefore the emission is limited by the excited-state lifetime. However, as the coupling to the PNR increases the lifetime drops and the saturation rate increases dramatically rendering the fluo-

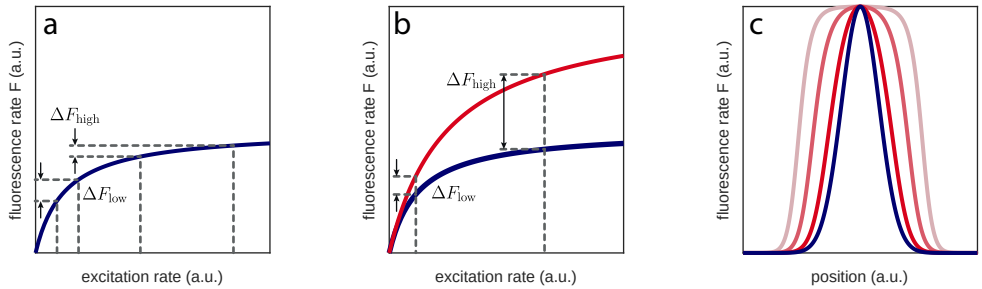

Figure 6.15 – Difference between excitation and emission enhancement. a, Excitation enhancement (factor 2) below saturation (ΔF_{low}) is much more efficient than above the saturation rate (ΔF_{high}). **b,** Emission enhancement (factor 2, red line) changes the fluorescence characteristic of the emitter. The fluorescence enhancement above saturation is much larger than below saturation. **c,** Calculated fluorescence peaks for different excitation rates for an emitter scanned through a Gaussian field profile with a Purcell factor of 1000. The Purcell factor profile (blue line) is the expected fluorescence profile for an infinitely high excitation rate. Finite excitation rates cause a broadening due to saturation before reaching the maximum enhancement.

rescence intensity limited by the excitation rate (light red line) before the maximum Purcell factor can be reached. As a consequence, the width of the fluorescence peak appears much broader than the field profile. As the excitation rate increases (red lines), the emission saturates at higher Purcell factors and causing a narrowing of the fluorescence profile.

In the measurements it has been observed that the fluorescence profile is broader than one would expect based on the actual mode field profile of the localized mode. The average excitation rates of $1 - 10\,\gamma_0$ is likely to be the main reason for the broadening of the fluorescence profile. In addition, the large QD size and its high refractive index can lead to further broadening as it tends to concentrate field energy in close proximity to the plasmon mode.

It is noted that these calculations are based on an ideal two-level system. Colloidal quantum dots have been shown to behave linear for low excitation rates. However, as the excitation rate increases non-linear effects such as biexciton excitation have a significant impact on the excited state lifetime as well as the excitation rate. Additionally, the fluorescence profiles as calculated in Fig. 6.15 are only valid for a constant excitation rate. The local near-field of the gold tip, however, also changes the excitation field which leads to a position dependent excitation rate.

6.4 Conclusion

This chapter has demonstrated the optical properties of colloidal semiconductor quantum dots and their interaction with a pure metal tip as well as a coupling with a localized surface plasmon. Characterizing the emission properties of the employed quantum dots has revealed the typical properties such as blinking and inhomoge-

neous broadening. In addition, excited state lifetime, saturation intensity as well as the dipole moment has been measured in order to obtain the necessary information for coupling experiments.

The promising application of scanning probe microscopy has been proven to be a vital tool for the investigation of light-matter interaction. The successful coupling of quantum dots with an edge of a single crystalline gold flake has demonstrated the impact on its emission properties. Evaluation of a set of spectra with different tip-to-QD distances has shown significantly enhanced fluorescence due to high local excitation fields at the apex of the tip. Furthermore the fluorescence did not show any substantial changes of polarization associated with the increased fluorescence intensity. The same observation applies to the peak wavelength of the emission spectrum. A small reduction of the spectral width can be attributed to a change of the charge distribution in the vicinity of the QD due to the presence of a metal surface.

Greater impact on the emission spectrum has been observed when the gold edge features a localized surface plasmon resonance. The resonant coupling of the quantum dot to the plasmon affects the emission properties, such as polarization and spectrum, according to the properties of the localized surface plasmon. Depending on the resonance wavelength of the plasmon the spectral peak can be shifted up to 150 meV while the emission is highly polarized according to the plasmon decay. It has also been demonstrated that the ability to locally confine electric fields and enhance the emission of quantum dots leads to a high fluorescence contrast with a spatial resolution of less than 26 nm.

Further improvements in future experiments are expected with regard to increased resolution and fluorescence contrast. Up until now all measurements have been carried out at an excitation wavelength of 532 nm which is beyond any plasmon resonance. The use of a wavelength close to 600 nm would math a 3^{rd} order resonance of the PNR. A combination of resonant excitation and emission enhancement poses a promising approach for unprecedented high-resolution microscopy.

The interaction of colloidal quantum dots with metal surfaces or particles has recently also sparked new interests as the increased emission of biexcitons has been observed in several studies. Application of the scanning probe technique allows distance dependent measurements of the auto-correlation function which is a promising approach to study the exciton/biexciton contribution of colloidal quantum dot emission.

7

Strong coupling of plasmons and quantum emitters

Strong coupling (SC) of light and matter occurs if photons stored in a cavity with mode volume V and quality factor Q are repeatedly exchanged with electronic excitations in matter. Under such conditions light and matter give up their separate identities and new dressed states arise which modulate the response of the system to external stimuli depending on the coupling strength and photon number. To achieve strong coupling with n emitters the interaction rate $g \propto \sqrt{n/V}$ needs to exceed the cavity loss rate $\kappa \propto 1/Q$ as well as the total emitter decay rate Γ. Yet strong coupling of only a single quantum emitter to a cavity mode is of particular interest since it results in single-photon nonlinearities for quantum gates [442] and efficient single-photon sources [443]. In high-Q cavities such single-emitter strong coupling has successfully been achieved, but only at cryogenic temperatures by coupling to single-emitter zero-phonon lines [1]. Conversely, by reducing the mode volume in plasmonic resonators and by using large numbers of emitters strong coupling has also been achieved at room temperature [95, 107, 110] with recent experiments reaching the single-emitter limit [13, 84]. The recent results of strong coupling at room temperature has been summarized in several reviews [52, 97, 444–448]

This section focuses on the demonstration of tunable strong coupling of single colloidal semiconductor quantum dots (QDs) and a broadband plasmonic nanoresonator (PNR) at room temperature. The use a slit-like plasmonic nanoresonator fabricated at a corner of a single-crystal gold flake serves as a scanning probe as illustrated in Fig. 7.1. Nanometer-precise raster scanning of such probes across a sample containing single colloidal quantum dots allows precise tuning and optimizing of the coupling strength and measurement of the corresponding intriguing changes in the fluorescence spectrum due to strong coupling as indicated in Fig. 7.1. The measurements in this chapter are performed with a scanning probe which, in comparison to the previous chapter, is on resonance with the QD emission wavelength. In addition, the small gap size gives rise to an extremely small mode volume and subsequent high coupling rates.

A comprehensive study on coherent interaction of a single quantum dot and a

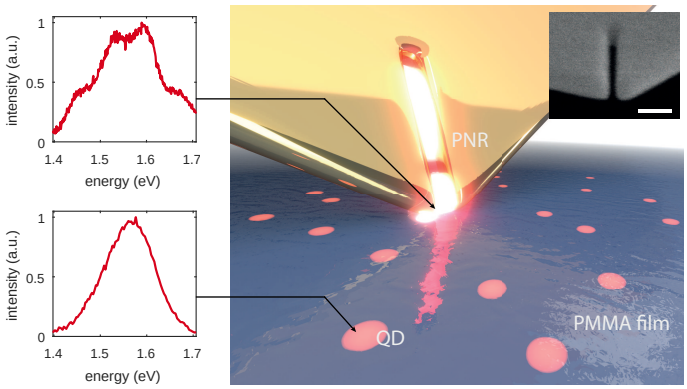

Figure 7.1 – Strong coupling via precise nano-positioning of a PNR probe. Illustration of the plasmonic nanoresonator probe interacting with quantum dots embedded in a polymer film. Left panel: The spectrum of a QD changes significantly when coupled to the slit-like plasmonic nanoresonator at the tip apex. Inset: SEM image of a PNR at the apex of a probe tip. Scale bar: 100 nm.

localized plasmonic field is presented in this chapter. The investigation includes experimental work as well as several theoretical models which account for the rich electronic structure of colloidal CdSeTe/ZnS quantum dots. In addition, the current models for predicting the coupling constant in the dipole approximation are explored for extended mesoscopic emitters. Further consideration show how the polarized particles in the proximity of plasmonic near-fields have a significant impact on the coupling strength. Large text parts and figures of this chapter are adopted from Groß et al [449].

7.1 SC Measurements

7.1.1 Cavity characterization

In order to achieve ideal coupling conditions between a localized plasmon and a QD it is necessary that the exciton emission wavelength is on resonance with the electric field. Since in this work the QD wavelength is fixed to roughly 800 nm it is required to properly characterize the PNR on the scanning probe to ensure the resonance condition is met.

Characterization via scanning electron microscope (SEM) imaging shows a slit length of about 250 nm and a gap width of 12 nm as demonstrated in Fig. 7.2a. The PNR is slightly displaced to the left with respect to the gold flake corner due to fabrication tolerances. This small asymmetry causes the right side of the PNR to be about 5 nm longer than the left side. Numerical FDTD simulations have shown that these patterning variations have a negligible impact on the plasmon resonance (see Fig. 7.2b for mode profile). The plasmon resonance of the PNR is measured via the intrinsic PL of gold as described in section 4.6.4. The recorded gold PL spectrum of the PNR is displayed in Fig. 7.2c (red line) and shows a single resonance on top

of a broad background (see section 4.6.4). The shape of the spectrum is modeled as the superposition of the bulk gold PL (blue dashed line) and the emission via the plasmon resonance (black dash-dotted line). As the PL of bulk gold peaks at 516 nm [410] it is possible to approximate its contribution via an exponential function in the wavelength range of $730-900$ nm. The via the plasmon resonance is modeled by a simulated far field spectrum which has a spectral width of 72 meV and a Q-factor of 22. The sum of both contributions, indicated by the thick red line, provides good agreement with the measured data. The resonance wavelength of the PNR obtained from the fit is found to be 780 nm which is in accordance with FDTD calculations shown in Fig. 7.2c.

It is noted that the contribution of the resonant emission is rather small compared to the photoluminescence of unstructured gold. As the gap width of the PNR gets smaller, the volume of gold penetrated by the resonant near-field decreases [36] causing a reduced coupling with the mode and therefore less emission of gold PL via the PNR. In addition, the quadrupolar character of the mode causes a weak coupling to the far field leading to a further reduction of emission intensity (see chapter 5).

It is also important to note that this measurement determines the near-field resonance wavelength of the PNR. In comparison, scattering techniques which measure the far-field properties can yield a different value for the maximum peak energy. This difference between near-field and far-field peak energies is attributed to the universal behavior of damped harmonic oscillators [450]. Similar observations have been reported when comparing gold PL spectra with white light scattering spectra which is attributed to the photoluminescence shaping mechanism [418]. As it will be seen later on in this chapter, the plasmon resonance wavelength used in a quantum optical model can slightly deviate from the value which has been determined in this characterization.

7.1.2 Tuning the coupling strength

The previously characterized PNR is in the following measurements used to demonstrate the coupling between localized plasmons and single quantum dots. Figure 7.3 shows a PL map with an overview of an area of $5 \times 5\,\mu$m with a prospect of about 20 single quantum emitter.

Before continuing to any further coupling measurements, the investigated emitter is verified as a single QD by confirming that the intensity autocorrelation $g^2(0)$ in absence of the tip is smaller than 0.5 (see Fig. 7.4a). Details on the autocorrelation measurement is described in appendix B.1. Figure 7.4b shows a photoluminescence (PL) map of a single QD (excitation rate $\Lambda = 10$ MHz, see appenix A.4 for calculation) obtained by scanning a QD beneath the PNR through the focus of an inverted confocal microscope as described in section 4.7 . Due to the asymmetry in the position of the slit at the probe apex as shown in Fig. 7.2a or possibly a small overall tilt of the probe, only one of the tines contributes significantly to the near-field intensity enhancement resulting in a single localized enhancement spot. The telegraphic

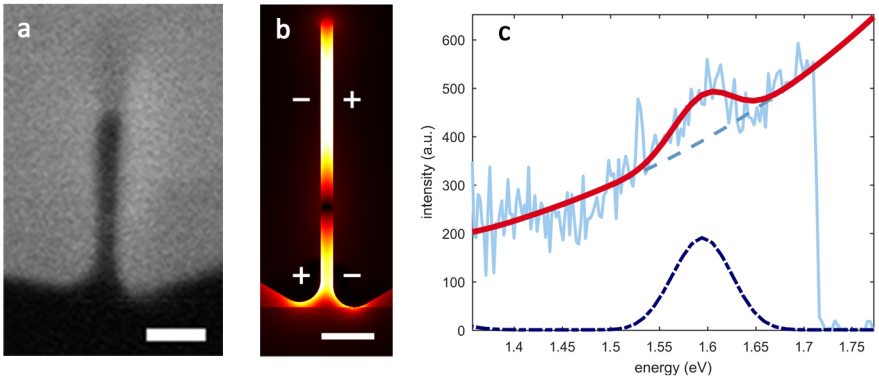

Figure 7.2 – Cavity characterization. **a,** SEM image of the PNR used for strong coupling recorded at an incident angle of 52°. Scale bar: 50 nm. **b,** Map of the electric field distribution of the PNR mode used in the experiment. The slightly different lengths of the two tines account for fabrication imperfections. The + and - signs indicate the instantaneous charge distribution highlighting the mode's weakly-radiative quadrupolar character. Scale bar: 50 nm. **c,** Gold PL emission spectrum of the PNR in **a** (thin blue line). The spectrum is fitted with the sum of an exponential background PL emission (blue dashed line) and the simulated cavity emission (blue dash dotted line). The sum of both contributions (red line) is in a good agreement with the measured spectrum.

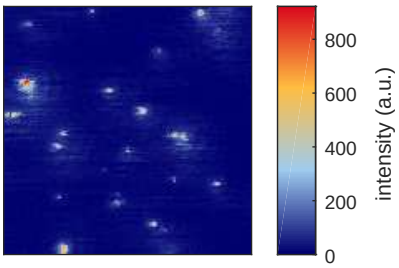

Figure 7.3 – Photoluminescence map of QDs with a resonant scanning probe. The map (range: $5 \times 5\,\mu$m) shows many isolated quantum dots.

on/off behavior which becomes apparent as the scan image is recorded line-by-line provides further proof for the coupling of a single QD to the PNR [250, 252]. The broad diffraction limited background in Fig. 7.4b is dominated by an intense 60 nm wide peak. Fig. 7.4c shows a vertical line cut of the PL map (yellow open circles) at the peak position indicated by two arrows in Fig. 7.4b. Since the excitation rate (10 MHz in this measurement) is below the saturation rate the increase of the absorption cross-section in presence of the probe dominates the fluorescence enhancement and the shape of the line cut (see section 6.3.3).

It is important to note that the occurrence of quenching, as it is reported for a single gold sphere and a single molecule in close proximity, has not been observed in this experiment [73]. Due to the highly enhanced resonant coupling the radiative decay remains faster than the non-radiative quenching process [451–453]. Also, a QD is much larger than a single molecule which even in the case of direct contact

with the metal has an average distance of about 4 nm.

To investigate the coupling with the PNR and the occurrence of strong coupling fluorescence spectra are recorded as a function of the QD's position with respect to the PNR as indicated by the white circles in Fig. 7.4b. To ensure that the drift of the tip between the recording of the PL map and the spectra is negligible during this process, the intensity of the integrated spectra (blue line) is compared with the spectrally integrated photoluminescence map and shows good agreement.

Further analysis of the particular shapes of the spectra reveals the coupling of electronic states of the QD with the PNR. Fig. 7.4d displays the recorded spectra which have been normalized for better comparison. For large QD-probe separations the shape of the spectrum matches the fluorescence spectrum of a weakly-coupled system. As the coupling strength increases, the coupled system displays pronounced changes in the emission spectrum. A transition into the strong coupling regime can be observed at the position of maximum resonant field. Contrary to the characteristic two-peak splitting of conventional strong coupling, the spectrum shows an unexpected appearance of four peaks. By moving the PNR further away from the QD the coupling strength decreases and the spectrum makes a transition back to that of a weakly coupled QD, signifying a truly reversible and controllable process.

7.1.3 Discussion

In this section it is briefly shown that the occurrence of four peaks can be attributed to a neutral and a charged QD state which both couple strongly with the PNR, each contributing with a Rabi doublet. This is possible as, in contrast to high-Q resonators with very narrow resonances, the 'broadband' PNR with a 78 meV bandwidth can coherently cover multiple exciton resonances giving rise to simultaneous probing of both QD charge states [454]. The QD has a diameter of about 8 nm, leading to a small energy separation of less than 20 meV between the neutral and the charged exciton [455]. Charge-carrier trapping of hot electrons upon incoherent excitation is a common process in QDs, leaving behind a positively charged nanocrystal core [267, 301, 348, 349]. More details on this topic are discussed in section 3.8. However, this charged exciton (trion) is optically dark due to highly efficient non-radiative Auger decay [252, 276]. Yet here, strong coupling via plasmons provides a radiative decay channel which is significantly faster than the Auger processes, rendering the charged trion state optically active [355]. A comprehensive summary on this topic is found in section 3.5. Consequently, the QD states involved in the spectral response are the neutral and the positively charged QD state. Generally, as an additional charge in the QD causes increased electron-hole interaction leading to a reduced wave function overlap [456], the neutral state can be assigned to the outer Rabi doublet and the charged state to the inner one. The relative Rabi splitting of both states is a direct measure of the relative magnitude of the involved total transition dipole moments. Recent dark-field spectroscopy experiments on quantum dots in bowtie nanoantenna gaps did not show four peaks [84]. This can be explained by the fact that resonant excitation via the antenna and the

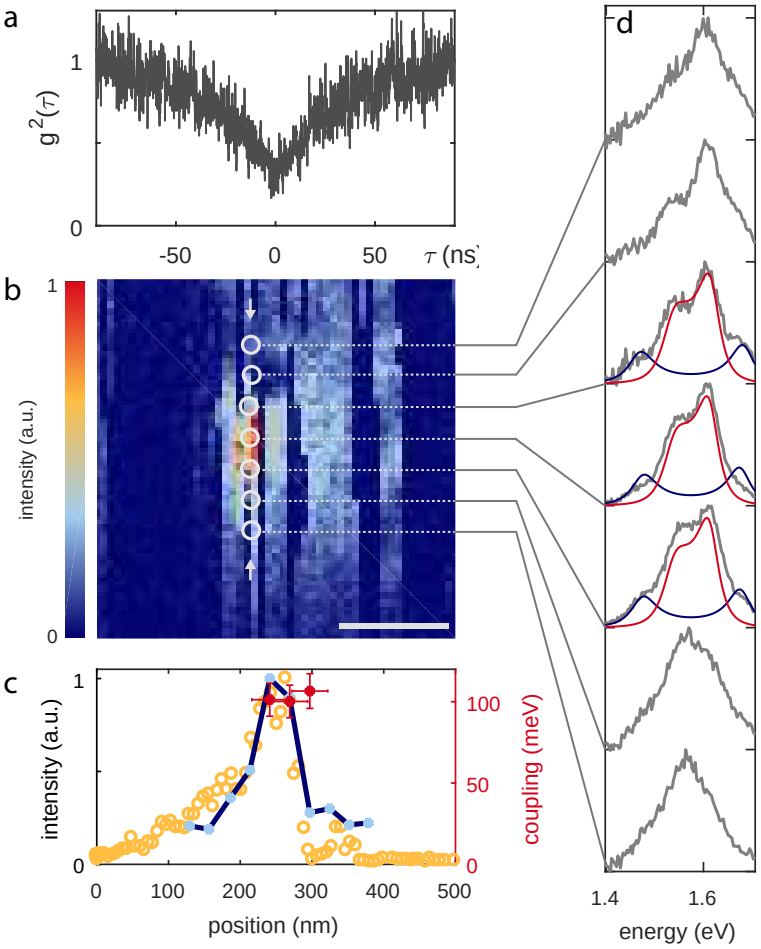

Figure 7.4 – Separation-dependent coupling strength. **a,** Second-order autocorrelation of the photons emitted by a single QD in absence of the probe. **b,** Photoluminescence map of the quantum dot scanned beneath a PNR. The white circles indicate the positions in which spectra have been recorded. Scale bar: 100 nm. **c,** Open yellow circles: Normalized line cut of the PL map in **b** (arrow). Full blue circles: Integrated spectral amplitude recorded at the positions indicated by white circles in **b**. Red circles: Coupling strength (right axis) used to model the strong-coupling spectra in **d**. **d,** Gray lines: Normalized spectra recorded for different coupling strengths. Solid lines: Spectra obtained from the quantum optical model with contribution of neutral state (blue) and charged state (red).

resulting absence of hot electrons leads to a low probability of charging events at low excitation rates.

A simple coupled-oscillator model is sufficient to predict plasmon-exciton hybridization on a semi-classical level but does not allow for the calculation of emission spectra without an (artificial) addition of stochastic noise terms. However, the measured spectra can be explained with a quantum optical model based on the Lindblad master equation. This model describes the interaction of a quantum emitter represented as a 5-level quantum system with a broadband cavity to capture the essential transitions of neutral and charged QD states. Here, the evolution of the density matrix ρ is given by equ. 2.50 where the Hamiltonian H_{I} describes the coherent interaction of the cavity with two transitions in the QD. The jump operators L_{k} take into account all incoherent processes including pumping, dephasing, radiative and non-radiative decay as well as population transfer between neutral and charged quantum dot states. As the majority of the photons emitted from the strongly coupled system reach the far field via the cavity the emission spectra are calculated via equ. 2.51. A complete introduction into the model is presented in the following section 7.2. The calculated spectra are shown in Fig. 7.4d (solid lines) in direct comparison with measured data and reveal a coupling strength of 110 meV and 44 meV for the neutral (g_n) and charged (g_c) exciton, respectively, resulting in a coupling strength ratio g_c/g_n of 0.4. The coupling strength g_c, extracted from a best fit to the experimental spectra, is plotted for each QD-PNR separation in Fig. 7.4c (red dots). It is observed that the three spectra with the highest coupling strength are recorded close to the QD emission peak. Interestingly, the spectrum with the highest coupling strength exhibits a comparably small emission intensity, an effect caused by the spatial displacement of the near-field intensity maxima of the non-resonant excitation field (532 nm) and the resonant mode field (800 nm) of the PNR as described in appendix A.3.

The model correctly describes the experimental data in the strong coupling regime where coherent light-matter quantum dynamics are dominant and allows to reproduce the shape and intensities of all four peaks. However, when extended to the weak coupling regime it tends to underestimate the width of the spectral features (not shown). This is not surprising since modeling a QD as a 5-level quantum emitter will always simplify several intrinsic QD dynamical degrees of freedom which are responsible for its broad emission spectrum but which do not contribute significantly to strong coupling. Indeed, using a well-established pure dephasing model with a dephasing rate of $\gamma_d = 160$ fs for the QD the quantum-optical master equation accurately reproduces the spectra in the strong coupling regime, where coherent coupling dominates over phononic processes. In the weak coupling regime the emission properties of the QD are heavily affected by phonons in a way that may not be accurately described by a pure dephasing model [457]. Furthermore, the spectral width can also be influenced in the experiment due to the reduced charge fluctuations induced by the presence of the metallic probe as a function of distance between QD and PNR [441,458]. Also, as shown experimentally in section 6.2, tip-induced spectral narrowing can be observed independently using an unstructured

gold tip.

The measurements which have been presented up until now show that it is possible to achieve strong coupling with a scanning probe PNR. The ability to tune the coupling strength is between a plasmon resonance and a single quantum dot is unprecedented. In the following section the quantum optical model is introduced in full detail after which further measurements which consolidate and underline the presented model.

7.2 Quantum model

This section introduces a quantum-optical model for the coupled QD-PNR system based on the master-equation formalism [180] in order to reproduce the experimentally measured spectra both qualitatively and quantitatively. As discussed in section 7.1.3, the four peaks observed in the strong-coupling spectra are interpreted as a pair of Rabi doublets arising from the coupling between the PNR and the either neutral or charged state of the quantum dot. Therefore, the quantum dot should possess at least four internal (quantum) states that can coherently couple to the PNR. In order to formulate a theory that is as simple as possible yet compatible with further observations, an additional single dark state is included in the model. The QD is thus represented by a 5-level system with internal quantum states $|1\rangle, ..., |5\rangle$ and associated bare energies $E_1, ..., E_5$. Level $|1\rangle$ is associated with the neutral ground state, $|3\rangle$ with a single charged state, and $|5\rangle$ with a double charged dark state. States $|2\rangle$ and $|4\rangle$ are occupied by excitation of states $|1\rangle$ and $|3\rangle$ with one exciton, respectively, and are assumed optically active (see Fig 7.5). The dot is coherently coupled to a single electro-magnetic field mode of the PNR (hereafter also referred as cavity) with central frequency ω_0. As per standard procedure, excitations in the cavity are described via an annihilation operator a satisfying the bosonic commutation relation $[a, a^\dagger] = 1$. For convenience the Hamiltonian is formulated in the interaction picture, so that the center of the cavity resonance ω_0 is shifted to the origin of the frequency axis. The free (non-interacting) part of the Hamiltonian H_0, in units such that $\hbar = 1$, is thus chosen to be

$$H_0 = E_1|1\rangle\langle 1| + (E_1+\omega_0)|2\rangle\langle 2| + E_3|3\rangle\langle 3| + (E_3+\omega_0)|4\rangle\langle 4| + E_5|5\rangle\langle 5| + \omega_0 a^\dagger a. \tag{7.1}$$

Next, the coupling of the states via coherent and incoherent processes are considered. As illustrated in Fig. 7.5, the transition $|1\rangle \leftrightarrow |2\rangle$ ($|3\rangle \leftrightarrow |4\rangle$) is coherently coupled to the cavity field via the coupling rate g_n (g_c). Detuning factors are introduced between each transition and the cavity field, $\Delta_n = E_2 - E_1 - \omega_0$ ($\Delta_c = E_4 - E_3 - \omega_0$). Further transitions between the energy levels occur due to pumping and other incoherent processes, such as Auger recombination and spontaneous emission into other (non-cavity) modes. States $|3\rangle$, $|4\rangle$ and $|5\rangle$ represent charged states of the quantum dot. It is noted that in absence of a cavity the transition $|3\rangle \leftrightarrow |4\rangle$ would be optically inactive due to its large non-radiative decay rate γ_a (attributed to Auger processes). In the coupled cavity-QD system this transition

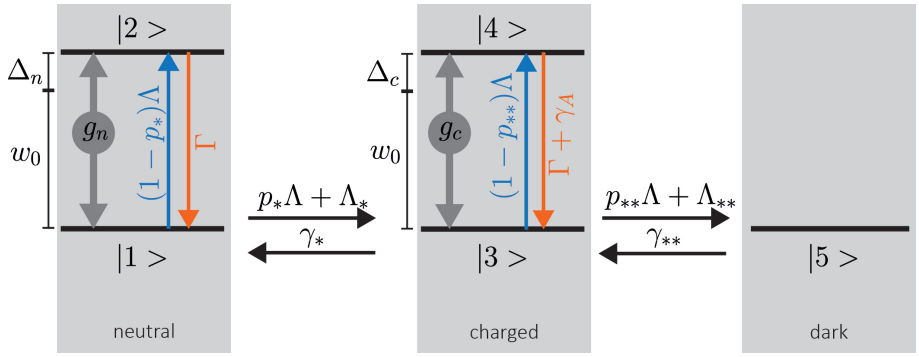

Figure 7.5 – 5-Level diagram of the quantum dot. The QD can switch between a neutral, charged (optically active) and dark state, which is optically inactive.

plays an important role as it becomes optically active due to an extremely strong coupling to the plasmonic cavity mode (at rate g_c), which is able to dominate over the non-radiative Auger processes [384]. In contrast, the doubly charged state $|5\rangle$ is assumed to remain optically passive as Auger rates rapidly increase with the number of charges/excitations in the QD [459]. Crucially, occupation of this dark state at higher excitation powers yields a saturation of fluorescence. This kind of level representation for the neutral and charged states of a colloidal quantum dot has also been used in other studies [291, 460].

Taking into account all of the above, the density matrix of the composite system 'quantum dot plus resonator' evolves under the following master equation in Lindblad form

$$\dot{\rho} = -i[H_I, \rho] + \frac{1}{2}\sum_k (2L_k \rho L_k^\dagger - L_k^\dagger L_k \rho - \rho L_k^\dagger L_k), \tag{7.2}$$

where the interaction picture Hamiltonian is given by

$$H_I = \Delta_n |2\rangle\langle 2| + \Delta_c |4\rangle\langle 4| + g_n(a|2\rangle\langle 1| + a^\dagger |1\rangle\langle 2|) + g_c(a|4\rangle\langle 3| + a^\dagger |3\rangle\langle 4|) \tag{7.3}$$

and describes the coherent processes taking place in the system. The 'jump' operators L_k appearing in the master equation describe a variety of incoherent processes, which include pumping, incoherent energy transfer between the dot levels, as well as cavity loss, spontaneous emission, non-radiative Auger processes and dephasing. The following list describes the jump operators employed in the model, subdivided into categories.

- **Cavity leakage**, characterized by a total decay rate κ including both radiative and non-radiative contributions:

$$L_1 = \sqrt{\kappa} a \tag{7.4}$$

- **Dephasing.** This is assumed to affect all internal states of the dot and is characterized by a rate γ_D (for simplicity assumed to be the same for all affected levels).

$$\begin{aligned} L_{11} &= \sqrt{\gamma_D}|1\rangle\langle 1| \\ L_{12} &= \sqrt{\gamma_D}|2\rangle\langle 2| \\ L_{13} &= \sqrt{\gamma_D}|3\rangle\langle 3| \\ L_{14} &= \sqrt{\gamma_D}|4\rangle\langle 4| \\ L_{15} &= \sqrt{\gamma_D}|5\rangle\langle 5| \end{aligned} \tag{7.5}$$

- **Pumping of the quantum dot** at rate Λ:

$$\begin{aligned} L_2 &= \sqrt{(1-p_*)\Lambda}|2\rangle\langle 1| \\ L_3 &= \sqrt{(1-p_{**})\Lambda}|4\rangle\langle 3| \end{aligned} \tag{7.6}$$

  where p_* (p_{**}) is the probability that the pump contributes to charging (double charging) of the quantum dot, i.e. the probability that it drives the incoherent transition $|1\rangle \dashrightarrow 3\rangle$ ($|3\rangle \dashrightarrow |5\rangle$), as opposed to exciting of the optically active level $|2\rangle$ ($|4\rangle$).

- **Spontaneous emission decay** of the excited optically active states of the quantum dot into non-cavity modes at a rate Γ

$$\begin{aligned} L_4 &= \sqrt{\Gamma}|1\rangle\langle 2| \\ L_5 &= \sqrt{\Gamma}|3\rangle\langle 4| \end{aligned} \tag{7.7}$$

- **Non-radiative decay** of level 4:

$$L_{10} = \sqrt{\gamma_A}|3\rangle\langle 4| \tag{7.8}$$

  Where γ_A is a non-radiative decay rate associated with Auger processes.

- **Incoherent energy transfer** between charged and neutral states of the quantum dot:

$$\begin{aligned} L_6 &= \sqrt{p_*\Lambda + \Lambda_*}|3\rangle\langle 1| \\ L_7 &= \sqrt{p_{**}\Lambda + \Lambda_{**}}|5\rangle\langle 3| \\ L_8 &= \sqrt{\gamma_*}|1\rangle\langle 3| \\ L_9 &= \sqrt{\gamma_{**}}|3\rangle\langle 5| \end{aligned} \tag{7.9}$$

The mechanisms of the dynamic charging processes in CdSeTe/ZnS QDs are complex and the mean lifetime distribution of the various charged states have been found to exhibit a power law dependency [254]. This universal behavior has been subject to many studies to explain different experimental observations [259, 262, 277, 303]. The primary focus of this model are the steady-state spectra of the coupled system under cw-excitation rather than in the time evolution following pulsed excitation. A combination of pump-dependent and -independent rates are used to

account for different charging mechanisms. The parameters Λ_*, Λ_{**} and γ_*, γ_{**} are the spontaneous trapping and release rates, respectively, which account for the incoherent energy transfer between neutral and charged states of the dot, persisting even in absence of external pumping. These rates account for charging processes induced by hot electrons, which is a spontaneous process and therefore independent of the excitation rate [267, 301, 302, 348, 349]. External pumping is assumed to contribute to charging processes through the rates $p_*\Lambda$ and $p_{**}\Lambda$, which account for multi-exciton processes such as Auger ionization [251,269,286,291,296,461,462]. A detailed overview of the charging behavior of CdSeTe/ZnS nanocrystals can be found in chapter 3.

The fluorescence spectra are calculated according to equ. 2.51. It can be verified numerically (and it can be checked easily by a back-of the envelope calculation given the experimental parameters) that the inclusion of higher photon numbers would not bring about significant quantitative changes to the analysis. The combined system quantum dot + cavity is thus represented in a 10-dimensional Hilbert space.

The system spectrum is calculated through the well-known technique of *vectorization*: the density matrices and operators are mapped into vectors of length 100, while the superoperator $\mathscr{L}$ is converted into a 100×100 matrix. $(\mathscr{L} - i\omega I)^{-1}$ thus amounts to a standard matrix inversion, while trace operations are mapped as $\mathrm{Tr}[\mathrm{AB}] = \mathrm{vec}(\mathrm{A}^\intercal) \cdot \mathrm{vec}(\mathrm{B})$, where A, B are two generic operators and vec() indicates the vectorization operation.

7.3 Further Measurements

7.3.1 Anti-crossing and Saturation

Uncoupled CdSeTe/ZnS nanocrystals display a blueshift for higher excitation intensities as the contribution of biexcition emission increases [463]. This spectral shift also occurs for the QDs used in the present experiment and is shown in Fig. 7.6a for three different excitation intensities (6, 15 and 45 µW). Measurements on the reversibility of the blueshift are shown in appendix B.3.1. Under strong coupling conditions this blueshift causes an intensity-dependent detuning of the QD with respect to the PNR mode. Fig. 7.6b shows a series of normalized strong-coupling spectra for increasing excitation rate (bottom to top, see appendix B.3.2 for reversibility). The increasing detuning to higher energies causes characteristic changes of the amplitudes and shifts of the Rabi peaks. The quantum model (solid line) reproduces this behavior by changing the individual resonance energy of the neutral and the charged state while keeping the cavity resonance fixed. In Fig. 7.6c the peak energies is plotted for increasing pump rate (blueshift) for several QDs showing different tuning ranges. The red markers include the peak positions of the spectra in Fig. 7.4d. For comparison, the peak energies of the neutral and charged state (black and gray solid line, respectively) extracted from the quantum model are shown for varying detunings (dashed line) with respect to the PNR mode (dotted

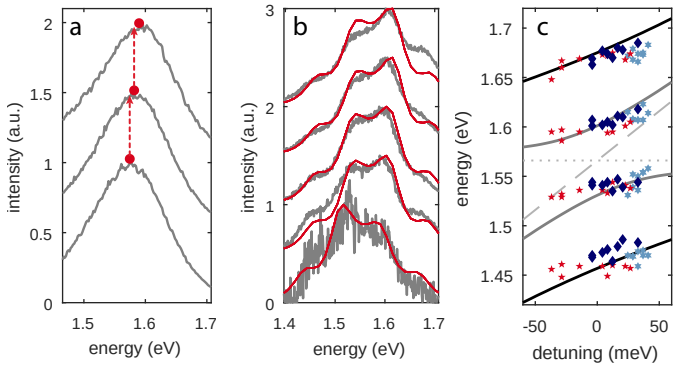

Figure 7.6 – QD detuning at high excitation rates. a, Fluorescence spectra of uncoupled QDs. With increasing excitation rate (bottom to top) the peak intensity indicates a blueshift. **b,** Spectra for increasing pump rate (gray lines, bottom to top) overlaid with calculated spectra (solid lines) for different detunings. **c,** Peak positions for a range of detunings induced by different excitation rates of three different QDs. The Rabi peak positions of the neutral (charged) QD state based on the quantum model are indicated by the solid black (gray) lines. The gray dashed (dotted) line indicates the QD (PNR) resonance.

line) demonstrating spectral anti-crossing of both QD states with the PNR spectrum - a well-known manifestation of strong coupling.

Another observation of the strongly coupled system is a fluorescence intensity saturation with increasing excitation rate. Figure 7.7 shows the saturation behavior of three different QDs coupled to the PNR as manifested in the dependence of the integrated spectra (marker) on the excitation rate (range 1 MHz to 20 GHz). It is noted that the saturation of the emission occurs for excitation rates in the GHz range, three orders of magnitude below the coupling rate. However, at those high excitation rates, the probability for multi-exciton generation increases significantly. Due to the rapid increase of Auger rates with the number of excited charge carriers multi-exciton states eventually become dark - even in the strong coupling regime [459]. It is this effective shelving into Auger-quenched dark states which is responsible for the observed saturation behavior. The inclusion of a non-radiative state in the quantum-optical model reproduces the saturation behavior (Fig. 7.7 solid lines) in good agreement with the experimentally measured data.

The high excitation rates with a photon energy much larger than the band gap causes a significant coupling to phonons due to non-resonant relaxation of the exciton (exciton cooling, see section 3.8). This heat generation can increases the QD temperature which might affect the population of the states near the band edge. However, a simple model has shown that the expected increase of temperature is less than 1 K and can therefore be neglected (see appendix A.8 for details).

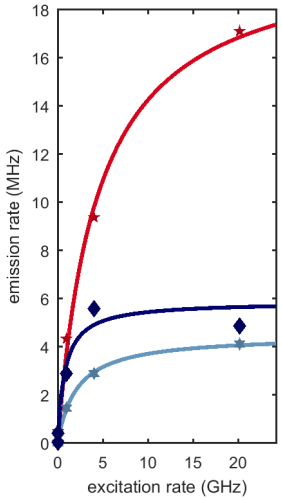

Figure 7.7 – Saturation of the strongly coupled system. Measured fluorescence saturation (markers) for different QDs in strong coupling conditions fitted according to the saturation behavior predicted by the quantum optical model (solid lines).

7.3.2 Exchanging the quantum dot

The experiments presented here highlight the ability of the scanning-probe setup to utilize a single PNR to probe a larger number of different QDs. If a particular PNR can achieve strong coupling for one QD, it is found that the majority of measured QDs also display strong coupling. Assuredly, the strong-coupling spectra of different single QDs obtained with the same PNR exhibit a qualitatively similar behavior. Nevertheless, fluctuations in coupling strength and detuning parameters are observed, owing to structural differences of the colloidal quantum dots as well as to their orientation with respect to the electric field polarization at the apex of the scanning probe.

The spectrum of the strongly coupled system can be significantly affected by the exciton resonance and the dipole moment of the QD. The measured spectrum of five different QDs are shown in Fig. 7.8 (open circles). The QDs are quickly approached consecutively in order to avoid a drift of the probe. All spectra are fitted with the quantum model (solid lines) and sorted by the detuning between exciton and cavity resonance.

While the highly asymmetric spectra are explained by a strong detuning, deviations in the coupling strengths can be observed as apparent from the variation of peak splitting. Both observations can be explained by variations in size and orientation of the chemically grown QDs. Furthermore, the fitting of the model shows also minor differences in the cavity resonance which can be attributed to a slight deformation of the PNR geometry while sliding over the substrate during the fast sequential QD approaches.

These findings underline that this scanning probe approach is readily capable of performing a characterization of individual QDs via strong-coupling spectroscopy

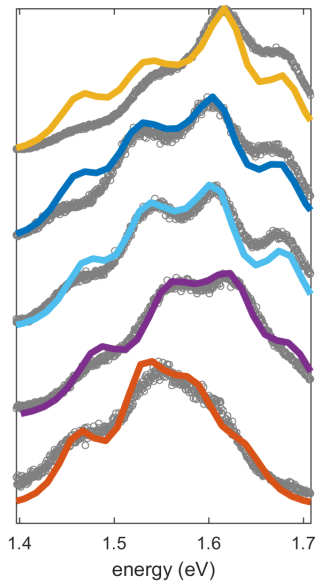

Figure 7.8 – Collection of spectra of five different QDs in strong coupling with the PNR. The measured spectra (open circles) are ordered by the detuning of the excitonic resonances. Each spectrum was fitted individually with the quantum optical model (solid lines). The coupling strength, detuning as well as the QD resonance can vary due to structural variations of the QDs (size, orientation).

at ambient conditions.

7.4 Coupling constant determination

Up until now the coupling rate g has been purely used as a fitting parameter. This section will focus on the numerical determination of the coupling strength via FDTD simulations and additional models and considerations.

To understand strong coupling of localized plasmons with colloidal QDs - which are normally not bestowed with the largest dipole matrix elements - it is necessary to focus in more detail on the coupling mechanism between quantum dots and the PNR at the scanning probe apex. The coupling strength as described in equ. 2.33, depends on the vacuum field strength and the related effective mode volume as well as the emitter's dipole moment. Before going into details about the coupling mechanism a brief overview is given with respect to the dipole moment and the mode volume.

Dipole moment considerations Regarding the dipole moment, colloidal quantum dots are known to exhibit a fine structure splitting due to their crystal lattice anisotropy and electron-hole interaction leading to eight different (partially degenerate) states near the band edge [456], with the lowest state usually being optically

dark (Fig. 7.9a top). As described in section 3.2, the lowest optically active state $\pm 1^L$ (f_{bright}) is thermally populated, determining the optical emission properties such as the resonance energy and excited state lifetime of uncoupled QDs [464]. The measured lifetime of 58 ± 4 ns (see section 6.1.5) corresponds, on the basis of the Weisskopf-Wigner approximation (equ. 2.24), to an electric dipole moment of 5 D. However, since the plasmon resonance width $\Delta\omega$ is larger than the total fine structure splitting Δ it can interact with all band edge states f_{k} simultaneously (Fig. 7.9a bottom) some of which are also reported to exhibit larger transition oscillator strengths than f_{bright} [246, 434]. As can be seen in the measurement, the slight asymmetry of the spectra in Fig. 7.4d is attributed to a blue shift of the QD emission when entering the strong coupling regime. This indicates the transition from pure emission of the lowest optically active state at the band edge to the blue shifted effective contribution of all available states f_{k}. Additionally, the near-field intensity close to the tip shows a significant gradient of one order of magnitude over length scales of the QD dimensions. In combination with a non-spherical QD shape the plasmonic mode is therefore expected to also couple to multipolar transitions [465–473]. A quantum-optical model which incorporates a non-degenerate multi-level emitter strongly coupled with a broadband resonator which will be fully introduced later on (see section 7.4.1) explains and quantifies this boost of coupling strength due to collective coupling to band-edge states. Indeed, the importance of the fine structure in cQED experiments has been recently studied in photonic crystal cavities [474] and the boost of the coupling constant is expected to be even more effective in plasmonic cavities due to a spectral width which is orders of magnitude larger. The quantum model shows that the coupling strength is effectively tripled by collective coupling of eight active transitions at the band-edge, veritably revealing the full potential of colloidal quantum dots as excitonic material for strong light-matter interaction.

Mode volume considerations In addition to the QD dipole moment, the evaluation of the vacuum field strength also requires a thorough study. In the dipole approximation the coupling rate as described in equ. 2.33 is proportional to the vacuum field strength which depends on the mode volume V. The mode volume of plasmonic quasi-normal modes (QNM) is calculated as an effective mode volume via equ. 2.47. FDTD simulations based on quasi-normal modes take into account the local field factor [92] by including a spherical semiconductor particle to mimic the QD interaction with the PNR. As will be shown in section 7.4.2, the coupling strength maps exhibit large variations of $g(r)$ especially in close proximity to and also inside the semiconductor particle. This observation demonstrates that due to the finite QD size, determination of the coupling rate in the dipole approximation via equ. 2.33 is no longer applicable. It also strengthens the assumption that multipolar transitions and therefore all fine structure states f_{k} are optically accessible. The occurrence of a hot spot between the semiconductor particle and the gold already indicates the importance of short-ranged influential confinement effects [101] even in absence of a QD exciton. One can therefore argue that due to a strong, distance-

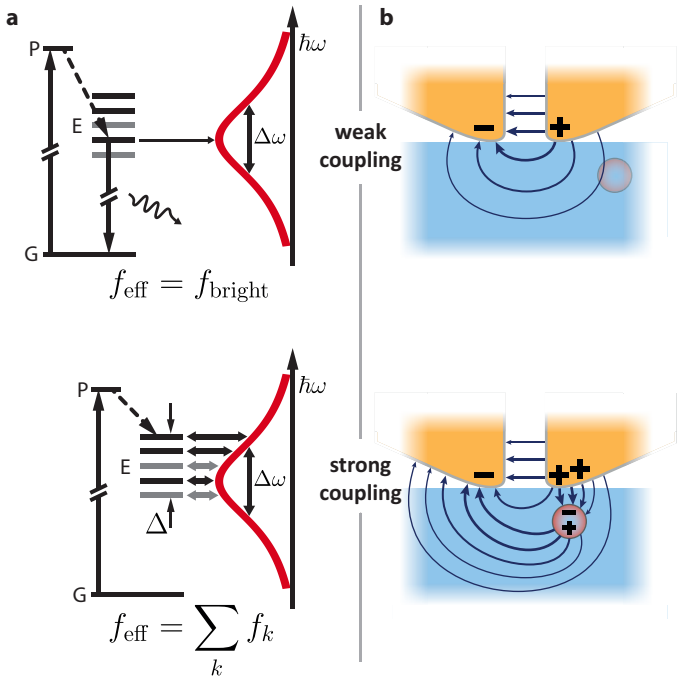

Figure 7.9 – QD near-field coupling. a, Diagram of energy levels of a CdSeTe/ZnS nanocrystal weakly coupled (top) and strongly coupled to a nanoresonator (bottom). Fine-structure splitting into bright (black lines) and dark states (gray lines). Incoherent excitation at $\lambda_{\text{ex}} = 532\,\text{nm}$ from the ground state G into a pump state P and subsequent relaxation to the band edge E. **b,** (top) Sketch of the near-field distribution at the apex of the nanoresonator (pure mode). (bottom) Strongly coupled mesoscopic emitter influences the pure mode field via near-field proximity interaction (influential and image charging).

dependent polarization of the metal surface for resonant interaction, the electric field and the (mesoscopic) QD can no longer be treated as independent entities if the emitter is in close proximity to the PNR (Fig. 7.9b). This is clearly important in experiments with plasmons, but also of general significance. The role of near-field proximity enhanced coupling can be demonstrated for a system of two coupled gold nano rods exhibiting classical mode splitting. A comprehensive study on this topic is given in section 7.4.3. The occurrence of such near-field proximity coupling consequently challenges the applicability of the standard dipolar strong-coupling formalism of cavity quantum electrodynamics which assumes that the mode field and the related effective mode volume can be determined independently and, in particular, in absence of the emitter.

7.4.1 Fine structure model

As it was briefly introduced above, plasmon resonances are much broader than the separation of individual exciton states near the band edge of colloidal quantum dots. In this section it is shown how, at the experimental conditions in this work, a multiplet of closely spaced excited sublevels may be well approximated by a single effective energy level, featuring an enhanced coherent coupling to the cavity field.

This coupling-enhancement effect is analogous to what occurs in the well-known phenomenon of 'Dicke superradiance', with the important difference that in the latter case one considers N identical emitters coherently coupled to the same field, as opposed to the case of N (approximately) degenerate levels of a single emitter [475, 476]. A recent theoretical study explored the case of two detuned orthogonal dipole moments strongly coupled to a photonic crystal [474].

For the purpose of this section the focus is kept on modeling the $|1\rangle \leftrightarrow |2\rangle$ transition of the quantum dot and the associated coupling to the cavity. A straightforward, yet cumbersome, extension of the model below may be devised to include the $|3\rangle \leftrightarrow |4\rangle$ transition, but such generalization is here omitted for brevity. In the original basis, the electronic ground state of the emitter is labeled as $|1\rangle$, while state $|2\rangle$ is now replaced by a collection of N sublevels $|e_k\rangle$, where $k = 1, ..., N$. An illustration of this level scheme is shown in Fig. 7.10a. For simplicity, each transition $|1\rangle \leftrightarrow |e_k\rangle$ is coupled to the cavity mode with the same strength g, the extension to different coupling constants being straightforward. It is emphasized that some of the considered transitions may be dipole-forbidden (e.g. some may be quadrupole-allowed), yet they could be activated by strong spatial gradients in the resonator's near-field [465–472]. As before, it is assumed that the cavity resonance has a central frequency ω_0, while the energy of the ground state $|1\rangle$ can be set to zero without loss of generality. Each sublevel $|e_k\rangle$ is characterized by a transition frequency $\omega_0 + \Delta_k$, where Δ_k is the detuning with respect to the cavity field. The coherent interaction between emitter and field is described by the following 'microscopic' Hamiltonian (recall that $\hbar = 1$):

$$H_{\mathrm{mic}} = \omega_0 a^\dagger a + \sum_{k=1}^{N} (\omega_0 + \Delta_k)|e_k\rangle\langle e_k| + \sum_{k=1}^{N} g(a|e_k\rangle\langle 1| + a^\dagger|1\rangle\langle e_k|). \qquad (7.10)$$

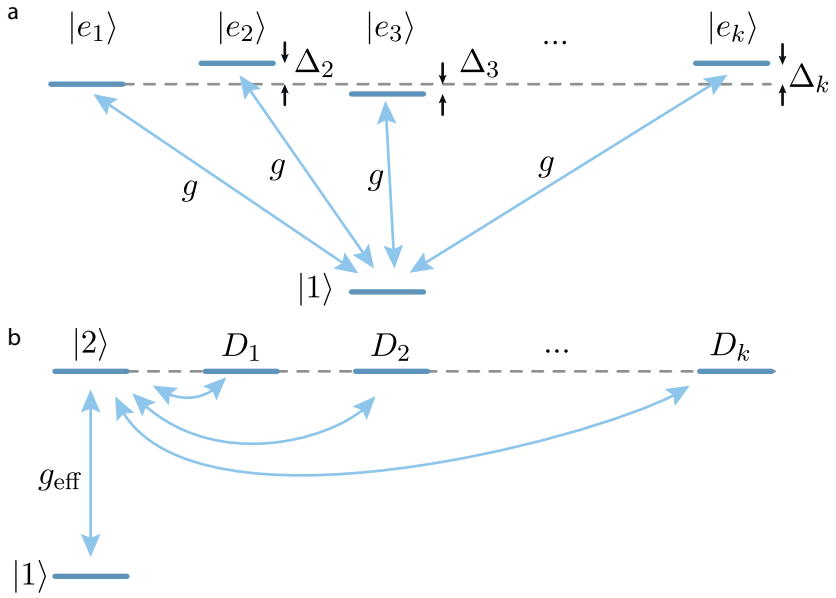

Figure 7.10 – Illustration of the change of basis and the occurrence of an effective coupling constant between the cavity and the multi-level system. a, Original basis: Detuned sublevels $|e_k\rangle$ and the ground state $|1\rangle$ couple to the cavity with a coupling strength g. **b,** Collective excitation basis: The cavity couples via an effective coupling strength g_{eff} to the transition $|1\rangle \leftrightarrow |2\rangle$. Additional dark states D_k can only interact weakly with level $|2\rangle$.

It is noted that if the sublevels were exactly degenerate, that is $\Delta_k = \Delta$ for all k, one could define $|2\rangle = \frac{1}{\sqrt{N}} \sum_{k=1}^{N} |e_k\rangle$ as the only linear combination of sublevels that couples to the cavity field, with an effective, and enhanced, coupling constant $g_{\text{eff}} = \sqrt{N} g$. In such highly symmetric conditions, all other combinations of the sublevels would not contribute to the optical response of the system. One could hence simplify the quantum dot description by only retaining the internal levels $|1\rangle$ and $|2\rangle$, coupled to the cavity via an effective Jaynes-Cummings Hamiltonian

$$H_{\text{eff}} = \omega_0 a^\dagger a + (\omega_0 + \Delta)|2\rangle\langle 2| + g_{\text{eff}}(a|2\rangle\langle 1| + a^\dagger|1\rangle\langle 2|). \tag{7.11}$$

The change of the basis is illustrated in Fig. 7.10b, where the transition $|1\rangle \leftrightarrow |2\rangle$ is the only bright transition. Additional dark states D_k which originate from the sublevels are able to interact with state $|2\rangle$. In case of complete degeneracy of all sublevels, this interaction is zero. It is important to note, that these dark states are neither related to quadrupole transitions nor to the 'off' state of colloidal quantum dots. The interaction between level $|2\rangle$ and the dark states can lead to additional peaks in the spectrum in case of significant detuning. However, in this work the detuning remains small compared to the width of the plasmon resonance and therefore the impact on the spectrum of the interaction $|2\rangle \leftrightarrow |D_k\rangle$ remains negligible.

In the experiment, the sublevels $|e_k\rangle$ are not exactly degenerate and may feature different detunings Δ_k in the range of 10 meV. Yet, the estimated detuning range is one order of magnitude smaller than the effective coupling constant g_{eff}, while

the presence of dephasing processes tends to broaden the sublevels and increase their spectral overlap. Hence, it is now shown that the effective Hamiltonian H_{eff} still provides a sufficiently good approximation for this purposes. Figure 7.11a-h compares the cavity emission spectra predicted by the two Hamiltonians H_{mic} and H_{eff} (for the latter $\Delta = \sum_k \Delta_k/N$ is fixed, i.e. the average detuning of the sublevels). Spectral calculations relate to the master equation techniques described in section 7.2, including in both cases the cavity decay at rate κ, as well as the dephasing of all excited sublevels at rate γ_d. Two pump terms of the form $\sqrt{\Lambda}|e_n\rangle\langle 1|$ ($\sqrt{\Lambda}|2\rangle\langle 1|$) are included for the H_{mic} (H_{eff}) case. The pumping populates the state $|e_n\rangle$, which is the highest state of the fine structure.

This is in accordance with the experiment where high energy excitons are created which undergo relaxation until they reach the upper level of the fine structure. In the case of a single level with coupling strength $g = 36\,\text{meV}$ (Fig. 7.11a), the cavity (orange line) and the exciton (black line) are on resonance ($\Delta_1 = 0\,\text{meV}$). The corresponding spectra calculated with the two Hamiltonians H_{mic} and H_{eff} (blue solid and red dashed line, respectively) yield exactly the same result ($\kappa = 78\,\text{meV}$, $\gamma_d = 57\,\text{meV}$). The system is on the verge to strong coupling as the Rabi splitting is already visible ($g_{\text{eff}} = g = 36\,\text{meV}$). Adding an additional level with the same coupling strength g ($\Delta_2 = 1.25\,\text{meV}$) shows an increase in total coupling strength as indicated in Fig. 7.11b.

Since the highest level is blueshifted with respect to the cavity, the resulting spectrum calculated with H_{mic} exhibits an asymmetry. It is noted that this system, as any SC system, is quite sensitive to the channel via which the energy is introduced [102]. The observed symmetry can flip if the pumping of the system is not carried out via the highest level of the fine structure. The spectrum with the Hamiltonian H_{eff} represents the case with a single transition is on resonance with an effective coupling strength of $g_{\text{eff}} = \sqrt{2}g$. Including up to eight levels (Fig. 7.11h) shows an increasing separation of the two Rabi peaks while maintaining exceptional good agreement between the two models. Notice how the pumping of the highest fine structure level yields a small asymmetry in the spectrum associated with H_{mic}, but the difference between the spectra predicted by the two models is hard to appreciate. The comparison between the two models clearly shows how the fine structure of quantum dots can contribute to the coupling of broadband plasmon resonances by boosting the coupling strength via an effective oscillator strength $f_{\text{eff}} = \sum_k f_k$.

Figure 7.11i-p also shows how the superposition of two independent multilevel systems evolves as the coupling strength is increased by adding additional levels. This case relates to the experiment where two QD states with different coupling strength are strongly coupled with the cavity. In Fig. 7.11i the superposition (purple solid line) of two strongly coupled systems is shown with a coupling strength of $g_1 = 36\,\text{meV}$ (gray dashed line) and $g_2 = 13\,\text{meV}$ (black dashed line) each containing a single excited state. Adding additional states (Fig. 7.11j-k) increases the effective coupling strength and shows the transition into a four peaked spectrum with a slight amplitude asymmetry.

This section has shown theoretically that the dipole moment, and therefore the

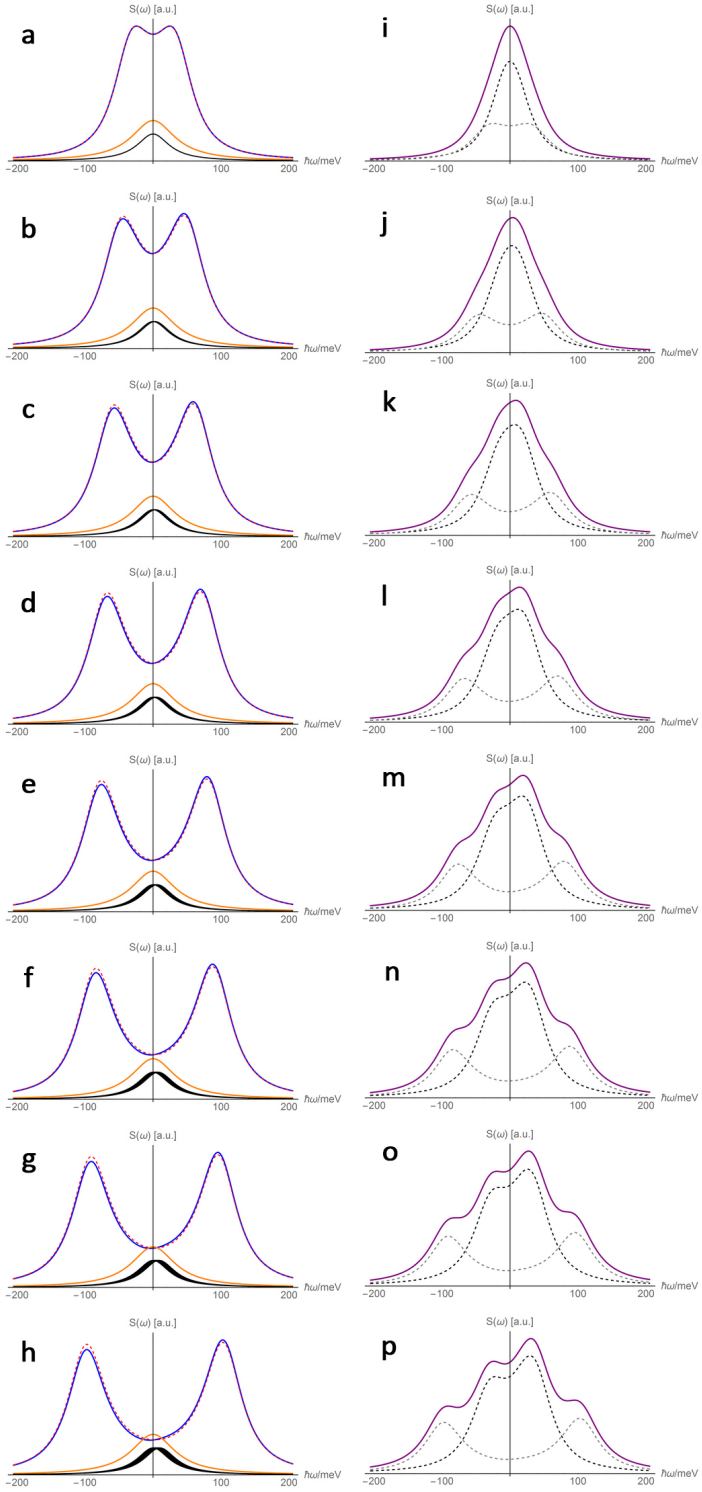

Figure 7.11 – Collective coupling of a multi-level emitter with a resonant cavity. a-h, The plasmon resonance (orange line) couples with one (**a**) to eight (**h**) levels (black lines). The corresponding coupled spectrum (blue line) calculated with H_{mic} indicates the transition into two symmetric Rabi peaks. The coupled spectrum calculated via H_{eff} (red dashed line) yields similar results. **i-p,** Superposition of two multi-level systems with coupling strength g_1 and g_2. Increasing the number of levels from one (**i**) to eight (**p**) shows the transition into a four peaked spectrum.

coupling strength, can effectively be tripled due to the contribution of additional band-edge states via coherent interaction.

7.4.2 In the dipole approximation

The coupling energy $\mathscr{E}(r)$ between a (point) dipole μ at position r and the electric field is defined by equ. 2.33 via the effective mode volume $V_{\text{eff}}(r)$ which has a minimum at the location of the field maximum. In case of strong interaction, the absorption and emission process of the emitter locally modifies the field distribution of the resonant mode. Since the physical dimensions of emitter and nanoresonator in the experiment differ only by one order of magnitude, the field distribution and excitonic wavefunctions within the quantum dot should, in principle, be considered to obtain accurate values for the coupling energies. Unfortunately, such a description would require detailed knowledge of shape, material composition and electronic wavefunctions of the QDs. In this section, the emitter is treated as a point dipole in order to obtain an estimate for the coupling rate. Based on this assumption and the calculated mode field distribution it is possible to determine the coupling constant for every position of the emitter. The physical volume of the PNR slit ($265 \times 12 \times 30\,\text{nm}$) yields a value of about 10^{-22}m^3, which overestimates the effective mode volume since this corresponds to a mode with a homogeneously distributed electric field throughout the resonator.

To obtain a more accurate result the electric field and the effective mode volume is determined based on the quasi-normal mode approach described in section 2.3.4. The fields E and H are the fields of the resonant QNM of the cavity, which are determined numerically using FDTD simulations by excitation with a Gaussian source. Values for the onset and width of the temporal window function were used according to Ge et al. [174] and perfectly matched layers (PML) boundary conditions were used to suppress back reflection of out-going radiative fields. An important aspect when simulating QNMs is the use of a homogeneous mesh. Introducing a refined mesh at the apex of the PNR reduces the local electric field amplitude which yields erroneous effective mode volumes. Convergence of the effective mode volume was obtained at a global mesh size of 0.6 nm in accordance with a recent study [13] which showed similar results.

This section focuses on the properties of the 2nd order resonance of the PNR. A comparison with the 3rd order mode is discussed in appendix A.6. The FDTD calculations include the QD as a dielectric sphere with a refractive index of 2.7 in order to account for the local field factor. This presence of a dielectric medium increases the local electric field and leads to a mode volume concentration [92]. The effect is shown in Fig. 7.12a where the effective mode volume of the PNR is shown with a logarithmic scale. Details on the determination of the energy density in equ. 2.46 is described in appendix A.5. Within the QD sphere the mode volume is reduced by almost two orders of magnitude. Figure 7.12b shows a map of the corresponding coupling energy $g(r)$ for a dipole moment of 15 D which is the effective dipole moment as calculated in section 7.4.1. The coupling strength can reach values on

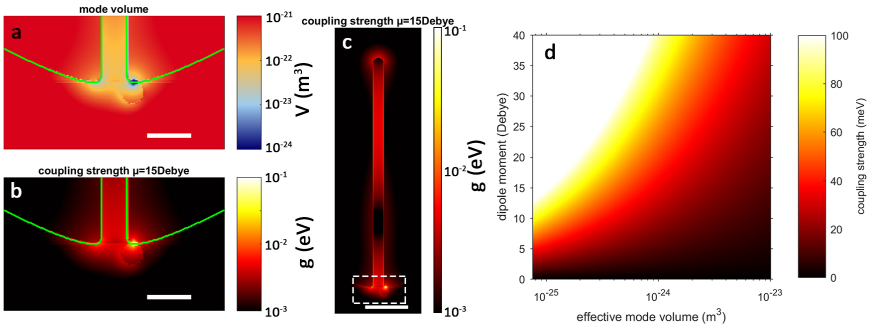

Figure 7.12 – Calculating the coupling strength. **a,** Effective mode volume at the apex of the tip. The mode volume is drastically concentrated within the quantum dot due to the increased refractive index. **b,** Map of the coupling strength $g(r)$ with a QD modeled as a dielectric sphere near the PNR apex. Scale bar 20 nm. c, Overall coupling strength of the PNR (white dashed rectangle marks the region of interest in **b**). Scale bar: 50 nm. **d,** Coupling strength as a function of mode volume and dipole moment.

the order of 100 meV in accordance with the measurements. The coupling energy of the complete PNR is shown in Fig. 7.12c (the dashed rectangle marks the region depicted in Fig. 7.12a,b). Figure 7.12d shows the coupling strength as a function of the mode volume and the dipole moment. These results indicate that for strong coupling with single transitions having dipole moments of 5 D extremely small mode volumes would be necessary. It can be concluded that additional states at the band edge of the quantum dot are necessary in order to boost the coupling strength as shown by the detailed theoretical analysis presented in section 7.4.1.

It is important to note that the presented description of the mode volume is still an approximation as an unambiguous extraction of a single value is not possible. Furthermore, the calculation of QNMs does not account for the excitonic nature of the emitter. For single point-like emitters, such as dye molecules, the dipole approximation holds and the mode volume calculation at the location of the emitter allows to determine the coupling strength. An experimental confirmation was realized recently for the first time by Chikkaraddy et al. [13]. For mesoscopic emitters, however, where the emitter's size becomes comparable to the spatial extension of the resonant field, the mode volume calculation becomes more complex.

There are currently only two experimental studies on the coupling of localized plasmons of individual nano structures with single nanocrystals [84, 122]. In the work of Hartsfield et al. the authors model the QD via a polarizable sphere with a largely overestimated dipole moment of 50 D in order to explain the changes to the scattering spectrum. Further information about the mode volume of the localized plasmon and how it is influenced by the quantum emitter has not been provided. Santhosh et al. presented a map of the calculated coupling strength at the gap region of a bowtie nano antenna reaching values of up to 200 meV without any dielectric material to represent the QD. However, with the approach used in this work to calculate the coupling strength it is not possible to reproduce these results. In fact, for

a silver bowtie antenna with the same dimensions the effective mode volume is on the order of $10^{-22}\mathrm{m}^3$ in the gap region which, in combination with a reasonable QD dipole moment, yields a coupling strength far below 200 meV (see Fig. 7.12 d). The reason for this discrepancy might be due to differences in the field distribution between the results of the BEM calculations by Santhosh et al. and FDTD calculations used in this work. In addition, their formalism to calculate the QNMs is based on the work of Koenderink [477] whereas here the approach of Sauvan et al. is used.

Those recent advances in experimental realization of coupling single mesoscopic emitters with plasmonic resonances uncovers the challenge to unambiguously quantify the coupling rate. The implicit assumption that the plasmon mode distribution is maintained during strong coupling with a QD within the near field likely does not reflect the correct picture. Section 7.4.3 shows how the current formalism underestimates the coupling rate in case of a polarizable particle in close proximity to a near-field resonance.

A more general overview on how the mode volume and decay rate of a PNR compares to other well-established nanoantennas is demonstrated in detail in appendix A.7. It is found that other structures, such as the bowtie antenna, can achieve even smaller mode volumes for similar geometric feature sizes. However, the performance of a bowtie in other crucial aspects, such as Q-factor and field accessibility, are worse than a PNR. This first comprehensive analysis for a variety of nanoantennas establishes a new benchmark on how to evaluate and compare different kind of structures. However, it is also not clear yet what kind of figure-of-merit is required in order to quantify the performance of a structure in terms of light-matter interaction. Future numerical studies and understanding of the coupling mechanism will provide more answers to find the ideal plasmonic structure.

7.4.3 Near-field proximity

The calculation of the mode volume is, as discussed in the previous section, based on the unperturbed electric field distribution of the PNR. However, in strong coupling of the mode with an excitonic material two hybridized modes emerge and further analysis based on the original uncoupled modes tend to be of limited validity [95]. This section demonstrates that it is to be expected that the original near-field distribution of the mode is modified due to near-field proximity coupling with the polarized QD.

To demonstrate this effect, the well-established strong coupling and associated mode hybridization of two interacting gold nanorods (length 120 nm, diameter 30 nm) is revisited. The resulting coupled modes of this nanorod dimer and other compositions is a standard example to illustrate strong coupling between localized surface plasmons as demonstrated in many studies [425, 478–483]. The qualitative evolution of the hybridized modes can be explained via two coupled classical harmonic oscillators [90, 484]. However, a quantitative analysis of non-trivial geometries requires detailed FDTD simulations in order to account for the shape of the metal

particles.

The simplest formalism of light matter coupling also follows the approach of two coupled harmonic oscillators as it is shown in section 2.3. It provides a quantitative description on how electric fields can interact with electric dipoles. In the following, this formalism adopted to study the interaction between to localized plasmon fields.

To determine the coupling strength between two nanorods one may calculate the electric near-field distribution $E_{\mathrm{A},0}(r)$ for nanorod A in absence of any excitation (vacuum field). A dipole moment μ_{B} is assigned to a second nanorod B based on its absorption cross-section on the order of $10^{-10}\mathrm{cm}^2$ via equ. 2.13. The resulting calculated coupling strength $g_{\mathrm{AB}} = \mu_{\mathrm{B}} \cdot E_{\mathrm{A},0}(r)$ only describes the observed mode splitting correctly as long as the rods are well separated and maintain a mutually unperturbed near field. Figure 7.13a shows the corresponding map of the coupling strength g_{AB} between nanorod A and a point dipole μ_{B} for various positions. A line cut across nanorod A is shown in Fig. 7.13b (dark blue line).

With increasing distance x the coupling strength decreases proportional to the vacuum field of the mode. The horizontal line (light blue) marks the spectral width of the far-field spectrum of the rod $\kappa_{\mathrm{rod}} = 64\,\mathrm{meV}$. The condition for strong coupling is $g_{\mathrm{AB}} = \Omega/2 > \kappa_{\mathrm{rod}}$, where Ω denotes the Rabi splitting of the peaks in the strongly coupled system. FDTD simulations carried out for discrete nanorod separations (center-center) are used to obtain the actual coupling strength $\Omega/2$ as a function of gap size (see Fig. 7.13b, open circles) by fitting the resulting near-field spectra using two Gaussians.

For large separation ($x = 200\,\mathrm{nm}$) nanorod A is only slightly influenced by nanorod B resulting in a coupling strength $g_{\mathrm{AB}} = 9\,\mathrm{meV}$. The near-field distribution of the two rods is shown in Fig. 7.13c and still roughly represents the superposition of two single-nanorod field distributions. Yet, the corresponding near-field spectrum (Fig. 7.13d, blue line) already shows a deviation from the near-field spectrum of the isolated nanorod A (red line). The extracted splitting corresponds to a coupling strength of 25 meV, which is still in the weak-coupling regime. In close proximity (nanorod separation 130 nm) the near-field distribution is drastically changed and strongly deviates from just the sum of the fields of two isolated nanorods (see Fig. 7.13e). Due to near-field proximity coupling, the influential charge accumulation in the nanorod ends close to the gap, the near-field intensity in the gap is greatly enhanced. The original field distribution $E_{\mathrm{A},0}(r)$ is not maintained and therefore the definition of the coupling strength g_{AB} does not apply anymore. The calculated coupling strength of 28 meV is much smaller than the actual coupling strength of the hybridized mode of $\Omega/2 = 124\,\mathrm{meV}$ (see Fig. 7.13f). Note that the actual mode overlap between the two rods is rather small as they approach each other end-to-end, which nonetheless can lead to an increased electric field inside the gap. As the coupling strength reaches the strong coupling condition in Fig. 7.13b, the calculated coupling strength g_{AB} significantly underestimates the actual coupling strength because near-field proximity coupling is not taken into account.

This near-field proximity effect also affects the resulting coupling strength in the case of a PNR interacting with a mesoscopic quantum dot. In case of the PNR used

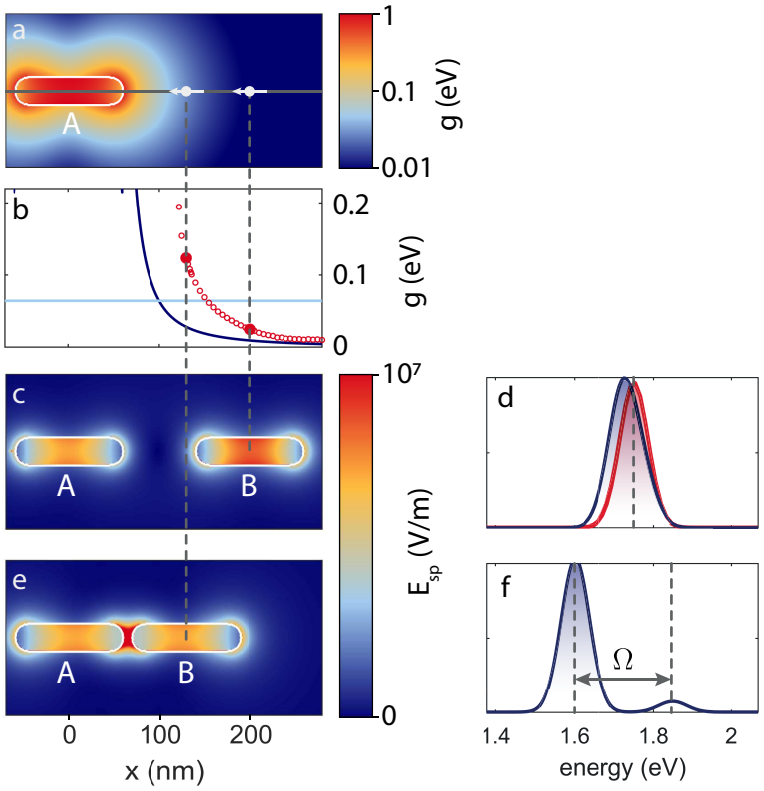

Figure 7.13 – Near-field proximity coupling. **a,** Coupling strength map between a single gold nanorod and a point dipole $\mu_B = 4000\,\mathrm{D}$. **b,** Line-cut of the coupling constant (dark blue line) in **a** along the longitudinal axis of nanorod A. The open circles indicate the coupling strength extracted from FDTD simulations. The horizontal light blue line shows the near-field spectral width κ_{rod} of a single nano rod. **c,** Vacuum field distribution of two rods (gap size 80 nm). **d,** Near-field spectrum (at 1.6 eV) of a single isolated gold nanorod (red) and two coupled gold nanorods with a gap size of 80 nm (blue). **e,** Electric field distribution of two hybridized nanorod modes (gap size 10 nm). **f,** Near-field spectrum of the mode shown in **e**. The resonance is shifted by 149 meV.

in the experiment and a resonant quantum dot the situation is equivalent as the QD cannot be approximated as a point-dipole. In the far-field the coupling is described via the dipole moment of the quantum dot and the electric field distribution of the PNR. However, when the mesoscopic QD approaches the near-field gradient of the nanorod the hybridization into two modes has an impact on the initial field distribution. In fact, the position outside the gap of the PNR might be even more desirable to impact the initial field distribution.

Thus, the mutual interaction between the mode and the emitter sets a limit to the validity of the usual coupling strength calculation via the plasmonic mode volume. However, as the field in between the emitter and the plasmonic structure is expected to increase with proximity, the current approach most likely to underestimate the coupling strength. It is therefore possible to argue that the calculated coupling strength in the configuration of the experiment as depicted in Fig. 7.12b matches the measurement only in the upper half of the QD sphere as a result of the neglected QD polarizability. Also, this section has shown how the formalism of light-matter coupling can be used to predict the hybridization between two localized surface plasmon resonances.

7.5 Conclusion

Strong coupling of a scanning plasmonic nanoresonator probe to a single semiconductor QD has been demonstrated at ambient conditions. This creates possibility to deliberately undergo the transition into (and out of) the strong coupling regime for any chosen QD in range. A hierarchy of quantum models accurately predicts the strong coupling dynamics as well as the resulting spectral response. Detailed analysis of the plasmonic field and the electronic structure of the semiconductor nanocrystal challenges the current understanding of strong coupling. In particular, the identification of collective coupling of a band-edge multiplet of states provides a novel formula to achieve single-emitter strong coupling. The revealed near-field proximity coupling requires a reconsideration of the direct applicability of standard strong-coupling theory in dipole approximation to plasmonic nanoresonators.

In future experiments additional confinement can be achieved by introducing a metal interface below the quantum dots as illustrated in Fig. 7.14a. By preparing a layer of quantum dots on a glass substrate with gold flakes it is possible to induce field enhancement due to the presence of the metal interface. Preliminary FDTD simulations have shown that the near-field distribution is indeed affected as shown in Fig. 7.14b.

Advances in nano-fabrication, such as helium-ion milling, will help to further reduce the width of the nanoslits well below 10 nm which may lead to the development of polaritonic devices and eventually facilitates the observation of ultra-strong coupling. The direct applicability of the presented methodology to any 0D, 1D and 2D quantum system promises a vast impact on the investigation of light-matter interaction on the nanometer scale.

Future experiment on the PNR-QD system will also allow to directly measure

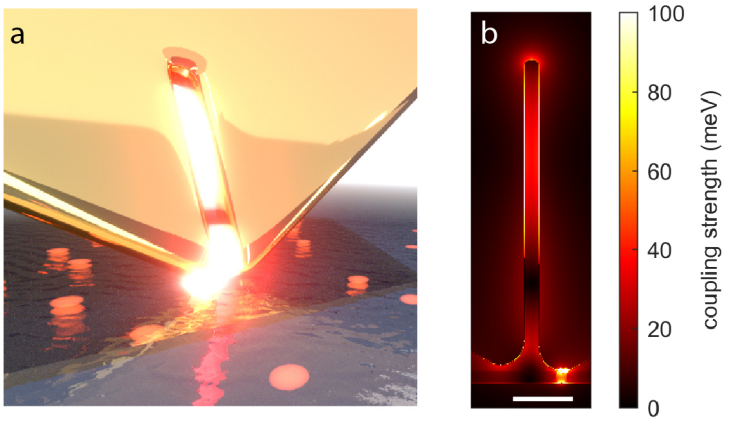

Figure 7.14 – Enhanced light-matter coupling via a metallic substrate. a, Artistic representation of a PNR scanning probe coupling to a quantum dot on top of a gold flake. **b,** Coupling strength calculations demonstrate the enhanced confinement due to the additional metal surface below the quantum dot.

Rabi oscillation in the time domain. By employing a pump-probe measurement scheme it is possible to reveal the non-exponential population decay of fs-dynamics [485]. Up until now, this type of experiment has been restricted to propagating surface plasmon strongly coupled to J-aggregates [106]. Observation of Rabi oscillations with a localized plasmon and a single emitter will provide further insights towards the realization of an all-optical switching device [105, 486–488].

8

Scanning microtubules for high resolution microscopy

The interaction between plasmonic near fields and single emitters, such as quantum dots, is a fundamental field of research. In previous chapters in this work it has been shown how resonant and non-resonant coupling affects the emission properties of quantum emitters. Experimental studies with a precise distance dependent investigation on how plasmonic near fields affect the emission properties of quantum emitter are scarce. Therefore, deep insights into this coupling mechanism is of valuable interest for applications where quantum emitters are used as a probe to detect and map the performance of optical near fields.

This section demonstrates how a biological transport machinery is capable of transporting individual quantum emitters across a nanostructured gold surface at a distances as close as 15 nm. The modification in fluorescence intensity yields vital information about the surface structure as well as the optical performance. Here, the self-propelling properties of microtubules on a functionalized surface are exploited to carry single quantum dots. This unique method facilitates a parallel scanning of a large array of quantum emitters across a surface which can be optically tracked in a similar fashion to any other wide field high-resolution microscopy technique such as STORM [489, 490] or PALM [491, 492].

The constant and predictable movement of the microtubules can be exploited in order to significantly enhance the localization accuracy of a single quantum emitter. The precision of a single localization fit is around 30 nm which is comparable to other high resolution techniques and ultimately limited by the amount of collected photons. When taking into account the linear motion of the QDs along the microtubules path the localization accuracy of the quantum emitter for each image drops below 5 nm.

This technique is especially of interest for mapping the near-field of plasmonic nanostructures due a minimum occurrence of localization artifacts. The coupling with plasmons can lead to a spatial shift of the location of light emission due to the propagation properties of surface plasmons. Most sub-diffraction microscopy techniques are based on the diffusion mechanism which propels a single molecule

[422]. It is therefore challenging to distinguish between the random motion of the molecule and an altered emission characteristic.

Being able to apply the microtubule transport system to a variety of substrates with a straightforward recipe renders this technique attractive for high-resolution microscopy of large arrays of nano-structures and meta surfaces [493, 494]. One specific goal of this method is eventually to be able to deliberately move a single quantum dot into close proximity of a resonant near-field and investigate the coupling between emitter and plasmon. This approach is reversed to the scanning probe method shown in chapter 6 and 7 since the emitter is mobile and the near-field is stationary on the substrate.

This chapter begins with an introduction into the field of mapping optical near fields via single molecule imaging. As a figure of merit the power of this method is demonstrated via localization measurements of a nano-slit array on a gold surface. These measurements are then supported by a fluorescence model based on numerical simulations. Large text parts as well as figures of this chapter are adopted from Groß et al [495].

8.1 General idea

The challenge of probing the local optical near-field of a nanostructure consists in converting its evanescent near-field into modes that can propagate to the far-field. In this regard, a single emitter constitutes a superior probe because it responds to the near-field modes of a nanostructure via both the local intensity and the zero-point fluctuations described by the local density of optical states (see section 2.2). The position-dependent coupling of the emitter to the nanostructure thereby leads to changes in the excitation rate as well as the excited-state lifetime. The resulting modulation of the emission rate (i.e. the Purcell enhancement and change in angular emission pattern) is proportional to the resonant near-field intensity of the nanostructure. Importantly, its small oscillator strength ensures a negligible impact of the emitter on the resonant-field distribution of the nanostructure (weak coupling).

Previously, diffusing single molecules in aqueous solution have been used as probes for a spatially-resolved local field mapping of the Purcell enhancement [422, 496, 497]. However, a recent study [83] clarified that such an endeavor is limited by the uncertainty of the exact location of the emitter which cannot be estimated by single-particle tracking methods due to coupling with the nanostructure (further on referred to as 'localization artefacts'). Surface-enhanced Raman scattering has also been used recently to observe a spatial offset between the localized fields and the center of mass of the plasmonic particle. More deterministic results can be obtained by scanning a fluorescent particle [498] and even a single molecule [499] or single N-V center [500] attached to a scanning tip. Such measurements, however, are inherently slow and suffer from the influence of the scanning tip on the local near field. An elegant approach to avoid such perturbations consists in controlling the emitter position by microfluidic flow [421], but this approach is limited in terms of scalability and accuracy of the position.

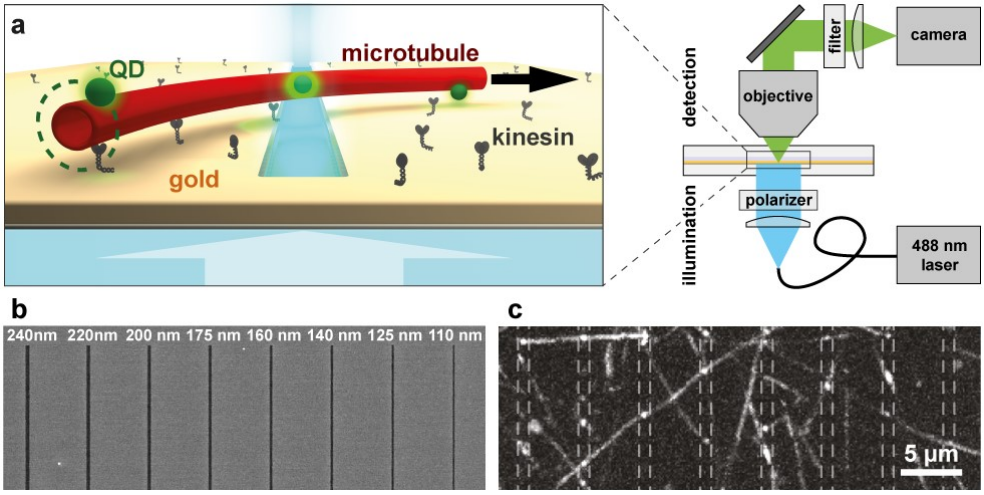

Figure 8.1 – Using biomolecular motors and microtubules to scan individual QDs across gold nanoslits. a, Schematic diagram of the setup: QDs are randomly attached to microtubules which are propelled across the sample by surface-bound kinesin-1 motors. The sample is illuminated by collimated laser light (488 nm, polarization along the long axis of the nanoslit) from below and the fluorescence signal is collected from above by a fluorescence microscope equipped with an EMCCD camera. Changes in the near-field interaction of the QDs with the gold nanoslits are detected in the far-field as spatially varying fluorescence intensities. **b,** SEM image of the investigated nanoslits with indicated widths in a 25 nm thick gold layer. **c,** Maximum-intensity projection of QDs being transported across the nanostructured sample depicted in **b**. The grey dashed lines are guides to the eye to roughly indicate the slit positions.

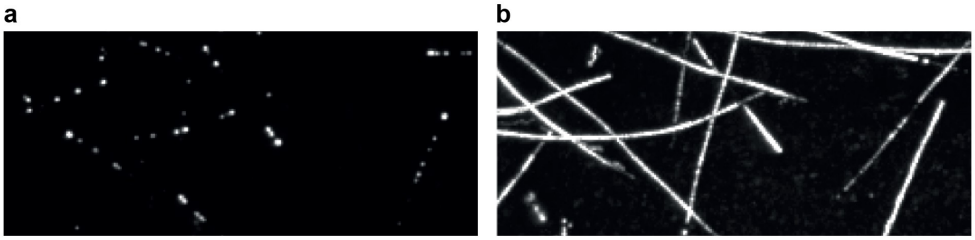

Figure 8.2 – Fluorescence microscopy of QD-labelled microtubules scanned across a bare glass surface. a, Single frame and **b,** maximum projection showing QDs being transported across a bare glass substrate. In contrast to the results from structured gold sample (Fig. 8.1c), the signal does not vary strongly on small spatial scales.

This chapter introduces a novel multi-probe method for parallel mapping of optical near-fields using individual dipole emitters in a virtually artefact-free fashion. In particular, using kinesin-1 motor proteins and microtubules - the biomolecular machinery responsible for cargo transport inside living cells - is a unique approach to scan quantum dots over nanostructured gold surfaces. In the experimental setup, the sample of interest is decorated with kinesin-1 motor proteins (Fig. 8.1a). When fueled with ATP, the surface-bound motors transport the QD-labelled microtubules across the substrate with a controlled uniform velocity, an assay well-established in the field of motor protein biophysics [501] and bio-nanotechnology [502]. Such 'gliding assays' are readily prepared following a simple, straightforward protocol. More details on the sample preparation can be found in appendix C.1. The samples are illuminated from below by collimated laser light and imaged from above by a fluorescence microscope equipped with an EMCCD camera (Fig. 8.1a). This allows parallel recording of the fluorescence emission from up to 100 individual QDs in a field of view of about $100 \times 100\,\mu m^2$ (see Fig. 8.1c and appendix C). Importantly, the impact of the 'scanning apparatus' on the near-field interaction is negligible due to the small scattering cross-section of the nm-sized proteinaceous transport components (globular size of kinesin-1 motor-domain about 5 nm; diameter of microtubules about 25 nm; refractive index 1.38). Motor-propelled QDs are thus well-suited scanning probes to investigate near-field interactions.

To demonstrate the potential of this approach, the near-field interactions of individual QDs with nanoslits of 110 to 240 nm widths engraved in a 25 nm thick gold layer (Fig. 8.1b) is mapped in a parallel fashion. Compared to unstructured regions, significantly increased fluorescence intensities can be observed when the QDs crossed a nanoslit (Fig. 8.1c and 8.3). In contrast, when imaged under homogeneous illumination on bare glass, the fluorescence intensities are independent of the QD positions as shown in Fig. 8.2.

8.2 Measurements

To quantitatively analyze the near-field interactions between the QD and the nanoslit, hundreds of QD trajectories are recorded by tracking individual QDs using the image analysis software FIESTA [503] (Fig. 8.3a). The precision of the QD position in each frame obtained by this conventional localization analysis varied due to QD blinking and different inherent QD brightnesses quantum yield and was typically around 30 nm. However, the localization precision can be substantially increased by exploiting the deterministic path and the uniform velocity of the microtubule-attached QDs. For each trajectory, the tracked positions around the nanoslit regions are fitted with a 3rd-degree polynomial function.

As exemplified in Fig. 8.3a, such a fit is a very good approximation for the paths which are taken by gliding microtubules across the surface due to their high persistence length. Owing to the uniform gliding velocity of the microtubules, the QD positions can then be reassigned as uniformly distributed along the path by minimizing the sum of squared distances to the originally tracked positions. Following this procedure the QD localization precision can be improved by one order of magnitude (to $\lesssim 5$ nm, Fig. 8.3b-d). This precision has been verified and was not compromised by fluctuations in the microtubule gliding velocity which might result from changes in the attachment geometry of the motors during gliding [504]. Due to the slow gliding velocities (about 300 nm/s at 40 µM ATP) in the assays and the fast acquisition rate (20 frames per second), the impact of these fluctuations remained below our localization precision. Importantly, the described interpolation strategy efficiently suppressed the localization artifacts present in the conventional tracking results near the edges of the nanoslits as shown in Fig. 8.4a,b. Here, the averaged localization accuracy shows an increase at the edge of the gold layer. This peak does not occur in a reference evaluation far away from the slit (Fig. 8.4c,d).

For each trajectory, the experimentally detected fluorescence intensity was then registered as function of the distance between the QD and the nanoslit center line and normalized to the average QD 'on'-intensity on the unstructured gold surface (Fig. C.1-C.3). By averaging the normalized QD intensities for each nanoslit width, the intensity variations caused by the characteristic QD blinking are minimized. Ultimately, nm-resolved, averaged fluorescence intensity profiles for all nanoslits under investigation (Fig. 8.3e-f) can be resolved. This resolution substantially surpasses the ones previously reported in experiments on similar structures [421, 422, 496, 498–500].

8.3 Fluorescence model

In order to support the measured fluorescence intensity profiles numerical finite-difference time-domain (FDTD) simulations have been carried out to investigate the local near fields (Fig. 8.5 and appendix C). Because the wavelengths for QD excitation (488 nm) and emission (655 nm) are well-separated, the detected fluorescence intensity can be described as a result from two distinct effects: (i) the excitation

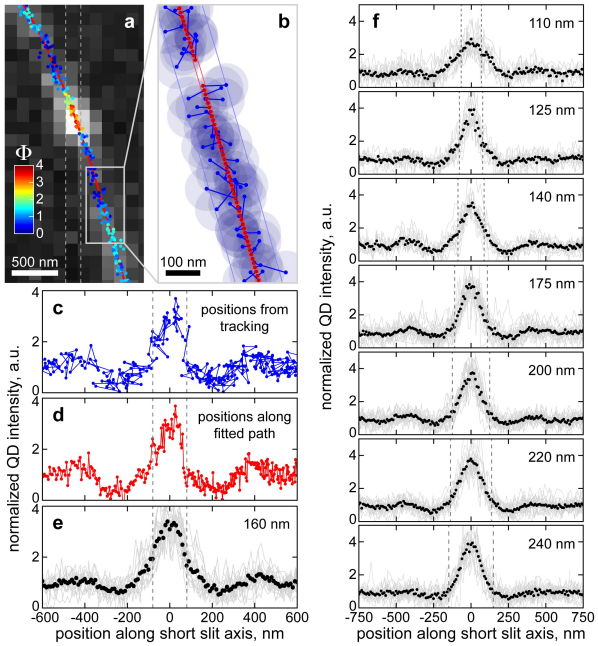

Figure 8.3 – Quantitative mapping of QD - nanoslit near-field interactions. **a,** Maximum-intensity projection (greyscale image, pixel width 129 nm) of a series of images showing a microtubule-bound QD being transported across a nanoslit (160 nm width) along with the QD positions in the individual frames as obtained from particle tracking (dots, 'tracked positions' color-coded with the normalized intensity). The tracked positions are fitted with a third-degree polynomial (red line) to approximate the path of the QD. **b,** Magnified segment of the QD path. Each tracked position is represented by a blue dot along with a semi-transparent circle with a radius of twice the mean fitting error of the tracking (i.e. representing the area in which the QD was located with 95 % probability). To improve the localization precision, the QD positions are reassigned as uniformly distributed points along the fitted path (red dots, connected to the tracked positions by blue lines), which effectively decreases the uncertainty in determining the QD position by one order of magnitude as evident from the comparison of the 95 % confidence- (blue lines) and prediction interval (red lines) of the polynomial fit. **c,** Normalized QD intensity plotted against the tracked position perpendicular to the nanoslit (blue dots in **b**). **d,** same as **c** but with reassigned positions (red dots in **b**). **e,** Averaged normalized QD intensity from all measured trajectories using the reassigned positions (dots, 10 nm bins) along with all individual normalized intensity profiles (lines) of the 160 nm wide slit. **f,** Same as **e** for all remaining slit widths. In plots **a**, **c-f**, the nanoslit edges are indicated by vertical dashed lines.

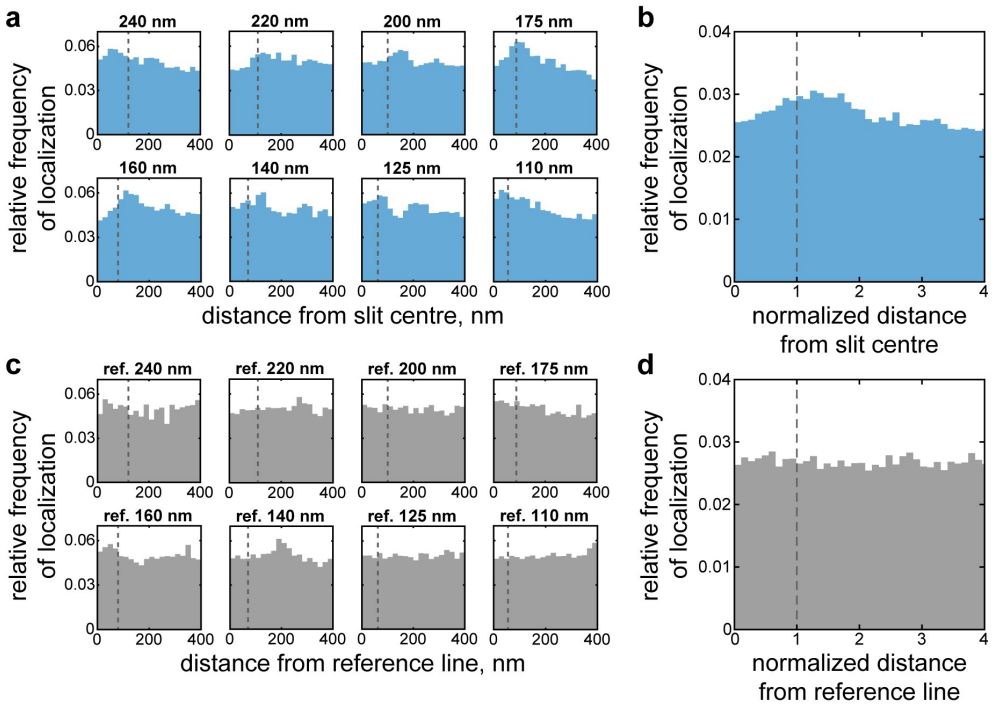

Figure 8.4 – Localization artifacts in conventional tracking data. a, For each slit width the normalized number of conventional localizations as function of the distance to the slit centerline is shown. Vertical dashed lines indicate the slit edges (i.e. half the slit width). Whereas one should expect a higher probability of localizing a QD close to the nanoslit center (due to the increased excitation intensity) it is found that the localization probability is lower in the center of the slit than close to the slit edges. **b,** Joint representation of all data in **a** by plotting against the normalized distance from the slit center, i.e. all distances are divided by the half of the slit width so that slit edges are at normalized distance 1 (vertical 10 dashed lines). **c** and **d,** As a negative control the same analysis was carried out for reference lines 2500 nm away from the respective slit centers (i.e. in the middle between the slits). No systematic localization artefacts were found in those cases.

of the QD via the inhomogeneous near-field distribution of the illuminated nanostructure and (ii) the resonant near-field coupling of the excited QD with the same nanostructure, which leads to enhanced radiative decay rates (Purcell enhancement) and changes in the quantum efficiency as well as the angular emission characteristics. The excitation intensity distribution of the near-field above the gold layer was simulated for the illumination wavelength of 488 nm (Fig. 8.5a, upper panels). For all slit widths, the excitation intensities I_{ex} (which determine the QD excitation rates) are highest directly above the nanoslits and small elsewhere due to absorption and reflection by the gold layer. Resonant near-field interaction of the QD with the nanoslit sample changes its emission efficiency η which is here described as the modification of the measured fluorescence intensity due to an altered quantum efficiency and emission direction. This quantity is simulated by placing an electric dipole emitting at 655 nm at distinct positions above the gold surface and calculating the resulting amount of emitted light which is captured by the numerical aperture of the objective (Fig. C.4). FDTD simulations therefore readily include effects of quenching as well as excitation of radiative surface plasmon polaritons. The random QD orientation is accounted for by averaging over all three dipole orientations (see appendix C).

The emission efficiency η is found to be strongly dependent on the horizontal distance x to the slit center line and the vertical distance y to the gold surface (Fig. 8.5a, lower panels). For excitation rates well below saturation, the average QD fluorescence intensity Φ detected in the far field, is given by

$$\Phi(x) = c \cdot \langle I_{\mathrm{ex}}(x,y) \cdot \eta(x,y) \rangle_y \tag{8.1}$$

where c is a scaling factor which accounts for the quantum efficiency of the optical setup. Due to a random distribution of QD binding sites on the microtubule surface and the fact that microtubules rotate around their longitudinal axis during transport [505], the QDs in the experiments were scanned across the surface at vertical distances between 15 and 55 nm (see appendix C and [506]). This is accounted for in numerical simulations by averaging the product of I_{ex} and η over the specified height range. A comparison between Φ and the mean normalized fluorescence intensities detected in the experiments shows excellent agreement for all slit widths (Fig. 8.5b).

These results provide a solid foundation for future studies of more complex nanostructures: While the electromagnetic field behind an illuminated nanostructure can often be calculated rather straightforward, calculating the Purcell enhancement of an emitter in the near-field of a nanostructure requires more advanced methods, which easily become intractable for complex geometries. The presented method provides a solution to this problem as it is capable of deducing 'Purcell enhancement maps' by deconvolving the measured fluorescence intensity maps with the electromagnetic field distributions calculated for the system of interest. Moreover, with the rapid evolution of plasmonic nanostructures self-assembled in aqueous environment, e.g. by arranging metallic nanoparticles on DNA origami [507, 508], there is an increased need for compatible near-field scanning methods. While traditional methods fall short in that respect because the sensitivity

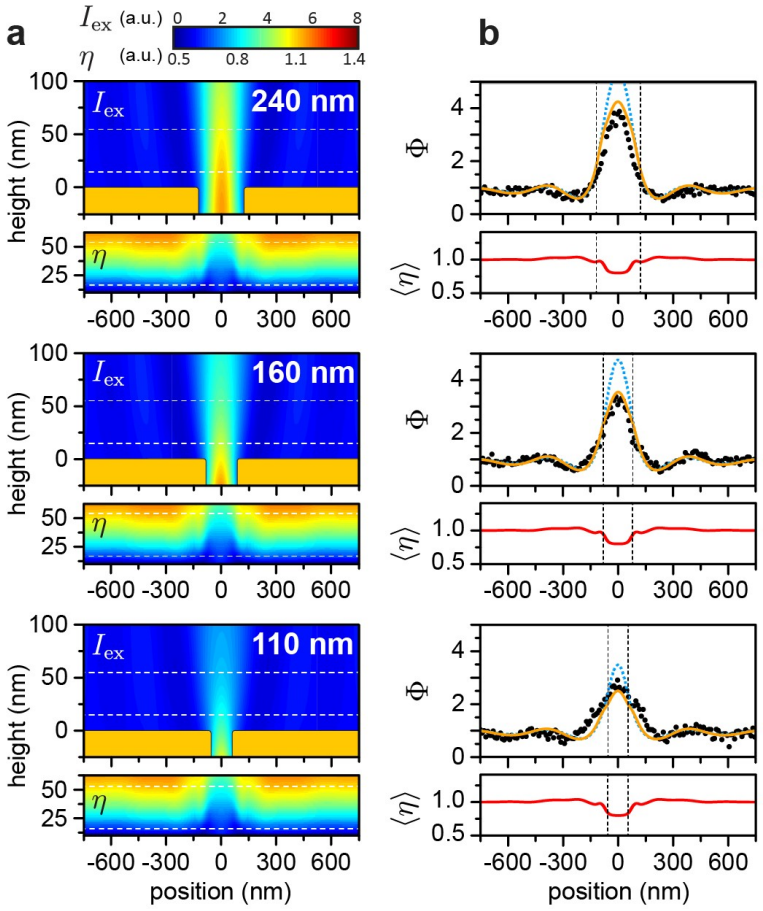

Figure 8.5 – Numerical simulation of the QD-nanoslit near-field interactions. a, (Upper panels) Near-field intensity distribution I_{ex} above the gold nanoslits upon plane wave excitation with 488 nm from below. (Lower panels) Far-field emission efficiency η of a dipole emitter with an emission wavelength of 655 nm as function of its position and height above the gold surface. **b,** Normalized excitation intensity $\langle I_{ex}\rangle$ (blue dashed lines) and emission efficiency $\langle\eta\rangle$ (red lines) averaged over the experimentally relevant height range ($15-55$ nm above the surface, see appendix C) as indicated by the horizontal dashed lines in **a**. Only the product of these two quantities $\langle I_{ex}\cdot\eta\rangle$, namely the normalized QD fluorescence intensity Φ (orange lines), agrees well with the normalized experimentally measured QD fluorescence intensity (black dots).

of cantilever- or tuning fork-based position control is decreased in water, the scanning microtubule approach is well adapted to these requirements. The ability of reducing the microtubule velocity via the ATP concentration also offers the unique possibility to park a QD inside the near-field of an optical antenna giving rise to more sophisticated exploration of the QD-plasmon coupling mechanism.

Scanning a single emitter via a biomolecular transport machinery directly integrated on the sample not only leads to an improved resolution of near-field mapping itself but also provides a number of crucial technological advantages. (i) The negligible influence of the proteinaceous transport machinery on the local refractive index minimizes any distortions of the QD-nanostructure near-field interactions. (ii) Due to its inherent mechanical stability, the system is not vulnerable to external influences, such as drift and vibrations, and thus, near-field mapping can be carried out using a standard fluorescence microscope. (iii) The fact that full intensity profile is obtained from each individual QD makes it possible to account for inhomogeneities in sample illumination and inherent QD brightnesses by normalizing each intensity profile individually. (iv) The deterministic motion of the QDs allows for the interpolation of their tracked positions in the areas of interest, resulting in a largely increased spatial resolution and a suppression of localization artefacts inherent to previous approaches using single-molecule localization microscopy near photonic nanostructures. Taken together, the presented method thus combines the precision of scanning probe approaches with the scalability of multi-emitter techniques. Consequently, it is possible to obtain high-quality near-field intensity profiles of the nanoslit samples by recording only few tens of QD trajectories per slit width.

8.4 Conclusion and Outlook

With regard to the resolution demonstrated in this section, further improvement to well below 5 nm can be achieved by increasing the number of recorded data points per probe trajectory as well as by employing non-blinking probes with higher brightness. At the same time, a reduction in the total measurement time is conceivable by implementing topographical and chemical guiding strategies [509] to direct the gliding microtubules to the regions of interest.

Further improvements of the scanning microtubule method include the additional tracking of the emitter's distance to the sample surface [510]. Together with the possibility to scan individual QDs dynamically up and down on microtubules rotating around their longitudinal axis, this approach thus holds potential to evolve into a 3D measurement technique. Alternatively, the height of the emitter can be controlled by incorporating it into the inner volume of the microtubule - thus removing the height variations - and adjusting the microtubule-to-sample distance by differently sized linker molecules or even smart polymer systems with *in-situ* adjustable conformational states. In both cases, the improved localization strategy based on position interpolation is applicable due to the deterministic motility behavior of the gliding microtubules. Notwithstanding, the inherent properties of this approach to employ

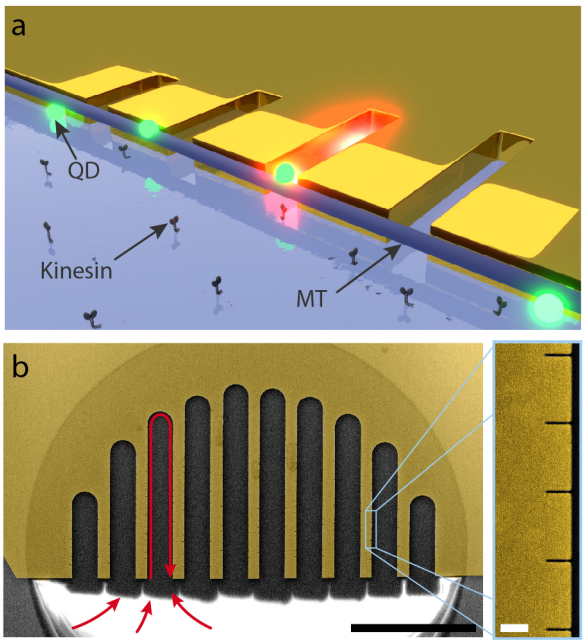

Figure 8.6 – Microtubules as a single emitter transport system. a, Artistic representation of quantum dots attached to a microtubule (MT) gliding along the edge of a gold flake on top of Kinesin motors. When a QD approaches a resonant nanoslit the fluorescence is enhanced by the plasmon resonance. **b,** SEM image of the proposed design (artificially colored). Red arrows indicate a possible path of the microtubules. Scale bar: 20 μm. Inset: Magnified area of the nano-slits. Scale bar: 400 nm

multiple QD probes in parallel and to carry out measurements without the necessity of any electronic feedback control promises applications of near-field scanning on large-scale devices, such as sensor chips and other metasurfaces, where current technologies fail.

The next step of embracing the capabilities to transport a single emitter in close proximity of a resonant near-field, is to increase the probability to strike the location of a single structure with a microtubule. A promising approach is to exploit the edge of a gold flake as a gliding border. As shown in Fig. 8.6a, the microtubule can glide along the flake edge as the kinesin motor distribution is restricted to the glass substrate via surface passivation methods. The flake edge is patterned with narrow slits which act as optical nanoantennas similar to the description in chapter 5. The localized fields at the open end of the slit leads to an enhanced fluorescence of the passing by quantum emitter.

A SEM image of a first realization of such a geometry is shown in Fig. 8.6b. The gold flake has multiple aisles to 'catch' a gliding microtubule and force it to move along the flake edge. On both sides nano-slits with different lengths are structured in order to realize resonant and non-resonant coupling. A round corner at the end of the aisle may cause a change of direction and a passage at the other side.

This is just one of the many concepts which highlight the capabilities of scanning quantum dots via microtubule transport. The scarce reports on controlled

separation-dependent experiments of single emitters and plasmonic near fields evidence the need for novel methods which further broadens the understanding of light-matter interaction. Whether a fundamental investigation of the coupling mechanism or an application for high-resolution near-field microscopy, a biological quantum emitter transportation coating for may serve as a far-reaching nanotechnology for future experiments.

9 Summary and Outlook

The physics of confined light in close proximity to metal surfaces shares many similarities with the well-known concept of propagating light within a dielectric medium. Reflection of electro-magnetic energy and interference effects give rise to standing waves and enhanced electric fields at optical wavelengths. The interaction of light and matter in the far field as well as in the near field are also similar within certain aspects. The most prominent observation relates to the spontaneous decay rate manipulation of a quantum emitter which is fundamentally described by the Purcell effect and has been demonstrated for both types of field.

However, there are also obvious differences in the appearance and description of near and far fields. One of the most important distinction involves the possible reduction of the mode volume far below the diffraction limit. The consequences on the interaction between light and matter as well as other differences has been the main topic of this work. Specifically, the possibility to demonstrate strong (coherent) interaction between a plasmon and a single emitter has been pursued for many years.

Ever since localized near-fields in the context of a nanoantenna have been reported, a variety of different antenna designs and concepts have been subject to experimental and theoretical studies. Nowadays the functionality of the most common optical nanoantennas (single rod, rod dimers) is well understood. New fabrication methods allow the patterning of high quality structures with tiny geometrical feature sizes to maximize the field enhancement capabilities.

The ease of fabrication of individual metal nanostructures has shifted the focus from the fundamental characterization of localized fields to the actual experimental investigation of light-matter interaction. This development has faced further experimental challenges which concerns the reliable and accurate positioning of a single emitter within the near-field of an optical nanoantenna. In most cases, the random distribution of structures and emitters eventually give rise to a coincidence of localized near fields and a quantum emitter [13, 69, 71]. But this issue of positioning a quantum emitter has also put forward a collection of techniques which include the usage of a patterned polymer film [84], functionalized nanoantennas [6] as well as DNA origami [508] to enhance the chances to 'catch' an emitter in proximity to the

near-field.

While every approach has its flaws, there is no conclusive technique for placing emitters close to structures with a defined distance. Therefore, no consistent study so far has shown how an emitter couples to an optical nanoantenna in direct comparison with theoretical models.

This work has been devoted to develop a durable resonant scanning probe to investigate the coupling mechanism of localized plasmon resonances and quantum emitters. Confocal microscopy in combination with scanning probe microscopy allows to dynamically tune the distance between an emitter on a substrate and a plasmonic structure at the apex of the tip. Similar attempts have been made in the past, but a poor quality of the plasmonic structure at the apex has prohibited a proper spectral characterization [81, 82].

The pivotal aspect of the scanning probe concept in this work has been the direct utilization of a single crystalline gold flake as a scanning probe. In direct comparison to evaporated or sputtered metal films, single crystalline gold has verifiable been proven to provide superior optical properties for plasmonic modes as well as exhibiting excellent patterning capabilities. On top of these properties, single crystalline gold flakes are flexible and durable as well as chemically inert which makes this type of material ideal for the usage in a scanning optical microscope. This work details the recipe to fabricate and the protocol to operate this novel type of scanning probe.

At the apex of the scanning probe a nanoslit has been patterned in order to introduce a localized surface plasmon resonance which overlaps with the contact area on the sample substrate. Extensive numerical simulations in this work have revealed the features of the nanoslit modes which are ideal to investigate the coupling mechanism between plasmons and quantum emitters. These characteristics include the mode volume as well as the lifetime of the plasmon mode.

Scanning probe measurements with colloidal semiconductor quantum dots have pushed the localization limit of the emitter to a resolution of 26 nm and revealed a strongly polarized emission according to the characteristic of the plasmon resonance. Consecutive spectral analysis has revealed the impact of the localized plasmon resonance on the shape of the fluorescence spectrum of the quantum emitter. A strong shift towards the plasmon resonance of 150 nm have indicated the significant, yet weak interaction between the quantum emitter and the plasmon.

Further coupling measurements with the plasmon on resonance with a single quantum emitter have shown fingerprints of strong coupling via the occurrence of additional spectral peaks. Extensive quantum mechanical analysis has revealed the complexity and the current frontier of understanding near-field strong coupling with colloidal quantum dots. In this study, every detail of the field distribution and the electronic structure of the quantum dot has been meticulously taken into account. These efforts have revealed the possibility to coherently address multiple optical transitions of a single emitter simultaneously due to the broad nature of plasmon resonances. The developed theoretical model has demonstrated a significant increase of the effective dipole moment for a quantum emitter with a narrow fine structure at

the band edge. In this work further concepts have been developed which critically address the validity of mode volume calculations in the regime of strong coupling.

As an alternative to scanning probe techniques, this work finally also explores another experimental method of using a protein based transportation technique for guiding an ensemble of single emitters towards plasmonic near fields. The possibility of attaching quantum dots to elongated microtubules which travel linearly on a functionalized surface gives also rise to unprecedented positioning accuracy. The proof-of-principle measurements demonstrates the novel method to approach the issue of positioning a quantum emitter at a distinct position inside a plasmonic near field. Future direct application of this method to resonant structures in combination with an adjustable velocity gives rise to further exploration of the coupling mechanism between quantum emitters and plasmons with a spatial resolution below 5 nm.

The course of this work mimics the overall development of the last decade in the field of plasmonics. While there are still efforts to study the understanding of plasmon resonances in general there is also a growing interest in applications of the localized fields with optically active materials. In particular, the trend pursues the interaction of optical antennas with new types of materials such as colloidal quantum dots (CdSe) and other crystalline monolayers of transition metal dichalcogenides (WSe_2) which will trigger the gradual approach of the different scientific communities of near-field optics, solid state physics as well as theoretical light-matter interaction [511]. The developments in near-field optics have become matured and are at the verge of attracting a broad interest with thriving prospects for many interdisciplinary applications.

10 Zusammenfassung und Ausblick

Die Physik von lokalisiertem Licht in an Metalloberflächen teilt sich viele Gemeinsamkeiten mit dem bekannten Konzept der Propagation von Licht in einem dielektrischen Medium. Die Reflexion von elektro-magnetischer Energie und Interferenzeffekte führen zu stehenden Wellen und gesteigerter Feldstärke bei optischen Wellenlängen. Auch die Wechselwirkung zwischen Licht und Materie im Fern- und Nahfeld zeigen Gemeinsamkeiten. Die bekannteste Beobachtung betrifft hierbei die Manipulation der spontanten Zerfallsrate eines Quantenemitters welche fundamental durch den Purcell-Effekt beschrieben ist und in beiden Feldarten demonstriert worden ist.

Es gibt jedoch auch offensichtliche Unterschiede in der Erscheinung und Beschreibung von Nah- und Fernfeldern. Eine der wichtigsten Unterscheidungsmerkmale ist die Möglichkeit der Reduzierung des Modenvolumens weit unterhalb des Beugungslimits. Deren Konsequenz auf die Wechselwirkung zwischen Licht und Materie und weitere Unterschiede stellt das Hauptthema dieser Arbeit dar. Die mögliche Demonstrierung von starker (koherenter) Wechelwirkung zwischen einem Plasmon und einem Einzelemitter im speziellen wurde jahrelang verfolgt.

Seit der ersten Beschreibung von lokalisierten Nahfeldern im Kontext einer Nanoantenne wurden viele verschiedene Antennen-Designs experimentell und theoretisch untersucht. Heutzutage ist die Funktionalität der gebräuchlichsten optischen Nanoantennen (Einzelstab und Stab-Dimer) weitestgehend verstanden. Neue Fabrikationsmethoden ermöglichen es Strukturen von höchster Qualität und kleinsten geometrischen Details zu strukturieren um dabei die Feldmaximierung bestmöglich auszunutzen.

The Vereinfachung der Fabrikationsmöglichkeiten von einzelnen Metallnanostrukturen hat die Aufmerksamkeit von der fundamentalen Plasmoncharakterisierung zur experimentellen Untersuchung von Licht-Materie Wechselwirkung verschoben. Diese Entwicklung zeigt jedoch weitere experimentelle Herausforderungen bezüglich der zuverlässigen und präzisen Positionierung von Einzelemittern innerhalb des Nahfeldes einer optischen Nanoantenne. In den meisten Fällen führt nur die zufällige Verteilung von Emittern und Strukturen zu einer Überlagerung von Nahfeld und Quantenemitter [13, 69, 71]. Doch das Problem der Positionierung

hat auch neue Technologien hervorgebracht (Strukturierte PMMA Schichten [84], funktionalisierte Antennen [6], DNA Origami [508]) die die Wahrscheinlichkeit einen Einzelemitter im Nahfeld einzufangen drastisch erhöht.

Da jede dieser Techniken jedoch ihre eigenen Probleme mit sich bringt gibt es keine endgültige Strategie wie man einen Emitter mit einem definierten Abstand an einer Struktur anbringt. Dadurch gibt es auch keine konsistenten Studien die die Kopplung eines Emitters an eine optische Nanoantenne direkt mit theoretischen Modellen vergleichen.

Diese Arbeit beschreibt die Entwicklung einer beständigen resonanten Rastersonde um den Kopplungsmechanismus zwischen lokalisierten Plasmonenresonanzen und Quantenemittern zu untersuchen. Der Einsatz von konfokaler Mikroskopie in Kombination mit Rastersondenmikroskopie erlaubt es den Abstand zwischen dem Emitter auf einem Substrat und der plasmonischen Struktur am Ende der Spitze dynamisch zu ändern. Ähnliche Versuche wurden in der Vergangenheit gemacht aber die mindere Qualität der plasmonischen Struktur an der Spitze verhinderte die spektrale Charakterisierung [81, 82].

Der Schlüsselaspekt des Rastersondenkonzepts in dieser Arbeit stellt die Verwendung einer monokristallinen Goldflocke als Rastersonde dar. Im direkten Vergleich zu aufgedampften oder gesputterten Metallfilmen besitzt monokristallines Gold nachweislich die besseren optischen Eigenschaften für plasmonische Moden und bietend darüber hinaus hervorragende Strukturierungsmöglichkeiten. Hinzu kommt noch, dass diese Goldflocken mechanisch flexibel und langlebig sind und in Kombination mit der chemischen Reaktionsträgheit ideale Voraussetzungen für den Einsatz als Rastersonde bieten. Diese Arbeit liefert den Bauplan für die Herstellung und das Protokoll zur Verwendung dieser neuartigen Rastersonde.

Mittels Rastersondenmessungen an kolloidalen Halbleiterquantenpunkten konnte deren Position auf bis zu 26 nm genau bestimmt werden und die Fluoreszenzphotonen zeigten sich aufgrund der Charakteristik der Plasmonenresonanz stark polarisiert. Die spektrale Analyse hat gezeigt, dass auch das Fluoreszenzspektrum des Quantenpunkts durch die Modenresonanz beeinflusst wird. Eine Verschiebung von bis zu 150 nm verdeutlicht diesen Effekt obwohl die Art der Kopplung noch innerhalb der schwachen Wechselwirkung einzuordnen war.

Weitere Messungen mit einer Plasmonenmode in Resonanz mit einem einzelnen Quantenpunkt haben Signaturen von starker Wechselwirkung aufgrund der Erscheinung weiterer Resonanzen gezeigt. Die darauf folgenden weitreichenden quantenmechanische Analysen haben die Komplexität und die aktuellen Grenzen des Verständnisses für starke Nahfeldkopplung mit kolloidalen Quantenpunkten aufgezeigt. In dieser Studie wurde jedes Detail der Feldverteilung und der elektronischen Struktur des Quantenpunktes mühsam berücksichtigt. Diese Anstrengungen haben gezeigt, dass aufgrund der breiten Resonanz eines Plasmons kohärente Wechselwirkung mit mehreren optischen Übergängen möglich ist. Die dazu entwickelten theoretischen Modelle haben bestätigt, dass das effektive Dipolmoment durch eine enge Feinstruktur an der Bandkante drastisch gesteigert werden kann. Die weiteren Konzepte, die im Rahmen dieser Arbeit erarbeitet wurden, haben sich kritisch mit der

Gültigkeit eines Modenvolumens im Bereich der starken Kopplung auseinandergesetzt.

Als Alternative zur Rastersondentechnik wird am Ende dieser Arbeit eine weitere experimentelle Methode basierend auf einer Protein-Transport-Technik untersucht um ein Ensemble von Einzelemittern in die Nähe von optischen Nahfeldern zu bringen. Die Möglichkeit Quantenpunkte an länglichen Mikrotubuli zu befestigen und entlang einer funktionalisierten Oberfläche gleiten zu lassen führt zu beispielloser Positionierungsgenauigkeit. Eine experimentelle Machbarkeitsstudie hat gezeigt, dass diese Methode einen neuartigen Ansatz bietet um einen Quantenemitter innerhalb eines Nahfeldes zu lokalisieren. Zukünftige Anwendungen dieser Technik auf resonante Strukturen bei gleichzeitiger Kontrolle über die Geschwindigkeit der Mirkotubuli wird es ermöglichen, den Kopplungsmechanismus zwischen Emittern und Plasmonen mit einer örtlichen Auflösung unterhalb von 5 nm untersuchen zu können.

Der Verlauf dieser Arbeit ist ein Abbild der gesamten Entwicklung des letzten Jahrzehnts im Gebiet der Plasmonik. Während es immer noch Anstrengungen gibt das generelle Verständnis von Plasmonen voranzutreiben, so existiert ein wachsendes Interesse daran die lokalisierten Felder mit optisch aktiven Materialien zu koppeln. Der Trend verfolgt insbesondere die Wechselwirkung von optischen Antennen und neuartigen Materialien wie z. B. kolloidale Quantenpunkte (CdSe) und andere kristalline Monoschichtsysteme aus Übergangsmetall Dichalkogeniden (WSe_2), was zur Folge hat, dass sich die verschiedenen wissenschaftlichen Gemeinschaften der Nahfeldoptik, Festkörperphysik und theoretischer Licht-Materie-Wechselwirkung langsam annähern werden [511]. Die Entwicklungen in der Nahfeldoptik werden ausgereifter und stehen an der Schwelle Mittelpunkt von breitem Interesse zu werden mit florierenden Aussichten für viele interdisziplinäre Anwendungen.

A Numerical calculations

A.1 Apodization and Q-Factor

The correct and accurate numerical determination of electric field distributions and scattering spectra of plasmonic modes does not follow a straightforward workflow. Its precise excitation via an external source and the differentiation between the excitation and the plasmon mode is one of the key challenges which sometimes also requires prior knowledge about the mode properties. In this section the impact of temporal apodization on the scattering spectrum of plasmon modes is discussed.

Acquisition of data in FDTD simulations is accomplished via monitors which determine the region of interest within the simulation volume. Depending on the settings they can record the electric and magnetic field at the specified location either as function of time or integrated over the complete simulation time. Recording the fields as a function of time requires a huge amount of memory and is therefore only reasonable for 1-D or small 2-D monitors. Therefore, the data acquired with monitors throughout this thesis is integrated over the whole simulation time.

The fields which are involved in FDTD simulations can be separated into two categories: (i) primary (source) fields and (ii) secondary (scattering) fields. When integrating the field strength over the whole simulation time both fields contribute to the final result. As in most cases only the scattered fields are the ones of interest and therefore have to be separated from the primary fields. In order to achieve this separation, a time apodization (window-) function can be applied to the field integration in order to suppress the source contribution. This function is determined via a center (start) time τ_c which marks the time after the beginning of the simulation and a width τ_w as sketched in Fig. A.1a. Depending on the type of source and the decay time of the scattered fields the apodization parameters have to be adjusted accordingly.

The effect of apodization on the field strength when examining a mode distribution at a single frequency is rather straightforward. For larger τ_c the field contribution of the source (which is broadband throughout the visible range) fades away and the scattered fields dominate. This can also be seen when monitoring near-field spectra, i.e. electric field intensity at different frequencies. The width of the

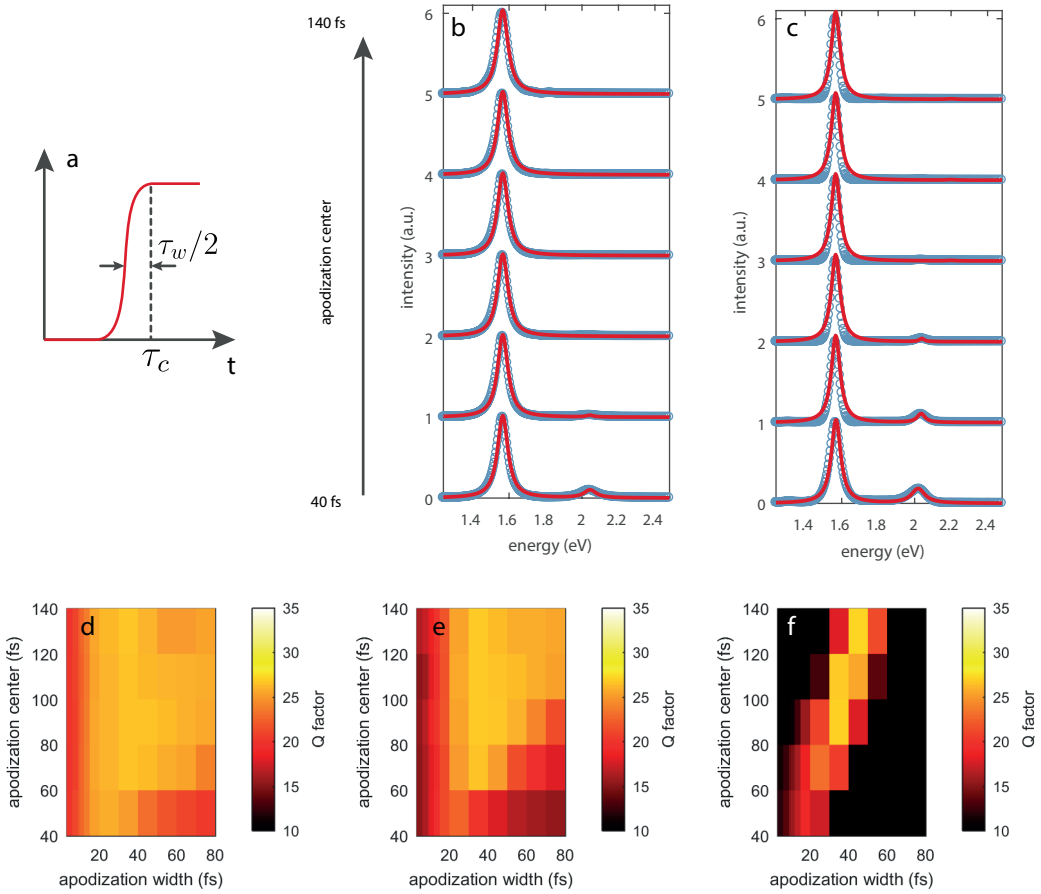

Figure A.1 – Effect of the apdodization on the width of the resonance. **a,** Time apodization function with center τ_c and width τ_w. **b,** Near field intensity ($|E|^2$) spectra of a plasmonic slit cavity (gap size 10 nm) for a fixed $\tau_w = 10$ fs and τ_c ranging from 40 fs to 140 fs (bottom to top, steps of 20 fs). **c,** Same as in **b** but with $\tau_w = 30$ fs. **d,** Q-factor of the 2$^{\text{nd}}$ order mode for a cavity gap size of 10 nm as a function of τ_w and τ_c. **e,** Same as **d** but with gap size 20 nm. **f,** Same as **d** but with gap size 30 nm.

apodization has an effect on the shape of the spectra. If the temporal window τ_w is to small, the resulting high-frequency components in k-space causes fringes in the spectra. Too large values results in residues of the primary fields being recorded by the monitor. Therefore, when extracting quantitative information from the spectrum (such as the Q-factor) it is important to vary τ_c and τ_w and to study the shape of the spectrum in order to draw reliable conclusions.

Figure A.1b shows the simulated near-field spectrum (open circles) of a nanoslit with a gap size of 10 nm at different τ_c and a fixed apodization width of $\tau_w = 10$ fs (range from 40 to 140 fs in 20 fs steps). The simulation geometry is the same as described in section 5.2. The excitation occurs after 9.4 fs into the simulation with a pulse width of 3.3 fs. With an apodization center of $\tau_c = 40$ fs the spectrum shows the 2$^{\text{nd}}$ (left) and 3$^{\text{rd}}$ (right) order resonance peak. As the τ_c increases, the recorded power of the monitor decreases which can be seen by the disappearance of the

3rd order resonance which decays faster at a resonance energy of 2 eV than the 2nd order resonance. The spectral shape, however, remains a Lorentzian as can be seen by the fit (red line). When the apodization width is increased to 30 fs the shape of the spectrum changes as shown in Fig. A.1c. At $\tau_c = 40$ fs the spectrum is almost identical compared to $\tau_w = 10$ fs. However, as τ_c increases the shape of the spectrum narrows and deviates from a Lorentzian when comparing with the fit (red line), which indicates that the emission does not reflect the properties of a harmonic oscillator. Therefore, the width does not represent the Q-factor of the mode.

In Fig.A.1d-f the Q-factor of the resonance is mapped as a function of τ_w and τ_c for nanoslits with gap sizes of 10, 20 and 30 nm (range from 3 to 80 fs in non-equal steps). The length is adjusted accordingly in order to remain at the same resonance wavelength of 800 nm (same as in Fig. 5.8b).

When τ_w becomes larger than τ_c the source fields obviously dominate the recorded electric fields. The broadband excitation leads to broadening of the plasmonic resonance features and reduces the Q-factor. Therefore, the lower right corner of these maps do not contain physical information about the plasmon resonances.

For small τ_w the Q-factor remains the same regardless of the apodization center. With increasing τ_w the Q-factor increases but the spectral shape also starts to deviate from a Lorentzian as shown in Fig. A.1c. Additionally, for resonances with a large gap of 30 nm the spectrum can't be resolved for larger τ_c due to the low field strength[1].

Nonetheless, the overall examination of the Q-factor of plasmonic nanoslits clearly shows an increase with decreasing gap size. It also demonstrates that the apodization parameters τ_w and τ_c are essential when judging the spectral width of different plasmonic geometries.

A.2 Focusing of optical fields

The ability to focus linear polarized paraxial laser light with an high numerical objective has a natural limit due to diffraction of light. In this section numerical FDTD simulations are carried out to study the focused field of an incident beam through a high-NA objective. In a first step, the isolated field at a planar dielectric interface is discussed. A second study investigates the impact of a gold flake edge as a function of position as well as orientation to the optical axis. It is found that minor shifts of the flake position (< 100 nm) can have a significant impact on the maximum achievable field strength.

The spatial distribution of the localized field intensity ($|E|^2$) in the focal plane can be described in first approximation as a Gaussian as shown in shown in Fig. A.2a. [15]. The incident light ($\lambda = 532$ nm) is polarized along the x-axis and a numerical aperture of 1.45 yields a focus diameter of about 220 nm. However, the initial electric field polarization is not maintained for highly focused fields.

[1] Larger gap sizes lead to smaller Q-factors and fast energy dissipation. Therefore, the amount of energy within the simulation volume decreases with increasing τ_c.

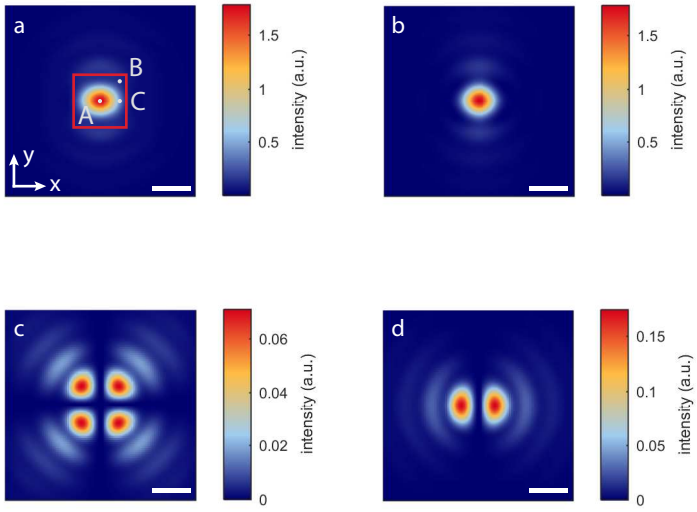

Figure A.2 – Focusing of optical fields. **a,** Total field intensity distribution of monochromatic light ($\lambda = 532\,\text{nm}$) with a NA of 1.45 polarized along the x-axis. Scale bar: 300 nm. **b,** Intensity distribution of $|E_x|^2$. **c,** Intensity distribution of $|E_y|^2$. **d,** Intensity distribution of $|E_z|^2$.

The x-component of the field intensity $|E_x|^2$ is shown in Fig. A.2b and displays a similar shape as $|E|^2$. The y- and z-components of the field intensity are shown in Fig. A.2c and d, respectively. Due to symmetry reasons the intensity $|E_y|^2$ and $|E_z|^2$ is zero along the optical axis. $|E_y|^2$ shows a four-lobe pattern with a maximum intensity of $|E_y|^2/|E|^2 = 0.04$. The maximum intensity appears displaced along the x- and y-direction of about 150 nm. Similarly, the z-component of the field intensity shows a two-lobe pattern with a maximum intensity of $|E_z|^2/|E|^2 = 0.1$ which is displaced by 150 nm along the x-axis.

The influence of a different field polarization at different positions can be demonstrated by scanning a single dye molecule through the focus. Depending on its dipole orientation the fluorescence intensity map appears different [512]. In case of isotropic absorption of a nanoparticle, i.e. incoherent excitation of a colloidal quantum dot, the fluorescence intensity map follows the profile of $|E|^2$.

A gold flake (thickness 60 nm) corner entering a high NA focus behaves similar to a single dye molecule. Depending on the polarization and the position with respect to the gold flake tip the field intensity at the apex of the flake can be different. The most interesting positions are marked in Fig. A.2a, where A, B and C correspond to the maximum intensity of the x, y and z field component, respectively. The region of interest is indicated by the red rectangle.

The field intensity distribution within an area of $150 \times 150\,\text{nm}$ 4 nm below the tip for all three position offsets is shown in Fig. A.3. The apex of the flake has a radius of 40 nm. For every position the flake is aligned in two orientations relative the excitation polarization. Figure A.3a shows the case of symmetric alignment at position

A (Fig. A.2a). For parallel polarization the *x*-component of the field intensity shows a hotspot directly below the apex. Contribution from the *z*-component leads to an overall enhancement throughout a lobe shaped region. In case of a perpendicular excitation polarization the intensity distribution E^2 overall remains similar but lacks a confinement of the *x*-component.

The field distribution at location *B* shows a completely different behavior and depicted in Fig. A.3b. Despite being positioned at the field maximum of $|E_y|^2$, the *y*-component of the fields, as well as the *x*-components, are extremely small. However, regardless of the flake orientation, $|E_z|^2$ shows significant confinement and enhancement directly below the apex since the excitation field at that location also has a significant *z*-component. The field strength at maximum confinement is comparable to the intensity at the center of an unperturbed Gaussian focus.

The most striking effect of the gold flake edge is observed at location *C* where the *z*-component of the incident field has its maximum. The intensity distribution $|E_z|^2$ indicates a confinement and field intensity enhancement by a factor of 2-3. Depending on the flake orientation, the *x*- and *y*- component contributes to the total intensity distribution via a highly asymmetric cone-like pattern.

Based on these exemplary configurations it becomes obvious that the exact location of the gold flake apex relative to the optical axis plays a decisive role on the shape of the field distribution. A greater overview on how the field is enhanced at the apex of the tip is shown in Fig. A.4. Here, the integrated field intensity over an area of $10 \times 10\,\mathrm{nm}$ (as indicated by a red rectangle in Fig. A.3c) 4 nm below the tip apex is mapped as a function of the tip position relative to the optical axis. This representation can be regarded as a benchmark to evaluate the positions of maximum confinement since only the fields within about 5 nm to the apex contribute. The tip is scanned in discrete steps of 15 nm (as indicated by the red dots in the sketch of Fig. A.4) in *x*- and *y*-direction for parallel and perpendicular orientation with respect to the excitation polarization. The most significant confinement can be achieved when the flake tip is displaced $\pm 150\,\mathrm{nm}$ along the *x*-axis regardless of the orientation of the flake. In both cases, the *z*-component of the incident electric field is substantially enhanced and dominates the field polarization. Some minor enhancement of the *x*-(*y*-)component of the electric field close to the apex is expected at zero displacement when the flake is parallel (perpendicular) to the excitation polarization.

This analysis shows that the concentric alignment of a flake edge with a highly focused Gaussian beam is not necessarily the ideal configuration for a maximum enhanced field below the apex of the tip. It also indicates that a lateral displacement of less than 100 nm (far below the diffraction limit) changes the field intensity and polarization at the apex.

It is important to note that the results presented above correspond to a tip radius of 40 nm. Variations of this geometry as well as the overall shape and alignment of the flake edge impacts the electric field confinement. Also, only the fields at a depth of 4 nm below the substrate surface have been considered in this study since this is a reasonable mean distance to colloidal quantum dots. At different distances the confinement as well as the field strength and polarization changes. Due to the

number of free parameters and their influence on each other it is challenging to break down their individual impact on the field distribution. In addition, an even more complex behavior is expected for a structured flake edge with a nanoslit.

Nonetheless, it is also worth mentioning with regard to a scanning probe experiment that this study only reflects the properties of the excitation field. A possible localized plasmon resonance at the apex of the probe is not influenced by the relative position of the incident field.

A.3 Excitation and emission fields

The large Stokes shift provided by the QDs requires separate investigation of the PNR near-field at the excitation and emission wavelengths. The spectral separation of almost 300 nm can lead to significant differences in the field distribution especially since the excitation and emission are off- and on-resonant, respectively. The resonant mode profile $E_{\mathrm{res}}/E_{\mathrm{res},0}$ of a PNR in close vicinity to the PMMA layer excited with a Gaussian source ($+z$ direction, x polarization) at a wavelength of 800 nm is shown in Fig. A.5a. The field is apodized to remove any remaining contribution from the excitation source. It is noted that the value of the field strength is proportional but not equal to the coupling strength since the mode is not normalized. It can be seen that the field strength in the substrate increases towards the PNR probe. Whereas the coupling is proportional to the resonant field strength (E_{res}), the excitation rate is proportional to the excitation field intensity (E_{ex}^2). In Fig. A.5b the excitation intensity profile $(E_{\mathrm{ex}}/E_{\mathrm{ex},0})^2$ of the same structure is shown after excitation in the same manner at 532 nm without apodization. It is noted that now the highest excitation field in the substrate occurs close to the tip but decreases towards the slit of the cavity. The line cut at a depth averaged between 2 and 3 nm below the surface is shown in Fig. A.5c. It is interesting to see that the excitation intensity $(E_{\mathrm{ex}}/E_{\mathrm{ex},0})^2$ (pink line) has already dropped significantly at the position where the resonant field strength is highest (blue line). In the experiment this leads to the observation that the spectrum can still show features of strong coupling while the fluorescence intensity has already declined due to reduced excitation intensity.

A.4 Absorption efficiency

The absorption efficiency of quantum dots (created excitons per incident photon) can be estimated via the size of the diffraction-limited focus diameter and the absorption cross-section of the quantum dots. At a wavelength of 532 nm and a microscope objective with a numerical aperture of 1.45 the calculated focus diameter according to equ.4.1 is 224 nm. The absorption cross-section extracted from the saturation measurements of single quantum dots is found to be $4 \times 10^{-15}\mathrm{cm}^{-2}$ in accordance with a recent study [513]. Based on the ratio of the absorption cross-section and the area of the diffraction-limited focus one can calculate an absorption efficiency of 10^{-5}. This value is used in this work to evaluate an excitation rate

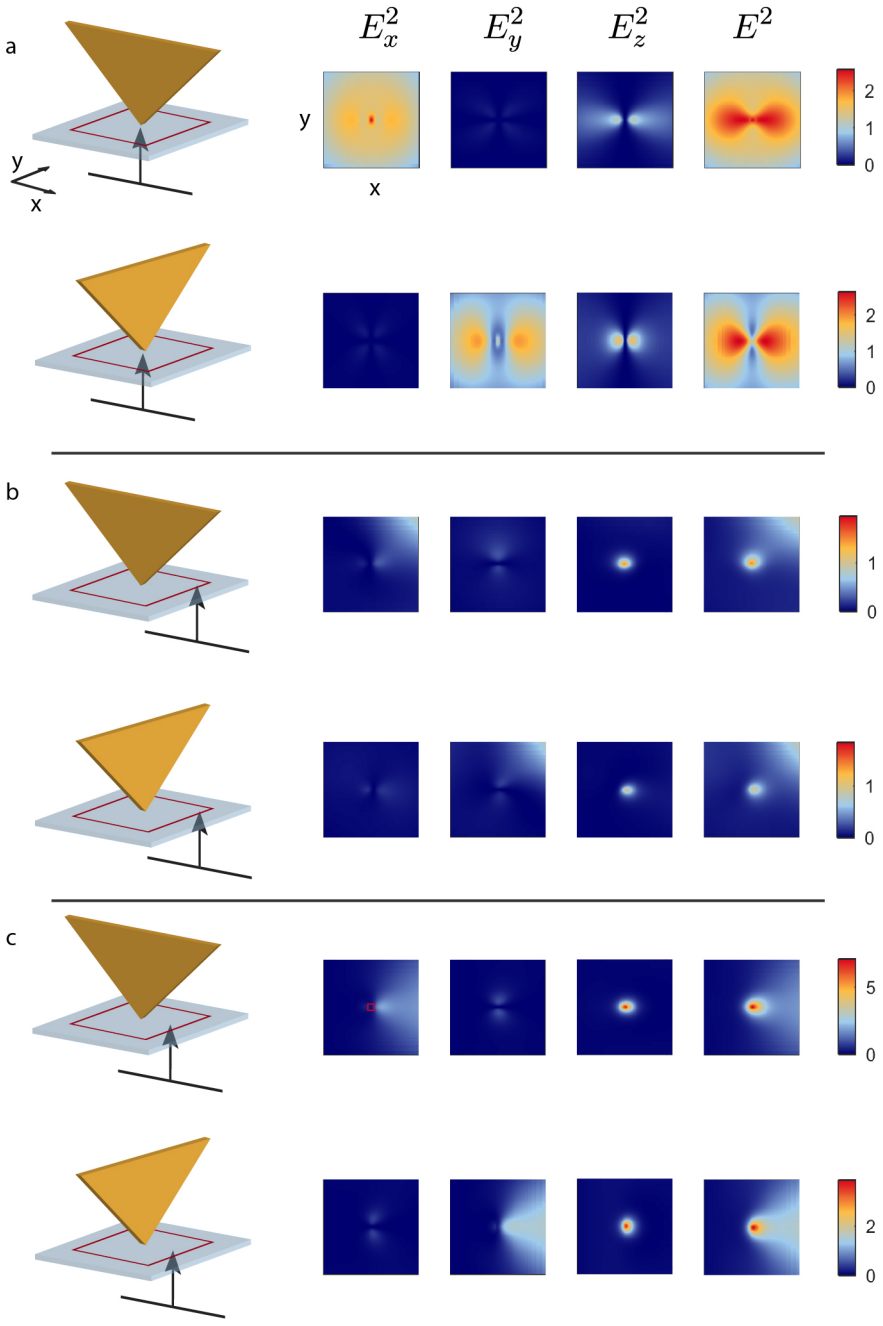

Figure A.3 – Field intensity for different flake orientations and positions relative to the focus. a, Symmetric alignment at location A. **b,** Tip located at position B where $|E_y|^2$ has its maximum. **c,** Tip located at position C where $|E_z|^2$ has its maximum.

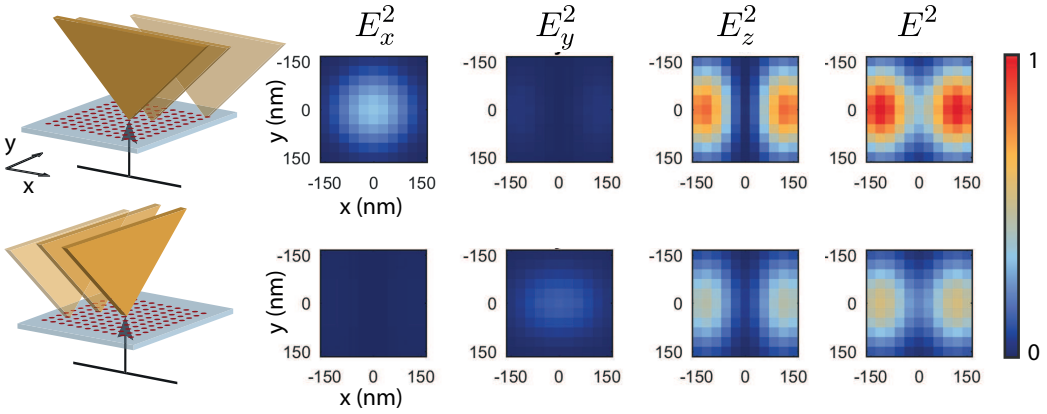

Figure A.4 – Confinement performance for different positions and orientations of the flake tip relative to the focus. Each pixel of the maps represents the integrated field intensity of a 10×10 nm area 4 nm below the tip. Upper (Bottom) row: flake alignment parallel (perpendicular) to the incident field polarization.

of the quantum dot based on the excitation power. It has to be noted, that an additional increase of the absorption efficiency is expected in case of a sharp gold tip in close proximity to the QD. However, this effect is omitted in the calculation of the absorption efficiency due to the complex geometry of most PNRs and the resulting difficulty to estimate the magnitude of the enhanced field strength.

A.5 Calculating the energy density

A calculation of the mode volume according to equ. 2.47 takes into account the energy density for different dispersive media. The factor $\frac{\partial \omega \varepsilon}{\partial \omega}$ includes the material dependent properties and is proportional to the stored electric energy per volume. An accurate determination of this value is critical for the proper calculation of the mode volume. Here, the crucial part is $\varepsilon(\omega)$, an experimentally acquired data set that is subject to uncertainties which become notably prominent when taking the derivative. For this purpose, the data of the dielectric function measured by Olmon et al. is being used as it is the most accuratley measured data which is currently available [514]. Figure A.6a shows experimental data of $\varepsilon(\omega)$ and a corresponding interpolation function. Finally, the pre-factor for the energy density is plotted in Figure A.6b. The slight jitter of the graph stems from the execution of the derivative. For an angular frequency of 2.35×10^{15} rad/s, which corresponds to a wavelength of $\lambda = 800$ nm the real part of the pre-factor has a value of about 40.

A.6 Comparison $2^{\text{nd}}/3^{\text{rd}}$ order resonance

In general, the usage of two resonances can be extremely beneficial for the purpose of enhanced light-matter coupling. Many types of single emitters exhibit a quite

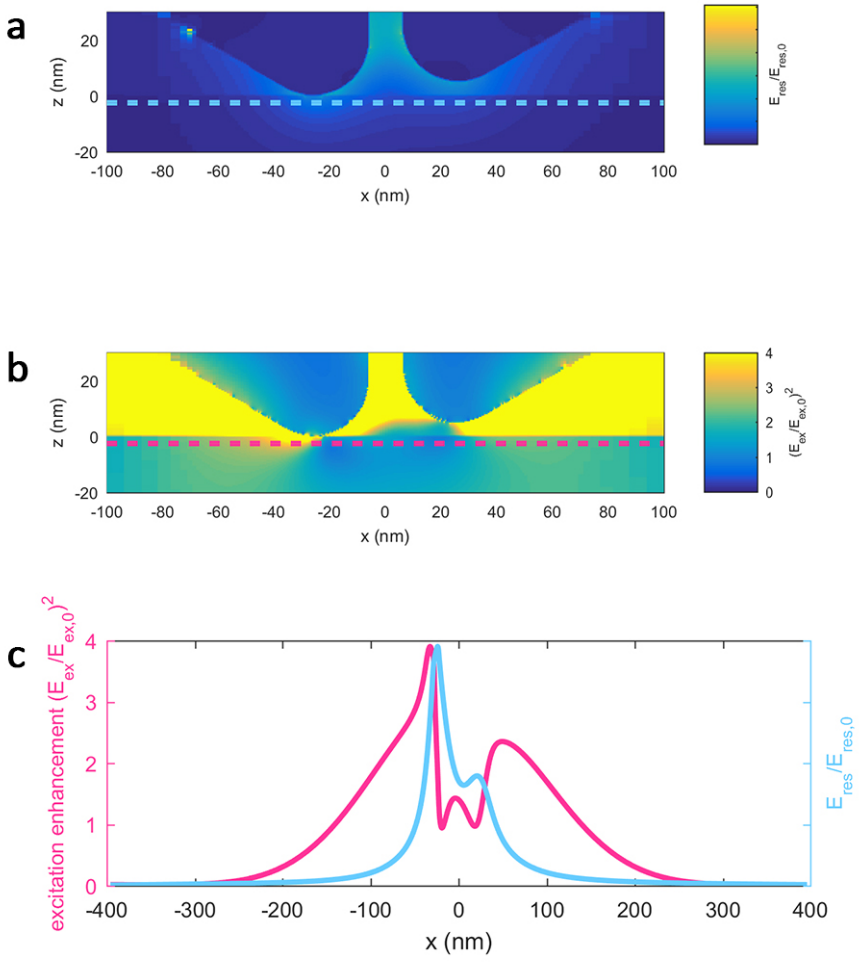

Figure A.5 – Emission and excitation near-field distribution. **a,** Near-field distribution of the cavity mode $E_{\mathrm{res}}/E_{\mathrm{res},0}$ at 800 nm (with temporal apodization). **b,** Total near-field intensity enhancement distribution $(E_{\mathrm{ex}}/E_{\mathrm{ex},0})^2$ after excitation with a Gaussian source at 532 nm. **c,** Line cut of the field averaged between 2 and 3 nm below the PMMA surface (indicated by dashed lines in **a** and **b**). The excitation near-field intensity enhancement $(E_{\mathrm{ex}}/E_{\mathrm{ex},0})^2$ (pink) drops before the emission field $E_{\mathrm{res}}/E_{\mathrm{res},0}$ (blue) reaches its maximum.

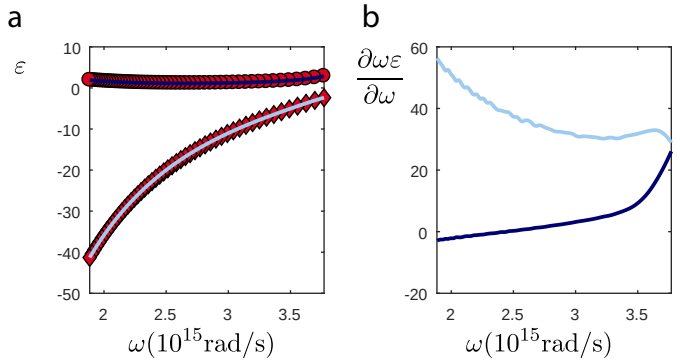

Figure A.6 – Calculation of the energy density for gold. a, Experimental data and interpolation of the dielectric function of gold. Circles and dark blue line: real part. Diamond markers and light blue line: imaginary part. **b,** Pre-factor for the energy density of gold. Same color scale as **a**.

substantial Stokes shift, the energy difference between the bands of maximum absorption and emission. The enhancement of both processes can be achieved via localized surface plasmons. Since a single plasmon resonance might be too narrow to cover the entire Stokes shift, two individual plasmon modes can be assigned to the excitation and emission process [515]. The occurrence of multiple resonances and higher-order modes for plasmonic nanostructures is a common observation especially for more complex geometries. However, an experimental realization of the simultaneous usage of two modes is quite rare as the field distribution and radiation characteristic of these modes usually differ significantly [482]. This causes that the location of the field maximum of two different modes does not coincide, which is necessary for an efficient coupling to a single emitter.

The geometry of the PNR nanostructure is able to overcome this issue. As already mentioned in chapter 5, localized plasmon resonances along a narrow slit at the edge of a gold sheet share a similar appearance and performance.

A direct comparison of the Purcell enhancement and mode volume of the 2$^{\mathrm{nd}}$ and 3$^{\mathrm{rd}}$ order resonance is illustrated in Fig. A.7a,c. The structure is aligned perpendicular to a glass substrate and features a slit width of 12 nm and a length of 265 nm. The resonance wavelengths of the 2$^{\mathrm{nd}}$ and 3$^{\mathrm{rd}}$ order mode are about 800 nm and 600 nm, respectively. Here, a dielectric sphere resembles the presence of a quantum dot. The most prominent observation is the previously mentioned field confinement at the open end of the slit. Both modes display a significant field overlap with the semiconductor sphere. The Purcell factor maps indicate the capability of each mode to enhance the spontaneous decay rate of a dipole emitter.

The direct comparison shows that the 2$^{\mathrm{nd}}$ order mode has a field distribution and subsequently Purcell factor which spreads more into the dielectric medium. In that region, the 3$^{\mathrm{rd}}$ order mode has a Purcell factor of about half the value compared to the 2$^{\mathrm{nd}}$ order. With a resonance at 600 nm the 3$^{\mathrm{rd}}$ order resonance has a short effective wavelength which also translates into short, more localized evanescent fields.

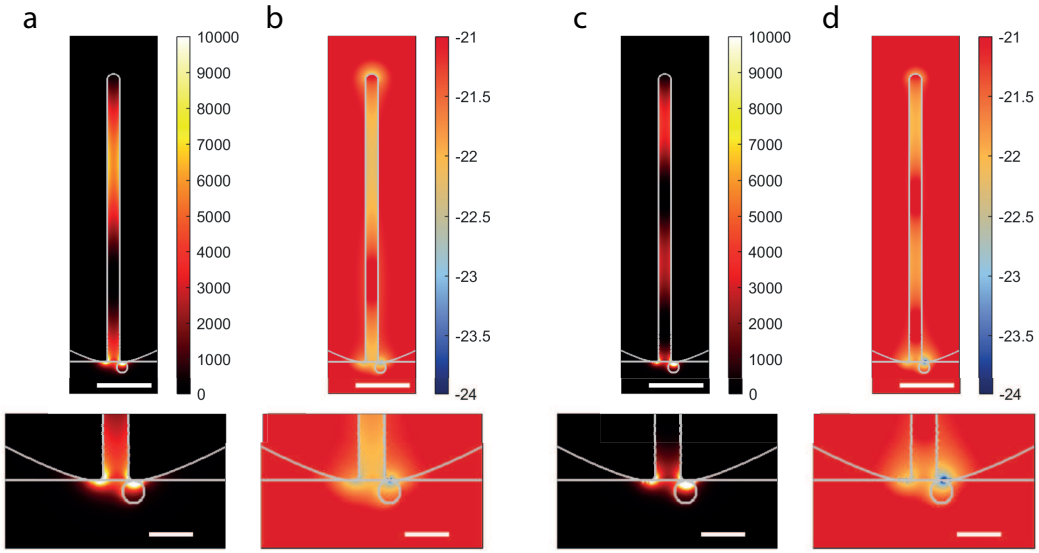

Figure A.7 – Performance comparison of the 2nd and 3rd order resonance. a, Top: Purcell factor map of the 2nd order mode of a PNR. Scale bar: 50 nm. Bottom: Zoom in. **b,** Logarithmic map of the the mode volume (m^3). **c,** Same as **a** for the 3rd order resonance. **d,** Same as **b** for the 3rd order resonance.

This observation is at odds with what one would expect when considering the dielectric function of gold. The 3rd order mode is at a wavelength regime where the negative real part of the dielectric function has a small absolute value. As described in section 2.1.1, this reduces the capability of metals to confine electric fields close to the interface. Nonetheless, the Purcell factor close to the semiconductor sphere does exceed values of 10,000.

The corresponding mode volume calculations indicate a similar behavior (see Fig. A.7b,d). Since both, the mode volume and the Purcell factor, scale with $|E|^2$ and both modes have a similar Q-factor, the corresponding difference in the mode volume in the dielectric material is also a factor of two. However, one can see that at the region close to the semiconductor sphere the field of the 3rd order mode shows higher confinement and therefore a smaller mode volume.

In summary, the studied nanostructure geometry can be considered as an ideal candidate for combining enhanced excitation and enhanced emission via the 3rd and 2nd order resonance, respectively. Especially in the case of colloidal quantum dots where the energy difference between excitation and emission can be readily more than 100 meV. Another important propierty of the modes which has not been subject of this study is the far-field emission characteristic. So far, a highly directional emission has already been observed for the 2nd order mode [430].

A.7 Mode volume comparison

The geometry of a metallic nanoantennas defines the properties of the supported localized surface plasmons. Over the past decades numerous antenna designs have been proposed, ranging from single and dimer designs to complex self-assembled structures, in order to fit various optical properties which include aspects such as radiation efficiency and directionality. However, the by far most studied aspect is the concept of near-field enhancement which quantifies the field intensity increase of a light source due to the presence of an optical nanoantenna. Near-field enhancement maps of arbitrary antennas can be obtained in a straightforward fashion via numerical FDTD simulations by exciting the structure with an appropriate source. Experiments with the same excitation configuration are able to accurately probe the field distribution by measuring the fluorescence intensity of a single emitter [7].

However, this characterization scheme has one fundamental problem as it also takes into account the type of excitation. Optical nanoantennas feature highly anisotropic excitation and emission characteristics. Depending on the direction and polarization of the incident electric field, some modes of an antenna can be efficiently excited whereas others do not exhibit any cross-section due to symmetry reasons [482].

For quantitative analysis of light-matter interaction it is necessary to calculate the local density of optical states (LDOS) which is proportional to the Purcell factor. The near-field enhancement gives only a qualitative insight on the locations of high LDOS and is therefore not directly suitable compare the light-matter coupling performance of different antenna designs.

A more promising approach is the calculation of the quasi-normal mode which describes the vacuum mode of the resonator. Details on this technique can be found in section 2.3.4. By taking into account the antenna as a whole the description of its performance is independent of the excitation source.

An artistic overview of several plasmonic nanoantennas is given in Fig. A.8. The distribution of the effective mode volume and Purcell factor is shown in Fig. A.9 for a single rod, linear rod dimer, cavity rod dimer, disc dimer, bowtie antenna and nanoslit cavity. For a fair comparison of all structures it is necessary to have the same geometrical dimensions at the positions where the fields have a maximum. All structures are composed of gold in a vacuum environment without any substrate. If the structure features a gap, this gap is fixed to a width of 10 nm. The structures which are composed of rods, such as the single rod, the rod dimer and the cavity rod dimer, all have a diameter of 30 nm and spherical caps. Also, all edges and corners are rounded in order to avoid the occurrence of hot spots. With the exception of the cavity rod dimer and the nanoslit cavity, which are excited with a dipole source, all structures are excited with a Gaussian source. However, since the monitor data has a temporal apodization any residues of the source are suppressed to a negligible value. Also, all structures are scaled in order to shift the resonance close to 800 nm. For each structure the effective mode volume and the Purcell factor are mapped in two different planes. The left column shows a top view of the structure where the

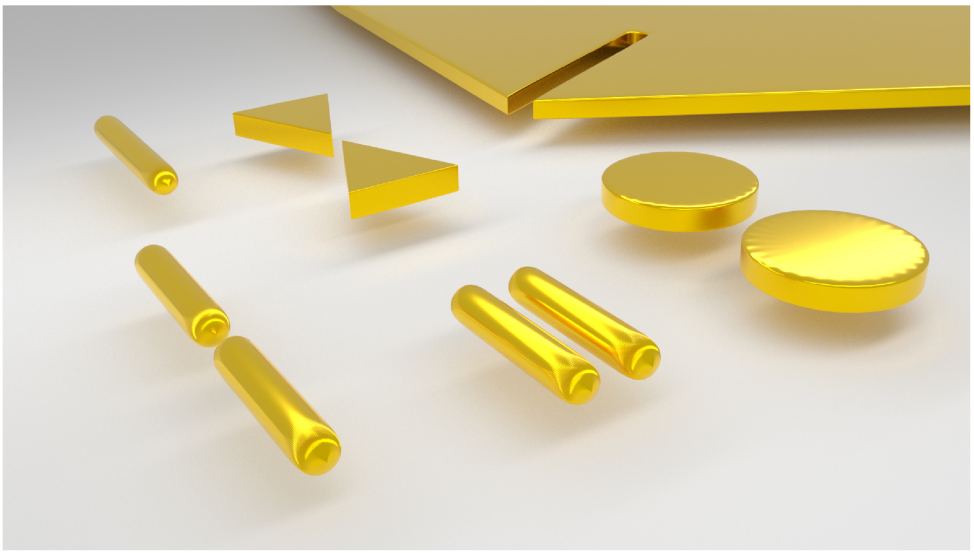

Figure A.8 – Artistic representation of a collection of nanoantennas.

dashed line indicates the position of the plane which is shown in the right column.

It is important to note that all of the previous mentioned structures are simulated without any substrate. The field distribution of all these modes, however, can be strongly affected by an asymmetric dielectric environment as it is the case in most experiments. A direct comparison between a linear rod dimer in vacuum and on a glass substrate is shown in Fig. A.10. Here, the structure on the substrate has only rounded edges at the top which is the most probable shape for common top-down fabrication techniques. The increased refractive index at the bottom and the slight change of the shape leads to a redshift of the plasmon resonance. In order to maintain a resonance wavelength of close to 800 nm the arm length is reduced to 110 nm. It can be seen that the field distribution, especially at the gap region, is shifted towards the glass substrate. This shift causes an increase of the effective mode volume directly at the center of the gap and therefore a reduction of the Purcell factor.

The values of the minimum effective mode volume and the corresponding Purcell factor at the position of highest symmetry, the location which is most desirable to occupy with a single emitter, are shown in Fig. A.11a. These locations are mostly at the center of the gap regions and are indicated by a green circle in Fig. A.10. Slight variations of this location (e.g. closer to the metal surface) has only a negligible impact on the Purcell factor and the effective mode volume.

The results show that the lowest Purcell factor can be accomplished by a single nanorod with a length of 150 nm. However, at the ends of the rod where the field is maximum, an enhancement factor of almost 5,000 is possible. All other structures are composed of dimers or gap structures which are able to exploit the influential charging of metal which is separated by a dielectric. Also, the field inside the metal rod is comparably high (as indicated by the small effective mode volume at that

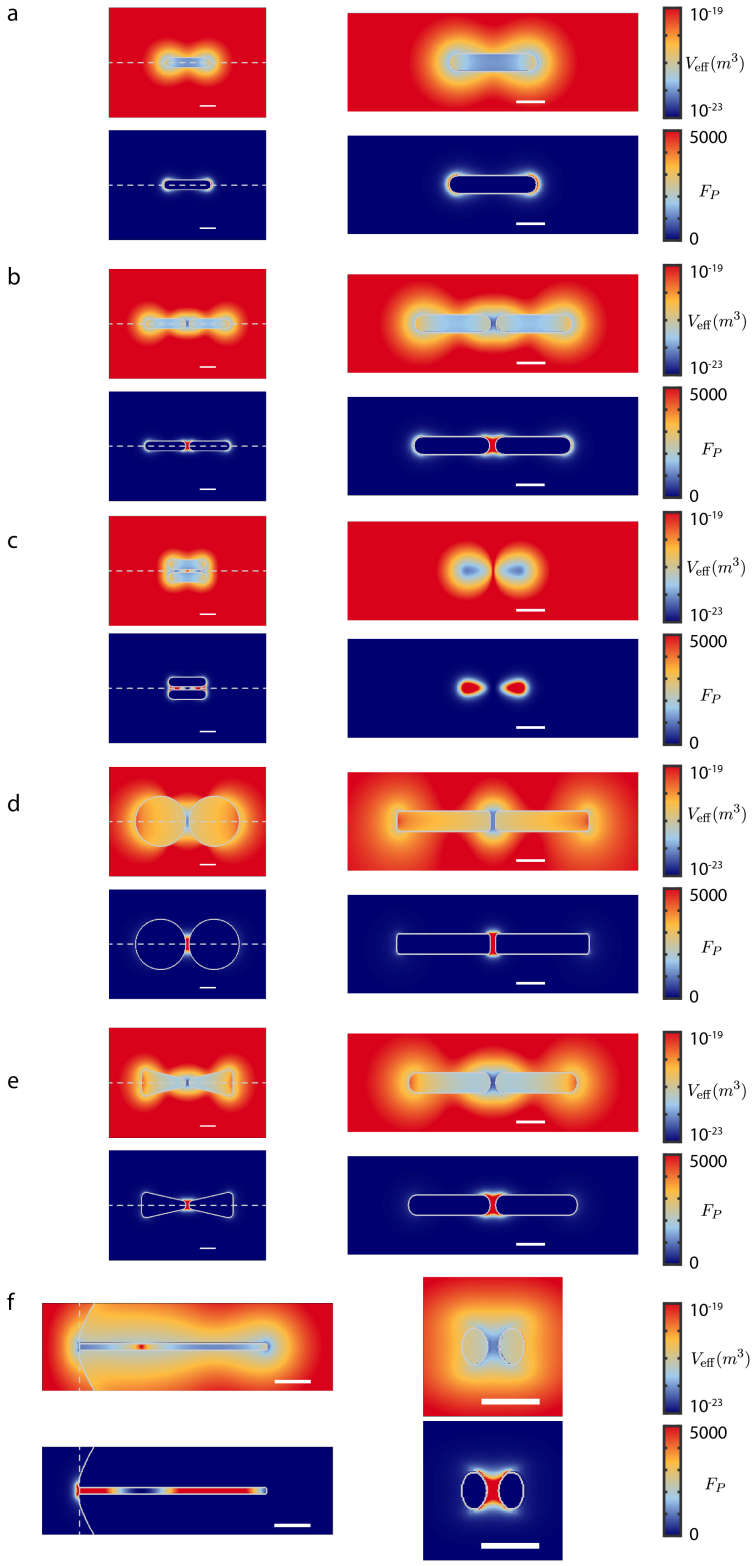

Figure A.9 – Map of the effective mode volume (logarithmic scale) and Purcell factor of various nanoantenna geometries. a, Single rod. **b,** Linear rod dimer. **c,** Cavity rod dimer. **d,** Disc dimer. **e,** Bowtie antenna. **f,** Nanoslit cavity. Scale bars: 50 nm.

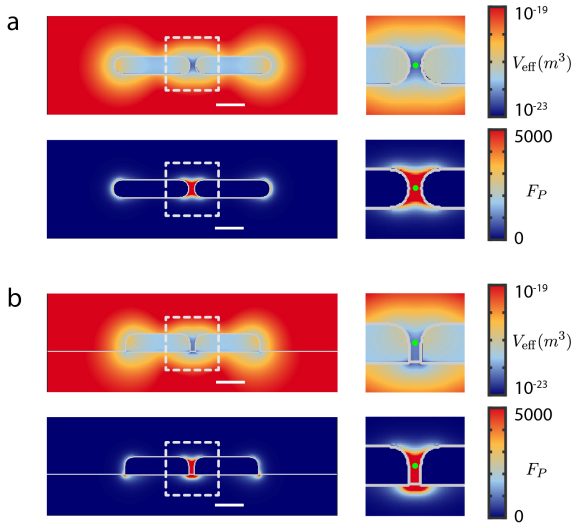

Figure A.10 – Influence of a substrate on the effective mode volume (logarithmic scale) and Purcell factor. a, Linear rod dimer in vacuum. **b,** Linear rod dimer on a glass substrate. Scale bars: 50 nm.

location) and therefore increases the overall effective mode volume in the dielectric. The largest Purcell factor, and also smallest mode volume, can be observed at the center of a bowtie antenna (triangle length: 130 nm, width: 80 nm, height: 35 nm). The narrowing of the two metal triangles towards the gap gives rise to a maximum field confinement without extensive losses in the metal. The linear rod dimer has the second best performance with a slightly larger effective mode volume and smaller Purcell factor at the center. The origin of this observation is ascribed to the uniformly distributed mode throughout the entire metal of the antenna as can be seen in the effective mode map in Fig. A.9b. In comparison, the bowtie antenna in Fig. A.9e shows a large effective mode volume in the outermost regions of both arms and a mode concentration towards the gap of the bowtie.

The structure composed of two discs has an even larger mode volume at the center of the gap and a smaller Purcell factor. Due to a disc radius of 70 nm the confinement decreases along this dimension in comparison to the linear rod dimer. The large effective mode volume inside the metal (and the subsequent small electric fields), however, leads to an effective mode volume in the dielectric of less than 10^{-23}m^3.

Almost the same performance is displayed by the nanoslit cavity structure. Despite the comparably long gap of 260 nm the mode remains concentrated inside the dielectric as can be seen by the large effective mode volume in the gold. The seamless connection of the structure with an extended metal sheet does not affect the confinement of the mode. Interestingly, the two rod cavity, which has a similar mode concept with a comparable Purcell factor in the gap, displays a much larger effective mode volume. The effective mode volume in the gold (Fig. A.9c) is comparable to the linear rod dimer but the field confinement inside the gap is smaller

(hence the Purcell factor is smaller). This observation is attributed to a confinement between two rounded edges (cavity rod dimer) as opposed to two rounded tips (linear rod dimer).

The results of this direct comparison shows that an intuitive ad hoc explanation is challenging. Numerous effects (mode overlap with the metal, antenna geometry at position of high fields) that contribute to the effective mode volume and Purcell factor can be in direct competition. The spatial distribution of the effective mode volume might be the key to get a physical understanding of the inner workings of optical nanoantennas. In typical intensity maps of plasmonic modes the field distribution inside the gold is usually much smaller than within the dielectric surrounding and therefore neglected. However, due to the significantly higher energy density at equal field strength increases the electric energy that is stored in the metal. Effective mode volume maps thoroughly reveal the true distribution of the mode energy and therefore allow for a better understanding of the optical performance.

Another optical characteristic which is hardly recognized by the field or effective mode volume distribution is the width of the plasmon resonance. As the width of a resonance is equivalent to the decay rate (see equ. 2.10), it is a crucial characteristic which determines the onset of strong coupling (see equ. 2.40). The resonance linewidth of each nanoantenna is shown in Fig. A.11b.

It can be easily seen that the Purcell factor does not relate to the width of the resonance. The more important characteristic is the instantaneous charge distribution of the mode as indicated in Fig. A.11b. There are two predominant types charge distribution that occur in this study. All of the structures except the nanoslit cavity and the cavity rod dimer structure exhibit a dipolar charge pattern. Here, all of the oscillating currents are in phase and moving along one direction. The main characteristic of a dipolar mode is the high radiation efficiency via far-field emission and the subsequent short lifetime of the plasmon. This results in a broader line width as can be seen by the width of the bowtie, linear rod dimer, disc dimer and single rod structure in Fig. A.11b. The disc dimer geometry, in particular, has by far the highest decay rate among all structures in this study which can be attributed to the overall size of the antenna. The large separation of the accumulated charge densities induces a large dipole moment and facilitates the emission into the far field.

The two structures with the smallest decay rate (nanoslit cavity, two rod cavity) exhibit a quadrupolar charge pattern. The lack of an apparent dipole gives rise to a reduced coupling efficiency with the far field which has been observed in other experimental studies [425, 482]. This kind of resonance is ideal for the study of enhanced light-matter interaction as prolonged plasmon lifetime increases the probability to transfer its energy to an electric excitation.

This study also yields insights on the experimental applicability of the different nanoantennas designs. All of the dimer structures feature their mode maximum enclosed between the two metal particles. In the presence of a substrate this maximum is pulled even further to a location with limited access for a single emitter. This matter of fact poses a great challenge for the experimental realization of an efficiently coupled antenna-emitter ensemble. The nanoslit cavity, however, shows its

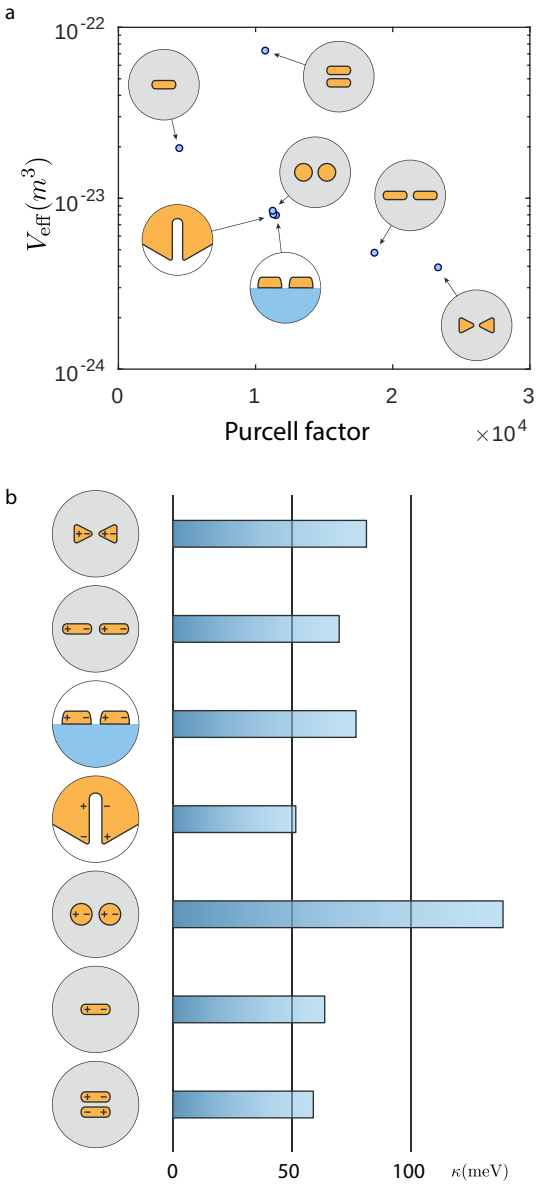

Figure A.11 – Comparison of the mode volume, Purcell factor and linewidth of various nanoantenna geometries. a, Minimum of the mode volume versus the corresponding Purcell factor. **b,** Corresponding linewidth of various nanoantenna geometries. The indicated $+/-$ signs indicate the instantaneous charge distribution of the resonant mode at 800 nm.

field maximum at the open end of the slit which yields a decisive advantage in comparison to the other structures. The full potential of this geometry can be released, in particular, when employed at the apex of a scanning probe tip.

A.8 Optical heating

Non-resonant excitation of a quantum emitter commonly leads to non-radiative decay processes before the exciton reaches the band edge. These decay processes represent a cascaded emission of phonons which ultimately causes heating of the emitter and the surrounding environment. The amount of generated heat P depends on the energy difference between the exciting photon energy and the band gap Δ, as well as the exciton generation rate Λ.

In the experiment, the excitation energy of 2.33 eV and the QD band gap of 1.55 eV leads to a total dissipation energy of $\Delta = 0.78\,\text{eV}$ per absorbed photon. Here, it is assumed that all of the energy contributes to heat generation. The highest excitation power in the experiments is in the range of 700 µW which corresponds to 1.9×10^{15} photons per second. Assuming an absorption efficiency of 10^{-5} the absorbed photons per second are on the order of $\Lambda = 10^{10}$. Therefore, the total heating power can be calculated to $P = \Delta \cdot \Lambda = 1.2\,\text{nW}$.

In this brief estimation, the QD is assumed to be a spherical energy source with a radius $r_{\text{QD}} = 4\,\text{nm}$ in an homogeneous PMMA environment with a thermal conductivity of $k = 0.1\,\frac{\text{W}}{\text{mK}}$. This conductivity value is chosen smaller than reported in the literature [516] in order to account for the real experiment geometry, where one hemisphere is air and has a much smaller k. The temperature distribution $T(r)$ which occurs in the steady state is defined by the heat conduction equation [517, 518]

$$\frac{1}{r^2}\frac{d}{dr}\left(r^2\frac{dT}{dr}\right) + \frac{q}{k} = 0, \tag{A.1}$$

where the heat flux $q = P/4\pi r_{\text{QD}}^2$ originates from the surface of the quantum dot. The solution of this differential equation is given by

$$T(r) = \frac{q r_{\text{QD}}^2}{k}\left(\frac{1}{r} - \frac{1}{r_2}\right) + T_2. \tag{A.2}$$

Here, the distance to the thermal bath r_2 is assumed at infinite distance and the reference temperature T_2 represents ambient conditions (300 K).

The radial temperature distribution is shown in Fig. A.12. At the interface between the QD and the PMMA environment the temperature has a maximum value of 300.24 K and decreases for larger distances to the QD surface.

Based on this estimation it is assumed that the temperature of the QD does not significantly increase during irradiation and does not affect the optical measurements.

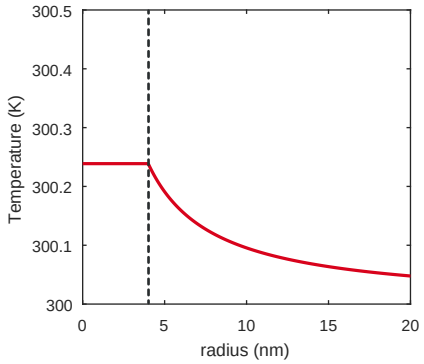

Figure A.12 – Calculated radial temperature distribution for an irradiated quantum dot. At the interface of the QD (radius 4 nm) the temperature reaches 238 mK above room temperature.

B Supplementary Methods and Measurements

B.1 Time-correlation measurements

Characterization of the excited state lifetime as well as photon statistics of quantum emitters requires time-correlated measurements. Depending on the type of measurement, the optical setup features a different excitation as well as detection scheme. A sketch of two different optical setups is shown in Fig. B.1.

Lifetime In order to determine the lifetime of a quantum emitter, it is necessary to use a pulsed light source and a single photon counting unit (Fig. B.1a). The confocal microscope uses a ps-laser source (GE-100, Time-Bandwidth) with a wavelength of $\lambda = 532\,\text{nm}$ to generate laser pulses with a repetition rate of 80 MHz. The corresponding time delay of 12.5 ns between two pulses is shorter than the excited state lifetime of the quantum dots. An electro-optical modulator (Conoptics, Model 350-160) is therefore used to reduce the repetition rate to 8 MHz with a suppression ratio of 300:1. The detection time of fluorescence photons is correlated with the reduced repetition time by a time-correlated counting unit (TimeHarp200, PicoQuant).

The excited state lifetime of a quantum dot depends on its charge state. In addition to a difference in the quantum yield between the 'on' and 'off' state, the decay rate is also significantly different [267]. A time averaged lifetime measurement therefore yields a superposition of the decay dynamics of both states which manifests itself in a bi-exponential decay. An elegant approach to separate these two states is by measuring the 'raw-data' of the QD fluorescence, a technique called time-tagged time-resolved (TTTR). Instead of adding every recorded correlation time τ_c directly to the histogram, this microscopic value τ_c is stored in addition to the macroscopic time t_m which corresponds to the elapsed time since the start of the measurement. This allows to perform offline data evaluation such as plotting the fluorescence timetrace with an arbitrary time resolution or generate the correlation histogram for a selection of photons. As discussed in section 6.1.5 and 6.1.6 it also permits to specifically select the photons from the 'on' or 'off' state.

Auto-Correlation Measurements of the intensity auto-correlation $g^2(\tau)$ are an important tool to quantify how many single emitters are involved in the light emitting process or, most importantly, whether a quantum dot is indeed a single emitter. These measurements are performed with a continuous-wave laser diode at $\lambda = 532\,\text{nm}$ as shown in Fig. B.1b. The fluorescence light is separated via a 50:50 beamsplitter onto two individual single photon counting units. This scheme is known as the Hanburry-Brown and Twiss configuration [15, 519]. A correlation of the time delay between a counting event on each detector yields an auto-correlation statistic of the quantum dot.

For N emitter the auto-correlation function can be described as [520]

$$g^2(\tau) = \frac{N-1}{N} + \frac{1}{N}\left(1 - e^{\frac{\tau-\tau_0}{\gamma_0}}\right), \tag{B.1}$$

where τ_0 is a delay offset and γ_0 represents the sum of the excitation and decay rate of the quantum emitter. A value of $g^2(0) < 1$ indicates the regime of non-classical light with a sub-Poissonian photon statistic [45]. This type of light can only originate from a finite amount of quantum emitters which display spontaneous emission. As the probability to observe two photons simultaneously ($\tau = 0$) is smaller than for any other delay τ it is commonly said that the correlation exhibits *antibunching*. In case of a single emitter the value of $g^2(0)$ can reach a value of zero. If the detected light originates from two quantum emitters or more, $g^2(0)$ has a value of 0.5 or larger.

In the specific case of colloidal quantum dots it is necessary to record the auto-correlation at a low excitation intensity where the probability for biexciton generation is low. These higher order processes impact the correlation and can eventually lead to *bunching* ($g^2(0) > 1$) [391]. The occurrence of QD charging and emission from the 'on' and 'off' state does not impact the auto-correlation as in both cases the single emitter state is preserved.

B.2 Extinction measurements

For this work, extinction measurements of colloidal quantum dots have been carried out in order to estimate the oscillator strength of the optical transitions near the band edge. Since the quantum dots which are used in the experiment are commercially fabricated, information on the optical properties is supplied by the manufacturer. However, in order to confirm that the emitter behave as expected, this data has been re-measured via an optical setup as depicted in Fig. B.2. The broadband light source consists of a pulsed infrared laser source which is coupled to a photonic crystal fiber. The non-linear effects create high harmonics over a broad wavelength range (SpectraK Dual, NKT Photonics, Birkerod, Denmark). Via an acousto-optical tunable filter any wavelength in the visible regime can be selected. A reference detector is used to ensure a constant excitation power. The light is focused onto a glass slide which is covered with a dense film of quantum dots where it is either absorbed, scattered or transmitted. The transmitted light is collected directly above

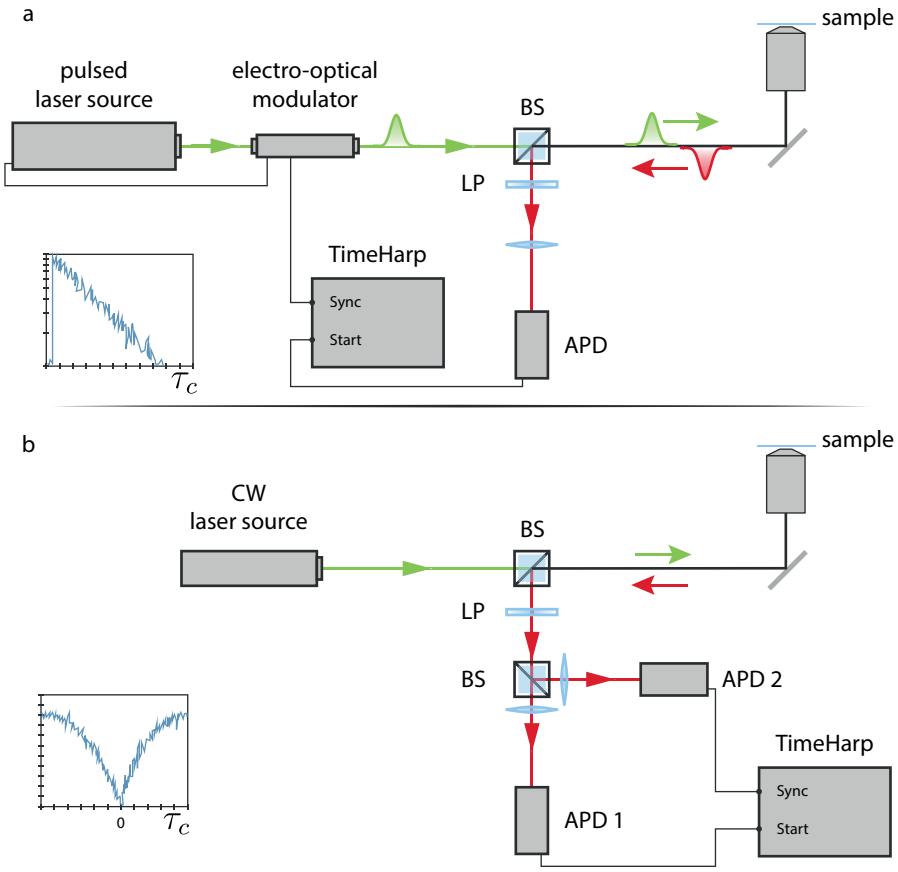

Figure B.1 – Optical setup for time-correlated measurements. **a,** Configuration with a pulsed laser source and a electro-optical modulator to excite the quantum dot. The fluorescence is detected via a 50:50 beamsplitter (BS) and a 540 nm longpass filter (LP) with an avalanche photo diode (APD). **b,** Detection scheme for auto-correlation measurements with a continuous-wave (CW) laser source to excite the quantum dot. A beamsplitter (50:50) is used to detect the fluorescence light with two APDs.

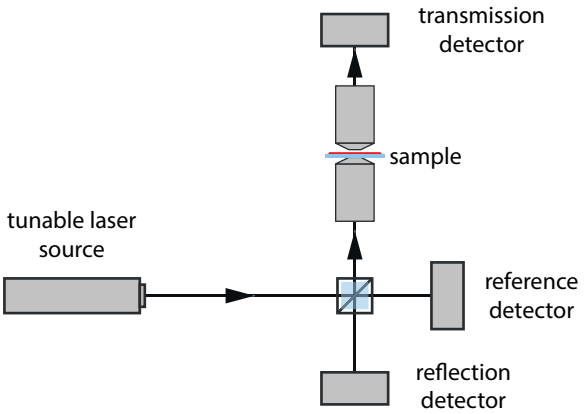

Figure B.2 – Optical setup for extinction measurements.

via collimation and subsequent detection with a photon diode. The scattered light of the quantum dot layer can be detected via the bottom objective which guides the light onto the reflection photo diode. The collected data is sufficient to calculate the extinction coefficient of quantum dots throughout the entire visible wavelength regime.

A crucial information in order to calculate the extinction coefficient of quantum dots is the concentration and layer thickness. Since a precise determination of those values is rather complex and beyond the scope of this work, the extinction measurements are compared qualitatively with the data supplied by the manufacturer (not shown here). The nearly perfect agreement allows to used the calibrate the extinction data $\varepsilon(\lambda)$.

It is important to note that this measurement includes any influence of remaining surfactants as well as functionalization molecules attached to the quantum dot. This is a common uncertainty when measuring the extinction of any emitter. More importantly, this measurement determines the inhomogeneous extinction which does not take into account the charging properties of the quantum dots. On average, there is a certain fraction of QDs which are constantly charged and therefore optically inactive. This measurement therefore underestimates the extinction coefficient which subsequently yields a smaller oscillator strength for a single quantum dot.

B.3 Reversible blueshift

B.3.1 Uncoupled quantum dots

The behavior of isolated QDs in a PMMA matrix on a glass substrate is investigated in absence of a scanning probe. When increasing the excitation rate above the saturation rate a shift of the QD resonance is observed due to increased biexciton (BX) generation [521]. The BX resonance is slightly blueshifted with respect to the single exciton energy and dominates the emission processes for higher excitation rates. In Fig. B.3 it is shown how the normalized spectrum of a QD is reversibly

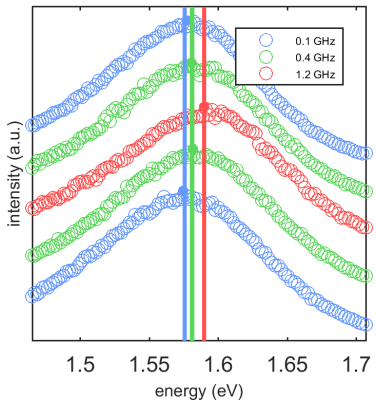

Figure B.3 – QD resonance shift for high excitation rates. The QD resonance exhibits a reversible blueshift when ramping the excitation rate up and down (bottom to top). Blueshifted BX emission dominates the emission for high excitation rates.

blueshifted by ramping the excitation rate up and down (spectra bottom to top). The magnitude of the resonance shift is comparable to the reported few tens of meV [521].

B.3.2 Strongly coupled quantum dots

The excitation power dependent emission spectrum has been studied in the previous section without any scanning probe. During strong coupling with a plasmon resonance, the effect of contribution of biexciton emission also affects the symmetry of the emission spectrum. The spectra of a complete power ramp are shown in Fig. B.4. All spectra are normalized in order to better appreciate their shape. The excitation power values are $0.05, 1, 36, 150, 700\,\mu W$. The acquisition times are adjusted according to the excitation power in order to increase the amount of detected light for low excitation rates and to decrease the amount of irradiation on the QD for high pump rates $(10, 5, 0.5, 0.3, 0.1\,s)$.

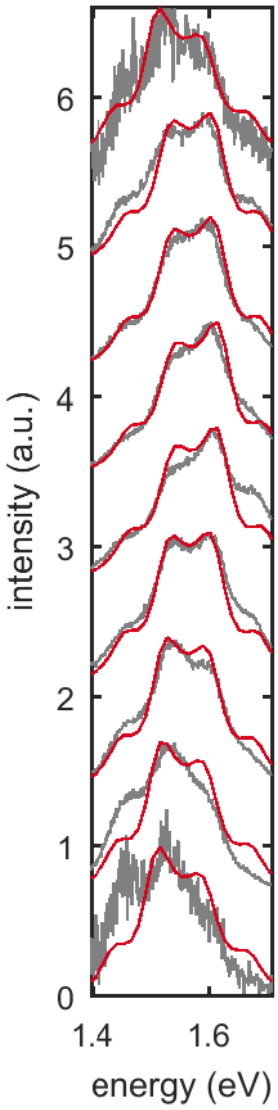

Figure B.4 – Reversible blueshift for increased excitation rates during SC. The spectra of the strongly coupled QD blueshifts as the excitation rate is increased (spectrum # 1- # 5, bottom to middle). Gradual reduction of the excitation rate (spectrum # 6-# 9, middle to top) shows the reverse change of the fluorescence spectra. The measured spectra (gray lines) are overlaid with the spectra obtained from the quantum-model (red lines) where the QD detuning for the neutral and the charged state are individually adjusted.

C

Microtubles Methods

C.1 Sample preparation and optical setup

Chemicals Casein, D-glucose, ATP, catalase, paclitaxel, NH4OH, H2O2, were purchased from Sigma-Aldrich (St. Louis, MO, USA). Glucose oxidase was purchased from SERVA (Heidelberg, Germany). GMPCPP was purchased from Jena Bioscience (Jena, Germany). Ultrapure water was produced in a Milli-Q water purification system from Merck Millipore (Darmstadt, Germany). Ethanol absolute was purchased from VWR (Darmstadt, Germany). mPEG-SH was purchased from Nanocs (New York, NY, USA). Hellmanex III solution was purchased from Omnilab (Bremen, Germany). Mucasol was purchased from Merz Hygiene GmbH (Frankfurt, Germany). Anti-His antibody was purchased from QIAGEN GmbH (Hilden, Germany). Tubulin was purified in house [522]. Biotinylated tubulin was purchased from Cytoskeleton Inc. (Denver, CO, USA). QD655 streptavidin conjugate, DTT, and Protein A/G were purchased from Thermo Fisher Scientific (Waltham, MA, USA).

QD-labelled microtubules Microtubules were polymerized by incubating 20 µg of a 1/100 mixture of biotinylated tubulin and tubulin in 160 µl polymerization buffer (BRB80 with 1 mM GMPCPP) at a temperature of 37°*C* for 2 hours. After spinning down the microtubules in a tabletop microcentrifuge (Heraeus Fresco 17, Thermo Fisher Scientific) at $17000 \times g$ and 23 °C for 20 min, the remaining pellet was resuspended in 85 µl BRB80 with 1 µM paclitaxel. Subsequently, the microtubules were labelled 'in tube' with QDs by incubating them for at least 10 min in BRB80 with 1 µM paclitaxel, 1 mM of ATP, 0.1 mg/ml casein, 10 mM DTT, 20 mM D-glucose, 55 µg/ml glucose oxidase, 11 µg/ml catalase and 1 nM of the QD655 solution.

Motor proteins The purification of full length Dm KHC kinesin 1 expressed in insect cells is described in full detail in [523]. The kinesin motor solution used for the gliding assays consisted of 12 µg/ml full length Dm KHC 6xHis, 10 mM DTT, 1 µM ATP, and 0.2 mg/ml Casein in BRB80.

Sample fabrication The nanoslit sample was fabricated on a 130 µm thick glass coverslip (Gerhard Menzel GmbH, Saarbrücken, Germany). A 3 nm chromium adhesion layer was deposited by electron beam evaporation followed by a 25 nm thick gold layer. Nanoslits were etched into the sample by focused ion beam milling (Helios Nanolab 600 DualBeam, FEI, Hillsboro, OR, USA) with an acceleration voltage of 30 kV and an ion current of 9.7 pA. SEM images of the nano-slit samples were obtained using a scanning electron microscope (Helios Nanolab 600 DualBeam, FEI) at 10 keV.

Sample preparation The sample was cleaned in 2 % Hellmanex III solution by incubation at 23 °C for 5 min. After rinsing the sample for 1 min with ultrapure water an RCA cleaning [524] was performed. For this the sample was incubated at 60 °C for 5 min in an RCA solution (50 ml ultrapure water and 10 ml of 28 % NH_4OH heated to 60 °C, then 10 ml of 30 % H_2O_2 were added). The clean surface was then coated with a self-assembling PEG layer. For this the sample was rinsed for 1 min with ultrapure water, dried with N_2 and then incubated for 12 h in a passivation solution (1 mM 350 Da mPEG SH in ethanol absolute). Finally, the sample was washed in ethanol absolute to remove the unbound PEG and dried with N_2.

QD scanning assay on nanostructured gold samples Flow cells are constructed by thermally bonding the sample to an 'Easy Clean' coverslip (22×50 mm #1; Corning, Wiesbaden, Germany) via spacer strips of parafilm at 60 °C for 1 min (with the gold-coated sample surface inside the resulting flow cell). The 'Easy Clean' procedure includes the following steps: First, the coverslips were sonicated for 15 min in Mucasol diluted in a 1:20 ratio with deionized water. After rinsing them for 2 min with deionized water they were sonicated for 10 min in ethanol absolute. In the next step the coverslips were again rinsed for 2 min with deionized water and then another 2 min with ultrapure water. Finally they were dried with N_2. The flow cells were filled with 0.1 mg/ml Protein A/G in BRB80. After 1 min of incubation, the solution was exchanged with 0.5 mg/ml Casein and in a second step with 2 µm/ml Anti-His antibody in BRB80. After another 1 min of incubation and flushing out the Anti-His antibody with at least two times the channel volume of 0.5 mg/ml Casein in BRB80, 20 µl kinesin motor solution were flushed into the channel. After another 1 min of incubation the solution was exchanged with 20 µl motility solution containing 1 mM ATP (0.22 mg/ml Casein, 22 mM D-glucose, 22 mM DTT, 1 mM ATP, 0.011 mg/ml catalase, 0.11 mg/ml glucose oxidase in BRB80T, 1 µM paclitaxel in BRB80). Finally, 20 µl of QD-labeled microtubules were added and incubated for 5 min, followed by a flush with 20 µl motility solution containing 40 µM ATP. During the measurement the last two steps were repeated every half an hour to replace microtubules which had detached and to ensure the supply with fresh oxygen scavengers and buffer solution.

QD scanning assay on bare glass The flow cell was constructed by thermally bonding two easy clean coverslips (18×18 mm and 22×22 mm, # 1.5, Gerhard

Menzel GmbH) via three parafilm spacers. At both ends of each channel reservoirs were constructed with a two-component silicon glue (picodent twinsil 22, picodent, Wipperfürth, Germany). The flow cell was flushed with 0.5 mg/ml Casein in BRB80. After 5 min the solution in the cell was replaced by a kinesin motor solution (20 µg/ml), 0.2 mg/ml casein, 1 mM ATP and 10 mM DTT in BRB80) which was washed out with a motility solution containing 1 mM ATP (0.22 mg/ml Casein, 22 mM D-glucose, 10 mM DTT, 1 mM ATP, 0.011 mg/ml catalase, 0.011 mg/ml glucose oxidase in BRB80T, 1 µM paclitaxel in BRB80) after 5 min incubation time. Finally, 20 µl of QD-labeled microtubules were added and incubated for 5 min, followed by a flush with 20 µl motility solution containing 1 mM ATP.

Optical setup The optical setup is shown schematically in Fig. 8.1. QDs were imaged using an inverted light microscope (Axio Observer Z3, Carl Zeiss AG, Oberkochen, Germany) equipped with an EMCCD camera (iXon ultra DU-888U3, Andor, Belfast, UK), a C-APOCHROMAT 1.2 NA, x63 water objective (Carl Zeiss AG) and an optovar with 1.6-fold magnification (resulting pixel width: 129 nm). The objective was held at a constant temperature of 20 °C using a self-build water-cooled ring together with a water bath (FC25; Julabo GmbH, Seelbach, Germany). Illumination of the sample was performed with close to parallel illumination (NA < 0.05) in transmission mode using a homebuilt collimator (micro bench system components, LINOS, Göttingen, Germany) and a polarization maintaining glass fibre coupled continuous-wave diode laser (Vortran Laser Technology, Sacramento, CA, USA) operated at 488 nm and 15 mW emission power (5 mW for reference measurements on bare glass, transmittance of the gold layer about 30 %). The excitation light was cleaned up with a 488/10 nm band pass filter (ZET 488/10; Chroma Technology GmbH, Olching, Germany) and the polarization was adjusted parallel to the long axis of the nano-slit structures. The QD655 emission light was filtered using a 655/40 nm band pass filter (655/40 Bright Line HC; Semrock, Rochester, NY, USA). Image streams were taken with 50 ms exposure time (100 ms for reference measurements on bare glass) in frame transfer mode, with the preamp setting '1' (which corresponds to 15.9 electrons per A/D count and 23.8 electrons of RMS readout noise), an EM-gain of 200 and 16 bit A/D-Conversion at a pixel rate of 1 MHz. From these values follows that on average about 335 ± 93 photons were collected from a single QD in each frame.

Data drift correction The drift was determined using stuck QDs as fiducial markers which were identified as follows. First, all fluorescent objects were localized in all frames using the ImageJ plugin ThunderSTORM [525]. The resulting position data were density-filtered to keep only positions occurring in a local radius of 60 nm for at least 15 consecutive frames. Subsequently, the fiducial markers were identified from those residual data by the following criteria: maximum traveling distance of 40 nm between frames and a minimum marker visibility of 15 % in all frames. The mean displacement of all fiducial markers in reference to the first frame was used as drift correction.

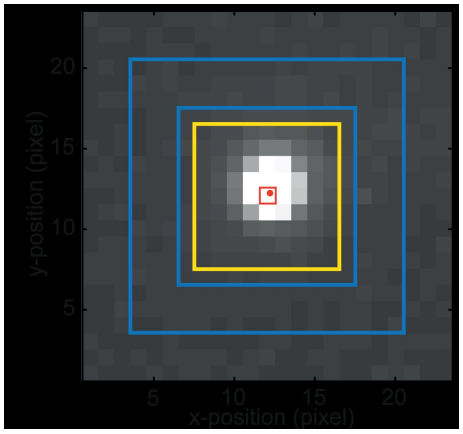

Figure C.1 – Visualization of the intensity analysis from camera data. For each recorded frame, the QD intensity is determined as the sum of pixel values in a 9×9 box around the localized QD position (yellow box). It is backgroundcorrected with the mean of pixel values in the outer region of a 17×17 box around the QD position (blue frame).

C.2 Image data analysis

The analysis of the intensity of each QD was performed as follows. First, QDs were tracked using the image analysis software FIESTA [503]. For each frame, the QD intensity was determined as the total integrated intensity in a 9×9 pixel window around the QD position (yellow box in Fig. C.1). It was background-corrected using the mean pixel value of a 17×17 pixel box around the QD position, but without the central 11×11 pixels (depicted in blue in Fig. C.1). Subsequently, QD positions were reassigned as uniformly distributed along the microtubule gliding path by minimizing the sum of squared distances to the originally tracked positions. The path was determined by a third-degree polynomial fit of the conventionally tracked positions. Occasionally, microtubule-transported QDs passed other QDs which were either also moving, stuck on the surface or, very rarely, diffusing in solution. In order not to distort the intensity analysis by such events, QD tracks with a high standard deviation in the mean background intensity are discarded. For individual QD tracks of several µm in length, the measured intensity values can show a long-range variation of up to 50 % (see Fig. C.2, upper panel). This is caused by inhomogeneous illumination and, possibly, emission fluorescence interference contrast (FLIC) effects [506]. The intensity data were corrected for this by using a 2 µm moving average filter.

$$I_{\mathrm{corr}}(n) = (I(n) - I_{\mathrm{filtered}}(n)) + \langle I_{\mathrm{filtered}} \rangle \tag{C.1}$$

The result of this procedure is shown in Fig. C.2 (lower panel). To obtain near-field interaction profiles, the intensity data were registered as a function of the distance to the slit center line, i.e. projected onto the short slit axis. In order to be able to average these profiles from all individual QDs measured per slit width, it is

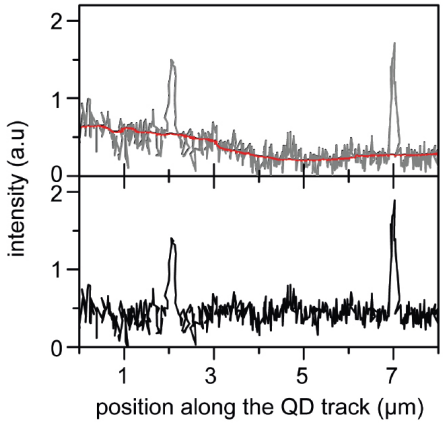

Figure C.2 – Compensation for long-range intensity fluctuations due to uneven illumination. The recorded intensity (gray curve in upper panel) is corrected using a 2 µm moving average filter (red curve) according to equ. C.1. The result of the correction procedure is shown in the lower panel.

required to first normalize the individual profiles to account for different QD brightnesses. For this, the mean on intensity of each QD was determined as described in the following.

A typical background-corrected intensity trace of a single QD (away from a nanoslit) is shown in Fig. C.3a. Due to the characteristic blinking behavior of QDs the intensity fluctuates strongly. The blinking times follow a power law distribution and, therefore, all timescales are covered [254] (this is also true for QDs in proximity of a metallic nanostructure [526]). In combination with the finite exposure time during imaging, this blinking behavior leads to the observation of mixed states [527]. The pure on state intensity can only be observed if the QD is not changing states during the exposure time of one frame. To identify such frames a filter-algorithm is used based on the following conditions. The intensity value has to be at least 80 % of the mean of the 15th to 5th largest values. Furthermore, the difference between its next nearest neighbors and its nearest neighbors should be smaller than 20 % of the mean of the 15th to 5th biggest values. By the latter condition values lying on the edge of a plateau are discarded because it is very likely that they are mixed states. The threshold of 20 % has turned out to perform best in minimizing the difference between mean and median of the resulting values. This is a useful criterion since the values of the pure on-intensities are expected to be normally distributed. Consequently, any intensity traces are discarded where the mean and median differ by more than one standard deviation. In Fig. C.3a the values determined as on-intensities are marked with red crosses. Fig. C.3b shows the distribution of all intensity values of the same trajectory along with the resulting filtered on-intensities and Fig. C.3c shows these distributions for a set of 203 different QDs. As stated above, the mean on intensity of each QD trajectory was used to normalize the intensity values. The distributions of the measured and filtered intensities after normalization with their respective on intensity is shown in Fig. C.3d.

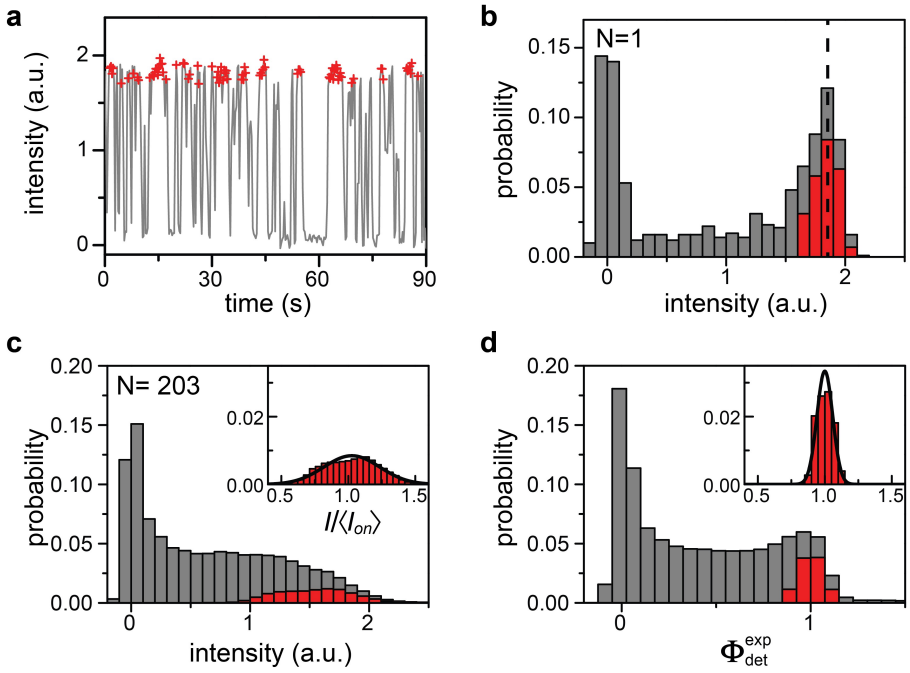

Figure C.3 – Determination of the mean on-intensity of individual QDs. a, Intensity trace of a QD (gray curve) along with the data points identified as QD on-state (+, see text). **b,** Distribution of all intensity values of trajectory shown in **a** (grey bars) along with only the pure on-intensities (red bars). The dashed line indicates the mean value of all on-intensities. **c,** Same as **b** but for a whole set of 203 different QDs. Inset: distribution of on-intensities normalized to the mean on-intensity of all trajectories along with a fit to a normal distribution. **d,** Distributions of intensities (same original data as in **c**) after normalization with their respective on-intensity. Inset: Only normalized on-intensities with finer binning along with a fit to a normal distribution.

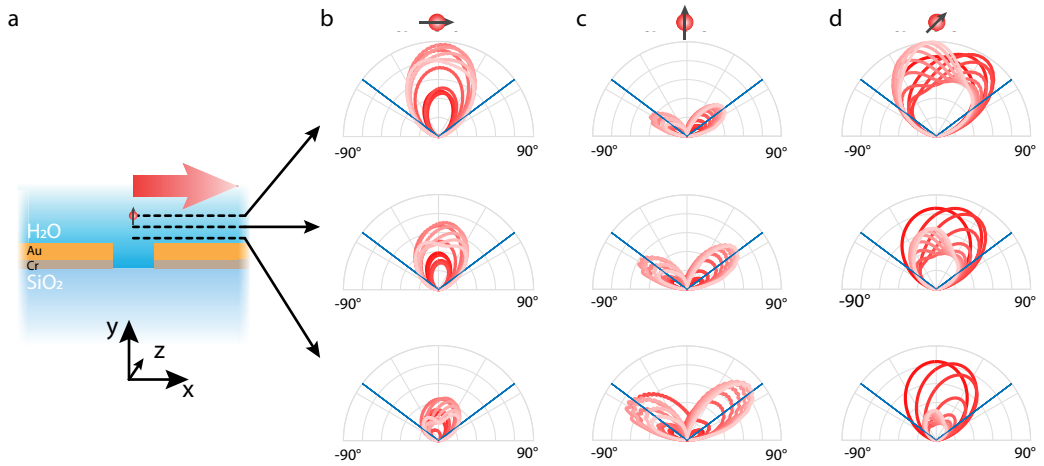

Figure C.4 – Simulated far-field projection density $\Theta_{xyz}(x,y,\phi)$ of an electric dipole oriented in x/y/z direction for various positions above the gold surface. a, Schematic representation of the sample geometry and the dipole position. **b,** Far-field distributions of a dipole oriented along the x axis at three exemplary heights of $y = 10, 30, 50$ nm (bottom to top) and lateral distances to the gap center of $x = 0 \ldots 40 \ldots 400$ nm (red to light red). Blue lines indicate the maximum detectable angle (set by the NA of the objective used in the experiments). **c** and **d,** same as **b** but for a dipole orientated along the y and z axis, respectively.

C.3 Numerical simulations

The excitation field distributions and emission efficiencies were calculated using FDTD simulations. The simulations were performed in 2D and included the SiO_2 substrate, the chromium adhesion layer, the gold layer and the aqueous solution (Fig. C.4a). The simulation volume was enclosed with a perfectly matched absorbing boundary. To determine the field distribution the experimental excitation was mimicked by a 488 nm plane wave source located below the substrate. A 2D field monitor recorded the electric field distribution at all positions above the gold layer.

For calculating the emission efficiency η, far-field projections and local density of states ρ were simulated for distinct emitter positions above the gold surface by using a point dipole source with a wavelength of 655 nm in the otherwise identical environment to simulate the emission of the QD. To account for various orientations of the QD on the rotating microtubule all three point-dipole orientations along the x-, y- and z-axis are simulated separately. A schematic representation of the geometry is depicted in Fig. C.4a.

The far-field projections were calculated via Fourier transformation of the electric field distributions recorded by a 1-D monitor with a lateral span of 20 µm and a height of 70 nm above the gold surface. A set of exemplary far-field projection densities $\Theta_{x,y,z}(x,y,\phi)$ are shown in Fig. C.4b-d for different dipole orientations and several positions (x,y) with respect to the gap. The maximum detectable angle ϕ is set by the numerical aperture of 1.2.

The differences between the shape of $\Theta_{x,y,z}(x,y,\phi)$ for various dipole orienta-

tions and positions can be explained by the variation in coupling efficiency of the emitter to surface plasmons. The calculated far-field projections represent an emitting dipole in the limit of saturation. As the experiments are carried-out well below saturation the far-field projections have to be normalized by the emitted power at the specific location which is proportional to the local density of states. The emitted intensity of the dipole $p_{x,y,z}(x,y)$ was recorded with a box monitor and represents a quantitative measure of the Purcell factor. An increased (decreased) power emission of a dipole is characteristic for an altered emission rate due to the presence of additional (reduced) radiative or non-radiative channels. Consequently, this type of simulation includes all effects such as quenching as well as Purcell enhancement which change the quantum yield of the emitter. Finally, the emission efficiency η is defined for distinct x-y positions above the gold surface by integrating the (power-) normalized far-field projection density $\Phi_{\mathrm{norm,xyz}}(x,y,\phi) = \Theta_{xyz}(x,y,\phi)/p_{x,y,z}(x,y)$ over the detectable angular range which yields

$$\eta(x,y) = \frac{1}{3}\sum_{x,y,z}\int_{NA=1.2}\Theta_{\mathrm{norm,xyz}}(x,y,\phi)d\phi. \tag{C.2}$$

The factor of one third can be approximated to account for the statistical average of all dipole orientations. The detected fluorescence intensity $\Phi(x,y)$ is given by

$$\Phi(x,y) = c\cdot I_{\mathrm{ex}}(x,y)\cdot\eta(x,y), \tag{C.3}$$

where $I_{\mathrm{ex}}(x,y)$ is the local excitation intensity and c accounts for the quantum efficiency of the emitter as well as for the detection setup. When considering an ensemble of fluorescence intensity profiles the y-position is averaged over the mean height of the QD with respect to the gold surface. The fluorescence intensity as described in the main manuscript is then calculated via

$$\Phi(x) = c\cdot\langle I_{\mathrm{ex}}(x,y)\cdot\eta(x,y)\rangle_y. \tag{C.4}$$

Here, an equal probability of the QD height is assumed throughout the range between $y = 15\,\mathrm{nm}$ and 55 nm. The maximum height of 55 nm is based on 17 nm free height of a gliding microtubule above the surface [506] plus 20 nm diameter of the microtubule plus 13 nm due to the QD radius. The minimum height of 15 nm is based on a 13 nm QD radius plus a 2 nm height of the casein passivation layer when the QD is pushed toward the surface underneath the microtubule. It is noted that full 3D simulations would yield a complete far-field projection and therefore more accurate representation compared to a linecut in the x-y plane. However, a 3D simulation would significantly increase the amount of necessary computation time by orders of magnitude to an extent which is not practical in view of the parameter scans required for the analysis. Individual 3D simulations for selected geometries have been carried out as shown in Fig. C.5 (upper row). Here, the 3D far-field pattern is shown for a dipole with different orientations at a height of $y = 5\,\mathrm{nm}$ above the gold surface and a distance of $x = 20\,\mathrm{nm}$ from the center of a 238 nm gap. Along the plane of $\cos(\theta) = 0$ the far-field projections between 2D and 3D simulations display a perfect agreement as shown in Fig. C.5 (bottom row).

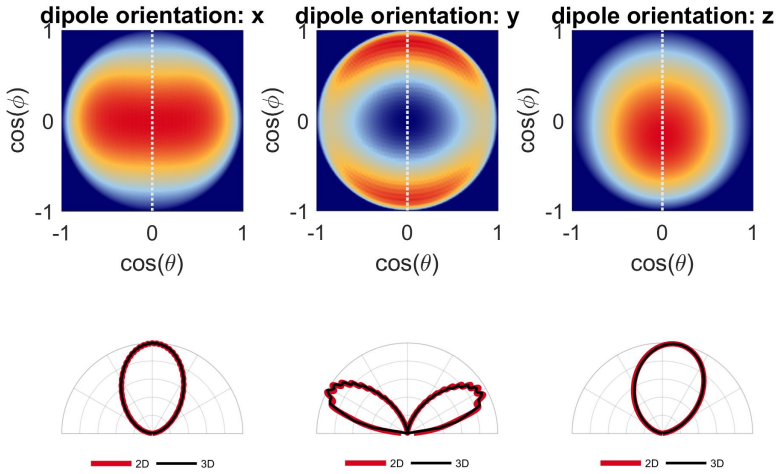

Figure C.5 – Comparison of the far-field emission pattern between 2D and 3D simulations. (upper row) 3D far-field pattern of a dipole at position $x = 20\,\text{nm}$, $y = 5\,\text{nm}$ for a 238 nm gap (normalized to 1). Each dipole orientation shows a different pattern due to different coupling and emission properties. The dashed line shows the plane of the 2D simulations. (bottom row) Comparison of the 2D and 3D simulations for $\cos(\theta) = 0$.

Bibliography

[1] Reithmaier, J. P. *et al.* Strong coupling in a single quantum dot–semiconductor microcavity system. *Nature* **432**, 197–200 (2004).

[2] Yoshie, T. *et al.* Vacuum Rabi splitting with a single quantum dot in a photonic crystal nanocavity. *Nature* **432**, 200–203 (2004).

[3] Peter, E. *et al.* Exciton-Photon Strong-Coupling Regime for a Single Quantum Dot Embedded in a Microcavity. *Physical Review Letters* **95**, 067401 (2005).

[4] Muhlschlegel, P. Resonant Optical Antennas. *Science* **308**, 1607–1609 (2005).

[5] Schuller, J. A. *et al.* Plasmonics for extreme light concentration and manipulation. *Nature Materials* **9**, 193–204 (2010).

[6] Curto, A. G. *et al.* Unidirectional Emission of a Quantum Dot Coupled to a Nanoantenna. *Science* **329**, 930–933 (2010).

[7] Kinkhabwala, A. *et al.* Large single-molecule fluorescence enhancements produced by a bowtie nanoantenna. *Nature Photonics* **3**, 654–657 (2009).

[8] Duan, H., Fernández-Domínguez, A. I., Bosman, M., Maier, S. A. & Yang, J. K. W. Nanoplasmonics: Classical down to the Nanometer Scale. *Nano Letters* **12**, 1683–1689 (2012).

[9] Boca, A. *et al.* Observation of the Vacuum Rabi Spectrum for One Trapped Atom. *Physical Review Letters* **93**, 233603 (2004).

[10] Pelton, M. Modified spontaneous emission in nanophotonic structures. *Nature Photonics* **9**, 427–435 (2015).

[11] Snijders, H. *et al.* Purification of a single-photon nonlinearity. *Nature Communications* **7**, 12578 (2016).

[12] Javadi, A. *et al.* Single-photon non-linear optics with a quantum dot in a waveguide. *Nature Communications* **6**, 8655 (2015).

[13] Chikkaraddy, R. *et al.* Single-molecule strong coupling at room temperature in plasmonic nanocavities. *Nature* **535**, 127–130 (2016).

[14] Farahani, J. N., Pohl, D. W., Eisler, H.-J. & Hecht, B. Single Quantum Dot Coupled to a Scanning Optical Antenna: A Tunable Superemitter. *Physical Review Letters* **95**, 017402 (2005).

[15] Novotny, L. & Hecht, B. *Principles of Nano-Optics* (Cambridge University Press, Cambridge, 2012), 2 edn.

[16] Johnson, P. & Christy, R. Optical constants of the noble metals. *Physical Review B* **6**, 4370–4379 (1972).

[17] Khurgin, J. B. How to deal with the loss in plasmonics and metamaterials. *Nature nanotechnology* **10**, 2–6 (2015).

[18] Khurgin, J. B. & Sun, G. In search of the elusive lossless metal. *Applied Physics Letters* **96**, 181102 (2010).

[19] Ozbay, E. Plasmonics: Merging Photonics and Electronics at Nanoscale Dimensions. *Science* **311**, 189–193 (2006).

[20] Naik, G. V., Shalaev, V. M. & Boltasseva, A. Alternative Plasmonic Materials: Beyond Gold and Silver. *Advanced Materials* **25**, 3264–3294 (2013).

[21] Boltasseva, A. & Atwater, H. A. Low-Loss Plasmonic Metamaterials. *Science* **331**, 290–291 (2011).

[22] Blaber, M. G., Arnold, M. D. & Ford, M. J. Optical properties of intermetallic compounds from first principles calculations: A search for the ideal plasmonic material. *Journal of Physics: Condensed Matter* **21**, 144211 (2009).

[23] Ndukaife, J. C., Shalaev, V. M. & Boltasseva, A. Plasmonics—turning loss into gain. *Science* **351**, 334–335 (2016).

[24] Miller, O. D. *et al.* Fundamental limits to optical response in absorptive systems. *Optics Express* **24**, 3329–3364 (2016).

[25] Stockman, M. I. Criterion for Negative Refraction with Low Optical Losses from a Fundamental Principle of Causality. *Physical Review Letters* **98**, 177404 (2007).

[26] Dimmock, J. O. Losses in left-handed materials. *Optics Express* **11**, 2397–2402 (2003).

[27] Economou, E. N. Surface Plasmons in Thin Films. *Physical Review* **182**, 539–554 (1969).

[28] Szentirmay, Z. Slow-mode surface plasma oscillations in layered structures. *Physical Review B* **36**, 2607–2613 (1987).

[29] Zia, R., Selker, M. D., Catrysse, P. B. & Brongersma, M. L. Geometries and materials for subwavelength surface plasmon modes. *JOSA A* **21**, 2442–2446 (2004).

[30] Bozhevolnyi, S. I. (ed.) *Plasmonic Nanoguides and Circuits* (Distributed by World Scientific Pub, Singapore; Hackensack, NJ, 2009). OCLC: ocn234380367.

[31] Dionne, J. A., Sweatlock, L. A., Atwater, H. A. & Polman, A. Plasmon slot waveguides: Towards chip-scale propagation with subwavelength-scale localization. *Physical Review B* **73**, 035407 (2006).

[32] Sarid, D. Long-Range Surface-Plasma Waves on Very Thin Metal Films. *Physical Review Letters* **47**, 1927–1930 (1981).

[33] Barnard, E. S., White, J. S., Chandran, A. & Brongersma, M. L. Spectral properties of plasmonic resonator antennas. *Optics Express* **16**, 16529–16537 (2008).

[34] Miyazaki, H. & Kurokawa, Y. Squeezing Visible Light Waves into a 3-nm-Thick and 55-nm-Long Plasmon Cavity. *Physical Review Letters* **96** (2006).

[35] Miyazaki, H. T. & Kurokawa, Y. Controlled plasmon resonance in closed metal/insulator/metal nanocavities. *Applied Physics Letters* **89**, 211126 (2006).

[36] Chandran, A., Barnard, E. S., White, J. S. & Brongersma, M. L. Metal-dielectric-metal surface plasmon-polariton resonators. *Physical Review B* **85**, 085416 (2012).

[37] Gordon, R. Light in a subwavelength slit in a metal: Propagation and reflection. *Physical Review B* **73**, 153405 (2006).

[38] Kurokawa, Y. & Miyazaki, H. T. Metal-insulator-metal plasmon nanocavities: Analysis of optical properties. *Physical Review B* **75**, 035411 (2007).

[39] Shen, H. *et al.* Molecule fluorescence modified by a slit-based nanoantenna with dual gratings. *Journal of the Optical Society of America B* **30**, 2420 (2013).

[40] Polyakov, A. *et al.* Plasmon resonance tuning in metallic nanocavities. *Scientific Reports* **2**, 933 (2012).

[41] Lindberg, J., Lindfors, K., Setälä, T., Kaivola, M. & Friberg, A. T. Spectral analysis of resonant transmission of light through a single sub-wavelength slit. *Optics Express* **12**, 623–632 (2004).

[42] Feichtner, T., Christiansen, S. & Hecht, B. Mode Matching for Optical Antennas. *Physical Review Letters* **119**, 217401 (2017).

[43] Khitrova, G., Gibbs, H. M., Kira, M., Koch, S. W. & Scherer, A. Vacuum Rabi splitting in semiconductors. *Nature Physics* **2**, 81–90 (2006).

[44] Hood, C. J., Chapman, M. S., Lynn, T. W. & Kimble, H. J. Real-Time Cavity QED with Single Atoms. *Physical Review Letters* **80**, 4157–4160 (1998).

[45] Fox, M. *Quantum Optics: An Introduction*. No. 15 in Oxford Master Series in Physics (Oxford University Press, Oxford; New York, 2006).

[46] Lalanne, P., Sauvan, C. & Hugonin, J. Photon confinement in photonic crystal nanocavities. *Laser & Photonics Reviews* **2**, 514–526 (2008).

[47] Sorger, V. J., Oulton, R. F., Yao, J., Bartal, G. & Zhang, X. Plasmonic Fabry-Pérot Nanocavity. *Nano Letters* **9**, 3489–3493 (2009).

[48] Gerry, C. C. & Knight, P. *Introductory Quantum Optics* (Cambridge University Press, Cambridge, UK; New York, 2005). OCLC: 79900897.

[49] Jain, P. K., Lee, K. S., El-Sayed, I. H. & El-Sayed, M. A. Calculated Absorption and Scattering Properties of Gold Nanoparticles of Different Size, Shape, and Composition: Applications in Biological Imaging and Biomedicine. *The Journal of Physical Chemistry B* **110**, 7238–7248 (2006).

[50] Zengin, G. *et al.* Realizing Strong Light-Matter Interactions between Single-Nanoparticle Plasmons and Molecular Excitons at Ambient Conditions. *Physical Review Letters* **114**, 157401 (2015).

[51] Hilborn, R. C. Einstein coefficients, cross sections, f values, dipole moments, and all that. *American Journal of Physics* **50**, 982–986 (1982).

[52] Baranov, D. G., Wersäll, M., Cuadra, J., Antosiewicz, T. J. & Shegai, T. Novel Nanostructures and Materials for Strong Light–Matter Interactions. *ACS Photonics* **5**, 24–42 (2017).

[53] Simpson, W. M. R. & Leonhardt, U. (eds.) *Forces of the Quantum Vacuum: An Introduction to Casimir Physics* (World Scientific, Hackensack, New Jersey, 2015).

[54] Weisskopf, V. & Wigner, E. Berechnung der natürlichen Linienbreite auf Grund der Diracschen Lichttheorie. *Zeitschrift für Physik* **63**, 54–73 (1930).

[55] Loudon, R. *The Quantum Theory of Light*. Oxford Science Publications (Oxford University Press, Oxford; New York, 2000), 3rd ed edn.

[56] Mollow, B. R. Power Spectrum of Light Scattered by Two-Level Systems. *Physical Review* **188**, 1969–1975 (1969).

[57] Grove, R. E., Wu, F. Y. & Ezekiel, S. Measurement of the spectrum of resonance fluorescence from a two-level atom in an intense monochromatic field. *Physical Review A* **15**, 227–233 (1977).

[58] McCall, S. L. & Hahn, E. L. Self-Induced Transparency. *Physical Review* **183**, 457–485 (1969).

[59] Gibbs, H. M. Spontaneous Decay of Coherently Excited Rb. *Physical Review Letters* **29**, 459–462 (1972).

[60] Gibbs, H. M. Incoherent Resonance Fluorescence from a Rb Atomic Beam Excited by a Short Coherent Optical Pulse. *Physical Review A* **8**, 446–455 (1973).

[61] Greffet, J.-J. Plasmonic Nanoantennas. In *World Scientific Handbook of Metamaterials and Plasmonics*, World Scientific Series in Nanoscience and Nanotechnology, 21–66 (World Scientific, 2017).

[62] Belacel, C. *et al.* Controlling Spontaneous Emission with Plasmonic Optical Patch Antennas. *Nano Letters* **13**, 1516–1521 (2013).

[63] Muskens, O. L., Giannini, V., Sánchez-Gil, J. A. & Gómez Rivas, J. Strong Enhancement of the Radiative Decay Rate of Emitters by Single Plasmonic Nanoantennas. *Nano Letters* **7**, 2871–2875 (2007).

[64] Yuan, C. T. *et al.* Modification of Fluorescence Properties in Single Colloidal Quantum Dots by Coupling to Plasmonic Gap Modes. *The Journal of Physical Chemistry C* **117**, 12762–12768 (2013).

[65] Ratchford, D., Shafiei, F., Kim, S., Gray, S. K. & Li, X. Manipulating Coupling between a Single Semiconductor Quantum Dot and Single Gold Nanoparticle. *Nano Letters* **11**, 1049–1054 (2011).

[66] Esteban, R., Teperik, T. V. & Greffet, J. J. Optical Patch Antennas for Single Photon Emission Using Surface Plasmon Resonances. *Physical Review Letters* **104**, 026802 (2010).

[67] Tam, F., Goodrich, G. P., Johnson, B. R. & Halas, N. J. Plasmonic Enhancement of Molecular Fluorescence. *Nano Letters* **7**, 496–501 (2007).

[68] Russell, K. J., Liu, T.-L., Cui, S. & Hu, E. L. Large spontaneous emission enhancement in plasmonic nanocavities. *Nature Photonics* **6**, 459–462 (2012).

[69] Hoang, T. B., Akselrod, G. M. & Mikkelsen, M. H. Ultrafast Room-Temperature Single Photon Emission from Quantum Dots Coupled to Plasmonic Nanocavities. *Nano Letters* **16**, 270–275 (2015).

[70] Hoang, T. B. *et al.* Ultrafast spontaneous emission source using plasmonic nanoantennas. *Nature Communications* **6**, 7788 (2015).

[71] Akselrod, G. M. *et al.* Probing the mechanisms of large Purcell enhancement in plasmonic nanoantennas. *Nature Photonics* (2014).

[72] Kühn, S., Håkanson, U., Rogobete, L. & Sandoghdar, V. Enhancement of Single-Molecule Fluorescence Using a Gold Nanoparticle as an Optical Nanoantenna. *Physical Review Letters* **97**, 017402 (2006).

[73] Anger, P., Bharadwaj, P. & Novotny, L. Enhancement and Quenching of Single-Molecule Fluorescence. *Physical Review Letters* **96**, 113002 (2006).

[74] Luo, Y. *et al.* Purcell-enhanced quantum yield from carbon nanotube excitons coupled to plasmonic nanocavities. *Nature Communications* **8** (2017).

[75] Ringler, M. *et al.* Shaping Emission Spectra of Fluorescent Molecules with Single Plasmonic Nanoresonators. *Physical Review Letters* **100**, 203002 (2008).

[76] Zhao, L., Ming, T., Chen, H., Liang, Y. & Wang, J. Plasmon-induced modulation of the emission spectra of the fluorescent molecules near gold nanorods. *Nanoscale* **3**, 3849–3859 (2011).

[77] Ming, T., Chen, H., Jiang, R., Li, Q. & Wang, J. Plasmon-Controlled Fluorescence: Beyond the Intensity Enhancement. *The Journal of Physical Chemistry Letters* **3**, 191–202 (2012).

[78] Munechika, K. *et al.* Spectral Control of Plasmonic Emission Enhancement from Quantum Dots near Single Silver Nanoprisms. *Nano Letters* **10**, 2598–2603 (2010).

[79] Le Ru, E. C. *et al.* Mechanisms of Spectral Profile Modification in Surface-Enhanced Fluorescence. *The Journal of Physical Chemistry C* **111**, 16076–16079 (2007).

[80] Chen, Y., Munechika, K. & Ginger, D. S. Dependence of Fluorescence Intensity on the Spectral Overlap between Fluorophores and Plasmon Resonant Single Silver Nanoparticles. *Nano Letters* **7**, 690–696 (2007).

[81] Neumann, L., van 't Oever, J. & van Hulst, N. F. A Resonant Scanning Dipole-Antenna Probe for Enhanced Nanoscale Imaging. *Nano Letters* **13**, 5070–5074 (2013).

[82] Taminiau, T. H., Stefani, F. D., Segerink, F. B. & van Hulst, N. F. Optical antennas direct single-molecule emission. *Nature Photonics* **2**, 234–237 (2008).

[83] Raab, M., Vietz, C., Stefani, F. D., Acuna, G. P. & Tinnefeld, P. Shifting molecular localization by plasmonic coupling in a single-molecule mirage. *Nature Communications* **8**, 13966 (2017).

[84] Santhosh, K., Bitton, O., Chuntonov, L. & Haran, G. Vacuum Rabi splitting in a plasmonic cavity at the single quantum emitter limit. *Nature Communications* **7**, 11823 (2016).

[85] Liao, H. Biomedical applications of plasmon resonant metal nanoparticles. *Nanomedicine* **1**, 201–208 (2006).

[86] Lakowicz, J. R. Plasmonics in Biology and Plasmon-Controlled Fluorescence. *Plasmonics* **1**, 5–33 (2006).

[87] Jaynes, E. T. & Cummings, F. W. Comparison of quantum and semiclassical radiation theories with application to the beam maser. *Proceedings of the IEEE* **51**, 89–109 (1963).

[88] Cummings, F. W. Stimulated Emission of Radiation in a Single Mode. *Physical Review* **140**, A1051–A1056 (1965).

[89] Eberly, J. H., Narozhny, N. B. & Sanchez-Mondragon, J. J. Periodic Spontaneous Collapse and Revival in a Simple Quantum Model. *Physical Review Letters* **44**, 1323–1326 (1980).

[90] Novotny, L. Strong coupling, energy splitting, and level crossings: A classical perspective. *American Journal of Physics* **78**, 1199–1202 (2010).

[91] Wersäll, M., Cuadra, J., Antosiewicz, T. J., Balci, S. & Shegai, T. Observation of Mode Splitting in Photoluminescence of Individual Plasmonic Nanoparticles Strongly Coupled to Molecular Excitons. *Nano Letters* **17**, 551–558 (2017).

[92] Yang, Z.-J., Antosiewicz, T. J. & Shegai, T. Role of material loss and mode volume of plasmonic nanocavities for strong plasmon-exciton interactions. *Optics Express* **24**, 20373 (2016).

[93] Wu, X., Gray, S. K. & Pelton, M. Quantum-dot-induced transparency in a nanoscale plasmonic resonator. *Optics Express* **18**, 23633–23645 (2010).

[94] Savasta, S. *et al.* Nanopolaritons: Vacuum Rabi Splitting with a Single Quantum Dot in the Center of a Dimer Nanoantenna. *ACS Nano* **4**, 6369–6376 (2010).

[95] Schlather, A. E., Large, N., Urban, A. S., Nordlander, P. & Halas, N. J. Near-Field Mediated Plexcitonic Coupling and Giant Rabi Splitting in Individual Metallic Dimers. *Nano Letters* **13**, 3281–3286 (2013).

[96] Zheng, D. *et al.* Manipulating Coherent Plasmon–Exciton Interaction in a Single Silver Nanorod on Monolayer WSe2. *Nano Letters* **17**, 3809–3814 (2017).

[97] Törmä, P. & Barnes, W. L. Strong coupling between surface plasmon polaritons and emitters: A review. *Reports on Progress in Physics* **78**, 013901 (2015).

[98] Van Vlack, C., Kristensen, P. T. & Hughes, S. Spontaneous emission spectra and quantum light-matter interactions from a strongly coupled quantum dot metal-nanoparticle system. *Physical Review B* **85**, 075303 (2012).

[99] Gonzalez-Tudela, A. *et al.* Effect of pure dephasing on the Jaynes-Cummings nonlinearities. *Optics Express* **18**, 7002–7009 (2010).

[100] Maier, S. A. Plasmonic field enhancement and SERS in the effective mode volume picture. *Optics Express* **14**, 1957–1964 (2006).

[101] Biagioni, P., Huang, J. S. & Hecht, B. Nanoantennas for visible and infrared radiation. *Reports on Progress in Physics* **75**, 024402 (2012).

[102] del Valle, E., Laussy, F. P. & Tejedor, C. Luminescence spectra of quantum dots in microcavities. II. Fermions. *Physical Review B* **79**, 235326 (2009).

[103] Bellessa, J., Bonnand, C., Plenet, J. C. & Mugnier, J. Strong Coupling between Surface Plasmons and Excitons in an Organic Semiconductor. *Physical Review Letters* **93**, 036404 (2004).

[104] Gómez, D. E., Vernon, K. C., Mulvaney, P. & Davis, T. J. Surface Plasmon Mediated Strong Exciton-Photon Coupling in Semiconductor Nanocrystals. *Nano Letters* **10**, 274–278 (2010).

[105] Vasa, P. *et al.* Ultrafast Manipulation of Strong Coupling in Metal-Molecular Aggregate Hybrid Nanostructures. *ACS Nano* **4**, 7559–7565 (2010).

[106] Vasa, P. *et al.* Real-time observation of ultrafast Rabi oscillations between excitons and plasmons in metal nanostructures with J-aggregates. *Nature Photonics* **7**, 128–132 (2013).

[107] Sugawara, Y., Kelf, T. A., Baumberg, J. J., Abdelsalam, M. E. & Bartlett, P. N. Strong Coupling between Localized Plasmons and Organic Excitons in Metal Nanovoids. *Physical Review Letters* **97**, 266808 (2006).

[108] Fofang, N. T. *et al.* Plexcitonic Nanoparticles: Plasmon-Exciton Coupling in Nanoshell-J-Aggregate Complexes. *Nano Letters* **8**, 3481–3487 (2008).

[109] Zheng, Y. B. *et al.* Dynamic Tuning of Plasmon–Exciton Coupling in Arrays of Nanodisk–J-aggregate Complexes. *Advanced Materials* **22**, 3603–3607 (2010).

[110] Fofang, N. T., Grady, N. K., Fan, Z., Govorov, A. O. & Halas, N. J. Plexciton Dynamics: Exciton-Plasmon Coupling in a J-Aggregate-Au Nanoshell Complex Provides a Mechanism for Nonlinearity. *Nano Letters* **11**, 1556–1560 (2011).

[111] Eizner, E., Avayu, O., Ditcovski, R. & Ellenbogen, T. Aluminum Nanoantenna Complexes for Strong Coupling between Excitons and Localized Surface Plasmons. *Nano Letters* **15**, 6215–6221 (2015).

[112] Zengin, G. *et al.* Evaluating Conditions for Strong Coupling between Nanoparticle Plasmons and Organic Dyes Using Scattering and Absorption Spectroscopy. *The Journal of Physical Chemistry C* **120**, 20588–20596 (2016).

[113] Roller, E.-M., Argyropoulos, C., Högele, A., Liedl, T. & Pilo-Pais, M. Plasmon–Exciton Coupling Using DNA Templates. *Nano Letters* **16**, 5962–5966 (2016).

[114] Melnikau, D. *et al.* Rabi Splitting in Photoluminescence Spectra of Hybrid Systems of Gold Nanorods and J-Aggregates. *The Journal of Physical Chemistry Letters* **7**, 354–362 (2016).

[115] Ramezani, M. *et al.* Plasmon-exciton-polariton lasing. *Optica* **4**, 31–37 (2017).

[116] Efremushkin, L., Sukharev, M. & Salomon, A. Molecular Plasmonics: Strong Coupling at the Low Molecular Density Limit. *The Journal of Physical Chemistry C* **121**, 14819–14825 (2017).

[117] Stete, F., Koopman, W. & Bargheer, M. Signatures of Strong Coupling on Nanoparticles: Revealing Absorption Anticrossing by Tuning the Dielectric Environment. *ACS Photonics* **4**, 1669–1676 (2017).

[118] Thomas, R. *et al.* Plexcitons: The Role of Oscillator Strengths and Spectral Widths in Determining Strong Coupling. *ACS Nano* (2017).

[119] Kato, F. *et al.* Active Tuning of Strong Coupling States between Dye Excitons and Localized Surface Plasmons via Electrochemical Potential Control. *ACS Photonics* (2018).

[120] Chen, X. *et al.* Mode Modification of Plasmonic Gap Resonances Induced by Strong Coupling with Molecular Excitons. *Nano Letters* **17**, 3246–3251 (2017).

[121] Zengin, G. *et al.* Approaching the strong coupling limit in single plasmonic nanorods interacting with J-aggregates. *Scientific Reports* **3** (2013).

[122] Hartsfield, T. *et al.* Single quantum dot controls a plasmonic cavity's scattering and anisotropy. *Proceedings of the National Academy of Sciences* **112**, 12288–12292 (2015).

[123] Liu, R. *et al.* Strong Light-Matter Interactions in Single Open Plasmonic Nanocavities at the Quantum Optics Limit. *Physical Review Letters* **118**, 237401 (2017).

[124] Antosiewicz, T. J., Apell, S. P. & Shegai, T. Plasmon–Exciton Interactions in a Core–Shell Geometry: From Enhanced Absorption to Strong Coupling. *ACS Photonics* **1**, 454–463 (2014).

[125] Chen, H., Shao, L., Woo, K. C., Wang, J. & Lin, H.-Q. Plasmonic–Molecular Resonance Coupling: Plasmonic Splitting versus Energy Transfer. *The Journal of Physical Chemistry C* **116**, 14088–14095 (2012).

[126] Chen, X.-W., Sandoghdar, V. & Agio, M. Coherent Interaction of Light with a Metallic Structure Coupled to a Single Quantum Emitter: From Superabsorption to Cloaking. *Physical Review Letters* **110**, 153605 (2013).

[127] Demetriadou, A. *et al.* Spatiotemporal Dynamics and Control of Strong Coupling in Plasmonic Nanocavities. *ACS Photonics* **4**, 2410–2418 (2017).

[128] Faggiani, R., Yang, J. & Lalanne, P. Quenching, Plasmonic, and Radiative Decays in Nanogap Emitting Devices. *ACS Photonics* **2**, 1739–1744 (2015).

[129] Filter, R., Słowik, K., Straubel, J., Lederer, F. & Rockstuhl, C. Nanoantennas for ultrabright single photon sources. *Optics Letters* **39**, 1246 (2014).

[130] Hakami, J., Wang, L. & Zubairy, M. S. Spectral properties of a strongly coupled quantum-dot–metal-nanoparticle system. *Physical Review A* **89**, 053835 (2014).

[131] Li, R.-Q., Hernángomez-Pérez, D., García-Vidal, F. J. & Fernández-Domínguez, A. I. Transformation Optics Approach to Plasmon-Exciton Strong Coupling in Nanocavities. *Physical Review Letters* **117**, 107401 (2016).

[132] Nerkararyan, K. V. & Bozhevolnyi, S. I. Entanglement of two qubits mediated by a localized surface plasmon. *Physical Review B* **92**, 045410 (2015).

[133] Sauvan, C., Hugonin, J. P., Maksymov, I. S. & Lalanne, P. Theory of the Spontaneous Optical Emission of Nanosize Photonic and Plasmon Resonators. *Physical Review Letters* **110** (2013).

[134] Yang, J., Perrin, M. & Lalanne, P. Analytical Formalism for the Interaction of Two-Level Quantum Systems with Metal Nanoresonators. *Physical Review X* **5** (2015).

[135] Shah, R. A., Scherer, N. F., Pelton, M. & Gray, S. K. Ultrafast reversal of a Fano resonance in a plasmon-exciton system. *Physical Review B* **88**, 075411 (2013).

[136] Waks, E. & Sridharan, D. Cavity QED treatment of interactions between a metal nanoparticle and a dipole emitter. *Physical Review A* **82**, 043845 (2010).

[137] Zhang, P., Protsenko, I., Sandoghdar, V. & Chen, X.-W. A Single-Emitter Gain Medium for Bright Coherent Radiation from a Plasmonic Nanoresonator. *ACS Photonics* **4**, 2738–2744 (2017).

[138] Trügler, A. & Hohenester, U. Strong coupling between a metallic nanoparticle and a single molecule. *Physical Review B* **77**, 115403 (2008).

[139] Słowik, K., Filter, R., Straubel, J., Lederer, F. & Rockstuhl, C. Strong coupling of optical nanoantennas and atomic systems. *Physical Review B* **88**, 195414 (2013).

[140] Sáez-Blázquez, R., Feist, J., Fernández-Domínguez, A. I. & García-Vidal, F. J. Enhancing photon correlations through plasmonic strong coupling. *Optica* **4**, 1363–1367 (2017).

[141] Ridolfo, A., Di Stefano, O., Fina, N., Saija, R. & Savasta, S. Quantum Plasmonics with Quantum Dot-Metal Nanoparticle Molecules: Influence of the Fano Effect on Photon Statistics. *Physical Review Letters* **105**, 263601 (2010).

[142] Ren, J. *et al.* Evanescent-Vacuum-Enhanced Photon-Exciton Coupling and Fluorescence Collection. *Physical Review Letters* **118**, 073604 (2017).

[143] Otten, M. *et al.* Origins and optimization of entanglement in plasmonically coupled quantum dots. *Physical Review A* **94**, 022312 (2016).

[144] Ko, M.-C. *et al.* Control of the Optical Response of an Artificial Hybrid Nanosystem Due to the Plasmon-Exciton Plasmon Coupling Effect. *arXiv:1708.06636 [physics]* (2017). 1708.06636.

[145] Hümmer, T., García-Vidal, F. J., Martín-Moreno, L. & Zueco, D. Weak and strong coupling regimes in plasmonic QED. *Physical Review B* **87**, 115419 (2013).

[146] He, Y., Jiang, C., Chen, B., Li, J.-J. & Zhu, K.-D. Optical determination of vacuum Rabi splitting in a semiconductor quantum dot induced by a metal nanoparticle. *Optics Letters* **37**, 2943–2945 (2012).

[147] González-Tudela, A., Huidobro, P. A., Martín-Moreno, L., Tejedor, C. & García-Vidal, F. J. Reversible dynamics of single quantum emitters near metal-dielectric interfaces. *Physical Review B* **89**, 041402 (2014).

[148] Ge, R.-C., Van Vlack, C., Yao, P., Young, J. F. & Hughes, S. Accessing quantum nanoplasmonics in a hybrid quantum dot-metal nanosystem: Mollow triplet of a quantum dot near a metal nanoparticle. *Physical Review B* **87**, 205425 (2013).

[149] Ge, R.-C. & Hughes, S. Quantum dynamics of two quantum dots coupled through localized plasmons: An intuitive and accurate quantum optics approach using quasinormal modes. *Physical Review B* **92**, 205420 (2015).

[150] Fauché, P., Kosionis, S. G. & Lalanne, P. Collective scattering in hybrid nanostructures with many atomic oscillators coupled to an electromagnetic resonance. *Physical Review B* **95**, 195418 (2017).

[151] Alpeggiani, F., D'Agostino, S., Sanvitto, D. & Gerace, D. Visible quantum plasmonics from metallic nanodimers. *Scientific Reports* **6**, 34772 (2016).

[152] Jurga, R., D'Agostino, S., Della Sala, F. & Ciracì, C. Plasmonic Nonlocal Response Effects on Dipole Decay Dynamics in the Weak- and Strong-Coupling Regimes. *The Journal of Physical Chemistry C* **121**, 22361–22368 (2017).

[153] Faucheaux, J. A., Fu, J. & Jain, P. K. Unified Theoretical Framework for Realizing Diverse Regimes of Strong Coupling between Plasmons and Electronic Transitions. *The Journal of Physical Chemistry C* **118**, 2710–2717 (2014).

[154] Gérard, J.-M. Solid-State Cavity-Quantum Electrodynamics with Self-Assembled Quantum Dots. In *Single Quantum Dots*, vol. 90, 269–314 (Springer Berlin Heidelberg, Berlin, Heidelberg, 2003).

[155] Chang, R. K. & Campillo, A. J. (eds.) *Optical Processes in Microcavities*. No. vol. 3 in Advanced Series in Applied Physics (World Scientific, Singapore; New Jersey, 1996).

[156] Kristensen, P. T., Van Vlack, C. & Hughes, S. Generalized effective mode volume for leaky optical cavities. *Optics Letters* **37**, 1649 (2012).

[157] de Lasson, J. R., Mørk, J. & Kristensen, P. T. Three-dimensional integral equation approach to light scattering, extinction cross sections, local density of states, and quasi-normal modes. *JOSA B* **30**, 1996–2007 (2013).

[158] Lai, H. M., Leung, P. T., Young, K., Barber, P. W. & Hill, S. C. Time-independent perturbation for leaking electromagnetic modes in open systems with application to resonances in microdroplets. *Physical Review A* **41**, 5187–5198 (1990).

[159] Leung, P. T., Liu, S. Y. & Young, K. Completeness and orthogonality of quasinormal modes in leaky optical cavities. *Physical Review A* **49**, 3057–3067 (1994).

[160] Leung, P. T., Liu, S. Y. & Young, K. Completeness and time-independent perturbation of the quasinormal modes of an absorptive and leaky cavity. *Physical Review A* **49**, 3982–3989 (1994).

[161] Lee, K. M., Leung, P. T. & Pang, K. M. Dyadic formulation of morphology-dependent resonances. I. Completeness relation. *JOSA B* **16**, 1409–1417 (1999).

[162] Lee, K. M., Leung, P. T. & Pang, K. M. Dyadic formulation of morphology-dependent resonances. II. Perturbation theory. *JOSA B* **16**, 1418–1430 (1999).

[163] Leung, P. T. & Pang, K. M. Completeness and time-independent perturbation of morphology-dependent resonances in dielectric spheres. *JOSA B* **13**, 805–817 (1996).

[164] Bai, Q., Perrin, M., Sauvan, C., Hugonin, J.-P. & Lalanne, P. Efficient and intuitive method for the analysis of light scattering by a resonant nanostructure. *Optics Express* **21**, 27371–27382 (2013).

[165] Zhan, T. R. & Chui, S. T. Theory of the spontaneous-decay enhancement in plasmonic nanoparticles based on a singularity representation of the scattering matrix. *Physical Review A* **90** (2014).

[166] Huang, S. *et al.* Ultrasmall Mode Volumes in Plasmonic Cavities of Nanoparticle-On-Mirror Structures. *Small* **12**, 5190–5199 (2016).

[167] Ge, R.-C. & Hughes, S. Quasinormal mode theory and modelling of electron energy loss spectroscopy for plasmonic nanostructures. *Journal of Optics* **18**, 054002 (2016).

[168] Ge, R.-C., Kristensen, P. T., Young, J. F. & Hughes, S. Quasinormal mode approach to modelling light-emission and propagation in nanoplasmonics. *New Journal of Physics* **16**, 113048 (2014).

[169] Kamandar Dezfouli, M. & Hughes, S. Quantum Optics Model of Surface-Enhanced Raman Spectroscopy for Arbitrarily Shaped Plasmonic Resonators. *ACS Photonics* **4**, 1245–1256 (2017).

[170] Kristensen, P. T., Ge, R.-C. & Hughes, S. Normalization of quasinormal modes in leaky optical cavities and plasmonic resonators. *Physical Review A* **92**, 053810 (2015).

[171] Shahbazyan, T. V. Mode Volume, Energy Transfer, and Spaser Threshold in Plasmonic Systems with Gain. *ACS Photonics* **4**, 1003–1008 (2017).

[172] Shahbazyan, T. V. Local Density of States for Nanoplasmonics. *Physical Review Letters* **117**, 207401 (2016).

[173] Weiss, T. *et al.* From Dark to Bright: First-Order Perturbation Theory with Analytical Mode Normalization for Plasmonic Nanoantenna Arrays Applied to Refractive Index Sensing. *Physical Review Letters* **116**, 237401 (2016).

[174] Ge, R.-C. & Hughes, S. Design of an efficient single photon source from a metallic nanorod dimer: A quasi-normal mode finite-difference time-domain approach. *Optics Letters* **39**, 4235 (2014).

[175] Kristensen, P. T. & Hughes, S. Modes and Mode Volumes of Leaky Optical Cavities and Plasmonic Nanoresonators. *ACS Photonics* **1**, 2–10 (2014).

[176] Muljarov, E. A. & Langbein, W. Exact mode volume and Purcell factor of open optical systems. *Physical Review B* **94** (2016).

[177] Muljarov, E. A. & Langbein, W. Comment on "Normalization of quasinormal modes in leaky optical cavities and plasmonic resonators". *Physical Review A* **96**, 017801 (2017).

[178] Kristensen, P. T., Ge, R.-C. & Hughes, S. Reply to "Comment on 'Normalization of quasinormal modes in leaky optical cavities and plasmonic resonators' ". *Physical Review A* **96**, 017802 (2017).

[179] Laussy, F. P., del Valle, E. & Tejedor, C. Strong Coupling of Quantum Dots in Microcavities. *Physical Review Letters* **101**, 083601 (2008).

[180] Breuer, H.-P. & Petruccione, F. *The Theory of Open Quantum Systems* (Clarendon Press, Oxford, 2010), repr edn. OCLC: 705944917.

[181] Born, M. & Wolf, E. *Principles of Optics: Electromagnetic Theory of Propagation, Interference and Diffraction of Light* (CUP Archive, 2000).

[182] Andreani, L. C., Panzarini, G. & Gérard, J.-M. Strong-coupling regime for quantum boxes in pillar microcavities: Theory. *Physical Review B* **60**, 13276–13279 (1999).

[183] Quesada, N. Strong coupling of two quantum emitters to a single light mode: The dissipative Tavis-Cummings ladder. *Physical Review A* **86**, 013836 (2012).

[184] del Valle, E. & Laussy, F. P. Regimes of strong light-matter coupling under incoherent excitation. *Physical Review A* **84**, 043816 (2011).

[185] del Valle, E. & Laussy, F. P. Mollow Triplet under Incoherent Pumping. *Physical Review Letters* **105**, 233601 (2010).

[186] Laussy, F. P., del Valle, E. & Tejedor, C. Luminescence spectra of quantum dots in microcavities. I. Bosons. *Physical Review B* **79**, 235325 (2009).

[187] Laussy, F. P., Laucht, A., del Valle, E., Finley, J. J. & Villas-Bôas, J. M. Luminescence spectra of quantum dots in microcavities. III. Multiple quantum dots. *Physical Review B* **84**, 195313 (2011).

[188] López Carreño, J. C., Sánchez Muñoz, C., Sanvitto, D., del Valle, E. & Laussy, F. P. Exciting Polaritons with Quantum Light. *Physical Review Letters* **115**, 196402 (2015).

[189] del Valle, E. & Laussy, F. Effective cavity pumping from weakly coupled quantum dots. *Superlattices and Microstructures* **49**, 241–245 (2011).

[190] del Valle, E. Distilling one, two and entangled pairs of photons from a quantum dot with cavity QED effects and spectral filtering. *New Journal of Physics* **15**, 025019 (2013).

[191] Quesada, N., Vinck-Posada, H. & Rodríguez, B. A. Density operator of a system pumped with polaritons: A Jaynes–Cummings-like approach. *Journal of Physics: Condensed Matter* **23**, 025301 (2011).

[192] Laussy, F. P., del Valle, E., Schrapp, M., Laucht, A. & Finley, J. J. Climbing the Jaynes–Cummings ladder by photon counting. *Journal of Nanophotonics* **6**, 061803–061803 (2012).

[193] Banin, U., Ben-Shahar, Y. & Vinokurov, K. Hybrid Semiconductor–Metal Nanoparticles: From Architecture to Function. *Chemistry of Materials* **26**, 97–110 (2014).

[194] Burda, C., Chen, X., Narayanan, R. & El-Sayed, M. A. Chemistry and Properties of Nanocrystals of Different Shapes. *Chemical Reviews* **105**, 1025–1102 (2005).

[195] Cichos, F., von Borczyskowski, C. & Orrit, M. Power-law intermittency of single emitters. *Current Opinion in Colloid & Interface Science* **12**, 272–284 (2007).

[196] Cordones, A. A. & Leone, S. R. Mechanisms for charge trapping in single semiconductor nanocrystals probed by fluorescence blinking. *Chemical Society Reviews* **42**, 3209–3221 (2013).

[197] Cui, J., Beyler, A. P., Bischof, T. S., Wilson, M. W. B. & Bawendi, M. G. Deconstructing the photon stream from single nanocrystals: From binning to correlation. *Chemical Society Reviews* **43**, 1287–1310 (2014).

[198] Donegá, C. d. M. Synthesis and properties of colloidal heteronanocrystals. *Chemical Society Reviews* **40**, 1512–1546 (2011).

[199] Efros, A. L. & Nesbitt, D. J. Origin and control of blinking in quantum dots. *Nature Nanotechnology* **11**, 661–671 (2016).

[200] Efros, A. L. Nanocrystals: Almost always bright. *Nature Materials* **7**, 612–613 (2008).

[201] Efros, A. L. & Rosen, M. The Electronic Structure of Semiconductor Nanocrystals [1]. *Annual Review of Materials Science* **30**, 475–521 (2000).

[202] Fernée, M. J., Tamarat, P. & Lounis, B. Cryogenic Single-Nanocrystal Spectroscopy: Reading the Spectral Fingerprint of Individual CdSe Quantum Dots. *The Journal of Physical Chemistry Letters* **4**, 609–618 (2013).

[203] Fernée, M. J., Tamarat, P. & Lounis, B. Spectroscopy of single nanocrystals. *Chemical Society Reviews* **43**, 1311–1337 (2014).

[204] Frantsuzov, P., Kuno, M., Jankó, B. & Marcus, R. A. Universal emission intermittency in quantum dots, nanorods and nanowires. *Nature Physics* **4**, 519–522 (2008).

[205] Gammon, D. & Steel, D. G. Optical studies of single quantum dots. *Physics Today* **55**, 36–41 (2002).

[206] Gómez, D. E., Califano, M. & Mulvaney, P. Optical properties of single semiconductor nanocrystals. *Physical Chemistry Chemical Physics* **8**, 4989–5011 (2006).

[207] Hens, Z. & Moreels, I. Light absorption by colloidal semiconductor quantum dots. *Journal of Materials Chemistry* **22**, 10406–10415 (2012).

[208] Hollingsworth, J. A., Htoon, H., Piryatinski, A., Götzinger, S. & Sandoghdar, V. When excitons and plasmons meet: Emerging function through synthesis and assembly. *MRS Bulletin* **40**, 768–776 (2015).

[209] Kambhampati, P., Mack, T. & Jethi, L. Understanding and Exploiting the Interface of Semiconductor Nanocrystals for Light Emissive Applications. *ACS Photonics* **4**, 412–423 (2017).

[210] Kambhampati, P. Unraveling the Structure and Dynamics of Excitons in Semiconductor Quantum Dots. *Accounts of Chemical Research* **44**, 1–13 (2011).

[211] Kambhampati, P. Hot Exciton Relaxation Dynamics in Semiconductor Quantum Dots: Radiationless Transitions on the Nanoscale. *The Journal of Physical Chemistry C* **115**, 22089–22109 (2011).

[212] Kilina, S., Kilin, D. & Tretiak, S. Light-Driven and Phonon-Assisted Dynamics in Organic and Semiconductor Nanostructures. *Chemical Reviews* **115**, 5929–5978 (2015).

[213] Kim, J. Y., Voznyy, O., Zhitomirsky, D. & Sargent, E. H. 25th Anniversary Article: Colloidal Quantum Dot Materials and Devices: A Quarter-Century of Advances. *Advanced Materials* **25**, 4986–5010 (2013).

[214] Klimov, V. I. Optical Nonlinearities and Ultrafast Carrier Dynamics in Semiconductor Nanocrystals. *The Journal of Physical Chemistry B* **104**, 6112–6123 (2000).

[215] Kovalenko, M. V. *et al.* Prospects of Nanoscience with Nanocrystals. *ACS Nano* **9**, 1012–1057 (2015).

[216] Lodahl, P., Mahmoodian, S. & Stobbe, S. Interfacing single photons and single quantum dots with photonic nanostructures. *Reviews of Modern Physics* **87**, 347–400 (2015).

[217] Lodahl, P. & Stobbe, S. Solid-state quantum optics with quantum dots in photonic nanostructures. *Nanophotonics* **2**, 39–55 (2013).

[218] Nirmal, M. & Brus, L. Luminescence Photophysics in Semiconductor Nanocrystals. *Accounts of Chemical Research* **32**, 407–414 (1999).

[219] Norris, D. J., Efros, A. L. & Erwin, S. C. Doped Nanocrystals. *Science* **319**, 1776–1779 (2008).

[220] Nozik, A. J. Spectroscopy and hot electron relaxation dynamics in semiconductor quantum wells and quantum dots. *Annual Review of Physical Chemistry* **52**, 193–231 (2001).

[221] Panfil, Y. E., Oded, M. & Banin, U. Colloidal Quantum Nanostructures; Emerging Materials for Display Applications. *Angewandte Chemie* (2017).

[222] Pietryga, J. M. *et al.* Spectroscopic and Device Aspects of Nanocrystal Quantum Dots. *Chemical Reviews* **116**, 10513–10622 (2016).

[223] Qin, H., Meng, R., Wang, N. & Peng, X. Photoluminescence Intermittency and Photo-Bleaching of Single Colloidal Quantum Dot. *Advanced Materials* **29**, 1606923 (2017).

[224] Schwartz, O. & Oron, D. A Present Understanding of Colloidal Quantum Dot Blinking. *Israel Journal of Chemistry* **52**, 992–1001 (2012).

[225] Stefani, F. D., Hoogenboom, J. P. & Barkai, E. Beyond quantum jumps: Blinking nanoscale light emitters. *Physics Today* **62**, 34–39 (2009).

[226] Talapin, D. V., Lee, J.-S., Kovalenko, M. V. & Shevchenko, E. V. Prospects of Colloidal Nanocrystals for Electronic and Optoelectronic Applications. *Chemical Reviews* **110**, 389–458 (2010).

[227] Tartakovskii, A. (ed.) *Quantum Dots: Optics, Electron Transport and Future Applications* (Cambridge University Press, Cambridge, 2012).

[228] Willets, K. A., Wilson, A. J., Sundaresan, V. & Joshi, P. B. Super-Resolution Imaging and Plasmonics. *Chemical Reviews* **117**, 7538–7582 (2017).

[229] Wang, Y. & Herron, N. Nanometer-sized semiconductor clusters: Materials synthesis, quantum size effects, and photophysical properties. *The Journal of Physical Chemistry* **95**, 525–532 (1991).

[230] Kayanuma, Y. Quantum-size effects of interacting electrons and holes in semiconductor microcrystals with spherical shape. *Physical Review B* **38**, 9797–9805 (1988).

[231] Klimov, V. I. *Nanocrystal Quantum Dots* (CRC Press, Boca Raton, 2010), 2nd edition edn. OCLC: ocn226357349.

[232] Labeau, O., Tamarat, P. & Lounis, B. Temperature Dependence of the Luminescence Lifetime of Single CdSe/ZnS Quantum Dots. *Physical Review Letters* **90**, 257404 (2003).

[233] van Driel, A. F. *et al.* Frequency-Dependent Spontaneous Emission Rate from CdSe and CdTe Nanocrystals: Influence of Dark States. *Physical Review Letters* **95**, 236804 (2005).

[234] Dabbousi, B. O. *et al.* (CdSe)ZnS Core-Shell Quantum Dots: Synthesis and Characterization of a Size Series of Highly Luminescent Nanocrystallites. *The Journal of Physical Chemistry B* **101**, 9463–9475 (1997).

[235] Van de Walle, C. G. & Neugebauer, J. Universal alignment of hydrogen levels in semiconductors, insulators and solutions. *Nature* **423**, 626–628 (2003).

[236] Chen, Y. *et al.* "Giant" Multishell CdSe Nanocrystal Quantum Dots with Suppressed Blinking. *Journal of the American Chemical Society* **130**, 5026–5027 (2008).

[237] Mahler, B. *et al.* Towards non-blinking colloidal quantum dots. *Nature Materials* **7**, 659–664 (2008).

[238] Yu, Z., Guo, L., Du, H., Krauss, T. & Silcox, J. Shell Distribution on Colloidal CdSe/ZnS Quantum Dots. *Nano Letters* **5**, 565–570 (2005).

[239] Kim, S., Fisher, B., Eisler, H.-J. & Bawendi, M. Type-II Quantum Dots: CdTe/CdSe(Core/Shell) and CdSe/ZnTe(Core/Shell) Heterostructures. *Journal of the American Chemical Society* **125**, 11466–11467 (2003).

[240] Vela, J. *et al.* Effect of shell thickness and composition on blinking suppression and the blinking mechanism in 'giant' CdSe/CdS nanocrystal quantum dots. *Journal of Biophotonics* **3**, 706–717 (2010).

[241] Norris, D. J. & Bawendi, M. G. Measurement and assignment of the size-dependent optical spectrum in CdSe quantum dots. *Physical Review B* **53**, 16338–16346 (1996).

[242] Zhang, L., Lin, Z., Luo, J.-W. & Franceschetti, A. The Birth of a Type-II Nanostructure: Carrier Localization and Optical Properties of Isoelectronically Doped CdSe:Te Nanocrystals. *ACS Nano* **6**, 8325–8334 (2012).

[243] Bailey, R. E. & Nie, S. Alloyed Semiconductor Quantum Dots: Tuning the Optical Properties without Changing the Particle Size. *Journal of the American Chemical Society* **125**, 7100–7106 (2003).

[244] Swafford, L. A. *et al.* Homogeneously Alloyed CdSxSe1-x Nanocrystals: Synthesis, Characterization, and Composition/Size-Dependent Band Gap. *Journal of the American Chemical Society* **128**, 12299–12306 (2006).

[245] Mallin, M. P. & Murphy, C. J. Solution-Phase Synthesis of Sub-10 nm Au-Ag Alloy Nanoparticles. *Nano Letters* **2**, 1235–1237 (2002).

[246] de Mello Donegá, C. & Koole, R. Size Dependence of the Spontaneous Emission Rate and Absorption Cross Section of CdSe and CdTe Quantum Dots. *The Journal of Physical Chemistry C* **113**, 6511–6520 (2009).

[247] Wei, S.-H., Zhang, S. B. & Zunger, A. First-principles calculation of band offsets, optical bowings, and defects in CdS, CdSe, CdTe, and their alloys. *Journal of Applied Physics* **87**, 1304–1311 (2000).

[248] Poon, H. C., Feng, Z. C., Feng, Y. P. & Li, M. F. Relativistic band structure of ternary II-VI semiconductor alloys containing Cd, Zn, Se and Te. *Journal of Physics: Condensed Matter* **7**, 2783–2799 (1995).

[249] Zunger, A. Structural Origin of Optical Bowing in Semiconductor Alloys. *Physical Review Letters* **51**, 662–665 (1983).

[250] Nirmal, M. *et al.* Fluorescence intermittency in single cadmium selenide nanocrystals. *Nature* **383**, 802–804 (1996).

[251] Peterson, J. J. & Nesbitt, D. J. Modified Power Law Behavior in Quantum Dot Blinking: A Novel Role for Biexcitons and Auger Ionization. *Nano Letters* **9**, 338–345 (2009).

[252] Efros, A. L. & Rosen, M. Random Telegraph Signal in the Photoluminescence Intensity of a Single Quantum Dot. *Physical Review Letters* **78**, 1110–1113 (1997).

[253] Banin, U. *et al.* Evidence for a thermal contribution to emission intermittency in single CdSe/CdS core/shell nanocrystals. *The Journal of Chemical Physics* **110**, 1195–1201 (1999).

[254] Kuno, M., Fromm, D. P., Hamann, H. F., Gallagher, A. & Nesbitt, D. J. Nonexponential "blinking" kinetics of single CdSe quantum dots: A universal power law behavior. *The Journal of Chemical Physics* **112**, 3117–3120 (2000).

[255] Amecke, N. & Cichos, F. Intermediate intensity levels during the emission intermittency of single CdSe/ZnS quantum dots. *Journal of Luminescence* **131**, 375–378 (2011).

[256] Rabouw, F. T. *et al.* Delayed Exciton Emission and Its Relation to Blinking in CdSe Quantum Dots. *Nano Letters* **15**, 7718–7725 (2015).

[257] Sher, P. H. *et al.* Power law carrier dynamics in semiconductor nanocrystals at nanosecond timescales. *Applied Physics Letters* **92**, 101111 (2008).

[258] Crouch, C. H. *et al.* Facts and Artifacts in the Blinking Statistics of Semiconductor Nanocrystals. *Nano Letters* **10**, 1692–1698 (2010).

[259] Verberk, R., van Oijen, A. M. & Orrit, M. Simple model for the power-law blinking of single semiconductor nanocrystals. *Physical Review B* **66**, 233202 (2002).

[260] Kuno, M., Fromm, D. P., Johnson, S. T., Gallagher, A. & Nesbitt, D. J. Modeling distributed kinetics in isolated semiconductor quantum dots. *Physical Review B* **67**, 125304 (2003).

[261] Kuno, M., Fromm, D. P., Hamann, H. F., Gallagher, A. & Nesbitt, D. J. "On"/"off" fluorescence intermittency of single semiconductor quantum dots. *The Journal of Chemical Physics* **115**, 1028–1040 (2001).

[262] Shimizu, K. T. *et al.* Blinking statistics in single semiconductor nanocrystal quantum dots. *Physical Review B* **63**, 205316 (2001).

[263] Neuhauser, R. G., Shimizu, K. T., Woo, W. K., Empedocles, S. A. & Bawendi, M. G. Correlation between Fluorescence Intermittency and Spectral Diffusion in Single Semiconductor Quantum Dots. *Physical Review Letters* **85**, 3301–3304 (2000).

[264] Tang, J. & Marcus, R. A. Diffusion-Controlled Electron Transfer Processes and Power-Law Statistics of Fluorescence Intermittency of Nanoparticles. *Physical Review Letters* **95**, 107401 (2005).

[265] Margolin, G., Protasenko, V., Kuno, M. & Barkai, E. Power-Law Blinking Quantum Dots: Stochastic and Physical Models. In Coffey, W. T. & Kalmykov, Y. P. (eds.) *Fractals, Diffusion, and Relaxation in Disordered Complex Systems*, 327–356 (John Wiley & Sons, Inc., 2006).

[266] Goushi, K., Yamada, T. & Otomo, A. Excitation Intensity Dependence of Power-Law Blinking Statistics in Nanocrystal Quantum Dots. *The Journal of Physical Chemistry C* **113**, 20161–20168 (2009).

[267] Galland, C. *et al.* Two types of luminescence blinking revealed by spectroelectrochemistry of single quantum dots. *Nature* **479**, 203–207 (2011).

[268] Jha, P. P. & Guyot-Sionnest, P. Electrochemical Switching of the Photoluminescence of Single Quantum Dots. *The Journal of Physical Chemistry C* **114**, 21138–21141 (2010).

[269] Galland, C. *et al.* Lifetime blinking in nonblinking nanocrystal quantum dots. *Nature Communications* **3**, 908 (2012).

[270] Houtepen, A. J. & Vanmaekelbergh, D. Orbital Occupation in Electron-Charged CdSe Quantum-Dot Solids. *The Journal of Physical Chemistry B* **109**, 19634–19642 (2005).

[271] Volkán-Kacsó, S., Frantsuzov, P. A. & Jankó, B. Correlations between Subsequent Blinking Events in Single Quantum Dots. *Nano Letters* **10**, 2761–2765 (2010).

[272] Hoogenboom, J. P., Hernando, J., García-Parajó, M. F. & van Hulst, N. F. Memory in Single Emitter Fluorescence Blinking Reveals the Dynamic Character of Nanoscale Charge Tunneling. *The Journal of Physical Chemistry C* **112**, 3417–3422 (2008).

[273] Stefani, F. D., Zhong, X., Knoll, W., Han, M. & Kreiter, M. Memory in quantum-dot photoluminescence blinking. *New Journal of Physics* **7**, 197 (2005).

[274] Zhao, J., Nair, G., Fisher, B. R. & Bawendi, M. G. Challenge to the Charging Model of Semiconductor-Nanocrystal Fluorescence Intermittency from Off-State Quantum Yields and Multiexciton Blinking. *Physical Review Letters* **104**, 157403 (2010).

[275] Rosen, S., Schwartz, O. & Oron, D. Transient Fluorescence of the Off State in Blinking CdSe/CdS/ZnS Semiconductor Nanocrystals Is Not Governed by Auger Recombination. *Physical Review Letters* **104**, 157404 (2010).

[276] Klimov, V. I., Mikhailovsky, A. A., McBranch, D. W., Leatherdale, C. A. & Bawendi, M. G. Quantization of Multiparticle Auger Rates in Semiconductor Quantum Dots. *Science* **287**, 1011–1013 (2000).

[277] Frantsuzov, P. A. & Marcus, R. A. Explanation of quantum dot blinking without the long-lived trap hypothesis. *Physical Review B* **72**, 155321 (2005).

[278] Hu, F., Zhang, Q., Zhang, C., Wang, X. & Xiao, M. Charged two-exciton emission from a single semiconductor nanocrystal. *Applied Physics Letters* **106**, 133106 (2015).

[279] Jeong, B. G. *et al.* Colloidal Spherical Quantum Wells with Near-Unity Photoluminescence Quantum Yield and Suppressed Blinking. *ACS Nano* **10**, 9297–9305 (2016).

[280] Manceau, M. *et al.* Effect of charging on CdSe/CdS dot-in-rods single-photon emission. *Physical Review B* **90**, 035311 (2014).

[281] Yu, M. & Van Orden, A. Enhanced Fluorescence Intermittency of CdSe-ZnS Quantum-Dot Clusters. *Physical Review Letters* **97**, 237402 (2006).

[282] Rogez, B. *et al.* Fluorescence Lifetime and Blinking of Individual Semiconductor Nanocrystals on Graphene. *The Journal of Physical Chemistry C* **118**, 18445–18452 (2014).

[283] Frantsuzov, P. A., Volkán-Kacsó, S. & Jankó, B. Model of Fluorescence Intermittency of Single Colloidal Semiconductor Quantum Dots Using Multiple Recombination Centers. *Physical Review Letters* **103**, 207402 (2009).

[284] Ji, B. *et al.* Non-blinking quantum dot with a plasmonic nanoshell resonator. *Nature Nanotechnology* **10**, 170–175 (2015).

[285] Schmidt, R., Krasselt, C., Göhler, C. & von Borczyskowski, C. The Fluorescence Intermittency for Quantum Dots Is Not Power-Law Distributed: A Luminescence Intensity Resolved Approach. *ACS Nano* **8**, 3506–3521 (2014).

[286] Osad'ko, I. S., Eremchev, I. Y. & Naumov, A. V. Two Mechanisms of Fluorescence Intermittency in Single Core/Shell Quantum Dot. *The Journal of Physical Chemistry C* **119**, 22646–22652 (2015).

[287] Ye, M. & Searson, P. C. Blinking in quantum dots: The origin of the grey state and power law statistics. *Physical Review B* **84**, 125317 (2011).

[288] Al-Attar, N., Kennedy, E., Kelly, G. & Rice, J. H. Photoluminescence Blinking from Single CdSeS/ZnS Quantum Dots in a Conducting Polymer Matrix. *The Journal of Physical Chemistry C* **119**, 6278–6287 (2015).

[289] Zhu, Z. & Marcus, R. A. Extension of the diffusion controlled electron transfer theory for intermittent fluorescence of quantum dots: Inclusion of biexcitons and the difference of "on" and "off" time distributions. *Physical Chemistry Chemical Physics* **16**, 25694–25700 (2014).

[290] Smyder, J. A. *et al.* The influence of continuous vs. pulsed laser excitation on single quantum dot photophysics. *Physical Chemistry Chemical Physics* **16**, 25723–25728 (2014).

[291] Osad'ko, I. S. Two types of the relation between the intensity and the life time of photoluminescence of core/shell semiconductor quantum dots: Important role of Coulomb field and tunneling transitions. *The Journal of Chemical Physics* **141**, 164312 (2014).

[292] Ihara, T., Sato, R., Teranishi, T. & Kanemitsu, Y. Delocalized and localized charged excitons in single CdSe/CdS dot-in-rods revealed by polarized photoluminescence blinking. *Physical Review B* **90**, 035309 (2014).

[293] Canneson, D. *et al.* Blinking suppression and biexcitonic emission in thick-shell CdSe/CdS nanocrystals at cryogenic temperature. *Physical Review B* **89**, 035303 (2014).

[294] Li, L., Tian, G., Luo, Y., Brismar, H. & Fu, Y. Blinking, Flickering, and Correlation in Fluorescence of Single Colloidal CdSe Quantum Dots with Different Shells under Different Excitations. *The Journal of Physical Chemistry C* **117**, 4844–4851 (2013).

[295] Schwartz, O. *et al.* Colloidal Quantum Dots as Saturable Fluorophores. *ACS Nano* **6**, 8778–8782 (2012).

[296] Cordones, A. A., Bixby, T. J. & Leone, S. R. Evidence for Multiple Trapping Mechanisms in Single CdSe/ZnS Quantum Dots from Fluorescence Intermittency Measurements over a Wide Range of Excitation Intensities. *The Journal of Physical Chemistry C* **115**, 6341–6349 (2011).

[297] Cordones, A. A., Bixby, T. J. & Leone, S. R. Direct Measurement of Off-State Trapping Rate Fluctuations in Single Quantum Dot Fluorescence. *Nano Letters* **11**, 3366–3369 (2011).

[298] Califano, M. Off-State Quantum Yields in the Presence of Surface Trap States in CdSe Nanocrystals: The Inadequacy of the Charging Model To Explain Blinking. *The Journal of Physical Chemistry C* **115**, 18051–18054 (2011).

[299] Wang, X. *et al.* Non-blinking semiconductor nanocrystals. *Nature* **459**, 686–689 (2009).

[300] Spinicelli, P. *et al.* Bright and Grey States in CdSe-CdS Nanocrystals Exhibiting Strongly Reduced Blinking. *Physical Review Letters* **102**, 136801 (2009).

[301] Knappenberger, K. L. *et al.* Excitation-Wavelength Dependence of Fluorescence Intermittency in CdSe Nanorods. *ACS Nano* **2**, 2143–2153 (2008).

[302] Knappenberger, K. L., Wong, D. B., Romanyuk, Y. E. & Leone, S. R. Excitation Wavelength Dependence of Fluorescence Intermittency in CdSe/ZnS Core/Shell Quantum Dots. *Nano Letters* **7**, 3869–3874 (2007).

[303] Tang, J. & Marcus, R. A. Mechanisms of fluorescence blinking in semiconductor nanocrystal quantum dots. *The Journal of Chemical Physics* **123**, 054704 (2005).

[304] Margolin, G., Protasenko, V., Kuno, M. & Barkai, E. Power-Law Blinking Quantum Dots: Stochastic and Physical Models. In Coffey, W. T. & Kalmykov, Y. P. (eds.) *Advances in Chemical Physics*, 327–356 (John Wiley & Sons, Inc., Hoboken, NJ, USA, 2005).

[305] Chung, I. & Bawendi, M. G. Relationship between single quantum-dot intermittency and fluorescence intensity decays from collections of dots. *Physical Review B* **70**, 165304 (2004).

[306] Wang. Calculating the Influence of External Charges on the Photoluminescence of a CdSe Quantum Dot. *The Journal of Physical Chemistry B* **105**, 2360–2364 (2001).

[307] Franceschetti, A. & Zunger, A. Optical transitions in charged CdSe quantum dots. *Physical Review B* **62**, R16287–R16290 (2000).

[308] Nirmal, M., Murray, C. B. & Bawendi, M. G. Fluorescence-line narrowing in CdSe quantum dots: Surface localization of the photogenerated exciton. *Physical Review B* **50**, 2293–2300 (1994).

[309] Empedocles, S. A., Norris, D. J. & Bawendi, M. G. Photoluminescence Spectroscopy of Single CdSe Nanocrystallite Quantum Dots. *Physical Review Letters* **77**, 3873–3876 (1996).

[310] Empedocles, S. A. & Bawendi, M. G. Quantum-Confined Stark Effect in Single CdSe Nanocrystallite Quantum Dots. *Science* **278**, 2114–2117 (1997).

[311] Empedocles, S. A. & Bawendi, M. G. Influence of Spectral Diffusion on the Line Shapes of Single CdSe Nanocrystallite Quantum Dots. *The Journal of Physical Chemistry B* **103**, 1826–1830 (1999).

[312] Müller, J. *et al.* Monitoring Surface Charge Movement in Single Elongated Semiconductor Nanocrystals. *Physical Review Letters* **93**, 167402 (2004).

[313] Müller, J. *et al.* Monitoring surface charge migration in the spectral dynamics of single CdSe/CdS nanodot/nanorod heterostructures. *Physical Review B* **72**, 205339 (2005).

[314] Rothenberg, E., Kazes, M., Shaviv, E. & Banin, U. Electric Field Induced Switching of the Fluorescence of Single Semiconductor Quantum Rods. *Nano Letters* **5**, 1581–1586 (2005).

[315] Coolen, L., Brokmann, X., Spinicelli, P. & Hermier, J.-P. Emission Characterization of a Single CdSe-ZnS Nanocrystal with High Temporal and Spectral Resolution by Photon-Correlation Fourier Spectroscopy. *Physical Review Letters* **100**, 027403 (2008).

[316] Fernée, M. J. *et al.* Charge hopping revealed by jitter correlations in the photoluminescence spectra of single CdSe nanocrystals. *Physical Review B* **81**, 155307 (2010).

[317] Plakhotnik, T. *et al.* Anomalous Power Laws of Spectral Diffusion in Quantum Dots: A Connection to Luminescence Intermittency. *Physical Review Letters* **105**, 167402 (2010).

[318] Fernée, M. J. *et al.* Spontaneous Spectral Diffusion in CdSe Quantum Dots. *The Journal of Physical Chemistry Letters* **3**, 1716–1720 (2012).

[319] Voznyy, O. Mobile Surface Traps in CdSe Nanocrystals with Carboxylic Acid Ligands. *The Journal of Physical Chemistry C* **115**, 15927–15932 (2011).

[320] Braam, D. *et al.* Role of the ligand layer for photoluminescence spectral diffusion of CdSe/ZnS nanoparticles. *Physical Review B* **88**, 125302 (2013).

[321] Ihara, T. & Kanemitsu, Y. Spectral diffusion of neutral and charged exciton transitions in single CdSe/ZnS nanocrystals due to quantum-confined Stark effect. *Physical Review B* **90**, 195302 (2014).

[322] Ibuki, H., Ihara, T. & Kanemitsu, Y. Spectral Diffusion of Emissions of Excitons and Trions in Single CdSe/ZnS Nanocrystals: Charge Fluctuations in and Around Nanocrystals. *The Journal of Physical Chemistry C* (2016).

[323] Kelley, A. M. Electron–Phonon Coupling in CdSe Nanocrystals from an Atomistic Phonon Model. *ACS Nano* **5**, 5254–5262 (2011).

[324] Krummheuer, B., Axt, V. M. & Kuhn, T. Theory of pure dephasing and the resulting absorption line shape in semiconductor quantum dots. *Physical Review B* **65**, 195313 (2002).

[325] Majumdar, A. *et al.* Linewidth broadening of a quantum dot coupled to an off-resonant cavity. *Physical Review B* **82**, 045306 (2010).

[326] Hohenester, U. Cavity quantum electrodynamics with semiconductor quantum dots: Role of phonon-assisted cavity feeding. *Physical Review B* **81**, 155303 (2010).

[327] Naesby, A., Suhr, T., Kristensen, P. T. & Mørk, J. Influence of pure dephasing on emission spectra from single photon sources. *Physical Review A* **78**, 045802 (2008).

[328] Auffèves, A., Gérard, J.-M. & Poizat, J.-P. Pure emitter dephasing: A resource for advanced solid-state single-photon sources. *Physical Review A* **79**, 053838 (2009).

[329] Auffèves, A. *et al.* Controlling the dynamics of a coupled atom-cavity system by pure dephasing. *Physical Review B* **81**, 245419 (2010).

[330] Yamaguchi, M., Asano, T. & Noda, S. Photon emission by nanocavity-enhanced quantum anti-Zeno effect in solid-state cavity quantum-electrodynamics. *Optics Express* **16**, 18067 (2008).

[331] Tarel, G. & Savona, V. Linear spectrum of a quantum dot coupled to a nanocavity. *Physical Review B* **81**, 075305 (2010).

[332] Suffczyński, J. *et al.* Origin of the Optical Emission within the Cavity Mode of Coupled Quantum Dot-Cavity Systems. *Physical Review Letters* **103**, 027401 (2009).

[333] Ates, S. *et al.* Non-resonant dot–cavity coupling and its potential for resonant single-quantum-dot spectroscopy. *Nature Photonics* **3**, 724–728 (2009).

[334] Tawara, T. *et al.* Cavity mode emission in weakly coupled quantum dot - cavity systems. *Optics Express* **17**, 6643 (2009).

[335] Ulhaq, A. *et al.* Linewidth broadening and emission saturation of a resonantly excited quantum dot monitored via an off-resonant cavity mode. *Physical Review B* **82**, 045307 (2010).

[336] Madsen, K. H. *et al.* Observation of Non-Markovian Dynamics of a Single Quantum Dot in a Micropillar Cavity. *Physical Review Letters* **106**, 233601 (2011).

[337] Toda, Y. & Arakawa, Y. Optical Characterization of In(Ga)As/GaAs Self-assembled Quantum Dots Using Near-Field Spectroscopy. In Rhodes, W. T. & Ohtsu, M. (eds.) *Progress in Nano-Electro-Optics I*, vol. 86, 83–117 (Springer Berlin Heidelberg, Berlin, Heidelberg, 2003).

[338] Inoshita, T. & Sakaki, H. Electron relaxation in a quantum dot: Significance of multiphonon processes. *Physical Review B* **46**, 7260–7263 (1992).

[339] Bockelmann, U. & Bastard, G. Phonon scattering and energy relaxation in two-, one-, and zero-dimensional electron gases. *Physical Review B* **42**, 8947–8951 (1990).

[340] Guyot-Sionnest, P., Shim, M., Matranga, C. & Hines, M. Intraband relaxation in CdSe quantum dots. *Physical Review B* **60**, R2181–R2184 (1999).

[341] Klimov, V. I. & McBranch, D. W. Femtosecond 1P-to-1S Electron Relaxation in Strongly Confined Semiconductor Nanocrystals. *Physical Review Letters* **80**, 4028–4031 (1998).

[342] Klimov, V. I., McBranch, D. W., Leatherdale, C. A. & Bawendi, M. G. Electron and hole relaxation pathways in semiconductor quantum dots. *Physical Review B* **60**, 13740–13749 (1999).

[343] Efros, A. L., Kharchenko, V. A. & Rosen, M. Breaking the phonon bottleneck in nanometer quantum dots: Role of Auger-like processes. *Solid State Communications* **93**, 281–284 (1995).

[344] Wang, L.-W., Califano, M., Zunger, A. & Franceschetti, A. Pseudopotential Theory of Auger Processes in CdSe Quantum Dots. *Physical Review Letters* **91**, 056404 (2003).

[345] Cooney, R. R. *et al.* Unified picture of electron and hole relaxation pathways in semiconductor quantum dots. *Physical Review B* **75**, 245311 (2007).

[346] Tisdale, W. A. *et al.* Hot-Electron Transfer from Semiconductor Nanocrystals. *Science* **328**, 1543–1547 (2010).

[347] Li, S., Steigerwald, M. L. & Brus, L. E. Surface States in the Photoionization of High-Quality CdSe Core/Shell Nanocrystals. *ACS Nano* **3**, 1267–1273 (2009).

[348] McGuire, J. A. *et al.* Spectroscopic Signatures of Photocharging due to Hot-Carrier Transfer in Solutions of Semiconductor Nanocrystals under Low-Intensity Ultraviolet Excitation. *ACS Nano* **4**, 6087–6097 (2010).

[349] Padilha, L. A. *et al.* Spectral Dependence of Nanocrystal Photoionization Probability: The Role of Hot-Carrier Transfer. *ACS Nano* **5**, 5045–5055 (2011).

[350] Lukosz, W. & Kunz, R. E. Light emission by magnetic and electric dipoles close to a plane interface. I. Total radiated power. *JOSA* **67**, 1607–1615 (1977).

[351] Marinica, D. C., Lourenço-Martins, H., Aizpurua, J. & Borisov, A. G. Plexciton Quenching by Resonant Electron Transfer from Quantum Emitter to Metallic Nanoantenna. *Nano Letters* **13**, 5972–5978 (2013).

[352] Kneipp, K. *et al.* Single molecule detection using surface-enhanced Raman scattering (SERS). *Physical Review Letters* **78**, 1667–1670 (1997).

[353] Michaels, A. M., Nirmal, M. & Brus, L. E. Surface Enhanced Raman Spectroscopy of Individual Rhodamine 6G Molecules on Large Ag Nanocrystals. *Journal of the American Chemical Society* **121**, 9932–9939 (1999).

[354] Bian, R. X., Dunn, R. C., Xie, X. S. & Leung, P. T. Single Molecule Emission Characteristics in Near-Field Microscopy. *Physical Review Letters* **75**, 4772–4775 (1995).

[355] Shimizu, K. T., Woo, W. K., Fisher, B. R., Eisler, H. J. & Bawendi, M. G. Surface-Enhanced Emission from Single Semiconductor Nanocrystals. *Physical Review Letters* **89**, 117401 (2002).

[356] Yuan, C. T., Yu, P., Ko, H. C., Huang, J. & Tang, J. Antibunching Single-Photon Emission and Blinking Suppression of CdSe/ZnS Quantum Dots. *ACS Nano* **3**, 3051–3056 (2009).

[357] Jin, S. *et al.* Distance-Engineered Plasmon-Enhanced Light Harvesting in CdSe Quantum Dots. *The Journal of Physical Chemistry Letters* **4**, 3527–3533 (2013).

[358] Toropov, A. A. *et al.* Enhancement of excitonic emission in semiconductor heterostructures due to resonant coupling to multipole plasmon modes in a gold particle. *Physical Review B* **84**, 085323 (2011).

[359] Canneson, D. *et al.* Enhancing the fluorescence of individual thick shell CdSe/CdS nanocrystals by coupling to gold structures. *New Journal of Physics* **14**, 063035 (2012).

[360] Ma, X., Tan, H., Kipp, T. & Mews, A. Fluorescence Enhancement, Blinking Suppression, and Gray States of Individual Semiconductor Nanocrystals Close to Gold Nanoparticles. *Nano Letters* **10**, 4166–4174 (2010).

[361] Naiki, H. *et al.* Highly Controlled Plasmonic Emission Enhancement from Metal-Semiconductor Quantum Dot Complex Nanostructures. *The Journal of Physical Chemistry C* **117**, 2455–2459 (2013).

[362] Ren, M. *et al.* Linearly Polarized Light Emission from Quantum Dots with Plasmonic Nanoantenna Arrays. *Nano Letters* **15**, 2951–2957 (2015).

[363] Ito, Y., Matsuda, K. & Kanemitsu, Y. Mechanism of photoluminescence enhancement in single semiconductor nanocrystals on metal surfaces. *Physical Review B* **75**, 033309 (2007).

[364] Ray, K., Badugu, R. & Lakowicz, J. R. Metal-Enhanced Fluorescence from CdTe Nanocrystals: A Single-Molecule Fluorescence Study. *Journal of the American Chemical Society* **128**, 8998–8999 (2006).

[365] Lyamkina, A. A. *et al.* Monolithically integrated single quantum dots coupled to bowtie nanoantennas. *Optics Express* **24**, 28936–28944 (2016).

[366] Sadeghi, S. M., West, R. G. & Nejat, A. Photo-induced suppression of plasmonic emission enhancement of CdSe/ZnS quantum dots. *Nanotechnology* **22**, 405202 (2011).

[367] Song, M. *et al.* Photoluminescence Plasmonic Enhancement of Single Quantum Dots Coupled to Gold Microplates. *The Journal of Physical Chemistry C* **118**, 8514–8520 (2014).

[368] Masuo, S., Tanaka, T., Machida, S. & Itaya, A. Photon antibunching in enhanced photoluminescence of a single CdSe/ZnS nanocrystal by silver nanostructures. *Journal of Photochemistry and Photobiology A: Chemistry* **237**, 24–30 (2012).

[369] Gómez, D. E., Lo, S. S., Davis, T. J. & Hartland, G. V. Picosecond Kinetics of Strongly Coupled Excitons and Surface Plasmon Polaritons. *The Journal of Physical Chemistry B* **117**, 4340–4346 (2013).

[370] Wang, F. *et al.* Quantum Optical Signature of Plasmonically Coupled Nanocrystal Quantum Dots. *Small* **11**, 5028–5034 (2015).

[371] Faggiani, R., Yang, J. & Lalanne, P. Quenching, Plasmonic, and Radiative Decays in Nanogap Emitting Devices. *ACS Photonics* **2** (2015).

[372] Bharadwaj, P. & Novotny, L. Robustness of Quantum Dot Power-Law Blinking. *Nano Letters* **11**, 2137–2141 (2011).

[373] Hartsfield, T. *et al.* Semiconductor Quantum Dot Lifetime Near an Atomically Smooth Ag Film Exhibits a Narrow Distribution. *ACS Photonics* **3**, 1085–1089 (2016).

[374] Fu, Y., Zhang, J. & Lakowicz, J. R. Suppressed blinking in single quantum dots (QDs) immobilized near silver island films (SIFs). *Chemical Physics Letters* **447**, 96–100 (2007).

[375] Dey, S. *et al.* An experimental and theoretical mechanistic study of biexciton quantum yield enhancement in single quantum dots near gold nanoparticles. *Nanoscale* **7**, 6851–6858 (2015).

[376] Wang, F. *et al.* Correlated structural-optical study of single nanocrystals in a gap-bar antenna: Effects of plasmonics on excitonic recombination pathways. *Nanoscale* **7**, 9387–9393 (2015).

[377] Wang, X., Morea, R., Gonzalo, J. & Palpant, B. Coupling Localized Plasmonic and Photonic Modes Tailors and Boosts Ultrafast Light Modulation by Gold Nanoparticles. *Nano Letters* **15**, 2633–2639 (2015).

[378] Masuo, S., Kanetaka, K., Sato, R. & Teranishi, T. Direct Observation of Multiphoton Emission Enhancement from a Single Quantum Dot Using AFM Manipulation of a Cubic Gold Nanoparticle. *ACS Photonics* **3**, 109–116 (2016).

[379] Liu, J., Kumar, P., Hu, Y., Cheng, G. J. & Irudayaraj, J. Enhanced Multiphoton Emission from CdTe/ZnS Quantum Dots Decorated on Single-Layer Graphene. *The Journal of Physical Chemistry C* **119**, 6331–6336 (2015).

[380] Ureña, E. B. *et al.* Excitation Enhancement of a Quantum Dot Coupled to a Plasmonic Antenna. *Advanced Materials* **24**, OP314–OP320 (2012).

[381] Cheng, H.-W. *et al.* Modification of Photon Emission Statistics from Single Colloidal CdSe Quantum Dots by Conductive Materials. *The Journal of Physical Chemistry C* **118**, 18126–18132 (2014).

[382] Masuo, S., Naiki, H., Machida, S. & Itaya, A. Photon statistics in enhanced fluorescence from a single CdSe/ZnS quantum dot in the vicinity of silver nanoparticles. *Applied Physics Letters* **95**, 193106 (2009).

[383] Park, Y.-S. *et al.* Single-Nanocrystal Photoluminescence Spectroscopy Studies of Plasmon–Multiexciton Interactions at Low Temperature. *The Journal of Physical Chemistry Letters* **4**, 1465–1470 (2013).

[384] Naiki, H., Masuo, S., Machida, S. & Itaya, A. Single-Photon Emission Behavior of Isolated CdSe/ZnS Quantum Dots Interacting with the Localized Surface Plasmon Resonance of Silver Nanoparticles. *The Journal of Physical Chemistry C* **115**, 23299–23304 (2011).

[385] Canneson, D. *et al.* Strong Purcell effect observed in single thick-shell CdSe/CdS nanocrystals coupled to localized surface plasmons. *Physical Review B* **84** (2011).

[386] Park, Y.-S. *et al.* Super-Poissonian Statistics of Photon Emission from Single CdSe-CdS Core-Shell Nanocrystals Coupled to Metal Nanostructures. *Physical Review Letters* **110**, 117401 (2013).

[387] Hoang, T. B. *et al.* Ultrafast spontaneous emission source using plasmonic nanoantennas. *Nature Communications* **6**, 7788 (2015).

[388] Mallek-Zouari, I. *et al.* Plasmon assisted single photon emission of CdSe/CdS nanocrystals deposited on random gold film. *Applied Physics Letters* **97**, 053109 (2010).

[389] Nair, G., Zhao, J. & Bawendi, M. G. Biexciton Quantum Yield of Single Semiconductor Nanocrystals from Photon Statistics. *Nano Letters* **11**, 1136–1140 (2011).

[390] LeBlanc, S. J., McClanahan, M. R., Jones, M. & Moyer, P. J. Enhancement of Multiphoton Emission from Single CdSe Quantum Dots Coupled to Gold Films. *Nano Letters* **13**, 1662–1669 (2013).

[391] Park, Y.-S. *et al.* Near-Unity Quantum Yields of Biexciton Emission from CdSe/CdS Nanocrystals Measured Using Single-Particle Spectroscopy. *Physical Review Letters* **106**, 187401 (2011).

[392] Yuan, G., Gómez, D., Kirkwood, N. & Mulvaney, P. Tuning Single Quantum Dot Emission with a Micromirror. *Nano Letters* **18**, 1010–1017 (2018).

[393] Dey, S. *et al.* Excitation wavelength dependent photon anti-bunching/bunching from single quantum dots near gold nanostructures. *Nanoscale* **10**, 1038–1046 (2018).

[394] García-Santamaría, F. *et al.* Suppressed Auger Recombination in "Giant" Nanocrystals Boosts Optical Gain Performance. *Nano Letters* **9**, 3482–3488 (2009).

[395] García-Santamaría, F. *et al.* Breakdown of Volume Scaling in Auger Recombination in CdSe/CdS Heteronanocrystals: The Role of the Core-Shell Interface. *Nano Letters* **11**, 687–693 (2011).

[396] Takata, H. *et al.* Detailed Observation of Multiphoton Emission Enhancement from a Single Colloidal Quantum Dot Using a Silver-Coated AFM Tip. *Nano Letters* **16**, 5770–5778 (2016).

[397] van Sark, W. G. J. H. M., Frederix, P. L. T. M., Bol, A. A., Gerritsen, H. C. & Meijerink, A. Blueing, Bleaching, and Blinking of Single CdSe/ZnS Quantum Dots. *ChemPhysChem* **3**, 871–879 (2002).

[398] Mivelle, M., van Zanten, T. S. & Garcia-Parajo, M. F. Hybrid Photonic Antennas for Subnanometer Multicolor Localization and Nanoimaging of Single Molecules. *Nano Letters* **14**, 4895–4900 (2014).

[399] Mivelle, M., van Zanten, T. S., Neumann, L., van Hulst, N. F. & Garcia-Parajo, M. F. Ultrabright Bowtie Nanoaperture Antenna Probes Studied by Single Molecule Fluorescence. *Nano Letters* **12**, 5972–5978 (2012).

[400] Taminiau, T. H., Moerland, R. J., Segerink, F. B., Kuipers, L. & van Hulst, N. F. $\lambda/4$ Resonance of an Optical Monopole Antenna Probed by Single Molecule Fluorescence. *Nano Letters* **7**, 28–33 (2007).

[401] Farahani, J. N. *et al.* Bow-tie optical antenna probes for single-emitter scanning near-field optical microscopy. *Nanotechnology* **18**, 125506 (2007).

[402] Weber-Bargioni, A. *et al.* Functional plasmonic antenna scanning probes fabricated by induced-deposition mask lithography. *Nanotechnology* **21**, 065306 (2010).

[403] Weber-Bargioni, A. *et al.* Hyperspectral Nanoscale Imaging on Dielectric Substrates with Coaxial Optical Antenna Scan Probes. *Nano Letters* **11**, 1201–1207 (2011).

[404] Hugall, J. T., Singh, A. & van Hulst, N. F. Plasmonic Cavity Coupling. *ACS Photonics* **5**, 43–53 (2018).

[405] Tuna, Y., Kim, J. T., Liu, H.-W. & Sandoghdar, V. Levitated Plasmonic Nanoantennas in an Aqueous Environment. *ACS Nano* **11**, 7674–7678 (2017).

[406] Huang, J.-S. *et al.* Atomically flat single-crystalline gold nanostructures for plasmonic nanocircuitry. *Nature Communications* **1**, 150 (2010).

[407] Guo, Z. *et al.* Facile synthesis of micrometer-sized gold nanoplates through an aniline-assisted route in ethylene glycol solution. *Colloids and Surfaces A: Physicochemical and Engineering Aspects* **278**, 33–38 (2006).

[408] Wu, X., Kullock, R., Krauss, E. & Hecht, B. Single-crystalline gold microplates grown on substrates by solution-phase synthesis. *Crystal Research and Technology* **50**, 595–602 (2015).

[409] Han, G. *et al.* Infrared spectroscopic and electron microscopic characterization of gold nanogap structure fabricated by focused ion beam. *Nanotechnology* **22**, 275202 (2011).

[410] Beversluis, M. R., Bouhelier, A. & Novotny, L. Continuum generation from single gold nanostructures through near-field mediated intraband transitions. *Physical Review B* **68**, 115433 (2003).

[411] Mohamed, M. B., Volkov, V., Link, S. & El-Sayed, M. A. The 'lightning' gold nanorods: Fluorescence enhancement of over a million compared to the gold metal. *Chemical Physics Letters* **317**, 517–523 (2000).

[412] Sivun, D. *et al.* Anticorrelation of Photoluminescence from Gold Nanoparticle Dimers with Hot-Spot Intensity. *Nano Letters* **16**, 7203–7209 (2016).

[413] Tcherniak, A. *et al.* One-Photon Plasmon Luminescence and Its Application to Correlation Spectroscopy as a Probe for Rotational and Translational Dynamics of Gold Nanorods. *The Journal of Physical Chemistry C* **115**, 15938–15949 (2011).

[414] Yorulmaz, M., Khatua, S., Zijlstra, P., Gaiduk, A. & Orrit, M. Luminescence Quantum Yield of Single Gold Nanorods. *Nano Letters* **12**, 4385–4391 (2012).

[415] Hu, H., Duan, H., Yang, J. K. W. & Shen, Z. X. Plasmon-Modulated Photoluminescence of Individual Gold Nanostructures. *ACS Nano* **6**, 10147–10155 (2012).

[416] Lumdee, C., Yun, B. & Kik, P. G. Gap-Plasmon Enhanced Gold Nanoparticle Photoluminescence. *ACS Photonics* **1**, 1224–1230 (2014).

[417] Wan, A. *et al.* Plasmon-Modulated Photoluminescence of Single Gold Nanobeams. *ACS Photonics* **2**, 1348–1354 (2015).

[418] Fang, Y. *et al.* Plasmon Emission Quantum Yield of Single Gold Nanorods as a Function of Aspect Ratio. *ACS Nano* **6**, 7177–7184 (2012).

[419] Mooradian, A. Photoluminescence of metals. *Physical Review Letters* **22**, 185 (1969).

[420] García de Abajo, F. J. & Manjavacas, A. Plasmonics in atomically thin materials. *Faraday Discuss.* **178**, 87–107 (2015).

[421] Ropp, C. *et al.* Nanoscale imaging and spontaneous emission control with a single nano-positioned quantum dot. *Nature Communications* **4**, 1447 (2013).

[422] Cang, H. *et al.* Probing the electromagnetic field of a 15-nanometre hotspot by single molecule imaging. *Nature* **469**, 385–388 (2011).

[423] Thacker, V. V. *et al.* DNA origami based assembly of gold nanoparticle dimers for surface-enhanced Raman scattering. *Nature Communications* **5**, 3448 (2014).

[424] Puchkova, A. *et al.* DNA Origami Nanoantennas with over 5000-fold Fluorescence Enhancement and Single-Molecule Detection at 25 μM. *Nano Letters* **15**, 8354–8359 (2015).

[425] Kern, J. *et al.* Atomic-Scale Confinement of Resonant Optical Fields. *Nano Letters* **12**, 5504–5509 (2012).

[426] Sakamoto, S., Tsuru, H., Toyoda, M. & Asakura, T. Finite-Difference Time-Domain Method. In Sakuma, T., Sakamoto, S. & Otsuru, T. (eds.) *Computational Simulation in Architectural and Environmental Acoustics*, 11–51 (Springer Japan, Tokyo, 2014).

[427] Alù, A. & Engheta, N. Input Impedance, Nanocircuit Loading, and Radiation Tuning of Optical Nanoantennas. *Physical Review Letters* **101**, 043901 (2008).

[428] Rogobete, L., Kaminski, F., Agio, M. & Sandoghdar, V. Design of plasmonic nanoantennae for enhancing spontaneous emission. *Optics Letters* **32**, 1623–1625 (2007).

[429] Mohammadi, A., Sandoghdar, V. & Agio, M. Gold nanorods and nanospheroids for enhancing spontaneous emission. *New Journal of Physics* **10**, 105015 (2008).

[430] Hancu, I. M., Curto, A. G., Castro-López, M., Kuttge, M. & van Hulst, N. F. Multipolar Interference for Directed Light Emission. *Nano Letters* **14**, 166–171 (2013).

[431] Livneh, N., Harats, M. G., Istrati, D., Eisenberg, H. S. & Rapaport, R. Highly Directional Room-Temperature Single Photon Device. *Nano Letters* **16**, 2527–2532 (2016).

[432] Talapin, D. V., Rogach, A. L., Kornowski, A., Haase, M. & Weller, H. Highly Luminescent Monodisperse CdSe and CdSe/ZnS Nanocrystals Synthesized in a Hexadecylamine-Trioctylphosphine Oxide-Trioctylphospine Mixture. *Nano Letters* **1**, 207–211 (2001).

[433] Murray, C. B., Norris, D. J. & Bawendi, M. G. Synthesis and characterization of nearly monodisperse CdE (E = sulfur, selenium, tellurium) semiconductor nanocrystallites. *Journal of the American Chemical Society* **115**, 8706–8715 (1993).

[434] Gong, K., Zeng, Y. & Kelley, D. F. Extinction Coefficients, Oscillator Strengths, and Radiative Lifetimes of CdSe, CdTe, and CdTe/CdSe Nanocrystals. *The Journal of Physical Chemistry C* **117**, 20268–20279 (2013).

[435] Gerton, J. M., Wade, L. A., Lessard, G. A., Ma, Z. & Quake, S. R. Tip-Enhanced Fluorescence Microscopy at 10 Nanometer Resolution. *Physical Review Letters* **93**, 180801 (2004).

[436] Frey, H. G., Witt, S., Felderer, K. & Guckenberger, R. High-Resolution Imaging of Single Fluorescent Molecules with the Optical Near-Field of a Metal Tip. *Physical Review Letters* **93**, 200801 (2004).

[437] Sánchez, E. J., Novotny, L. & Xie, X. S. Near-Field Fluorescence Microscopy Based on Two-Photon Excitation with Metal Tips. *Physical Review Letters* **82**, 4014–4017 (1999).

[438] Johnson, T. W. *et al.* Highly Reproducible Near-Field Optical Imaging with Sub-20-nm Resolution Based on Template-Stripped Gold Pyramids. *ACS Nano* **6**, 9168–9174 (2012).

[439] Kalkbrenner, T., Ramstein, M., Mlynek, J. & Sandoghdar, V. A single gold particle as a probe for apertureless scanning near-field optical microscopy. *Journal of Microscopy* **202**, 72–76 (2001).

[440] Höppener, C., Lapin, Z. J., Bharadwaj, P. & Novotny, L. Self-Similar Gold-Nanoparticle Antennas for a Cascaded Enhancement of the Optical Field. *Physical Review Letters* **109**, 017402 (2012).

[441] Segura, J. M., Zumofen, G., Renn, A., Hecht, B. & Wild, U. P. Tip-induced spectral dynamics of single molecules. *Chemical Physics Letters* **340**, 77–82 (2001).

[442] Reiserer, A., Kalb, N., Rempe, G. & Ritter, S. A quantum gate between a flying optical photon and a single trapped atom. *Nature* **508**, 237–240 (2014).

[443] He, Y.-M. *et al.* On-demand semiconductor single-photon source with near-unity indistinguishability. *Nature Nanotechnology* **8**, 213–217 (2013).

[444] Vasa, P. & Lienau, C. Strong Light–Matter Interaction in Quantum Emitter/Metal Hybrid Nanostructures. *ACS Photonics* (2017).

[445] Moilanen, A. J., Hakala, T. K. & Törmä, P. Active Control of Surface Plasmon–Emitter Strong Coupling. *ACS Photonics* **5**, 54–64 (2018).

[446] Marquier, F., Sauvan, C. & Greffet, J.-J. Revisiting Quantum Optics with Surface Plasmons and Plasmonic Resonators. *ACS Photonics* (2017).

[447] Bozhevolnyi, S. I., Martin-Moreno, L. & Garcia-Vidal, F. (eds.) *Quantum Plasmonics*, vol. 185 of *Springer Series in Solid-State Sciences* (Springer International Publishing, Cham, 2017).

[448] Dovzhenko, D. S., Ryabchuk, S. V., Rakovich, Y. & Nabiev, I. Light–matter interaction in the strong coupling regime: Configurations, conditions, applications. *Nanoscale* **10**, 3589–3605 (2018).

[449] Groß, H., Hamm, J. M., Tufarelli, T., Hess, O. & Hecht, B. Near-field strong coupling of single quantum dots. *Science Advances* **4**, eaar4906 (2018).

[450] Zuloaga, J. & Nordlander, P. On the Energy Shift between Near-Field and Far-Field Peak Intensities in Localized Plasmon Systems. *Nano Letters* **11**, 1280–1283 (2011).

[451] Kongsuwan, N. *et al.* Suppressed Quenching and Strong-Coupling of Purcell-Enhanced Single-Molecule Emission in Plasmonic Nanocavities. *ACS Photonics* **5**, 186–191 (2017).

[452] Yang, J., Faggiani, R. & Lalanne, P. Light emission in nanogaps: Overcoming quenching. *Nanoscale Horizons* **1**, 11–13 (2015).

[453] Delga, A., Feist, J., Bravo-Abad, J. & Garcia-Vidal, F. J. Quantum Emitters Near a Metal Nanoparticle: Strong Coupling and Quenching. *Physical Review Letters* **112** (2014).

[454] Winger, M., Badolato, A., Hennessy, K. J., Hu, E. L. & Imamoğlu, A. Quantum Dot Spectroscopy Using Cavity Quantum Electrodynamics. *Physical Review Letters* **101**, 226808 (2008).

[455] Oron, D., Kazes, M., Shweky, I. & Banin, U. Multiexciton spectroscopy of semiconductor nanocrystals under quasi-continuous-wave optical pumping. *Physical Review B* **74**, 115333 (2006).

[456] Efros, A. L. *et al.* Band-edge exciton in quantum dots of semiconductors with a degenerate valence band: Dark and bright exciton states. *Physical Review B* **54**, 4843–4856 (1996).

[457] McCutcheon, D. P. S. & Nazir, A. Model of the Optical Emission of a Driven Semiconductor Quantum Dot: Phonon-Enhanced Coherent Scattering and Off-Resonant Sideband Narrowing. *Physical Review Letters* **110**, 217401 (2013).

[458] Wilma, K. *et al.* Tracing Single Electrons in a Disordered Polymer Film at Room Temperature. *The Journal of Physical Chemistry Letters* **7**, 1478–1483 (2016).

[459] Klimov, V. I., McGuire, J. A., Schaller, R. D. & Rupasov, V. I. Scaling of multiexciton lifetimes in semiconductor nanocrystals. *Physical Review B* **77**, 195324 (2008).

[460] Eremchev, I., Osad'ko, I. & Naumov, A. Auger Ionization and Tunneling Neutralization of Single CdSe/ZnS Nanocrystals Revealed by Excitation Intensity Variation. *The Journal of Physical Chemistry C* **120**, 22004–22011 (2016).

[461] Zhao, J., Chen, O., Strasfeld, D. B. & Bawendi, M. G. Biexciton Quantum Yield Heterogeneities in Single CdSe (CdS) Core (Shell) Nanocrystals and Its Correlation to Exciton Blinking. *Nano Letters* **12**, 4477–4483 (2012).

[462] Klimov, V. I. & McBranch, D. W. Auger-process-induced charge separation in semiconductor nanocrystals. *Physical Review B* **55**, 13173–13179 (1997).

[463] Avidan, A. & Oron, D. Large Blue Shift of the Biexciton State in Tellurium Doped CdSe Colloidal Quantum Dots. *Nano Letters* **8**, 2384–2387 (2008).

[464] de Mello Donegá, C., Bode, M. & Meijerink, A. Size- and temperature-dependence of exciton lifetimes in CdSe quantum dots. *Physical Review B* **74**, 085320 (2006).

[465] Tighineanu, P., Sørensen, A. S., Stobbe, S. & Lodahl, P. Unraveling the Mesoscopic Character of Quantum Dots in Nanophotonics. *Physical Review Letters* **114**, 247401 (2015).

[466] Tighineanu, P., Andersen, M. L., Sørensen, A. S., Stobbe, S. & Lodahl, P. Probing Electric and Magnetic Vacuum Fluctuations with Quantum Dots. *Physical Review Letters* **113**, 043601 (2014).

[467] Kristensen, P. T., Mortensen, J. E., Lodahl, P. & Stobbe, S. Shell theorem for spontaneous emission. *Physical Review B* **88**, 205308 (2013).

[468] Stobbe, S. *et al.* Spontaneous emission from large quantum dots in nanostructures: Exciton-photon interaction beyond the dipole approximation. *Physical Review B* **86**, 085304 (2012).

[469] Kern, A. M. & Martin, O. J. F. Strong enhancement of forbidden atomic transitions using plasmonic nanostructures. *Physical Review A* **85**, 022501 (2012).

[470] Zurita-Sánchez, J. R. & Novotny, L. Multipolar interband absorption in a semiconductor quantum dot. I. Electric quadrupole enhancement. *JOSA B* **19**, 1355–1362 (2002).

[471] Andersen, M. L., Stobbe, S., Sørensen, A. S. & Lodahl, P. Strongly modified plasmon-matter interaction with mesoscopic quantum emitters. *Nature Physics* **7**, 215–218 (2011).

[472] Jain, P. K., Ghosh, D., Baer, R., Rabani, E. & Alivisatos, A. P. Near-field manipulation of spectroscopic selection rules on the nanoscale. *Proceedings of the National Academy of Sciences* **109**, 8016–8019 (2012).

[473] Takase, M. *et al.* Selection-rule breakdown in plasmon-induced electronic excitation of an isolated single-walled carbon nanotube. *Nature Photonics* **7**, 550–554 (2013).

[474] Madsen, K. H., Lehmann, T. B. & Lodahl, P. Role of multilevel states on quantum-dot emission in photonic-crystal cavities. *Physical Review B* **94**, 235301 (2016).

[475] Gross, M. & Haroche, S. Superradiance: An essay on the theory of collective spontaneous emission. *Physics Reports* **93**, 301–396 (1982).

[476] Scheibner, M. *et al.* Superradiance of quantum dots. *Nature Physics* **3**, 106–110 (2007).

[477] Koenderink, A. F. On the use of Purcell factors for plasmon antennas. *Optics letters* **35**, 4208–4210 (2010).

[478] Prodan, E. A Hybridization Model for the Plasmon Response of Complex Nanostructures. *Science* **302**, 419–422 (2003).

[479] Maier, S. A. *Plasmonics: Fundamentals and Applications* (Springer, New York, 2007).

[480] Atay, T., Song, J.-H. & Nurmikko, A. V. Strongly Interacting Plasmon Nanoparticle Pairs: From Dipole-Dipole Interaction to Conductively Coupled Regime. *Nano Letters* **4**, 1627–1631 (2004).

[481] Nordlander, P., Oubre, C., Prodan, E., Li, K. & Stockman, M. I. Plasmon Hybridization in Nanoparticle Dimers. *Nano Letters* **4**, 899–903 (2004).

[482] Huang, J.-S. *et al.* Mode Imaging and Selection in Strongly Coupled Nanoantennas. *Nano Lett.* **10**, 2105–2110 (2010).

[483] Funston, A. M., Novo, C., Davis, T. J. & Mulvaney, P. Plasmon Coupling of Gold Nanorods at Short Distances and in Different Geometries. *Nano Letters* **9**, 1651–1658 (2009).

[484] Rechberger, W. *et al.* Optical properties of two interacting gold nanoparticles. *Optics Communications* **220**, 137–141 (2003).

[485] Aeschlimann, M. *et al.* Cavity-assisted ultrafast long-range periodic energy transfer between plasmonic nanoantennas. *Light: Science & Applications* **6**, e17111 (2017).

[486] Chang, D. E., Sørensen, A. S., Demler, E. A. & Lukin, M. D. A single-photon transistor using nanoscale surface plasmons. *Nature Physics* **3**, 807–812 (2007).

[487] Dintinger, J., Robel, I., Kamat, P. V., Genet, C. & Ebbesen, T. W. Terahertz All-Optical Molecule- Plasmon Modulation. *Advanced Materials* **18**, 1645–1648 (2006).

[488] MacDonald, K. F., Sámson, Z. L., Stockman, M. I. & Zheludev, N. I. Ultrafast active plasmonics. *Nature Photonics* **3**, 55–58 (2008).

[489] Bates, M., Huang, B., Dempsey, G. T. & Zhuang, X. Multicolor Super-Resolution Imaging with Photo-Switchable Fluorescent Probes. *Science* **317**, 1749–1753 (2007).

[490] Rust, M. J., Bates, M. & Zhuang, X. Sub-diffraction-limit imaging by stochastic optical reconstruction microscopy (STORM). *Nature Methods* **3**, 793–796 (2006).

[491] Hess, S. T., Girirajan, T. P. K. & Mason, M. D. Ultra-High Resolution Imaging by Fluorescence Photoactivation Localization Microscopy. *Biophysical Journal* **91**, 4258–4272 (2006).

[492] Betzig, E. *et al.* Imaging Intracellular Fluorescent Proteins at Nanometer Resolution. *Science* **313**, 1642–1645 (2006).

[493] Ebbesen, T. W., Lezec, H. J., Ghaemi, H. F., Thio, T. & Wolff, P. A. Extraordinary optical transmission through sub-wavelength hole arrays. *Nature* **391**, 667–669 (1998).

[494] Kildishev, A. V., Boltasseva, A. & Shalaev, V. M. Planar Photonics with Metasurfaces. *Science* **339**, 1232009–1232009 (2013).

[495] Groß, H. *et al.* Parallel mapping of optical near-field interactions by molecular motor-driven quantum dots. *Nature Nanotechnology* **13**, 691–695 (2018).

[496] Wertz, E., Isaacoff, B. P., Flynn, J. D. & Biteen, J. S. Single-Molecule Super-Resolution Microscopy Reveals How Light Couples to a Plasmonic Nanoantenna on the Nanometer Scale. *Nano Letters* **15**, 2662–2670 (2015).

[497] Stranahan, S. M. & Willets, K. A. Super-resolution Optical Imaging of Single-Molecule SERS Hot Spots. *Nano Letters* **10**, 3777–3784 (2010).

[498] Aigouy, L. *et al.* Near-field scattered by a single nanoslit in a metal film. *Applied Optics* **46**, 8573–8577 (2007).

[499] Michaelis, J., Hettich, C., Mlynek, J. & Sandoghdar, V. Optical microscopy using a single-molecule light source. *Nature* **405**, 325–328 (2000).

[500] Kühn, S., Hettich, C., Schmitt, C., Poizat, J.-P. & Sandoghdar, V. Diamond colour centres as a nanoscopic light source for scanning near-field optical microscopy. *Journal of Microscopy* **202**, 2–6 (2001).

[501] Nitzsche, B. *et al.* Chapter 14 - Studying Kinesin Motors by Optical 3D-Nanometry in Gliding Motility Assays. In Wilson, L. & Correia, J. J. (eds.) *Methods in Cell Biology*, vol. 95 of *Microtubules, in Vitro*, 247–271 (Academic Press, 2010).

[502] Hess, H., Clemmens, J., Howard, J. & Vogel, V. Surface Imaging by Self-Propelled Nanoscale Probes. *Nano Letters* **2**, 113–116 (2002).

[503] Ruhnow, F., Zwicker, D. & Diez, S. Tracking Single Particles and Elongated Filaments with Nanometer Precision. *Biophysical Journal* **100**, 2820–2828 (2011).

[504] Palacci, H. *et al.* Velocity Fluctuations in Kinesin-1 Gliding Motility Assays Originate in Motor Attachment Geometry Variations. *Langmuir* **32**, 7943–7950 (2016).

[505] Nitzsche, B., Ruhnow, F. & Diez, S. Quantum-dot-assisted characterization of microtubule rotations during cargo transport. *Nature Nanotechnology* **3**, 552–556 (2008).

[506] Kerssemakers, J., Howard, J., Hess, H. & Diez, S. The distance that kinesin-1 holds its cargo from the microtubule surface measured by fluorescence interference contrast microscopy. *Proceedings of the National Academy of Sciences* **103**, 15812–15817 (2006).

[507] Gür, F. N., Schwarz, F. W., Ye, J., Diez, S. & Schmidt, T. L. Toward Self-Assembled Plasmonic Devices: High-Yield Arrangement of Gold Nanoparticles on DNA Origami Templates. *ACS Nano* **10**, 5374–5382 (2016).

[508] Acuna, G. P. *et al.* Fluorescence Enhancement at Docking Sites of DNA-Directed Self-Assembled Nanoantennas. *Science* **338**, 506–510 (2012).

[509] van den Heuvel, M. G. L., Butcher, C. T., Smeets, R. M. M., Diez, S. & Dekker, C. High Rectifying Efficiencies of Microtubule Motility on Kinesin-Coated Gold Nanostructures. *Nano Letters* **5**, 1117–1122 (2005).

[510] Sun, Y., McKenna, J. D., Murray, J. M., Ostap, E. M. & Goldman, Y. E. Parallax: High Accuracy Three-Dimensional Single Molecule Tracking Using Split Images. *Nano Letters* **9**, 2676–2682 (2009).

[511] Aharonovich, I. & Toth, M. Quantum emitters in two dimensions. *Science* **358**, 170–171 (2017).

[512] Sick, B., Hecht, B. & Novotny, L. Orientational Imaging of Single Molecules by Annular Illumination. *Physical Review Letters* **85**, 4482–4485 (2000).

[513] Ihara, T. & Kanemitsu, Y. Absorption cross-section spectrum of single CdSe/ZnS nanocrystals revealed through photoluminescence excitation spectroscopy. *Physical Review B* **92**, 155311 (2015).

[514] Olmon, R. L. *et al.* Optical dielectric function of gold. *Physical Review B* **86**, 235147 (2012).

[515] Liu, S.-Y. *et al.* Simultaneous Excitation and Emission Enhancement of Fluorescence Assisted by Double Plasmon Modes of Gold Nanorods. *The Journal of Physical Chemistry C* **117**, 10636–10642 (2013).

[516] Cahill, D. G. & Pohl, R. O. Thermal conductivity of amorphous solids above the plateau. *Physical Review B* **35**, 4067–4073 (1987).

[517] Incropera, F. *Fundamentals of Heat and Mass Transfer, Seventh Edition Binder Ready Version* (John Wiley and Sons, Chichester, 2011). OCLC: 746224526.

[518] Çengel, Y. A. & Ghajar, A. J. *Heat and Mass Transfer: Fundamentals & Applications* (McGraw Hill Education, New York, NY, 2015), fifth edition edn. OCLC: ocn870517093.

[519] Brown, R. H. & Twiss, R. Q. Correlation between Photons in two Coherent Beams of Light. *Nature* **177**, 27–29 (1956).

[520] Kitson, S. C., Jonsson, P., Rarity, J. G. & Tapster, P. R. Intensity fluctuation spectroscopy of small numbers of dye molecules in a microcavity. *Physical Review A* **58**, 620–627 (1998).

[521] Htoon, H. *et al.* Highly Emissive Multiexcitons in Steady-State Photoluminescence of Individual "Giant" CdSe/CdS Core/Shell Nanocrystals. *Nano Letters* **10**, 2401–2407 (2010).

[522] Castoldi, M. & Popov, A. V. Purification of brain tubulin through two cycles of polymerization–depolymerization in a high-molarity buffer. *Protein Expression and Purification* **32**, 83–88 (2003).

[523] Korten, T., Chaudhuri, S., Tavkin, E., Braun, M. & Diez, S. Kinesin-1 Expressed in Insect Cells Improves Microtubule in Vitro Gliding Performance, Long-Term Stability and Guiding Efficiency in Nanostructures. *IEEE Transactions on NanoBioscience* **15**, 62–69 (2016).

[524] Kern, W. The Evolution of Silicon Wafer Cleaning Technology. *Journal of The Electrochemical Society* **137**, 1887–1892 (1990).

[525] Ovesný, M., Křížek, P., Borkovec, J., Švindrych, Z. & Hagen, G. M. ThunderSTORM: A comprehensive ImageJ plug-in for PALM and STORM data analysis and super-resolution imaging. *Bioinformatics* **30**, 2389–2390 (2014).

[526] Bharadwaj, P., Bouhelier, A. & Novotny, L. Electrical Excitation of Surface Plasmons. *Physical Review Letters* **106**, 226802 (2011).

[527] Arnspang, E. C., Brewer, J. R. & Lagerholm, B. C. Multi-Color Single Particle Tracking with Quantum Dots. *PLOS ONE* **7**, e48521 (2012).

List of publications

This thesis is based in parts on the following publications:

Chapter 7:

H. Groß, J. M. Hamm, T. Tufarelli, O. Hess, B. Hecht
Near-field strong coupling of single quantum dots
Science Advances **4**, eaar4906 (2018)

Chapter 8:

H. Groß, H. S. Heil, J. Ehrig, F. W. Schwarz, B. Hecht, S. Diez
Parallel mapping of optical near-field interactions by molecular motor-driven quantum dots
Nature Nanotechnology **13**, 691-695 (2018)

Further publication by the author:

K. Chen, G. Razinskas, H. Vieker, **H. Groß**, X. Wu, André Beyer, A. Gölzhäuser, B. Hecht
High-Q, Low-Mode-Volume and Multiresonant Plasmonic Nanoslit Cavities Fabricated by Helium Ion Milling
Nanoscale **10**, 17148-17155 (2018)

Acknowledgments

A thesis of this extend would have never been possible without the constant help and support of many. Here, I'd like to acknowledge the most important colleagues and friends who I got to know throughout the past years and who I was able to rely on for scientific as well as private matters.

First of all, I'd like to thank **Prof. Dr. Bert Hecht** for mentoring me throughout all these years and for always taking care of my funding. Thank you for guiding me through my projects and for the fact thank you always had an open ear for me. I also really appreciate the freedom you have given me to pursue my own ideas.

My special thanks goes to **Prof. Dr. Ortwin Hess**, **Dr. Joachim Hamm** and **Dr. Tommaso Tufarelli** who were the main contributor of the theoretical modeling of my data. You have always been supportive and I really enjoyed the kick-off meeting in London and the countless Skype conversations.

I also appreciate the work and help of the colleagues from Dresden, **Prof. Dr. Stefan Diez**, **Dr. Jens Ehring**, **Hannah Heil** and **Dr. Friedrich Schwarz**, who performed the experimental part and the data analysis of the microtubule project. I also enjoyed the meetings on multiple occasions and I am thankful for the pleasant and productive collaboration.

For the help in the clean room and the chemistry lab I would like to thank **Prof. Dr. Martin Kamp**, **Monika Emmerling** and **Sabine Voll**. Being able to count on this kind of reliable technical support has really helped to speed up my work.

In case of a problem with my optical setup I was able to rely on **Dr. Xiaofei Wu** who had always time for me to share his knowledge and experience.

I always enjoyed spending time in the office with my friends **Dr. Thorsten Feichtner**, **Enno Krauss**, **Alexander Knapp** and **Peter Geisler**. Coffee break and discussions beyond physics have made everyday life at the university worthwhile.

I also want to thank the **rest of EP 5** for a friendly and comfortable atmosphere throughout all these years and the many afternoon cakes.

For my recreational time on many evenings and weekends I want to thank all my teammates of my **Ultimate Frisbee team**. Being able to free up my mind has really helped me a lot to get a fresh start when I was stuck on a problem.

Of course, the persistent support from my **family** has been indispensable. I thank my parents, my sister and her fiancé for their time and the fact that I know that I can always count on them.

Finally, I would like to thank my fiancée **Anna** for all her support and love. Knowing to have someone like you who stands by me when things get tough has given me the confidence and motivation for this work.